



HAL
open science

Control of powder flowability of active pharmaceutical ingredients through spherical agglomeration : case studies of crystal structure retention

Aurelien Lemerrier

► **To cite this version:**

Aurelien Lemerrier. Control of powder flowability of active pharmaceutical ingredients through spherical agglomeration : case studies of crystal structure retention. Cristallographie. Normandie Université, 2023. Français. NNT : 2023NORMR037 . tel-04257340

HAL Id: tel-04257340

<https://theses.hal.science/tel-04257340>

Submitted on 25 Oct 2023

HAL is a multi-disciplinary open access archive for the deposit and dissemination of scientific research documents, whether they are published or not. The documents may come from teaching and research institutions in France or abroad, or from public or private research centers.

L'archive ouverte pluridisciplinaire **HAL**, est destinée au dépôt et à la diffusion de documents scientifiques de niveau recherche, publiés ou non, émanant des établissements d'enseignement et de recherche français ou étrangers, des laboratoires publics ou privés.

THÈSE

Pour obtenir le diplôme de doctorat

Spécialité CHIMIE

Préparée au sein de l'Université de Rouen Normandie

Control of powder flowability of active pharmaceutical ingredients through spherical agglomeration: case studies of crystal structure retention

Présentée et soutenue par
AURELIEN LEMERCIER

Thèse soutenue le 02/06/2023
devant le jury composé de

M. HERVE MUHR	MAITRE DE CONFERENCES, UNIVERSITE DE LORRAINE	Rapporteur du jury
M. KHASHAYAR SALEH	PROFESSEUR DES UNIVERSITES, UNIV TECHNOLOGIE COMPIEGNE UTC COMPIEGNE	Rapporteur du jury
M. YOHANN CARTIGNY	MAITRE DE CONFERENCES, Université de Rouen Normandie	Membre du jury
MME CHRISTELLE GOUTAUDIER	PROFESSEUR DES UNIVERSITES, UNIVERSITE LYON 1 CLAUDE BERNARD	Président du jury
M. GÉRARD COQUEREL	PROFESSEUR DES UNIVERSITES, Université de Rouen Normandie	Directeur de thèse
M. MASSIMILIANO FORCATO	,	Co-directeur de thèse

Thèse dirigée par GÉRARD COQUEREL (SCIENCES ET METHODES SEPARATIVES) et MASSIMILIANO FORCATO (Université de Rouen Normandie)





Normandie Université

THÈSE

Pour obtenir le diplôme de doctorat

Spécialité CHIMIE

Préparée au sein de l'Université de Rouen Normandie

**Control of Powder Flowability of Active Pharmaceutical
Ingredients through Spherical Agglomeration:
Case studies of crystal structure retention**

Présentée et soutenue par

AURÉLIEN LEMERCIER

Soutenance de thèse prévue le 02/06/2023
devant le jury composé de

Mme GOUTAUDIER Christelle	PROFESSEUR DES UNIVERSITÉS, Université de Lyon 1	Membre du jury
M. SALEH Khashayar	PROFESSEUR DES UNIVERSITÉS, Université Technologique de Compiègne	Rapporteur du jury
M. MUHR Hervé	DIRECTEUR DE RECHERCHE, Université de Lorraine	Rapporteur du jury
M. COQUEREL Gérard	PROFESSEUR DES UNIVERSITÉS, Université de Rouen Normandie	Directeur de thèse
M. FORCATO Massimiliano	DOCTEUR, Zach System	Co-directeur de thèse
M. CARTIGNY Yohann	MAITRE DE CONFERENCES, Université de Rouen Normandie	Encadrant de thèse

Thèse dirigée par GÉRARD COQUEREL (Sciences et Méthodes Séparatives) et MASSIMILIANO FORCATO (Zach System)



Remerciements

Je tiens tout d'abord à remercier le Prof. Gérard Coquerel pour son accueil au sein du laboratoire SMS durant ces 6 dernières années. Merci pour l'opportunité que vous m'avez offerte en me proposant ce sujet de thèse, pour votre soutien scientifique ainsi que l'ensemble des échanges que nous avons pu avoir, tant sur la cristallisation que sur d'autres sujets !

J'aimerais également remercier le Dr. Massimiliano Forcato, sans qui cette thèse n'aurait pas existé. Merci pour ton accueil dans ton équipe R&D, d'avoir suivi ce travail et de m'avoir laissé explorer des voies qui sortaient du chemin initial de cette thèse.

Merci au Pr. Khashayar Saleh et au Dr Hervé Muhr d'avoir accepté de rapporter cette thèse. Vos remarques et la discussion lors de la soutenance ont permis d'apporter de nouvelles perspectives à ce travail. Merci pour le temps que vous y avez consacré. Merci au Pr. Christelle Goutaudier qui a accepté de présider cette soutenance.

Merci à mes collègues de Zach System pour leur accueil lors de mes passages dans l'entreprise.

Je tiens à remercier particulièrement le Dr Yohann Cartigny sans qui cette thèse ne serait probablement pas ce qu'elle est. Un énorme merci pour votre accompagnement qui a commencé avant cette thèse, pour votre dévouement dans la lecture de mes rapports, votre investissement et l'ensemble de vos conseils durant ces années. Je ne vous retiendrais qu'un seul défaut : votre passion pour la clarinette....

Merci à l'ensemble des membres du laboratoire SMS, permanents et non permanents pour les moments que j'ai pu échanger avec vous, avec une pensée particulière pour Marine et Laureline. Merci aux anciens docteurs pour leurs conseils et bonne chance aux suivants !

Enfin, merci à tous ceux qui m'ont accompagné de près ou de loin pendant ces années d'études.

Table of Contents

GENERAL INTRODUCTION	1
1 GENERALITIES	6
1.1 THERMODYNAMICS AND HETEROGENEOUS EQUILIBRIA.....	6
1.1.1 <i>Thermodynamics</i>	6
1.1.2 <i>Heterogeneous equilibria</i>	6
1.1.2.1 Notion of system and phase	6
1.1.2.2 Introduction to polymorphism	8
1.1.2.3 Unary phase diagram	8
1.1.2.1 Polymorphism in unary system	9
1.1.2.2 Binary phase diagram	10
1.1.2.3 Polymorphism in binary system	13
1.1.3 <i>Salt, solvates and hydrates</i>	14
1.1.3.1 Salt	14
1.1.3.2 Solvates and Hydrates.....	14
1.1.3.3 Ternary phase diagram	18
1.2 CRYSTAL STRUCTURE AND CRYSTAL GENESIS:.....	19
1.2.1 <i>Crystal Structures</i>	19
1.2.1.1 Crystal Lattices	19
1.2.1.2 Symmetry in crystals	19
1.2.1.3 Space group.....	21
1.2.2 <i>Crystal genesis</i>	21
1.2.2.1 Driving force of crystallization from solution: Supersaturation	21
1.2.2.2 Classical Nucleation Theory	22
1.2.2.3 Crystal Growth.....	24
1.2.2.4 Growth kinetics	24
1.2.2.5 Ostwald ripening.....	25
1.3 STATE OF THE ART OF SPHERICAL AGGLOMERATION.....	25
1.3.1 <i>Spherical crystallization</i>	25
1.3.2 <i>Ammonia diffusion</i>	25
1.3.3 <i>Quasi-Emulsion Solvent Diffusion (QESD)</i>	26
1.3.4 <i>Spherical agglomeration</i>	27
1.3.4.1 Wetting period	28
1.3.4.2 Consolidation and growth period.....	30
1.3.4.3 Breakage and attrition	32
1.3.4.4 Experimental parameters influencing spherical agglomeration	33
2 HYDRATION – DEHYDRATION BEHAVIOR OF PREDNISOLONE, A CASE STUDY ON AN ISOMORPHOUS DESOLVATE.....	45
2.1 STATE OF THE ART OF PREDNISOLONE CRYSTALLINE LANDSCAPE	45
2.1.1 <i>Introduction on Prednisolone</i>	45
2.1.2 <i>Prednisolone polymorphic landscape</i>	45
2.1.3 <i>Prednisolone sesquihydrate</i>	47
2.2 HYDRATION/DEHYDRATION BEHAVIOR OF PREDNISOLONE SESQUIHYDRATE	48
2.2.1 <i>Thermal behavior of prednisolone sesquihydrate</i>	48
2.2.1.1 Obtention of the sesquihydrate	48
2.2.1.2 TGA-DSC analyses of prednisolone sesquihydrate	49
2.2.1.3 Hot-stage microscopy of prednisolone sesquihydrate.....	52
2.2.2 <i>Hydration/dehydration behavior versus RH of prednisolone</i>	57
2.3 CLASSIFICATION OF THE SESQUIHYDRATE	59
2.3.1 <i>Energetically based classification</i>	60
2.3.2 <i>Dehydration mechanistic based classification</i>	60

2.4	CONCLUSIONS ON THE PREDNISOLONE ANHYDROUS DESOLVATE	62
3	CHARACTERIZATION OF SAFINAMIDE MESYLATE SOLID-STATE LANDSCAPE.....	65
3.1	SAFINAMIDE MESYLATE	65
3.2	SAFINAMIDE MESYLATE POLYMORPHISM.....	65
3.2.1	<i>Characterization of the Safinamide mesylate high temperature form (A1)</i>	66
3.2.2	<i>Characterization of Safinamide mesylate low temperature form (A2)</i>	69
3.2.3	<i>Structure filiation between A1 and A2</i>	72
3.3	STUDY OF THE POLYMORPHIC TRANSITION A1 ⇔ A2	75
3.3.1	<i>Thermal behavior of anhydrous safinamide mesylate</i>	75
3.3.1.1	Monitoring of the polymorphic transition with temperature-controlled x-ray diffraction by using In-situX® measurement.....	76
3.3.2	<i>Calculation of the A1 ⇔ A2 activation energy of the polymorphic transition</i>	77
3.4	SAFINAMIDE MESYLATE HEMI-HYDRATE.....	80
3.4.1	<i>Characterization of Safinamide mesylate H1</i>	80
3.4.2	<i>Study of the binary system Safinamide mesylate/water</i>	83
3.4.2.1	Thermodynamic behavior of binary system Safinamide mesylate/water	83
3.4.2.2	Safinamide mesylate behavior vs relative humidity.....	85
3.4.2.3	Effect of storage conditions.....	88
3.5	CONCLUSIONS ON THE SAFINAMIDE CRYSTALLINE LANDSCAPE	89
4	DEVELOPMENT OF THE SPHERICAL AGGLOMERATION PROCESS OF SAFINAMIDE MESYLATE	93
4.1	CRYSTALLIZATION OF SAFINAMIDE MESYLATE.....	93
4.1.1	<i>Industrial crystallization procedure</i>	93
4.1.2	<i>Monitoring of the crystalline phase during crystallization</i>	94
4.2	SPHERICAL AGGLOMERATION OF SAFINAMIDE MESYLATE	98
4.2.1	<i>Selection of the agglomeration solvents</i>	98
4.2.1.1	Determination of the solvent system from the literature	98
4.2.1.2	Determination of the solvent system based on phase equilibria and European pharmacopoeia	100
4.2.2	<i>Presentation of the agglomeration setup</i>	102
4.2.2.1	Geometry of the crystallizer	102
4.2.2.2	Determination of the stirring setup	103
4.2.3	<i>Development of the spherical agglomeration process</i>	109
4.2.3.1	Evaluation of the most influencing parameters	109
4.2.3.2	Effect of water amount in bridging liquid on the crystalline phase of SAFIM.....	115
4.2.3.3	Optimization of SAFIM spherical agglomeration process	118
4.2.4	<i>Study on the amount of residual solvent after agglomeration procedure</i>	126
4.3	CONCLUSIONS AND PERSPECTIVES ON THE SPHERICAL AGGLOMERATION OF SAFIM.....	127
5	FEASIBILITY OF THE SPHERICAL AGGLOMERATION IN A COUETTE TAYLOR REACTOR	132
5.1	INTRODUCTION TO THE COUETTE TAYLOR TECHNOLOGY	132
5.1.1	<i>Historical of Couette-Taylor technology</i>	132
5.1.2	<i>Presentation of the Couette Taylor crystallizer</i>	133
5.2	APPLICATION OF SPHERICAL AGGLOMERATION IN COUETTE TAYLOR CRYSTALLIZER	134
5.2.1	<i>State of the art</i>	134
5.2.2	<i>Spherical Agglomeration of Timapiprant with Couette Taylor Reactor</i>	136
5.2.2.1	Experimental conditions	136
5.2.2.2	Results	137
5.2.3	<i>Spherical agglomeration of SAFIM</i>	142
5.2.3.1	Experimental conditions	142
5.2.3.2	Results	143
5.3	DISCUSSIONS AND PERSPECTIVES	149
	GENERAL CONCLUSION	153
	REFERENCES	158

APPENDICES	I
APPENDIX I	I
APPENDIX II	VI
APPENDIX III	VIII
APPENDIX IV	XI

Table of abbreviations

AD	Ammonia Diffusion
API	Active Pharmaceutical ingredient
ASD	Agglomerate Size Distribution
BL	Bridging Liquid
BSR	Bridging Liquid to Solid Ratio
CI	Carr Index
CPP	Critical Process Parameters
CQA	Critical Quality Attributes
CTR	Couette Taylor Reactor
DFT	Density Functional Theory
DoE	Design of Experiment
DRS	Dehydration-Rehydration Classification System
DSC	Differential Scanning Calorimetry
DVS	Dynamic Vapor Sorption
HR	Hausner Ration
HS-GC	Head Space Gas Chromatography
ICH	International Council for Harmonisation
IUPAC	International Union of Pure and Applied Chemistry
KF	Karl Fischer
LRO	Long Range Order
MS	Mass Spectroscopy
OFAT	One Factor At a Time
PBC	Periodic Bond Chain
PSD	Particle Size Distribution
QbD	Quality by Design
QESD	Quasi Emulsion Solvent Diffusion
RPM	Rotation Per Minute
SA	Spherical Agglomeration
SAFIM	Safinamide Mesylate
SC	Spherical Crystallization
SOF	Statistical Occupancy Factor
SRO	Short Range Order
TGA	Thermo-Gravimetric Analysis
TR-XRD	Temperature Resolved X-Ray Diffraction
XRPD	X-Ray Powder Diffraction

Nomenclature

<i>Symbol</i>	<i>Unit</i>	<i>Definition</i>
Ea	$\text{kJ}\cdot\text{mol}^{-1}$	activation energy
Mw	$\text{g}\cdot\text{mol}^{-1}$	molar mass
P	bar / Pa	pressure
RH	%	Relative humidity
T	$^{\circ}\text{C}$ / K	temperature
Tg	$^{\circ}\text{C}$	Glass transition
ΔG	J	Free energy variation
ΔH	J	Enthalpy variation
ΔS	$\text{J}\cdot\text{K}^{-1}$	Entropy variation

Table 1-1: Type of invariant transformations in a binary equilibrium phase diagram at constant pressure (L and S referred to as Liquid phase and solid phase, respectively).....	11
Table 1-2: The seven crystal systems and their associated point group.....	20
Table 1-3: Summary of experimental (E) and modeling (M) studies focused on the mechanisms occurring during spherical agglomeration, reproduced from Pitt et al. ⁶⁸	33
Table 1-4: Chow's classification for the choice of the bridging liquid.....	34
Table 1-5: Agglomeration parameters and their influence on the process.....	42
Table 2-1: Crystallographic data of prednisolone Form I and Form II from Suitchmezian ⁸¹	46
Table 2-2: Crystallographic data of prednisolone sesquihydrate from Suitchmezian ⁸¹	47
Table 3-1: crystallographic parameters of SAFIM A1 according to Pawlak and Schlueter.....	66
Table 3-2: crystallographic parameters of SAFIM A2 according to Pawlak and Schlueter.....	69
Table 3-3: Different methods used for determination of the activation energy in non-isothermal conditions.....	78
Table 3-4: Thermal data for SAFIM at six different heating rates (average of two set of measurements).....	78
Table 3-5: Structure parameters of SAFIM H1 according to Pawlak and Schlueter.....	80
Table 4-1: non-exhaustive list of agglomerated material with spherical crystallization processes and their associated solvent system.	98
Table 4-2: Chow's classification for the choice of the bridging liquid.....	100
Table 4-3: Various polar and non-polar solvent exhibiting an oiling out for the spherical agglomeration of SAFIM.	100
Table 4-4: solubilities of SAFIM A1 in acetonitrile and n-heptane at different temperatures.....	101
Table 4-5: Comparison of the dispersion states for different stirrers as a function of the stirring rate.....	107
Table 4-6: Evolution of the emulsion of acetonitrile in n-heptane as a function of the stirring setup and stirring rate.....	108
Table 4-7: Monitoring of the agglomeration with a homogenization step performed with Ultra Turrax.	114
Table 4-8: Size of the initial particles and agglomerates before and after agglomeration process when using Ultra Turrax.	115
Table 4-9: Evolution of the crystalline form during the agglomeration process of SAFIM for different amount of water in acetonitrile.....	117
Table 4-10: first matrix of experiments for the DoE of SAFIM agglomeration process.	120
Table 4-11: Responses for every experiment of the first matrix of experiment.....	121
Table 4-12: Comparison of the agglomerate shape and particle size distribution between two experiments of the first design of experiment.....	122
Table 4-13: Extended matrix of experiments for the DoE of SAFIM spherical agglomeration.	123
Table 4-14: Responses for every experiment of the extended matrix of experiment.....	124
Table 4-15: Comparison between SAFIM properties before and after spherical agglomeration with the set of optimized conditions.	126
Table 5-1: Different experimental conditions used to perform spherical agglomeration of Timapiprant in CTR.	137
Table 5-2: Microscopy pictures of agglomerates after 8 hours of stirring from experiment 1 in CTR; agglomeration at 500 rpm with addition of toluene in the CTR.	137
Table 5-3: Experimental data from granulometric measurement; agglomeration in CTR (addition of toluene in CTR) at 500 rpm.	139
Table 5-4: Microscopy pictures of agglomerates from agglomeration in CTR; agglomeration at 500 rpm with precipitation of RM in CTR.....	140
Table 5-5: Experimental data from granulometric measurement; agglomeration in CTR (precipitation in CTR) at 500 rpm.	141
Table 5-6: Different experimental conditions used to perform SAFIM spherical agglomeration in CTR.	142
Table 5-7: Optical microscopy and scanning electron microscopy pictures of SAFIM after agglomeration in CTR for experiment 1.....	144

General Introduction

During the early 1990s, the switch from a phenotypic to a target-based approach for the research of new active pharmaceutical ingredients has led to the development of poorly water soluble and complex organic molecules. To improve bioavailability of such APIs, crystal size distribution, shape and crystallinity could be modified to enhance the rates of dissolution (e.g. micronization, amorphization, and polymorphic transformation). However, these modified crystals often exhibit low flowability properties impacting downstream processes (e.g., filtration, handling, storage, and tabletization). Therefore, attention has been paid to the control of micromeritic properties (*i.e.*, properties resulting from the particle size) of API powders (e.g., flowability, packability, compressibility, and dissolution rates). Granulation methods were developed to overcome these problems. Among these, spherical crystallization (SC) was developed to simultaneously improve intrinsic and assembled crystals micromeritic properties. SC combines crystallization and spheronization in one step, where more conventional methods such as wet granulation, require several steps of drying and mixing before obtaining a powder with the targeted micromeritic properties, increasing the manufacturing costs. Kawashima applied the SC to organic materials in a series of publications dedicated to the spherical agglomeration (SA, one method of SC).

The aim of this work is to develop the spherical agglomeration of an API and to isolate the agglomerates in the targeted crystalline form.

Chapter 1 focuses on the necessary generalities concerning the crystallization, the heterogeneous equilibria and the spherical agglomeration for the understanding of this work.

Chapter 2 depicts a new case of isomorphous desolvate (anhydrous form which shares a similar crystal packing that of the solvated form). A new form (Form III) of prednisolone is identified and characterized as an isomorphous desolvate of prednisolone sesquihydrate. The stability of this new form is discussed in terms of heterogeneous equilibria.

Chapter 3 focuses on the API to agglomerate: safinamide mesylate. The API being marketed as an anhydrous (**A1**), its crystalline landscape is thoroughly described, and the relative stability of the different solid phases discussed to identify the conditions to obtain pure **A1** and avoid the formation of the hemi-hydrate **H1**.

Chapter 4 is dedicated to the development of the spherical agglomeration process of safinamide mesylate. After the identification of the main experimental parameters, these last were investigated and optimized to obtain spherical agglomerates of safinamide with the required micromeritic properties and crystalline form.

Chapter 5 presents the spherical agglomeration in a Couette Taylor reactor and aims at demonstrating the possibility to perform the agglomeration process in such a geometry. The agglomeration in the reactor is first applied to Timapiprant, another API, in a series of batch experiments. Then, the process is applied to safinamide mesylate, first in a batch mode, and secondly

as a continuous process to enhance agglomeration productivity. The feasibility of spherical agglomeration in the Couette Taylor reactor is discussed and perspectives of development are proposed.

Chapter I

Generalities

1 GENERALITIES

1.1 THERMODYNAMICS AND HETEROGENEOUS EQUILIBRIA

1.1.1 Thermodynamics

Matter exists in three main states: gas, liquid and solid, differentiated by the different degrees of atomic or molecular orders. In the gaseous state, entities can move freely without interaction between each other (ideal case). In the liquid state, entities exhibit a Short-Range Order (SRO). In the solid state they can exhibit either an SRO, i.e. amorphous state, or a Long-Range Order (LRO), i.e. crystalline state.

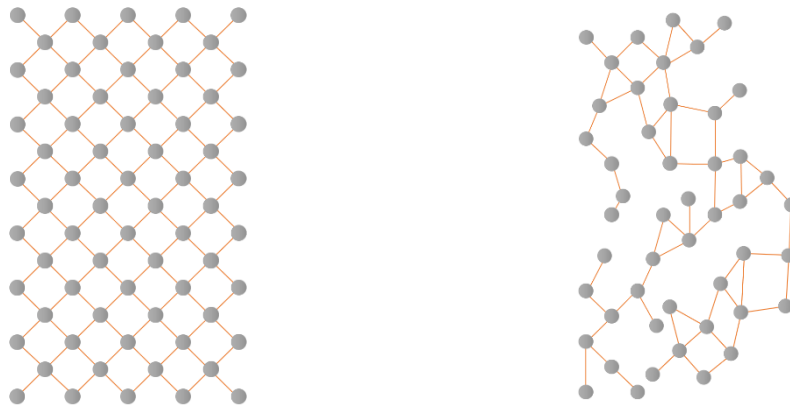


Figure 1-1: Schematic representation of LRO (left) and SRO (right)

Amorphous state can be defined having the structural characteristics of a liquid, but with much higher viscosity, a kind of “frozen” liquid state.¹ Amorphous materials present a glass transition temperature (T_g): below this temperature, the material is kinetically frozen into a thermodynamically out of equilibrium glassy state.²

Differently, the ideal crystalline state exhibits a LRO, consisting in a periodic, three dimensional and strict arrangement of molecules, ions, or atoms.

1.1.2 Heterogeneous equilibria

1.1.2.1 Notion of system and phase

A system can be defined as a part of the universe delimited by real or fictive boundaries (e.g.: flame, crystallizer, or calorimeter). In open systems, both matter and energy transfers with the surroundings take place. In a close system only energy transfers can occur, whereas isolated systems are characterized by total absence of transfers.

A phase is a part of the system considered as homogeneous with uniform physical and chemical properties (e.g.: temperature, composition, pressure).³

Under constant pressure, the Gibbs free energy relationship is defined as:

$$G = H - TS \quad \text{Equation 1-1}$$

With H the molar enthalpy, T the temperature, and S the entropy of the system

A system is considered in equilibrium when the condition of equation 1-2 applies:

$$d(G) = 0 \quad \text{Equation 1-2}$$

The most stable state of a system is reached when the value of G is the lowest possible value and any other $d(G) = 0$ equilibrium state will be considered as metastable (Figure 1-2).^{4,5}

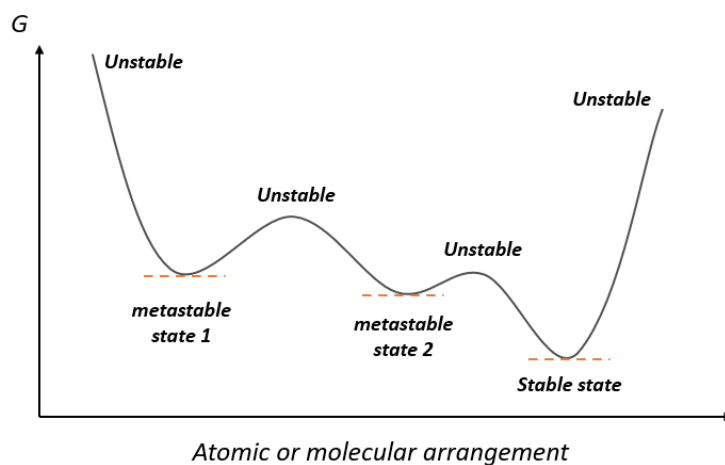


Figure 1-2 : Energetic landscape for a system exhibiting two metastable equilibria

In order to observe a phase transition between phase 1 and 2, the following condition must be fulfilled:

$$\Delta G = G_2 - G_1 < 0 \quad \text{Equation 1-3}$$

G_1 and G_2 are the Gibbs free energies of the initial and final states, respectively. This condition is reached by modifying the temperature, the pressure, or the composition of the system. According to Oswald rule of stages, the system can undergo several transitions (metastable states) before reaching the most stable equilibrium state.^{6,7}

The equilibria between phases of different nature (solid, liquid, gas) are called heterogeneous equilibria and can be graphically represented as a function of intensive variable (e.g., pressure and temperature) in a phase diagram.

The Gibb's phase rule⁸, also known as the variance (v), is the number of degrees of freedom, *i.e.*, the number of variables which can be changed without modifying the equilibrium of the system. It is given by:

$$v = C + N - \varphi \quad \text{Equation 1-4}$$

With C the number of independent component of the system, N the number of intensive variables, and φ the number of phases in equilibrium.

1.1.2.2 Introduction to polymorphism

Polymorphism, from the Greek poly (=many) and morph (=form) is “a solid crystalline phase of a given compound, resulting from the possibility of at least two different arrangements of the molecules of that compound in the solid state”.⁹ The polymorphic form of a drug substance or excipient can have a profound impact on multiple aspects, such as morphological, rheological, and biological properties, the efficiency of the production and formulation process, right of intellectual property protection. The interest in the solid-state properties of drugs has grown tremendously in recent decades.¹⁰

As seen previously, each phase has its own molar free energy which is temperature and pressure dependent. It's also the case for two polymorphic forms. These two solid forms can be related by either a monotropic or an enantiotropic relationship.¹¹

1.1.2.3 Unary phase diagram

If C (the number of independent components of the system) equals to 1, the system is constituted of one pure component. A convenient way to represent unary phase diagrams is to use the pressure and the temperature as the intensive variables ($N = 2$). The variance becomes therefore:⁵

$$v = 3 - \varphi \quad \text{Equation 1-5}$$

Unary phase diagrams could be represented as it follows (Figure 1-3):

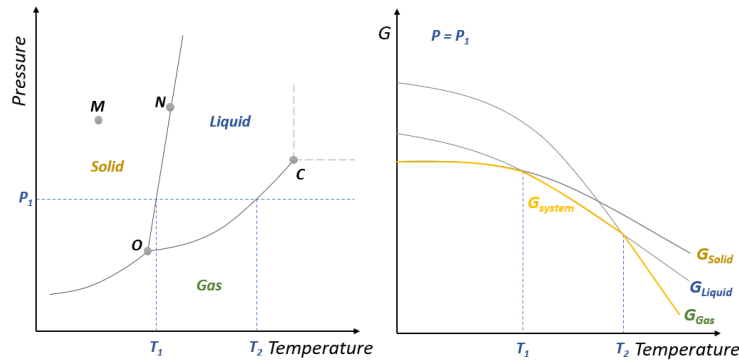


Figure 1-3: Unary (P, T) phase diagram (left) and (G, T) diagram at P_1 (right)

- At the point M: stability domain of the solid ($\varphi = 1$) and $\nu = 2$. Pressure and temperature can be modified without alteration of the system.
- At the point N: the solid and liquid coexist on this line, $\varphi = 2$ and $\nu = 1$. If one intensive variable is changed the other must be adjusted to remain on this equilibrium.
- At the point O: the solid, liquid and vapor coexist, $\varphi = 3$ and $\nu = 0$. There is no degree of freedom. Temperature and pressure are fixed at this point called the *triple point*.
 - At the point c: it corresponds to a merging of both liquid and solid phase into a unique one called super-critical fluid.
 - Gibb's free energy diagram for a given pressure (P_1) shows the evolution of the phases as the function of the temperature (figure 1-3 (right)). Such diagrams depict the Gibb's free energy of each phase (gas, liquid, and solid) The Gibb's free energy of the system corresponds to the lowest values of the 3 curves.

1.1.2.1 Polymorphism in unary system

Monotropy

Two phases are said monotropically related if one of them is more stable than the other, whatever P and T . Figure 1-4 depicts a unary phase diagram exhibiting a monotropic behavior. The G curve of form A is always lower than the G curve of form B until the melting of form A (T_2). Then, the G curve of the system corresponds to the G curve of A which is the most stable and there is no conversion of form A into form B.

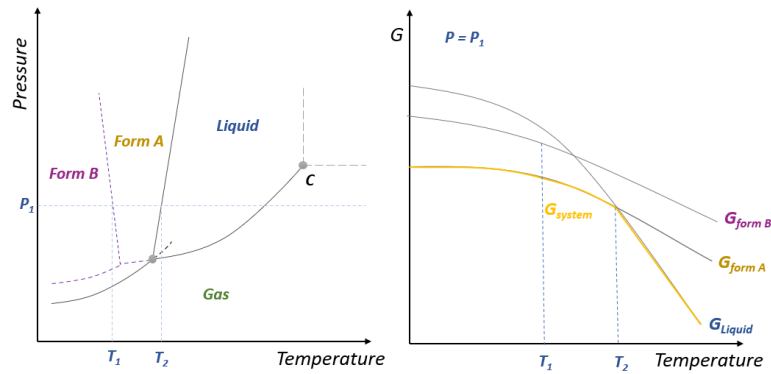


Figure 1-4: Unary phase diagram of a compound exhibiting two monotropic polymorphs with associated G_{curves} at a given pressure P_1

Enantiotropy

Two solid phases are enantiotropically related when, by changing temperature and- or pressure, there is a reversibility of the transition between the two phases. In such cases, the unary phase diagram of the corresponding system exhibits two stability domains corresponding to these two solids. Figure 1-5 is an example of such behavior. The G curve of the system (yellow curve, Figure 1-5) first corresponds to the G curve of form B. However, at T_1 , G curve of A become lower than G curve of B. Therefore, form A become the stable form and G curve of the system fit with G curve of A until the melting T_2 .

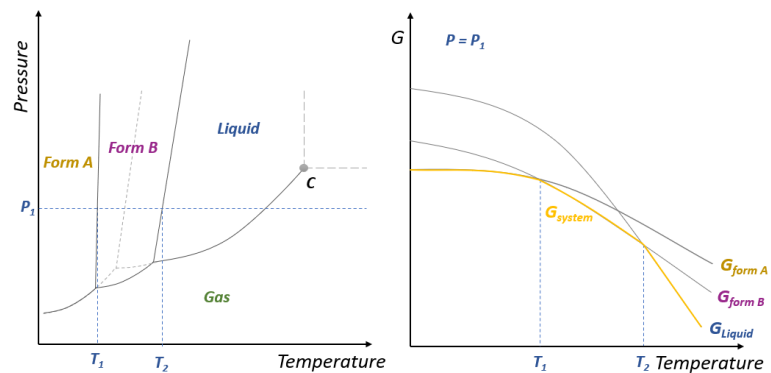


Figure 1-5: Unary phase diagram of a compound exhibiting two enantiotropic polymorphs with associated G_{curves} at P_1 . Metastable equilibria are represented is dashed lines.

In order to predict thermodynamic relationship between polymorphs, several rules have been proposed¹². One of the most accepted is the “Heat of fusion rule” by Burger and Ramburger:¹³

- The heat of fusion rule states that if the higher melting polymorph has the lower heat of fusion, then the two polymorphs are enantiotropic, otherwise they exhibit a monotropic behavior.

1.1.2.2 Binary phase diagram

Binary phase diagrams deal with 2 independent components (A and B). A new intensive variable is then integrated to the variance: the composition in A and B.

$$X_A = \frac{n_A}{n_A+n_B} \quad X_B = \frac{n_B}{n_A+n_B} \quad X_A + X_B = 1 \quad \text{Equation 1-6}$$

With X the molar fraction of A or B , and n the number of moles of A or B .

The graphical representation of such a system is a 3D diagram P, T , and composition (% A or % B).¹⁴ However, these diagrams are commonly represented at a fixed pressure (isobaric representation).

The variance is expressed as follow ($N=1$, P is fixed):

$$v = 3 - \phi \quad \text{Equation 1-7}$$

In these systems, 3 phases can be simultaneously in equilibrium giving rise to an equilibrium for which the variance is equal to 0 (= invariant equilibria). The different possible invariant equilibria that can be encountered in binary system are listed in Table 1-1.^{15,16}

Table 1-1: Type of invariant transformations in a binary equilibrium phase diagram at constant pressure (L and S referred to as Liquid phase and solid phase, respectively)

Name of the equilibrium	Eutectic	Peritectic	Monotectic	Metatectic
equilibrium	$L \leftrightarrow S1 + S2$	$S1 + L \leftrightarrow S2$	$L1 \leftrightarrow S1 + L2$	$S1 \leftrightarrow S2 + L$
Name of the equilibrium	Eutectoid	Peritectoid	Monotectoid	Syntectic
equilibrium	$S1 \leftrightarrow S2 + S3$	$S1 \leftrightarrow S2 + S3$	$S1a \leftrightarrow S1b + S2$	$L1 + L2 \leftrightarrow S$

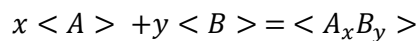
Among these invariant equilibria, we will describe those that we have encountered during this study.

Eutectic invariant:



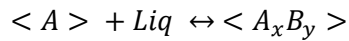
It corresponds to the crystallization of a liquid phase into two different solid phases. The reaction takes place at a given temperature (eutectic temperature) and at a composition called eutectic point (point E, Figure 1-6).

Defined compound:



A defined compound, either stoichiometric or not, is obtained by the crystallization of the different components in a unique and original crystalline phase. It is represented by a vertical straight line on a binary phase diagram in the case of stoichiometric compound (Figure 1-6, red line).

Peritectic invariant:



In our case, it corresponds to the melting of the defined compound $A_x B_y$: upon melting it decomposes into a liquid and a new solid phase, $\langle A \rangle$ in our example.

Figure 1-6 is an example of an isobaric representation of binary systems.

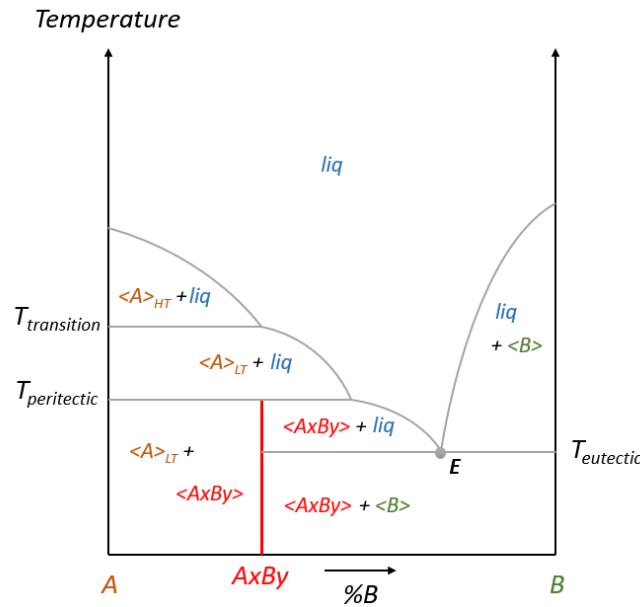


Figure 1-6: Isobaric binary phase diagram exhibiting: a stoichiometric compound (vertical red line), a eutectic invariant (horizontal line at $T_{eutectic}$), a peritectic transition (horizontal line at $T_{peritectic}$), and a polymorphic transition (horizontal line at $T_{transition}$)

Lever rule:

The phases in equilibrium and their compositions could be directly determined from the phase diagram. In order to deduce the proportion of each phases, the *lever rule* can be used.¹⁷ This is a consequence of the matter conservation during transformation of phases and it is a mathematical tool based on the reading of the tie line (*i.e.*, a line that associates the different phases in equilibrium in biphasic domain, here the segment [MN] at T_x , Figure 1-7). Hence, at the composition x , the weight fractions of liquid and solid $\langle A \rangle$ are:

$$w^{liq} = \frac{[MX]}{[MN]} \text{ and } w^{sol} = \frac{[XN]}{[MN]}$$

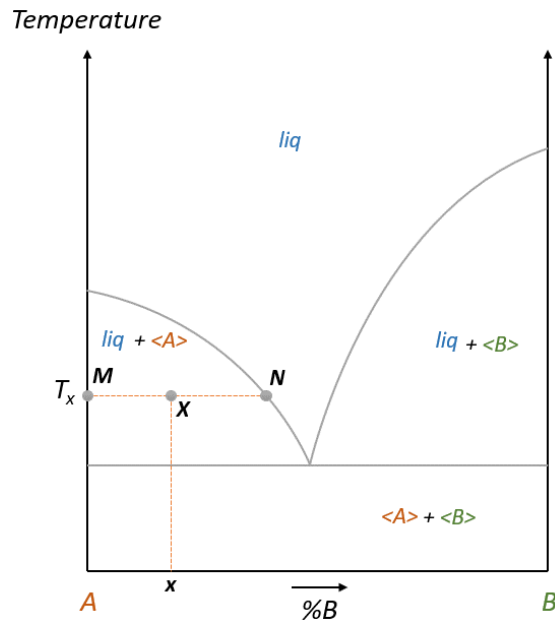


Figure 1-7: Isobaric binary phase diagram with a tie line (orange horizontal dashed line)

1.1.2.3 Polymorphism in binary system

In binary system, when two polymorphs are in an enantiotropic relationship, the binary phase diagram exhibits an invariant equilibrium at $T_{\text{transition}}$:



Solid/solid transition can also be graphically represented on a binary phase diagram with a horizontal line at $T_{\text{transition}}$ (Figure 1-6).

In the case of two polymorphs that are in a monotropic relationship, one polymorph remains stable whatever the temperature and composition. An example of binary phase diagram of two monotropic polymorphs is represented in Figure 1-8. A_{HT} is the stable form. Dashed lines correspond to the equilibrium of the metastable form A_{LT} with B.

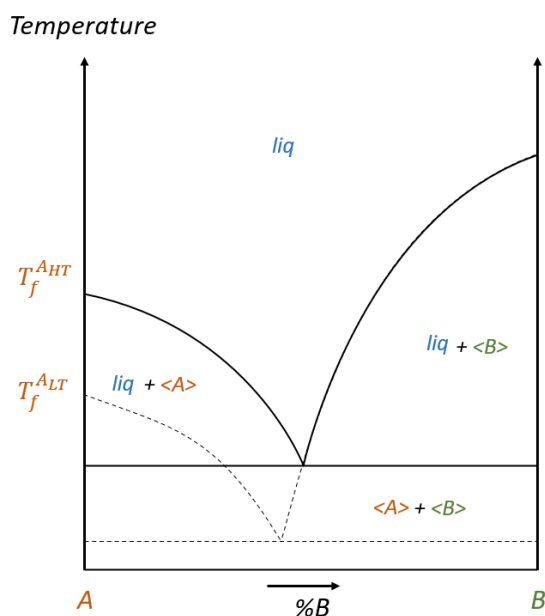


Figure 1-8: Schematic representation of a binary system with a polymorphic pure component exhibiting a monotropic behavior. Metastable equilibria are represented in dashed lines

1.1.3 Salt, solvate and hydrate

1.1.3.1 Salt

According to *Compendium of chemical Terminology* provided by the IUPAC, a salt is a “chemical compound consisting of an assembly of cations and anions”.¹⁸ Thus, for a pharmaceutical salt, it comprises a cationic or anionic active pharmaceutical ingredient (API) and a counter ion that might be molecular or monatomic (e.g., a halide anion). The requirement for charge balance means that a salt must have a definite stoichiometry. Salt formation is one of the primary solid-state approaches used to modify the physical properties of APIs. Among these properties, some of them are deciding factors for the APIs commercialization, such as stability (regarding to heat, pH, stress, etc.), solubility, dissolution rate and bioavailability.¹⁹

1.1.3.2 Solvate and Hydrate

Haleblian²⁰ defined a solvate as a crystalline molecular compound in which molecules of the solvent of crystallization are incorporated into the host lattice, consisting of unsolvated molecules. A hydrate is a special case of the class of solvates when the incorporated solvent is water. The presence of solvent molecules in the crystal lattice influences the intermolecular interactions and confers unique physical properties to each solvate. Therefore, a solvate has its own characteristic values of internal energy, enthalpy, entropy, Gibbs free energy, and thermodynamic activity. Consequently, the solubility and dissolution rate of a solvate differ from those of the corresponding unsolvated phase and can result in differences in bioavailability of drugs. Solvation and desolvation phenomena occur in suspension but also through solid/vapor equilibria (e.g., during storage), as a function of the solvent

partial pressure. In order to characterize such transitions, a thermodynamic approach dedicated to liquid/solid and gas/solid equilibria could be helpful.²¹

1.1.3.2.1 Liquid/solid equilibria

In the presence of solvates, the binary phase diagram between a constituent A and a solvent S exhibits a defined compound at a discrete stoichiometry $\langle A, xS \rangle$. A majority of solvates present a non-congruent melting on heating thanks to a peritectic transition:

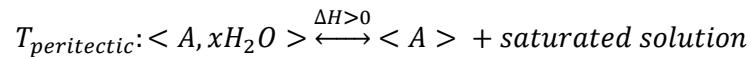


Figure 1-9 shows an example of a binary phase diagram A/H_2O with the presence of a stoichiometric hydrate.

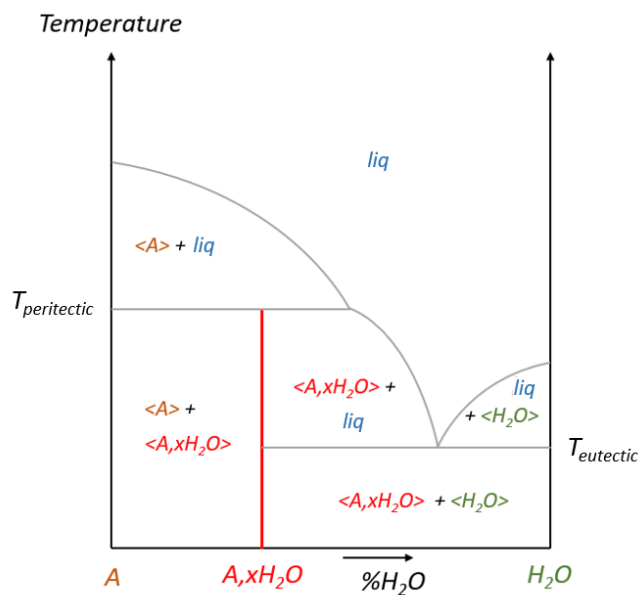


Figure 1-9: Schematic representation of a binary system with a stoichiometric hydrate

1.1.3.2.2 Gas/Solid equilibria

When the gas is considered as a perfect gas, the vapor pressure of a solvent at a given temperature is defined by:

$$P_{solvent} = x_{solvent} * P_{total} \tag{Equation 1-8}$$

With $x_{solvent}$ the molar fraction of solvent and P_{total} the total pressure of the system

When considering water as the solvent, Relative Humidity (RH) is defined as:

$$\%RH_{T=cst} = \frac{P_{H_2O}}{P_{H_2O}^{sat}} * 100 \quad \text{Equation 1-9}$$

With $P_{H_2O}^{sat}$ the saturation partial vapor pressure of water and P_{H_2O} the partial pressure of water at a given temperature.

The reactivity of a solid with water vapor is described by its hygroscopicity (*i.e.*, the ability of a material to capture water).²² When a dried powder is in contact of the atmosphere containing water vapor, two type of phenomena could occur:

- Adsorption: water molecules are bonded to the surface of the powder.
- Absorption: water molecules are integrated into the crystal lattice of the initial solid, with generation of a hydrated form.

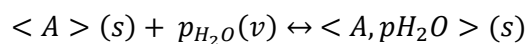
1.1.3.2.3 Behavior of solids during hydration

When the powder absorbs water molecules above a critical RH until formation of a saturated solution, the solid is classified as deliquescent.

If a hydrate powder evolves spontaneously (under ambient P_{H_2O}) into a phase with a lower degree of hydration, the hydrate is qualified as “efflorescent”.

The incorporation of water in the crystallized solid (hydration), occurs over a minimum value of RH. A hydrated solid could be classified in two different families: stoichiometric or non-stoichiometric hydrates. The classification of different hydrates could be understood thanks to a thermodynamic approach based on solid/gas equilibria.^{12,23}

The equilibrium of hydration in isothermal conditions is given by the reaction:



In such cases, the number of independent components is 2 ($\langle A \rangle$, water), φ the number of phases and the temperature is fixed. The variance becomes:

$$v = 3 - \varphi \quad \text{Equation 1-10}$$

For a stoichiometric hydrate, the water content in the solid is well-defined (= defined compound) and the hydrate and the anhydrous form have a different crystal structure. The variance of the equilibrium is reduced to $v = 0$ ($\varphi = 3$: A (anhydrous), water, and A, pH_2O (hydrate)) implying that there is a discrete water partial pressure of hydration, P_{hydr} at a given temperature.

For non-stoichiometric hydrates, the incorporated water in the solid does not affect the global crystal structure. By consequence, the structures of the solid phases involved in the equilibrium are the same. The variance of the system is reduced to $\nu = 1$. Only one intensive parameter of the system, P_{H_2O} , can vary without altering the nature of the equilibrium: there is no discrete value for hydration but a wide range of RH. The consequence is that the quantity of water molecules in the solid can vary progressively as a function of RH.

The stoichiometric or non-stoichiometric behavior of hydrates can be characterized by monitoring the evolution of the mass of a solid versus the relative humidity variation at a given temperature (Gravimetric Vapor Sorption experiments). Such monitoring leads to isotherm sorption plots represented on Figure 1-10.

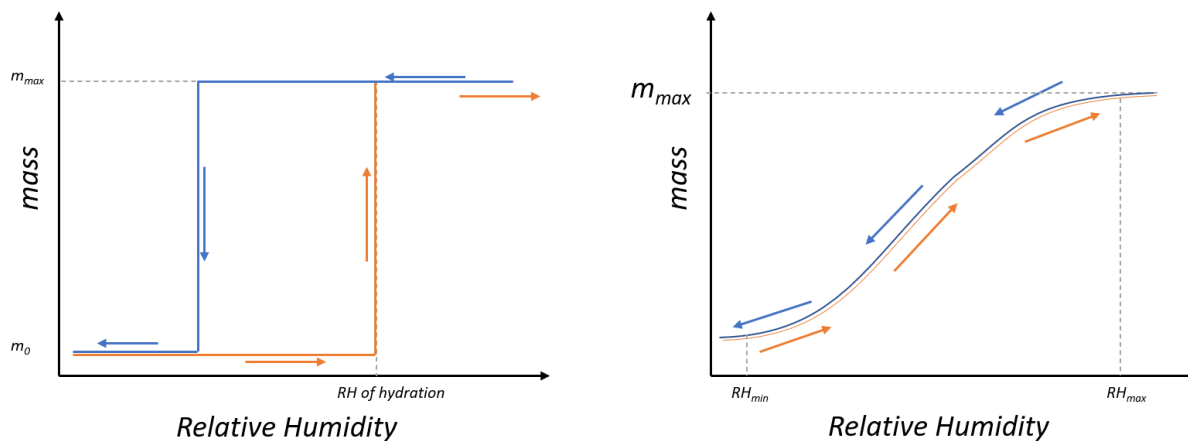


Figure 1-10: Isotherm of sorption for a stoichiometric hydrate (left) and a non-stoichiometric hydrate (right)

Important information can be deduced from these representations:

- The RH for solid-solid transition (RH of hydration in the case of stoichiometric hydrates)
- The kinetics associated to these transitions
- The maximum mass uptake of the solid during the transition which corresponds to the stoichiometry of water molecules (p) incorporated in the solid (Eq. 1-11)

$$p = \frac{\% \text{ water uptake}}{100} * \frac{M_A}{M_{H_2O}} \quad \text{Equation 1-11}$$

With p the quantity of incorporated water, M_A the molar mass of the anhydrous form, and the M_{H_2O} of the water.

In the case of non-stoichiometric hydrates, solid phase can adsorb water from RH_{min} to RH_{max} (Figure 1-10).

1.1.3.3 Ternary phase diagram

Ternary phase diagrams deal with 3 independent components (A, B, C). To represent a ternary phase diagram a 4D representation is required (T, P, and composition) which is impossible. Usually, the pressure is considered as fixed and the diagram is 3D represented (Temperature, %A, %B, and %C).

Such diagrams can be described as a combination of three binary phase diagrams, representing the faces of the ternary phase diagram. In the case of (Figure 1-11), joining three eutectic binary phase diagrams leads to a ternary eutectic phase diagram.

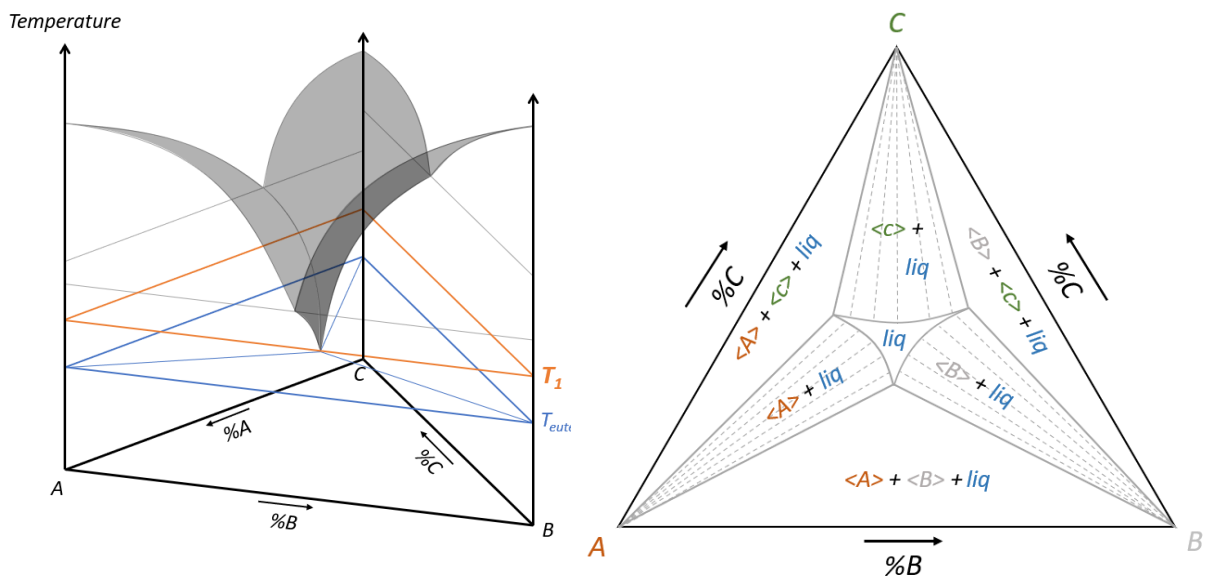


Figure 1-11: Isobaric ternary phase diagram (left) and an isothermal section at T_1 . Dashed lines represent the tie lines (right)

For an isobaric representation, the variance is:

$$v = 4 - \varphi \quad \text{Equation 1-12}$$

However, surfaces and limits of domain are complex to visualize in a 3D representation. Then, a 2D representation is preferred: the temperature, as the pressure, is fixed (Figure 1-11). The variance is then:

$$v = 3 - \varphi \quad \text{Equation 1-13}$$

Similarly to binary diagrams, the proportion on each phase can be determined thanks to the lever rule by using the tie lines.

One should note that phase diagrams can also apply for more than 3 independent components. However, these systems are out of the scope of this study.

1.2 CRYSTAL STRUCTURE AND CRYSTAL GENESIS:

1.2.1 Crystal Structures

1.2.1.1 Crystal Lattices

Geometrical and analytical properties of crystals were first conceptualized by the work on group theory. Then, Romé de l'Isle and René Haüy mentioned the periodicity in a crystal through the macroscopic observation of calcite crystals: the notions of unit cell and Miller indices were introduced.^{24–26} However, the major breakthroughs in crystallography have been made possible with the development of X-ray diffraction. With X-ray diffraction, lattice dimensions and interfacial angles of crystals were revealed with high precisions.²⁷

Crystals are defined as three-dimensional, periodic stacking of atoms or molecules giving rise to the crystal lattice. The smallest entity which contains the complete structural information is called the primitive unit cell, represented by a parallelepiped form made of three vectors. It is defined by the lattice parameters a , b , and c (the lengths of the vectors) and α , β , and γ (the angles between the vectors, Figure 1-12).

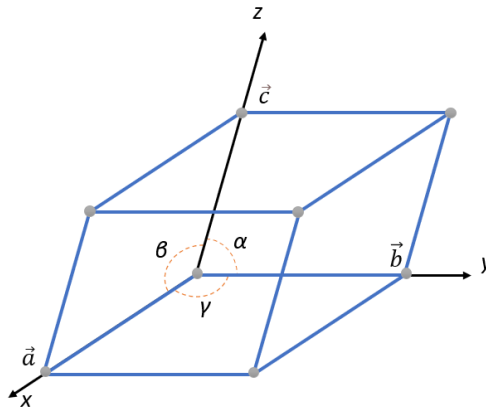


Figure 1-12: Schematic representation of a unit cell defined by primitive translation vectors

1.2.1.2 Symmetry in crystals

Many symmetry operations can be found in crystalline solids, based on three symmetry elements: symmetry with respect: to a point (center of symmetry), to a line (axial symmetry), and to a plane (planar symmetry).

By combination of these simple symmetry elements, ten symmetry elements can be encountered in a crystal:

- The proper rotation around an axis named 1, 2, 3, 4, and 6 (x rotations of $2\pi/x$, x being the name of the axis)

- The improper rotation \bar{x} , corresponding to a proper rotation x followed by an inversion i .
With $\bar{1}$ (inversion operation), $\bar{2}$ (mirror operation), $\bar{3}$, $\bar{4}$, and $\bar{6}$.

Point groups are the combination of the different symmetry elements and are used to describe the morphology and macroscopic properties of the crystals. They are 32-point groups classified in 7 crystal systems: triclinic, monoclinic, orthorhombic, trigonal, hexagonal, and cubic (Table 1-2).

Table 1-2: The seven crystal systems and their associated point group

Crystal System	Dominant Symmetry	Point Group	Cell Parameters
Triclinic	1 (identity)	1 and $\bar{1}$	$a \neq b \neq c$ $\alpha \neq \beta \neq \gamma$
Monoclinic	2 along \vec{b}	2, m and $2/m$	$a \neq b \neq c$ $\alpha = \beta = \frac{\pi}{2} \neq \gamma$
Orthorhombic	2 along \vec{a} , \vec{b} , and \vec{c}	222, $mm2$ and $2/m2/m2/m$	$a \neq b \neq c$ $\alpha = \beta = \gamma = \frac{\pi}{2}$
Trigonal	3 along \vec{c}	3, $\bar{3}$, 32, $3m$, and $\bar{3}m$	$a = b = c$ $\alpha = \beta = \gamma \neq \frac{\pi}{2}$
Tetragonal	4 along \vec{c}	4, $\bar{4}$, 422, $4mm$, $\bar{4}2m$, $4/m$, and $4/m2/m2/m$	$a = b \neq c$ $\alpha = \beta = \gamma = \frac{\pi}{2}$
Hexagonal	6 along \vec{c}	6, $\bar{6}$, 622, $6mm$, $\bar{6}m2$, $6/m$, and $6/m2/m2/m$	$a = b \neq c$ $\alpha = \beta = \frac{\pi}{2} \neq \gamma = \frac{3\pi}{2}$
Cubic	3 along the space diagonal	23, $m3$, 432, $\bar{4}3m$, and $m3m$	$a = b = c$ $\alpha = \beta = \gamma = \frac{\pi}{2}$

However, these crystal systems are not sufficient to describe all the possible lattices. Therefore, Bravais has introduced 4 lattice modes:²⁸

- P: primitive mode
- A, B, or C: based centered mode
- I: body centered mode
- F: face centered mode

The combination of the 7 crystal systems and 4 modes leads to the 14 Bravais lattices.

1.2.1.3 Space group

Other symmetry operations exist to fully describe a crystal structure. They combine translation and rotation from a microscopic point of view:

- Screw axis (rotation followed by a translation: $2_1, 3_1, 3_2, 4_1, 4_2, 4_3, 6_1, 6_2, 6_3, 6_4,$ and 6_5)
- Glide plane (reflection followed by a translation: $a, b, c,$ and n)

Finally, the combination of point group, lattice mode, and translational symmetry leads to the 230 space groups.²⁹

1.2.2 Crystal genesis

Crystallization is a first order and an exothermic phase transition which results in the formation of an ordered crystal phase from a disordered one: liquid, gaseous, amorphous or from supersaturated solution.

1.2.2.1 Driving force of crystallization from solution: Supersaturation

The solubility (S) is defined as the maximum quantity of compound A dissolved in a solvent at a given temperature and pressure. Even if saturation corresponds to a thermodynamic equilibrium, it is possible to overpass this value. The ratio between the concentration C of A in the solvent and the solubility S is the supersaturation ratio:³⁰

$$\beta = \frac{C}{S} \quad \text{Equation 1-14}$$

- If $\beta = 1$, the solution is saturated
- If $\beta < 1$, the system is undersaturated and crystallization cannot occur
- If $\beta > 1$, the system is supersaturated and is in a favorable condition for crystallization

This supersaturation is the driving force of the crystallization and can be reached via different ways: evaporation of the solvent, variation of the temperature, antisolvent addition (drowning out), pH variation (salting out), etc.

Thermodynamically, the condition $\beta > 1$ is sufficient to induce the crystallization. However, supersaturation must overcome a limit called Ostwald metastable limit (Figure 1-13) to induce a spontaneous nucleation of the system.⁶

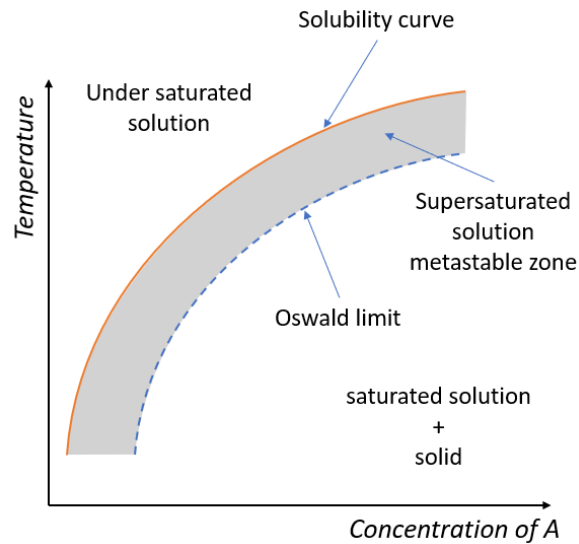


Figure 1-13: Solubility curve (orange curve) and Oswald limit (blue dashed curve) of compound in solution

The width of Ostwald metastable zone relies on kinetic factors: the cooling rate, evaporation rate, stirring mode and rate, time, impurities.

1.2.2.2 Classical Nucleation Theory

Homogeneous nucleation

The first step toward the formation of crystals after the establishment of a supersaturation is nucleation.

According to the Classical Nucleation Theory (CNT)^{31,32}, the aggregation of molecule of A leads to the formation of nuclei, which present the same degree of order than the final crystal form (i.e., the same structure), this phenomenon is considered as a stochastic step and corresponds to the nucleation process. The energy of nuclei is an equilibrium between cooperative and disruptive interactions represented by the variation of free enthalpy of nucleation:

$$\Delta G_{nucleation} = \Delta G_v + \Delta G_s \quad \text{Equation 1-15}$$

With ΔG_v the volume contribution to the free energy of nucleation related to solid/solid interactions (stabilization of the nuclei) and ΔG_s the surface contribution to the free energy of nucleation related to the surface solid/liquid interactions (destabilization of the nuclei).

If the nucleus is considered as a spherical cluster, $\Delta G_{nucleation}$ is written:

$$\Delta G_{nucleation} = -\frac{4}{3}\pi r^3 \Delta g_v + 4\pi r^2 \gamma \quad \text{Equation 1-16}$$

Δg_v is the free enthalpy variation per unit of volume, r the nucleus radius, and γ the surface tension of the nucleus.³³

By expressing nucleus free energy ΔG_v and ΔG_s as a function of the radius of the nucleus, the $\Delta G_{nucleation}$ is obtained (Figure 1-14).

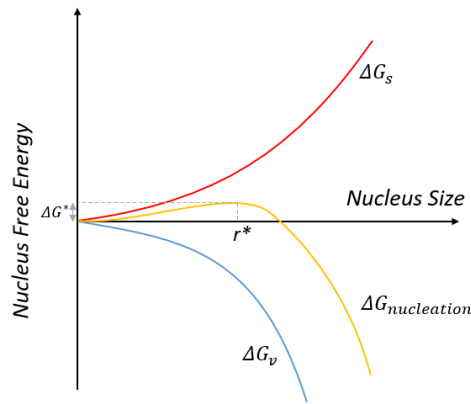


Figure 1-14: Free energy change associated with homogeneous nucleation of a sphere of radius r (yellow curve) as function a of volume contribution (blue curve) and surface contribution (red curve)

The evolution of $\Delta G_{nucleation}$ (yellow line, Figure 1-14) depicts the fact that the formation of the nucleus is at first energetically unfavorable since the contribution from the created solid/liquid surfaces prevails. If the critical radius threshold, r^* , is overcome, the growth of the nucleus stabilizes the system. Any nucleus with a size $r < r^*$ should re-dissolve and any nucleus with $r > r^*$ should grow. The nucleation process is governed by kinetics, then the energy barrier can be locally overcome and can lead to crystallization.

The apparition of a critical radius r^* , is concomitant with the apparition of barrier energy, ΔG^* .
By derivation of r^* and ΔG^* :

$$r^* = \frac{2\gamma}{\Delta g_v} \quad \Delta G^* = \frac{16\pi\gamma^3}{3(\Delta g_v)^2} \quad \text{Equation 1-17}$$

Heterogeneous nucleation

Heterogeneous nucleation consists in the aggregation of molecules A on foreign surfaces (crystallizer wall, stirrer, impurities, ...). Then, the contribution of ΔG_s to the free enthalpy of crystallization is diminished, due to less unfavorable solid/foreign surface interface. The ΔG^*_{hetero} is then lower than ΔG^*_{homo} which results in a better ability to crystallize than from homogeneous nucleation.

Homogeneous and heterogeneous nucleation are considered as primary nucleation since nuclei are formed spontaneously. Secondary nucleation occurs after these primary processes, by seeding of a solution or because of smashed crystals.³⁴

1.2.2.3 Crystal Growth

When ΔG^* is overcome and $r > r^*$, the nucleus will grow until the thermodynamic equilibrium is restored (*i.e.*, attainment of the saturation). There are several mechanisms of growth for a crystal. Solvated molecules will dock onto crystal surfaces and release energy to the system. The growth rate is defined by the intermolecular interactions between the surface of the crystal and the entity to dock at the surface: it will be faster for stronger intermolecular interactions. There are two major ways to incorporate molecule to the surface of the crystal (Figure 1-15):

- Spiral growth:¹⁷ crystal growth occurs through a screw dislocation regenerated at each layer. It mostly occurs at low supersaturation.
- Two-dimensional nucleation:³⁵ if the crystal presents no defect at its surface, there is no preferential adsorption sites. Then, 2D islands nucleate on the flat surface and spread all over the surface of the crystal. This mechanism occurs for high supersaturation.

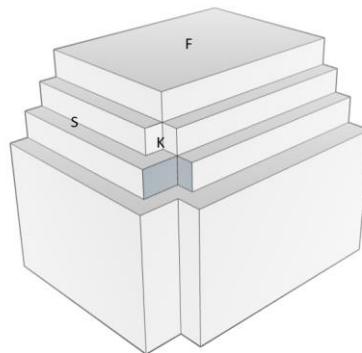


Figure 1-15: Distinction of the different kinds of crystal faces: flat *F*, step *S*, and kink *K*

1.2.2.4 Growth kinetics

Crystal growth depends on both intrinsic and external parameters. The nature of bonds, crystal defects, crystalline structure will modify the growth rate as well as external factors, such as the nature of the solvent (interactions between the growing crystal and the solvent can induce modifications of the growth rates and of the final morphology), impurities, temperature, or supersaturation. Due to these parameters, crystal growth rate is anisotropic, *i.e.*, the faces grow at different rates, leading to different crystal morphology. For a given face of the crystal, the lower the growth rate the more prominent the face is (Figure 1-16).

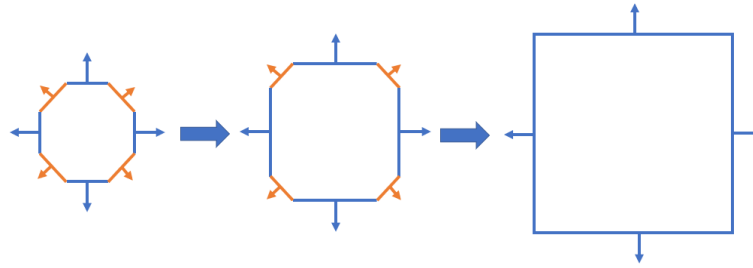


Figure 1-16: Schematic representation of the crystal growth; Blue arrows symbolize high growth rate and orange arrows low growth rate

1.2.2.5 Ostwald ripening

Ostwald ripening³⁶ corresponds to the dissolution of small crystals in favor of the growth of the larger ones. The driving force of this phenomenon is the Gibbs-Thomson effect which states that small particles have a higher dissolution than larger ones due to minimization of the interfacial energy.

1.3 STATE OF THE ART OF SPHERICAL AGGLOMERATION

1.3.1 Spherical crystallization

Spherical crystallization (SC) is an ensemble of techniques allowing the control of the particle physical properties of a crystallized material. It is applied in various activities such as pharmaceutical or food industries.³⁷⁻⁴⁴ Even if the first mention of agglomeration was published by D. I. Stock in 1952⁴⁵ on the aggregation of Barium sulphate, the first use of a SC technique for an organic molecule was published in 1981 with the spherical agglomeration of lactose.⁴⁶

The particle size and distribution will impact both flowability and bioavailability properties.^{47,48} These two properties are particularly critical for the pharmaceutical industry because of their impact on production. The different spherical crystallization techniques rely on the use of binder, also called bridging liquid (BL) to agglomerate particles and form spherical agglomerates.

There are three main SC techniques: ammonia diffusion, quasi-emulsion solvent diffusion, and spherical agglomeration.^{49,50}

1.3.2 Ammonia diffusion

The ammonia diffusion (AD) method relies on the use of an ammonia aqueous solution that can dissolve the solid to agglomerate. An anti-solvent, exhibiting a high miscibility in the aqueous ammonia solution, is also used.⁴⁸ A last solvent is required which is immiscible with water.⁵¹

The addition of the anti-solvent in ammonia solution leads to the precipitation of the solid by diffusion of the anti-solvent in ammonia solution droplets. Then by addition of the immiscible solvent,

ammonia is forced out of the droplets. The immiscible solvent reduces the amount of ammonia around the crystals impacting the agglomeration process. Indeed, ammonia acts as the BL for this technique.

A schematic representation of the process was proposed by Puechagut et al. in 1997 for the AD agglomeration of Norflaxacin (Figure 1-17).⁵²

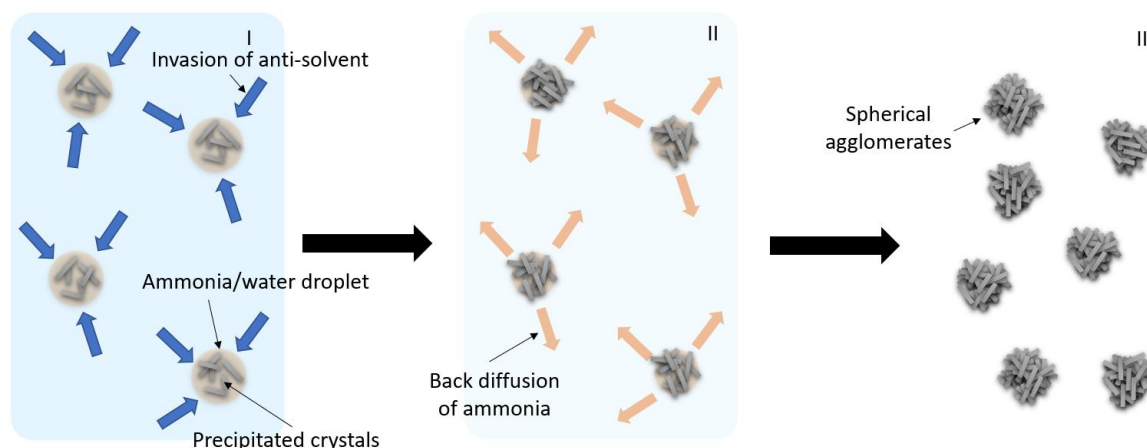


Figure 1-17: Schematic representation of Ammonia Diffusion, reproduced from Puechagut et al.⁵² Phase I: diffusion of the anti-solvent in ammonia/water droplet. Phase II: Back diffusion of ammonia and formation of the agglomerates in suspension. Phase III: Isolation of the agglomerates by filtration and drying

During the phase I, invasion of anti-solvent causes the precipitation of crystals in aqueous ammonia solution. Then, by addition of the immiscible solvent (phase II), the diffusion of ammonia out of the droplets is observed. Finally, the spherical agglomerates are obtained and isolated. One can note that ammonia diffusion is the only technique to agglomerate amphoteric compounds.

1.3.3 Quasi-Emulsion Solvent Diffusion (QESD)

QESD method also requires the dissolution of a compound in a solvent. The solution is then added to an anti-solvent.⁵³ The critical parameter of this method is the interactions between the dissolved compound and the dissolution solvent which must be stronger than those of the dissolution with the anti-solvent. By mixing the solution (solvent + dissolved compound) to the anti-solvent, a quasi-emulsion is formed (Step I, Figure 1-18). The difficulty to apply this technique relies on the capability of maintaining the two solvents emulsified despite their miscibility. Over time, the diffusion of solvent out of the droplet occurs and is replaced by diffusion of the anti-solvent in the droplet. The solubility modification of the compound in the droplet leads to its precipitation. The solvent will act as the BL to form the agglomerates (Step II, Figure 1-18).⁵⁴⁻⁵⁶ After filtration and drying, isolated spherical agglomerates are isolated (Step III, Figure 1-18).

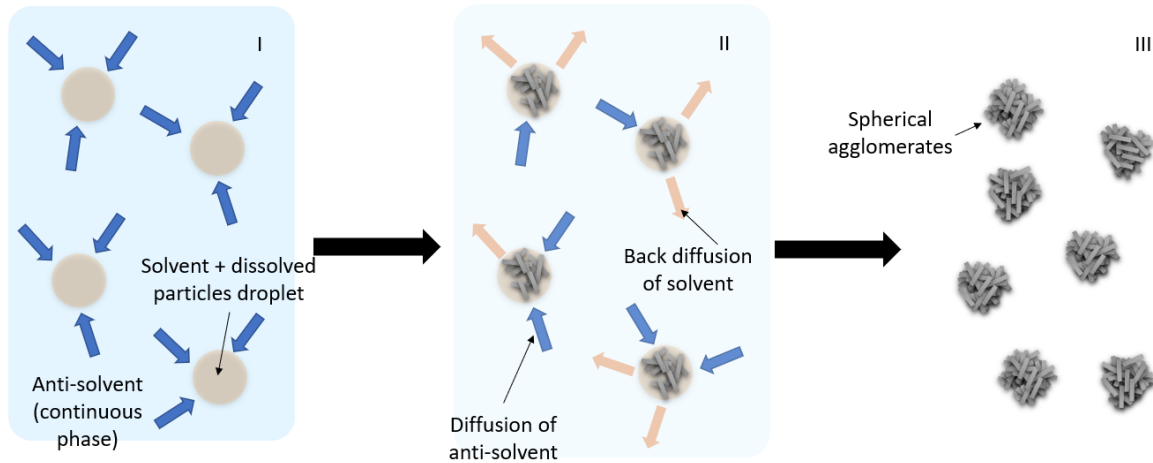


Figure 1-18: Schematic representation of Quasi Emulsion Solvent Diffusion, reproduced from Nocent et al.⁵⁷ Step I: formation of the quasi emulsion by addition of an anti-solvent in a solvent+dissolved particle solution. Step II: Diffusion of the anti-solvent in the droplets and back diffusion of the solvent. Step III: Isolation of the agglomerates.

1.3.4 Spherical agglomeration

Spherical agglomeration was developed by Kawashima et al. during the 1970s.^{37,38,42} First applied to inorganic compounds (coal, sulfate, carbonate, etc.), the method was extended to organic compounds (salicylic acid, benzoic acid, etc.).

The method (schematic representation proposed in Figure 1-19) consists of the dissolution of a compound in a solvent. Then, an anti-solvent is added causing the precipitation of the compound (1^{ary} Particle Size Distribution (PSD)). A last solvent is added, known as the BL. This one must exhibit an oiling out with the initial solvent/anti-solvent mixture. Moreover, the BL must have a high affinity for the crystals.⁵⁸ Due to particle – particle interactions, flocs (i.e. clusters of particles loosely aggregated together) of crystals are formed. The flocs grow and densify due to floc – floc and/or floc - droplet interactions. It has been shown by Huang et al. that the strength of the inter-particulate liquid bridges is proportional to the interfacial tension between the bridging liquid and the medium.⁵⁹ Indeed, in an agglomerate, particles are bounded through the formation of liquid bridges due to interfacial tension and capillary forces between the particles and the BL. (Figure 1-20).⁶⁰ By mean of the stirring, attrition and/or breakage of the agglomerates lead to an equilibrium between cohesive and disruptive mechanisms (3^{ary} PSD). The solid is then isolated by filtration and dried to obtain the final agglomerates (2^{ary} PSD). During the drying step, the crystallization of the liquid bridges leads to an increase of the compressive strength compared to agglomerates in liquid suspension.

The different steps of the spherical agglomeration mechanism are discussed hereafter.

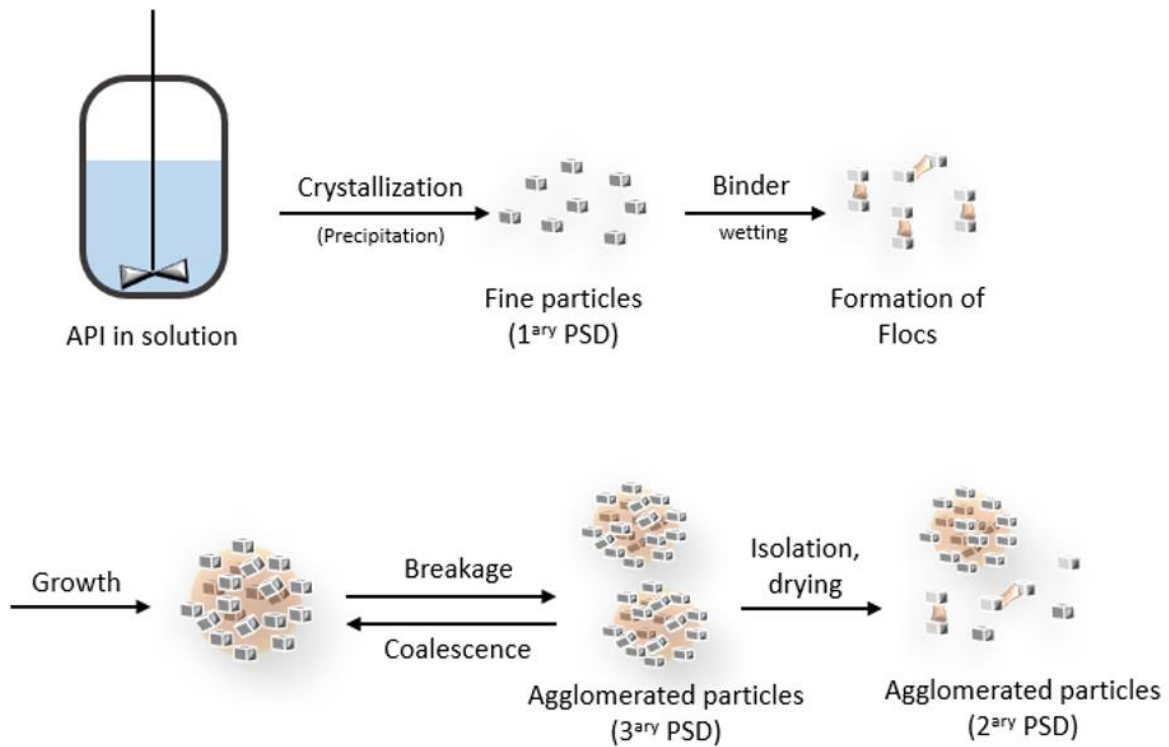


Figure 1-19: Schematic representation of the agglomeration process (binding agent is represented in orange)

1.3.4.1 Wetting period

The first step of the agglomerate formation refers to the wetting period.^{43,62} This step corresponds to the period during which the precipitated crystals interact with the bridging liquid. Amaro-González et al. have presented two possible mechanisms during the wetting period, depending on the size of the droplets (Dd) and particles (Dp):⁶³

- $Dd < Dp$ (Figure 1-21): It refers to a *distribution* mechanism. The BL will coat the particles resulting in an adhesive surface. Due to coated particle/particle or coated particle/coated particle interactions, the particles adhere to each other.

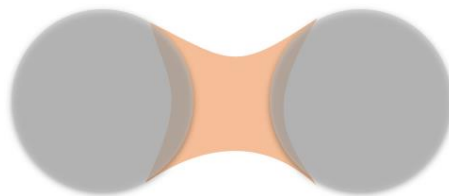


Figure 1-20: Schematic representation of two particles bonded with bridling liquid solvent⁶¹

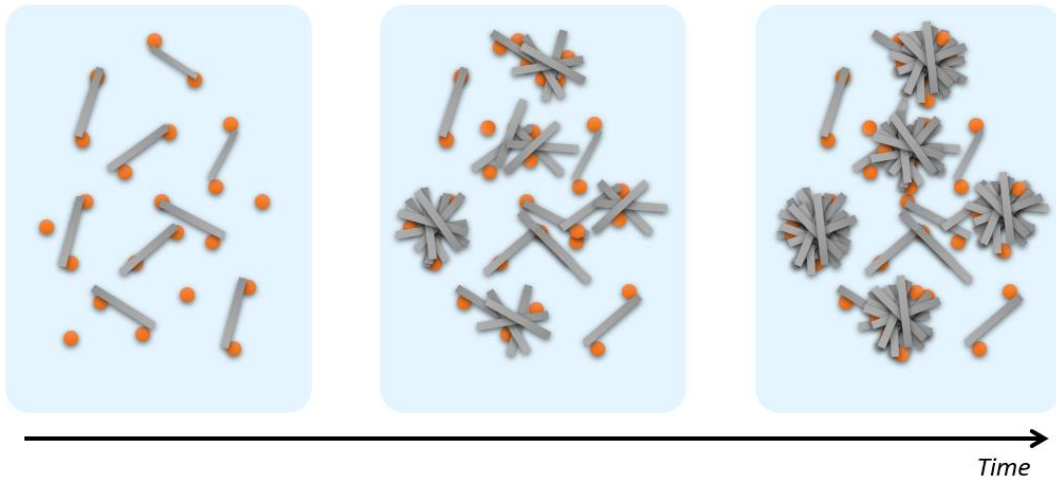


Figure 1-21: Schematic representation of the distribution mechanism proposed by Amaro-Gonzales

- $Dd > Dp$ (Figure 1-22). It refers to an *immersion* mechanism. The particles are gathered in and around the BL droplets.

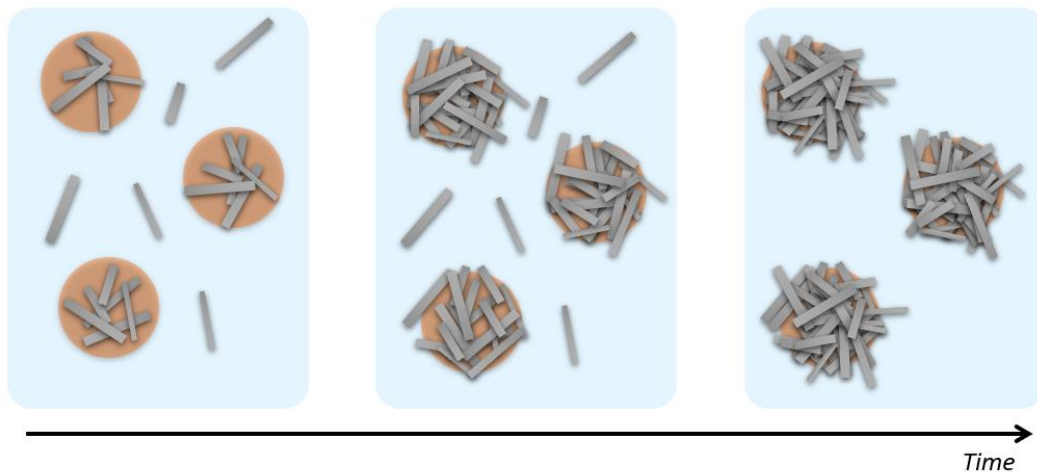


Figure 1-22: Schematic representation of the immersion mechanism proposed by Amaro-Gonzales

The immersion mechanism was studied by Subero-Courayer et al.⁶⁴ An experimental setup was developed to observe the crystal behavior around a BL droplet (Figure 1-23). The setup consists of a microscope equipped with a CCD camera. The camera is focused on the tip of a 10 μm inner diameter capillary immersed inside a salicylic acid suspension. Droplets are prepared to be of higher diameter than the initial crystals. Experiment has shown that initial crystals first enter inside the droplet (pictures 2 to 4, Figure 1-23). After the complete saturation in solid particles of the droplet, the particles remain stuck to the surface of the droplet until there is no BL available on the surface (pictures 5 to 9, Figure 1-23). This observation is in accordance with the immersion mechanism.

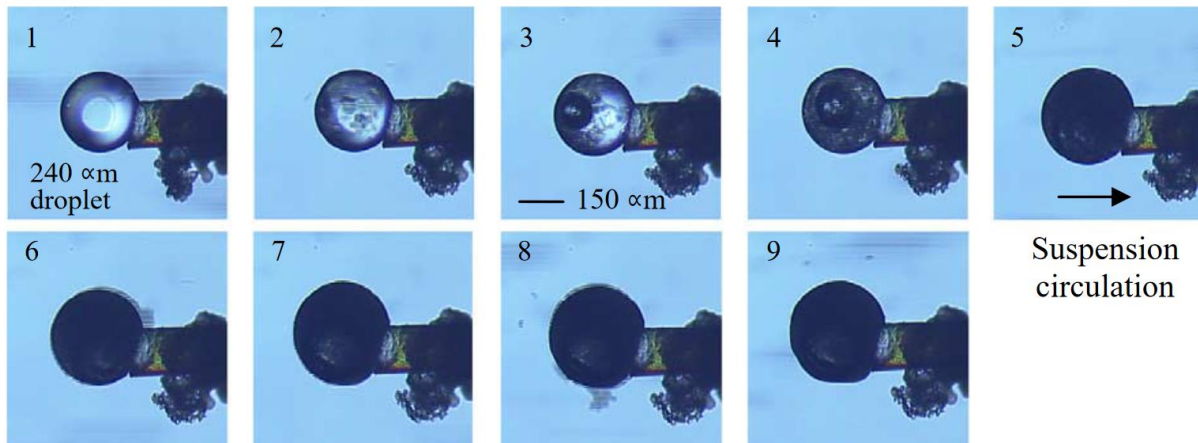


Figure 1-23: Sequences of photographs of liquid binder droplet at the extremity of a 10 μm internal diameter capillary tube and its interaction with acid salicylic crystals, reproduced from Subero-Courayer

Madec et al.⁶⁵ also proposed a similar mechanism in the case of the immersion. However, they suggest that the BL droplet surfaces are firstly coated with particles, preventing the coalescence of the droplets. Then, due to collisions, the particles enter the droplets, and more particles can adhere to the surface of the droplets (Figure 1-24).

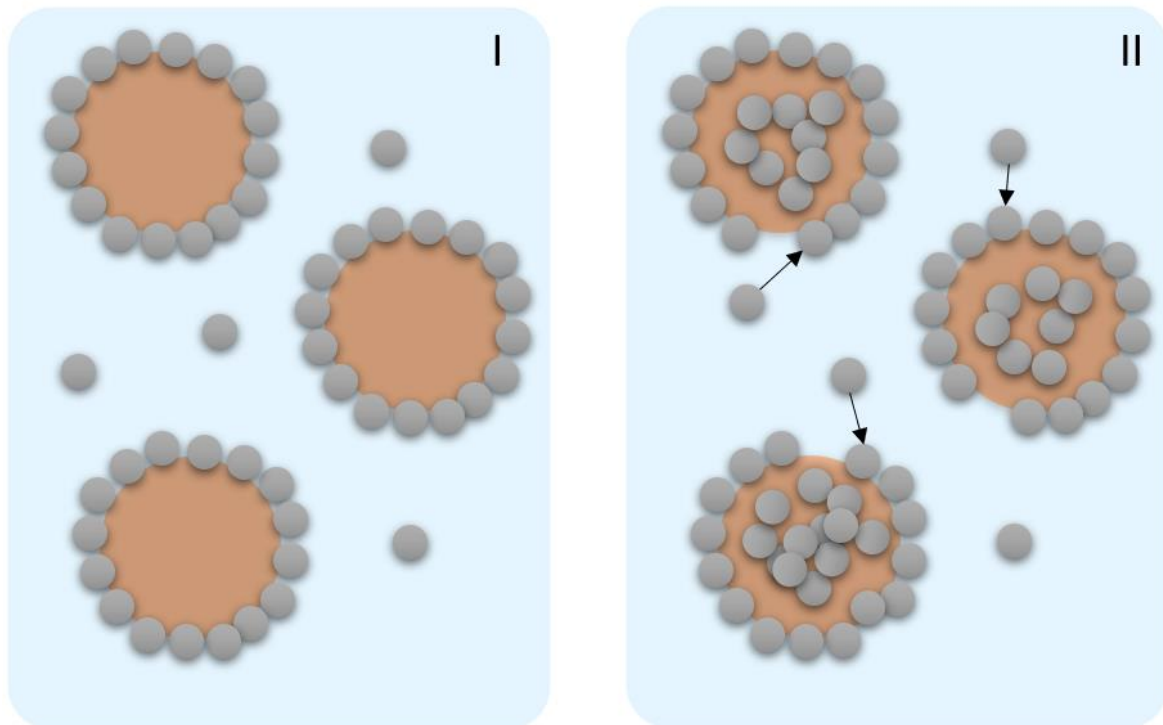


Figure 1-24: Formation of a protective coating layer of particles at the droplet surface (I) and incorporation of these particles towards the inner volume of the droplet (II), reproduced from Madec et al.

1.3.4.2 Consolidation and growth period

During the agglomeration process, the agglomerate growth can be separated into two successive steps:

- (i) Zero growth regime: After the wetting of initial crystals by the BL, a consolidation period of the flocs, where their diameter decrease, is observed. This compaction is attributed to the shearing forces which promote the floc-floc and floc-vessel collisions (Figure 1-25). Due to the compaction, the BL is squeezed out of the formed agglomerates until it reaches the surface of the agglomerates.

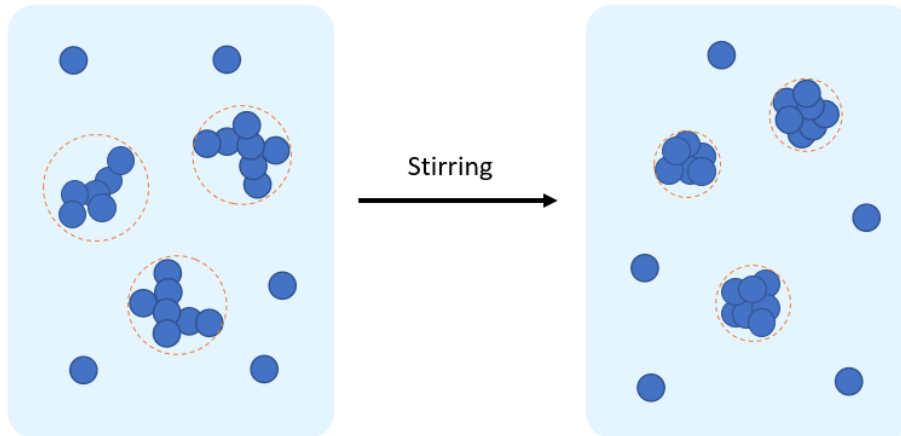


Figure 1-25: Effect of stirring during the zero-growth regime period. dashed orange circles correspond to the equivalent diameter of the initial flocs and consolidated flocs and show the reduction of the mean diameter due to compaction of the flocs

- (ii) Fast growth regime: After being squeezed out to the surface of the agglomerates, the BL is available for further adhesion of particles. During this period a fast growth of the agglomerate is reported.

Two main growth mechanisms can occur during the agglomeration: layering (Figure 1-26) and coalescence (Figure 1-27).

During layering, crystals adhered to the surface of the consolidate flocs until the complete coating of the flocs. Then, under further stirring, the BL reaches the surface of the growing agglomerate and is available to form successive layers of crystals.

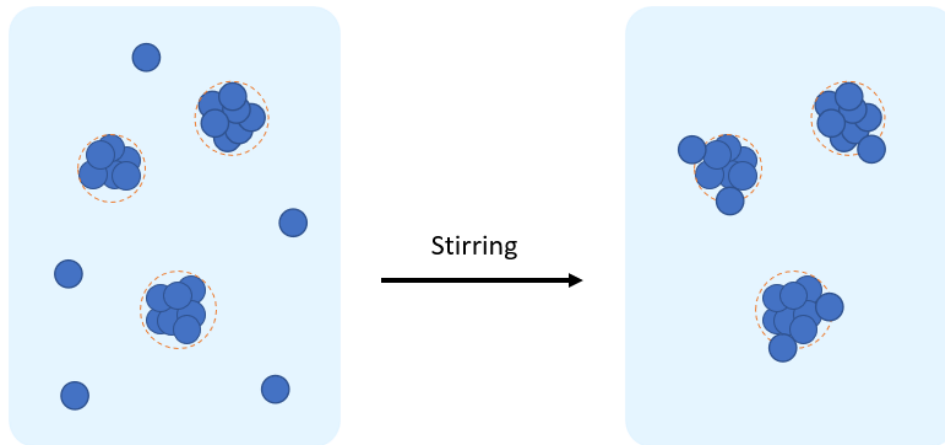


Figure 1-26: agglomerate growth through layering mechanism

In the case of coalescence, the floc-floc collisions lead to the formation of the agglomerates. This mechanism is often reported in the literature and was experimentally proved: a fast decrease of the agglomerate number, together with a fast increase of the agglomerate size distribution (ASD) was measured.

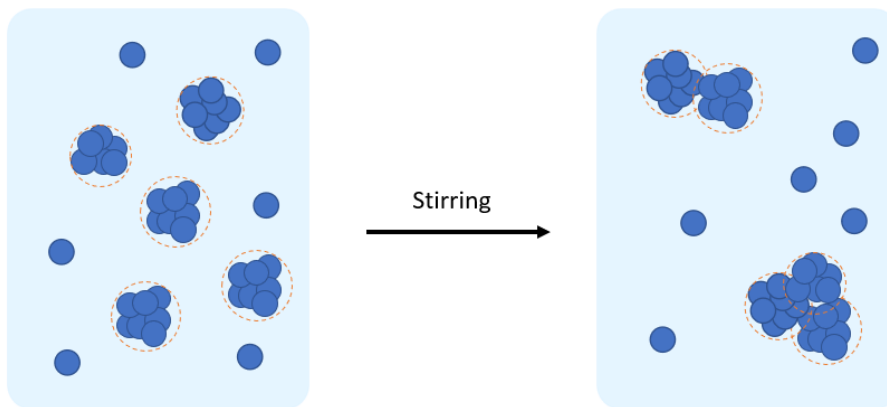


Figure 1-27: agglomerate growth through coalescence mechanism

One can note that the prevalence of one mechanism over the other depends on the process parameters.

After the fast growth period, the growth progressively slows down until the agglomerates reach a mean size plateau.

1.3.4.3 Breakage and attrition

A mechanism of breakage and/or attrition is often proposed in the literature to explain the agglomerate mean size plateau.⁶⁶ High stirring rates during the agglomeration in the vessel lead to high shearing forces which may cause agglomerate-agglomerate and/or agglomerate-vessel collisions. The

particle coming from attrition will adhere to agglomerate surface through a layering process and agglomerate fragments from breakage will participate to the coalescent growth. These phenomena apply for wet granulation (*i.e.*, addition of a BL on a dried powder) but Blandin *et al.*⁶⁷ suggest that, based on the elasticity of the agglomerate in suspension, the plateau is reached when the adhesion force between two agglomerates become too weak to maintain the link between the two agglomerates regarding to the shearing forces. The coalescence is prevented, and the agglomerates cannot grow anymore.

Table 1-3 summarizes the studies performed for a better understanding of these rate processes during spherical agglomeration.

Table 1-3: Summary of experimental (E) and modeling (M) studies focused on the mechanisms occurring during spherical agglomeration, reproduced from Pitt *et al.*⁶⁸

Wetting period	Mechanism				Ref
	Consolidation	Growth		Breakage	
		Coalescence	Layering		
	E	E			69
E	E				43
	E	E	E		70
	E + M	E + M			67
E					64
	E	E	E	E	71

1.3.4.4 Experimental parameters influencing spherical agglomeration

1.3.4.4.1 Solvent selection

The very first and crucial step to perform a spherical agglomeration is the determination of different type of solvents: (i) a good solvent to solubilize the solute, (ii) an anti-solvent to precipitate the crystals and (iii) a BL to agglomerate the crystals together.

Even if the selection of the crystallization solvents (*i.e.*, the good solvent and the anti-solvent) is a well-known procedure based on the solubility of the material to agglomerate, the choice of the BL can be more challenging. Different approaches are proposed in the literature:

General guidelines of Chow *et al.*⁶¹

After an extensive review of agglomeration conditions for different compounds, Chow *et al.* have proposed to classify them in four groups, depending on their solubility (Table 1-4). Then, agglomeration conditions are proposed as a function of the defined group.

Table 1-4: Chow's classification for the choice of the bridging liquid

	Solubilization solvent of the compound	Anti-solvent	Bridging liquid
Group 1	Water soluble	Water-miscible organic solvent	Salt solution of high concentration
Group 2	Organic solvent	water	Organic solvent
Group 3	Water-miscible organic solvent	Saturated aqueous solution	Organic solvent mixture
Group 4	Insoluble in water and organic solvent	Water-immiscible organic solvent	Salt solution of high concentration + binding agent

Ternary phase diagram approach:

The determination of the ternary phase diagram between the solvent, the anti-solvent, and the BL, can be a useful tool to determine different agglomeration parameters.

First, it gives information on the oiling out occurring between the crystallization solvents and the BL. As previously mentioned, the BL must be immiscible in the crystallization solvents to form an emulsion and initiate the wetting period. In Figure 1-28, the oiling out occurs in the shaded area (biphasic domain where two immiscible liquids coexist).

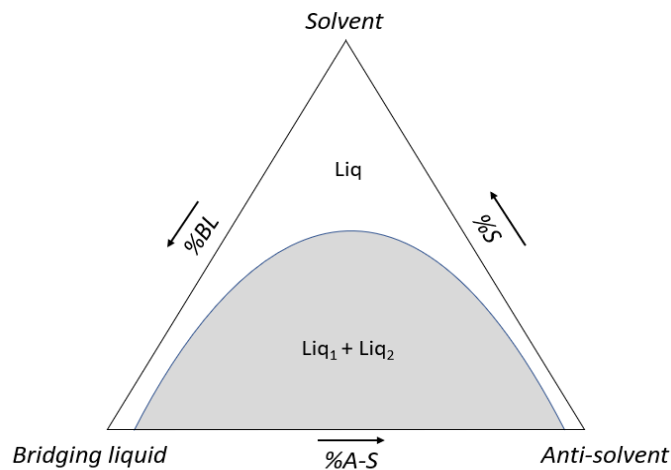


Figure 1-28: Isobaric and isotherm ternary phase diagram composed of a solvent, anti-solvent and a bridging liquid exhibiting an oiling out in the shaded biphasic domain (tie-lines)

Moreover, ternary phase diagrams have also been used to identify the best solvent concentration's region to perform an agglomeration. As an example, the Figure 1-29 from Cheng et al.,⁷² shows a ternary phase diagram combined with a "regime map" for the spherical agglomeration of Cefotaxime sodium. This "regime map" gives information on the agglomeration efficiency as a function of the solvent's composition.

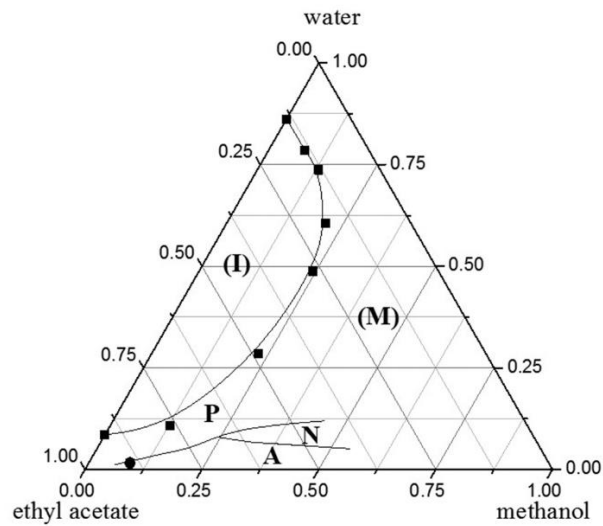


Figure 1-29: Ternary phase diagram of methanol-water-ethyl acetate at 285.15K; (I) immiscible region; (M) miscible region; combine with a regime map of agglomeration: (P) pasty zone; (N) non-crystallizing zone; (A) agglomeration zone. Reproduced from Cheng et al.⁷²

Calculation based method:

The previously discussed methods are mostly based on trial-and-error approaches. Such a method is time consuming and requires a non-negligible quantity of raw powder. Cheng et al.⁷² recently proposed a theoretical prediction flowchart to guide the selection of the wetting liquid (Figure 1-30), based on the Lifshitz-van der Waals acid-base theory, the flowchart uses the adhesion free energy between particles and wetting agent.⁷³

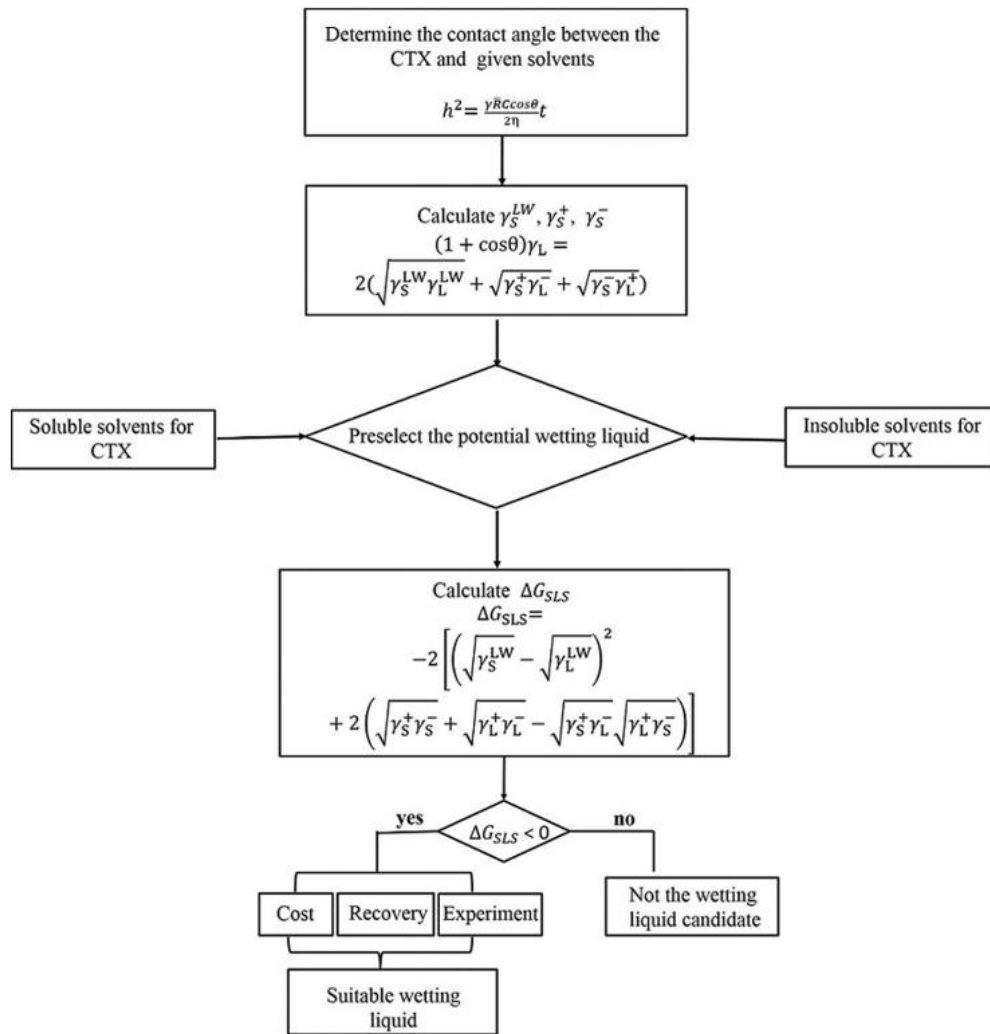


Figure 1-30: Flow chart of the selection of wetting liquid by adhesion free energy, reproduced from Cheng et al.

However, the proposed flowchart required some experiments of validation and optimization. To date there is no study proposing a fully predictive method to choose the solvent system for spherical agglomeration.

1.3.4.4.2 Bridging liquid

The bridging liquid is often cited as the most influencing parameter during spherical agglomeration. Its nature, amount, introduction method, etc., can drastically change the agglomerate properties (e.g., size distribution, strength, agglomeration time).

Nature of the bridging liquid

In order to determine the BL to use for spherical agglomeration, several methods are possible such as Chow's classification⁶¹ or a ternary phase diagram approach (as for solvent and anti-solvent, (cf part 1.4.4.4.1)). One additional method is specific to the BL selection: the capillary risen method.

This one was proposed by Amaro-González et al.⁶³ and is based on the Washburn's equation.⁷⁴ In this method, the wettability of particles in different solvents is determined by the wetting angle. The Washburn's equation is given below:

$$\frac{h^2}{t} = \frac{\gamma \bar{R} C}{2\eta} \cos \theta \quad \text{Equation 1-18}$$

With h the covered distance by the liquid in the powder bed (Figure 1-29), t the time to cover the distance h , γ the interfacial tension, η the viscosity, \bar{R} the particle mean radius of the particle in the bed powder, C the tortuosity of the bed powder, and θ the wetting angle between the solid and the saturated solvent.

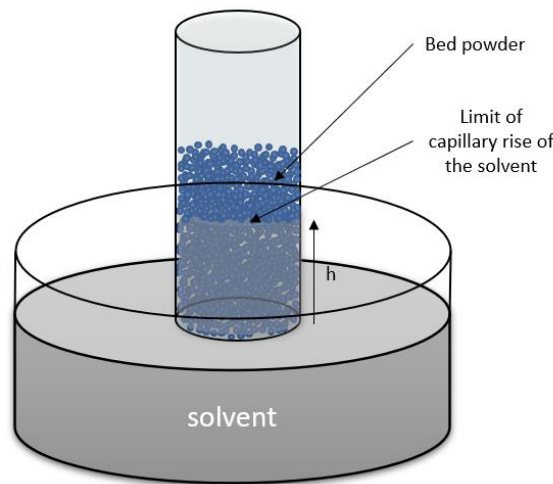


Figure 1-31: Schematic representation of the experimental setup for Washburn measurements

4 restrictions must be respected to apply the method: (i) steady-state with laminar flow during the capillary rise, (ii) zero velocity of the liquid at the solid-liquid interface, (iii) no externally applied pressure, and (iv) negligible gravitational differences.

For a more accurate measurement of the capillary action, the weight variation of the powder is preferred to the capillary rate. It is expressed with the relation:

$$m = \epsilon \rho S h \quad \text{Equation 1-19}$$

With m the mass of the powder bed, ϵ the porosity of the packed powder bed, ρ the density of the solvent, and S the inner section of the bed. Combined with the Washburn's equation (equation 1-19), the wetting angle is measured with the relation:

$$\frac{m^2}{t} = \frac{\gamma \rho^2 (S\epsilon)^2}{\eta} \frac{C \bar{R}}{2} \cos \theta \quad \text{Equation 1-20}$$

In practice, the ratio between a "perfect" wetting liquid ($\cos \theta = 1$) and a liquid with unknown $\cos \theta$ is used. Unknown $\cos \theta$ is measured with the relation:

$$\cos \theta = \frac{\gamma_1 \rho_1^2}{\gamma_2 \rho_2^2} \left(\frac{m_1}{t} \right) \left(\frac{m_2}{t} \right)^{-1} \quad \text{Equation 1-21}$$

The authors show that the higher the wettability, the greater the agglomerate properties (density, size, circularity).

Bridging liquid to solid ratio (BSR)

The BSR is probably the most cited parameter in the literature.^{63,66,67,70,71,75} It directly links the amount of added BL to the amount of solid to be agglomerated. It is given by the relation:

$$BSR = \frac{\text{Volume of BL}}{\text{Volume of crystals}} \quad \text{Equation 1-22}$$

Depending on the BSR value, the reaction medium during agglomeration will exhibit different behaviors: a too low BSR leads to a partial agglomeration while a too high BSR leads to the formation of an unfilterable pasty medium. A critical BSR (or range of BSR, noted BSR_{crit}), where the agglomeration is considered at its higher yield, was proposed for different material. However, this critical BSR is highly dependent on the material and solvent composition and requires several experiments to be obtained. For example, the agglomeration of salicylic acid with chloroform as BL has been studied⁷⁰; the acid was dispersed in a sulfuric acid solution or a water/ethanol mixture. In the first case, the critical range was observed between 0.35 and 0.50 but when salicylic acid particles are dispersed in the water/ethanol mixture, the BSR critical value was reconsidered at 0.72.

Figure 1-32 details the effect of BSR on the agglomeration.

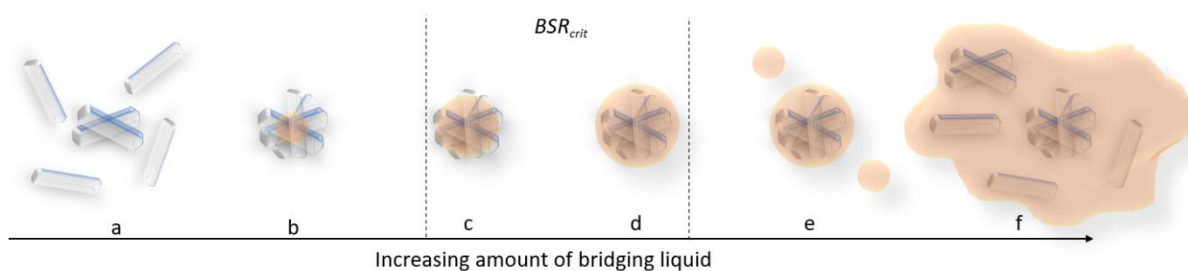


Figure 1-32: Schematic representation of the agglomeration process with an increasing amount of bridging liquid

Starting from $BSR = 0$, only Van der Waals interactions (*i.e.*, electrostatic interactions) are responsible for the particles binding (Figure 1-32, a). When increasing the value of BSR below BSR_{crit} , agglomerates are observed in suspension, but the agglomeration remains partial, the agglomerates exhibit weak mechanical properties, and some primary crystals are not agglomerated (Figure 1-32, b). Within the BSR_{crit} range, the crystals are fully agglomerated, agglomerates exhibit high mechanical properties and are highly spherical (Figure 1-32, c). Increasing the BSR, within the BSR_{crit} , increases the agglomeration efficiency and agglomerate size distribution (ASD) (Figure 1-32, d). However, an

opposite behavior is also reported where the ASD decreases with the BSR increase (within BSR_{crit} range). Above BSR_{crit} , the amount of bridging liquid is too high compared to the amount of crystals to agglomerate and some BL droplets will remain empty or will not wet crystals (depending on either immersion or distribution mechanism occurs during the wetting period) (Figure 1-32, e). By further increasing the BSR, the BL droplets will coalesce and form a unique, pasty medium (Figure 1-32, f). Agglomerates formed above BSR_{crit} exhibit poor mechanical properties and are irregular in shape.

One can note that BSR does not consider the concentration of the solid in the crystallization solvents. It is worth noting that, for a same volume of solid, a higher suspension concentration will promote the particle-particle collisions which influence the whole agglomeration process (*i.e.*, wetting period, growth rate and breakage/attrition mechanisms).

Introduction mode of BL

The BL can be added in two different ways: (i) before the crystallization/precipitation step or (ii) after the crystallization/precipitation step.

In case (i), the BL is pre-dispersed in the solution containing the dissolved material. The size of the BL droplets may be controlled through the shearing forces and the process driven to an immersion or a distribution mechanism. However, up to date, no studies have investigated the size of the droplet during the agglomeration process because of the technique limitations to observe droplet through a stirred, opaque suspension. In this case, agglomerates are more compact with a higher sphericity and exhibit improved flowability properties compared to agglomerates obtained from case (ii).^{76,77}

In case (ii), the BL addition can be either dropwise at different addition rates or added at once after the crystallization/precipitation step.⁶⁰ Increasing the BL feeding rate leads to a decrease of the ASD. It has been suggested that the decrease is due to an increase of the droplet number, which increases the number of initial flocs. No information is available in the literature on the addition of BL in one shot.

1.3.4.4.3 Temperature and initial particle size distribution

As mentioned in part 1.2.2, the control of the temperature is of great importance during a crystallization process as it directly influences the supersaturation ratio. Increasing the supersaturation ratio promotes the nucleation and the formation of numerous small crystals, while low supersaturation promotes the crystal growth. In the case of a “classical” solubility (contrary to a retro-solubility), decreasing the temperature in a given set of agglomeration conditions decreases the initial crystal size distribution.

Moreover, the temperature also affects the solvent inter-solubilities. The solubility of the BL in the solvent/anti-solvent mixture can significantly increase and reduce the available amount of BL to perform the agglomeration, thus impacting the BSR. Kawashima *et al.* have found that increasing the temperature leads to a decrease of the agglomerate size distribution. With further increases of temperature, the ASD increases and is broader.⁶⁰

Increasing the temperature also reduces the agglomeration yield. Indeed, less particles are precipitated due to the increase of solubility. The BSR being modified, the density and sphericity of agglomerates are also decreased.

The influence of the particle concentration (dependent on the temperature of precipitation) on the agglomeration process has been studied by Blandin *et al.*⁷⁰ It is suggested that the higher the solid concentration, the higher the agglomeration rate and ASD. Above a certain solid concentration, there is no evolution of the ASD. Moreover, increasing the solid concentration leads to a densification of the agglomerate correlated to the increased agglomerate collisions.

1.3.4.4.4 Hydrodynamic forces

Hydrodynamic forces in the agglomeration vessel govern the whole agglomeration process:

- The stability of the emulsion
- The particle- BL droplet interactions, *i.e.*, the wetting period
- The particle-particle interactions, *i.e.*, the growth period
- The particle-particle, particle-vessel collisions responsible for the breakage and attrition

It is worth noting that without sufficient shearing forces produced by agitation type and rates, agglomeration cannot occur.

The agitation rates first influence the dispersion of the BL. Increasing the stirring rate leads to smaller droplets of BL. It also leads to a better dispersion of the BL and thus, to a higher probability of particle-BL droplet interactions. Wu *et al.* shows that increasing the stirring rate leads to the decrease of the BSR_{crit} range.^{64,78}

When increasing the agitation rate, the ASD increases due to the increase of floc-floc collisions which promotes the coalescence mechanism. However, at higher stirring rates the ASD decreases due to the inhibition of coalescence mechanisms. Moreover, the agglomerate-agglomerate and agglomerate-vessel collisions increase, promoting breakage mechanisms, the agglomerate densification, and compressive strength.

Most of the studies focused on hydrodynamic forces at different agitation rates, without considering the vessel and stirrer geometries. The hydrodynamic forces between a beaker equipped with a magnetic stirrer are far lower than a 1 L flat bottom crystallizer equipped with baffles and a radial turbine.

1.3.4.4.5 Residence time

The residence time (*i.e.*, duration of the stirring) can also influence the agglomeration process. By increasing the residence time, the probabilities of agglomerate – agglomerate interactions increase allowing the growth of the agglomerates. Thus, the agglomerate diameter increases with the residence time. After a period of time, the agglomerate size reaches a plateau corresponding to the equilibrium between growth and breakage. Moreover, the residence time also influences the density of the agglomerates attributed to the increase of agglomerate – agglomerate and agglomerate – vessel collisions. The compaction of the agglomerates leads to an increase of the mechanical properties such as compressive strength.^{42,60,79}

Table 1-5, summarizes the different mentioned parameters and their influence on the agglomeration process.

Table 1-5: Agglomeration parameters and their influence on the process

Parameter	Influence on the agglomeration process
Dissolution solvent and precipitation anti-solvent	On the crystallization parameters (solubility of the compound, concentration of solid)
BL nature	On the solid/BL interactions. The higher the interactions the higher the ASD
BL amount (BSR)	There is a critical range of BSR to perform the agglomeration and obtain the optimal agglomerate properties (ASD, mechanical properties, ...)
Introduction mode of BL	<i>Addition prior to the precipitation:</i> Higher sphericity and compactness <i>Addition dropwise after the precipitation:</i> the higher the feeding rate the lower the ASD
Temperature	On the solubility (API/solvent/antisolvent/BL) Increasing T leads to the decreasing of the ASD. With further increase of T, ASD increases and is narrower
Stirring rate	Increasing the stirring rate decreases the BSR critical range and increases the ASD. With further increase of the stirring rate, the ASD decreases, and agglomerates are denser
Residence time	Increasing the residence time increases the ASD up to a plateau. Agglomerates exhibit higher compactness and better mechanical properties

Chapter II

Hydration – Dehydration behavior of Prednisolone, a case study on an isomorphous desolvate

2 HYDRATION – DEHYDRATION BEHAVIOR OF PREDNISOLONE, A CASE STUDY OF AN ISOMORPHOUS DESOLVATE

2.1 STATE OF THE ART OF PREDNISOLONE CRYSTALLINE LANDSCAPE

2.1.1 Introduction on Prednisolone

Prednisolone (IUPAC: (8S,9S,10R,11S,13S,14S,17R)-11,17-dihydroxy-17-(2-hydroxyacetyl)-10,13-dimethyl-7,8,9,11,12,14,15,16-octahydro-6H-cyclopenta[a]phenanthren-3-one, Figure 2-1) is a worldwide used corticosteroid to treat types of allergies, inflammatory conditions, autoimmune disorders and cancers. It is chemically derived from cortisone.

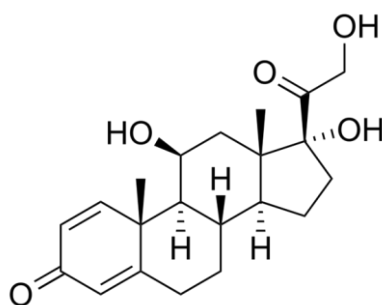


Figure 2-1: molecular structure of Prednisolone ($M_w = 360.44$ g/mol)

As many APIs, prednisolone exhibits solid-state landscape with several crystalline phases; so far two polymorphs (Form I and II), and a sesquihydrate (1.5 H₂O) have been described.

2.1.2 Prednisolone polymorphic landscape

Prednisolone polymorphic landscape was investigated and debated by several authors, notably by Kuhnert-Brandstätter,⁸⁰ and a consensus was finally proposed by Switchmezian in 2008,⁸¹ It was stated that prednisolone can crystallize in two polymorphs called Form I and Form II.

Form I crystallizes in the monoclinic $P2_1$ space group and exhibits a melting temperature of 239 °C. Form II crystallizes in the orthorhombic $P2_12_12_1$ space group with a melting temperature of 227 °C (crystallographic data available in Table 2-1).

Table 2-1: Crystallographic data of prednisolone Form I and Form II from Suitchmezian⁸¹

	Form I	Form II
Resolution mode	Single crystal	Single crystal
Resolution temperature (°C)	103	103
Crystal system	Monoclinic	Orthorhombic
Space group	$P2_1$	$P2_12_12_1$
<i>a</i> (Å)	6.3052(5)	5.9774(3)
<i>b</i> (Å)	12.9392(7)	11.7916(7)
<i>c</i> (Å)	10.9984(9)	25.5228(14)
α (°)	90	90
β (°)	91.167(9)	90
γ (°)	90	90
Volume (Å³)	897.11(11)	1798.93(17)
Calculated density	1.334	1.331
Z	2	4
R₁	0.0337	0.0351
Ref code	JIWPEL01	JIWPEL

The two polymorphs are enantiotropically related (confirmed with the melting enthalpies and the Burger and Ramburger rule¹³), Form I is the high temperature form and Form II the low temperature form. The authors have estimated the thermodynamic transition temperature between 120 and 130 °C. However, no direct conversion occurs upon heating from Form II towards Form I (Figure 2-3).

Corvis⁸² has recently reported the transformation of Form II to Form I during DSC experiment at 20 °C/min, transition occurs around 154 °C. However, the conversion was only partial and randomly observed (Figure 2-2).

A recent article details a part of the condensed phases of unary system between the two polymorphs.⁸³

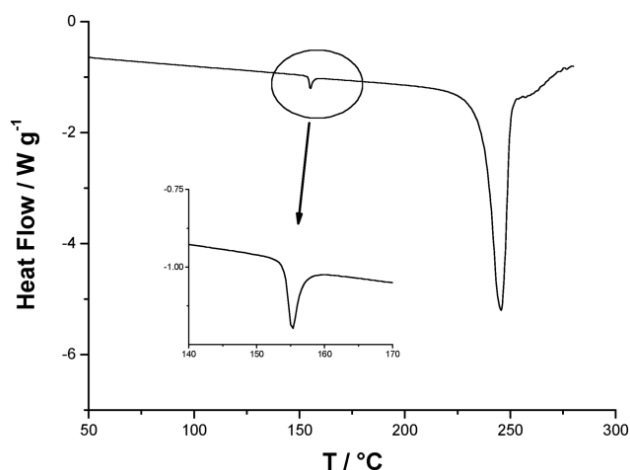


Figure 2-2 : DSC curve of prednisolone Form II (recrystallized from anhydrous methanol) at 20 °C/min. Reproduced from Corvis *et al.*⁸²

In addition to these two anhydrous forms, a sesquihydrate was isolated and characterized.⁸¹

2.1.3 Prednisolone sesquihydrate

Prednisolone sesquihydrate crystallizes in a $P2_12_12_1$ space group (Table 2-2).

Table 2-2: Crystallographic data of prednisolone sesquihydrate from Switchmezian⁸¹

Prednisolone sesquihydrate	
Resolution mode	Single crystal
Resolution temperature (°C)	103
Crystal system	Orthorhombic
Space group	$P2_12_12_1$
a (Å)	6.3945(3)
b (Å)	24.5789(10)
c (Å)	24.8376(11)
α (°)	90
β (°)	90
γ (°)	90
Volume (Å ³)	3903.7(3)
Calculated density	1.319
Z	8
R_1	0.0337
Ref code	JIWPIP

Thermal behavior of the hydrated phase was also investigated by Switchmezian *et al.*⁸¹ Starting from the sesquihydrate, obtained from an acetonitrile/water 90:10 (v/v) mixture, a highly energetic endotherm assigned to dehydration was revealed at circa 99 °C and then only melting/degradation of anhydrous Form I $T_m = 245$ °C was recorded on the thermograms (Figure 2-3). This was confirmed by

TR-XRD presented in the publication (data not shown), highlighting that the thermal dehydration of sesquihydrate directly leads to anhydrous Form I.

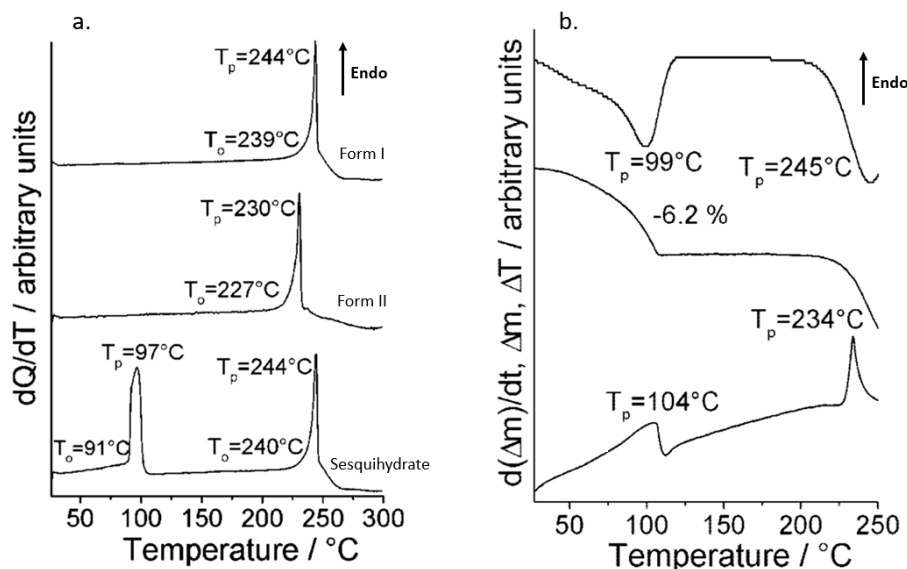


Figure 2-3: a. DSC curves for Forms I and II and the sesquihydrate (3 °C/min). b. DTA, TG, and DTG curves of prednisolone sesquihydrate (4 °C/min). Extracted from Switchmezian et al.

However, during attempts to isolate prednisolone sesquihydrate in order to thoroughly study its dehydration process, such behavior was never encountered, and the dehydration mechanism appeared much more complicated than that of the publication of Switchmezian in 2008.⁸¹

2.2 HYDRATION/DEHYDRATION BEHAVIOR OF PREDNISOLONE SESQUIHYDRATE

2.2.1 Thermal behavior of prednisolone sesquihydrate

2.2.1.1 Obtention of the sesquihydrate

Due to a poor solubility of prednisolone in pure water (223 mg/L at 25 °C), sesquihydrate crystals were obtained in acetone/water 90:10 (v/v) mixture either by simple stirring of a suspension during 24h (whatever the starting anhydrous form in suspension), or by total recrystallization followed by a partial evaporation of a homogeneous liquid.

Figure 2-4 displays the comparison between experimental XRPD patterns of the obtained prednisolone sesquihydrate and the two anhydrous polymorphic forms.

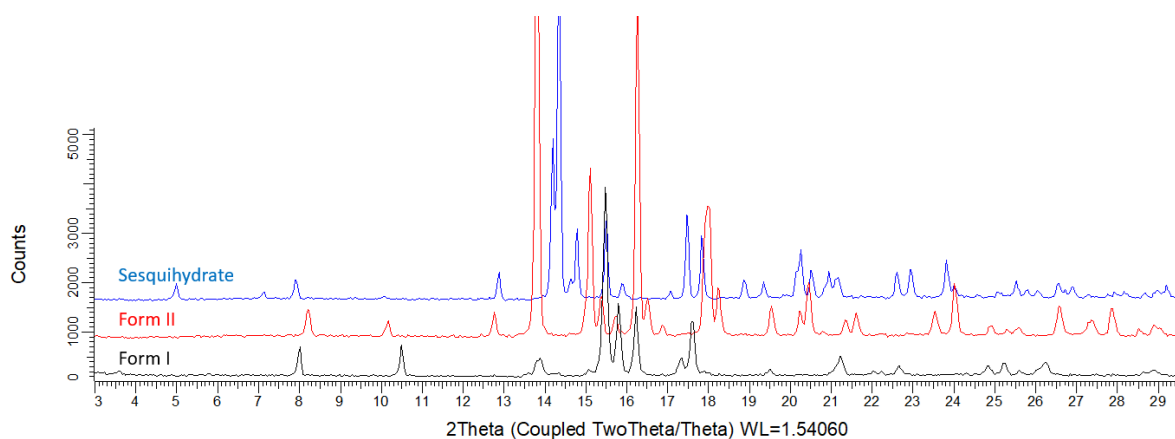


Figure 2-4: Comparison between XRPD patterns of prednisolone solid phases

2.2.1.2 TGA-DSC analyses of prednisolone sesquihydrate

Form I and Form II behave upon heating as depicted by Switchmezian *et al*,⁸¹ exhibiting only their respective melting points concomitant to their degradation. However, the behavior of the sesquihydrate upon heating was significantly different from that previously reported. Figure 2-5 displays the TGA-DSC-MS of prednisolone sesquihydrate.

Hydration – Dehydration behavior of Prednisolone, a case study of an isomorphous desolvate

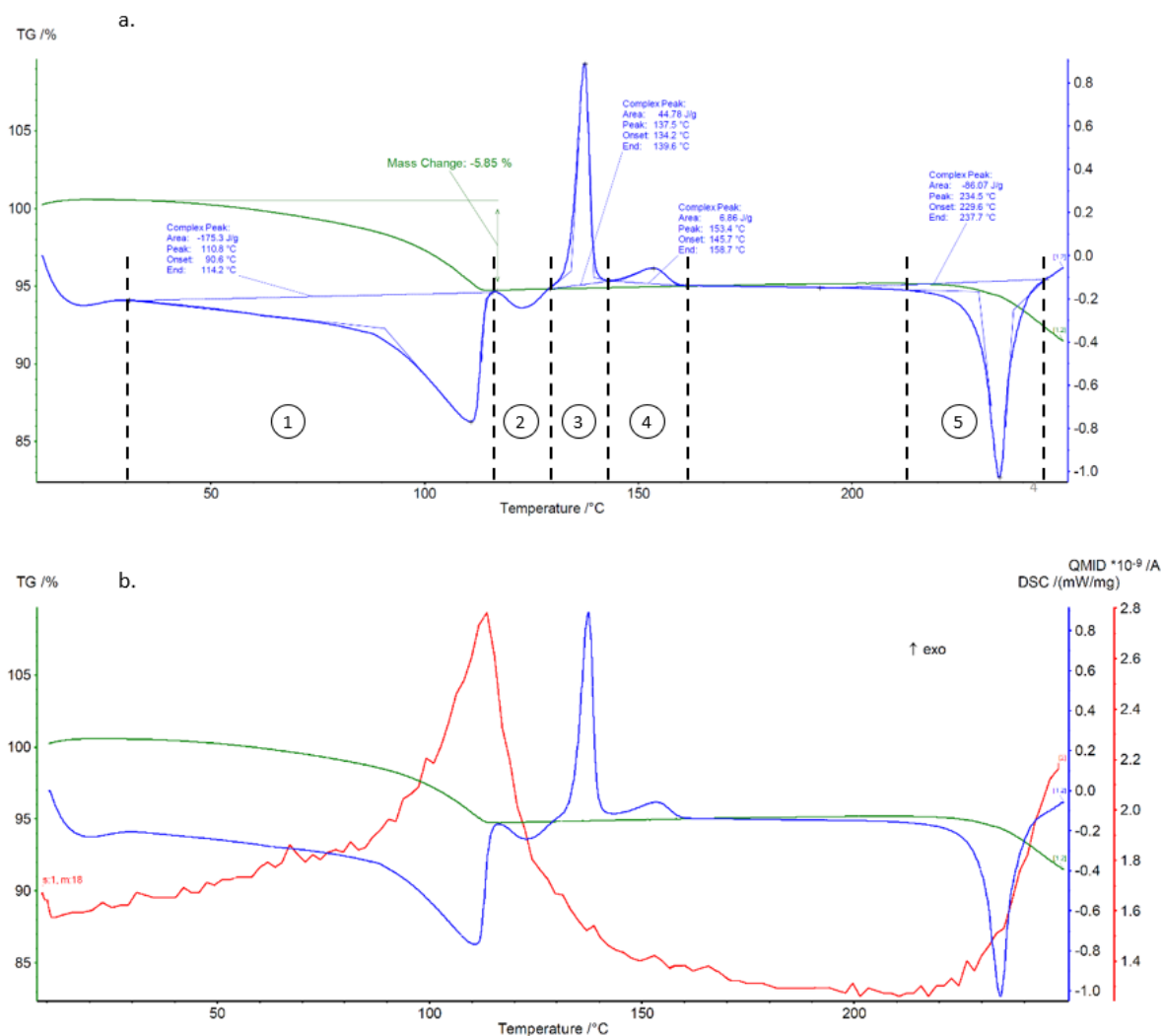


Figure 2-5: a. TGA-DSC analysis (5 K/min) of prednisolone sesquihydrate. b. Concomitant MS analysis for m/z 18 (in red) during TGA (green curve)-DSC (blue curve) analysis of the sesquihydrate.

This analysis reveals an unexpected complex behavior. Indeed, after the dehydration (peak 1, Figure 2-5, characterized by a large endotherm coupled to a mass loss of circa 5.9%_{wt} attributed to water loss and confirmed by MS (Figure 2-5b)), successive thermal phenomena occur:

- Peak 2, a first weak endotherm at circa 120 °C
- Peaks 3 and 4, two successive exothermic peaks (between 130 °C and 150 °C)
- Peak 5, an endotherm which could be assigned to the melting point/degradation of Form I.

If the starting situation (sesquihydrate) and the final situation (Form I) were identified by X-ray powder diffraction, the pathway in between appeared unclear and thus necessitates further investigations.

Other TGA-DSC analyses conducted at different heating rates (1 to 10 K/min, Figure 2-6) helped to classify the phenomena. In particular, the small endotherm after dehydration which seems to remain at an invariant temperature (at circa 125 °C).

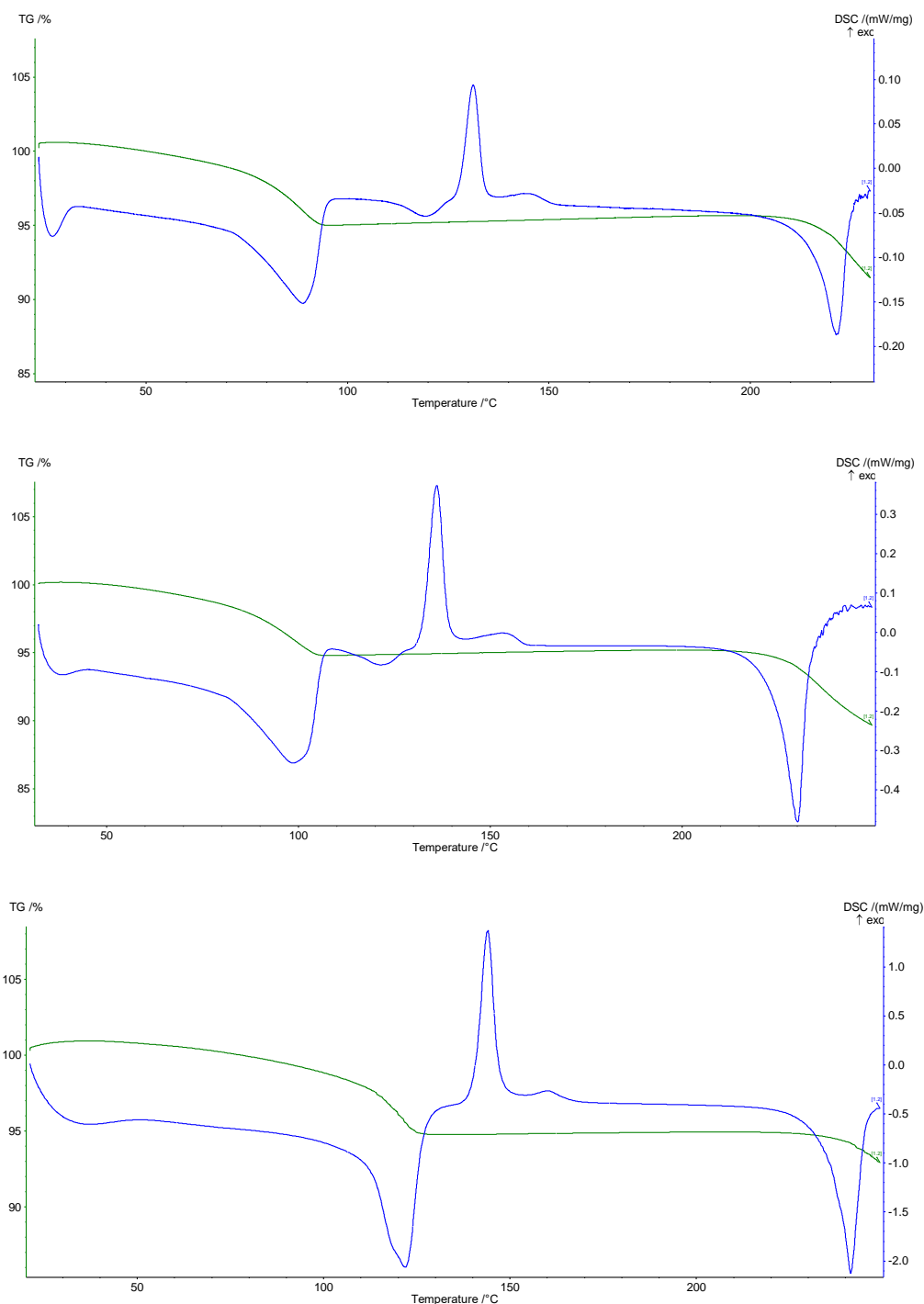


Figure 2-6: TGA-DSC analyses of prednisolone sesquihydrate at 1, 3 and 10 K/min from top to bottom, respectively

Moreover, these DSC experiments performed at different heating rates could be exploited in order to determine the activation energy of dehydration by using a simple mathematical kinetic model.

The activation energy of a transition can be determined by measuring the conversion rate (eq. 2-1 and Figure 2-7) under isothermal or non-isothermal conditions.

$$x = \frac{S_t}{S} \quad \text{Equation 2-1}$$

With x the conversion rate, S the total area of the endothermic peak between t_i and t_f , and S_t the partial area of the endothermic peak from t_i up to t_x .

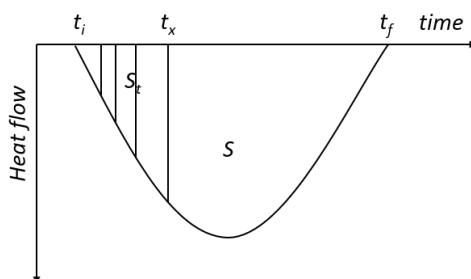


Figure 2-7: Illustration of the converted fraction x (hatched surface) in isothermal or non-isothermal conditions

Several mathematical functions, based on Avrami equation (eq 2-2), have been proposed to compute the activation energy of transition.⁸⁴

$$x = 1 - e^{(-kt)^n} \quad \text{Equation 2-2}$$

With k the rate constant, n the Avrami constant and t the time of transformation.

In this study, the transition was studied in non-isothermal conditions by means of calorimetric measurements with the Kissinger⁸⁵ approach (Eq. 2-3):

$$\ln\left(\frac{\varphi}{T_p^2}\right) = -\frac{E_a}{RT_p} + \ln\left[\frac{AR}{E_a}\right] \quad \text{Equation 2-3}$$

With φ the heating rate, T_p the peak temperature of transition, E_a the activation energy, A a constant and R the gas constant.

Based on the displacement of the dehydration peak versus heating rate, activation energy could be estimated from Kissinger Equation.^{85,86} The fitting led to an activation energy of circa 68 kJ/mol (linear regression correlation factor = 0.97).

2.2.1.3 Hot-stage microscopy of prednisolone sesquihydrate

Hot-stage microscopy revealed the nature of the successive phenomena observed with TGA-DSC analyses (Figure 2-8).

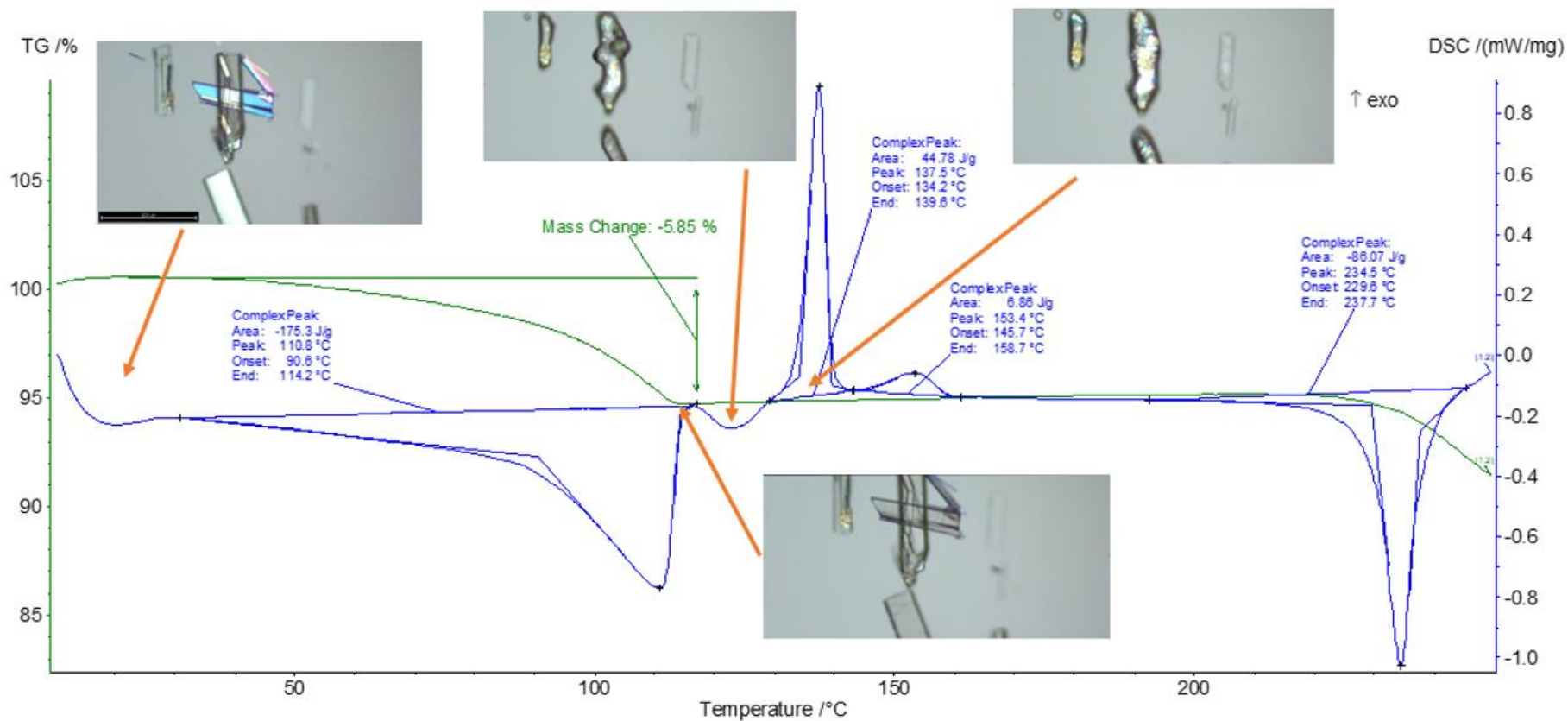


Figure 2-8: Thermal evolution and hot-stage microscopy photos of the sesquihydrate at 5K/min

After dehydration (visually occurring at circa 100 °C), the crystals display characteristic cracks perpendicular to the major growth axis of the crystal but keep their overall shape, edges, and facets until the melting of this dehydrated solid. On subsequent heating, these macroscopic defects have been healed, highlighting certainly an extensive structural analogy between the sesquihydrate and the corresponding dehydrated solid (Figure 2-9).

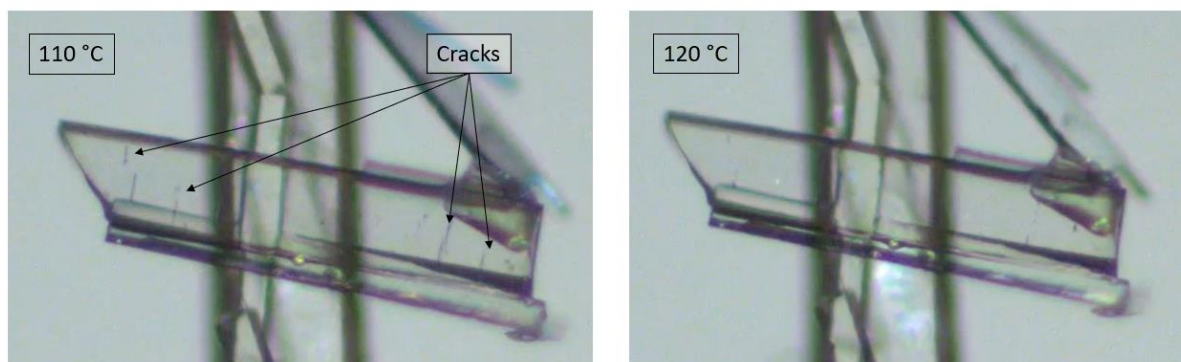


Figure 2-9: Microscopy pictures of a crystal of dehydrated prednisolone (form III) at 110°C exhibiting cracks (left) and the same crystal at 120 °C exhibiting healed cracks (right)

The crystal-to-crystal transformation clearly indicates that the resulting anhydrous form results from a topotactic dehydration of the sesquihydrate (*i.e.*, loss of water molecules without irreversible alteration of the crystal packing) and could be characterized as an isomorphous dehydrate (*i.e.*, an anhydrous form exhibiting a crystal packing similar to the sesquihydrate). This new anhydrous form will now be labelled prednisolone Form III.

Its structural filiation with the sesquihydrate is confirmed by TR-XRD measurements (Figure 2-10 and Figure 2-11). Indeed, the pattern at 100 °C (fully dehydrated*) is highly similar to that of the sesquihydrate but specific peak shifts or peak merging could be noticed between them (15.5°, 22.6°, 22.9°, 24°, orange boxes in Figure 2-10).

*By contrast to TGA-DSC experiments, TR-XRD is not a fully dynamic experiment: the heating rate between every step scan (10 °C) was fixed at 1.8 K/min and then the sample remains 6 minutes at every analyzing temperature during XRD scan. Therefore, the average heating rate of the analysis could be estimated lower than 1 K/min. At this heating rate, at 100 °C, the product was confirmed to be fully dehydrated (see Figure 2-6).

Hydration – Dehydration behavior of Prednisolone, a case study of an isomorphous desolvate

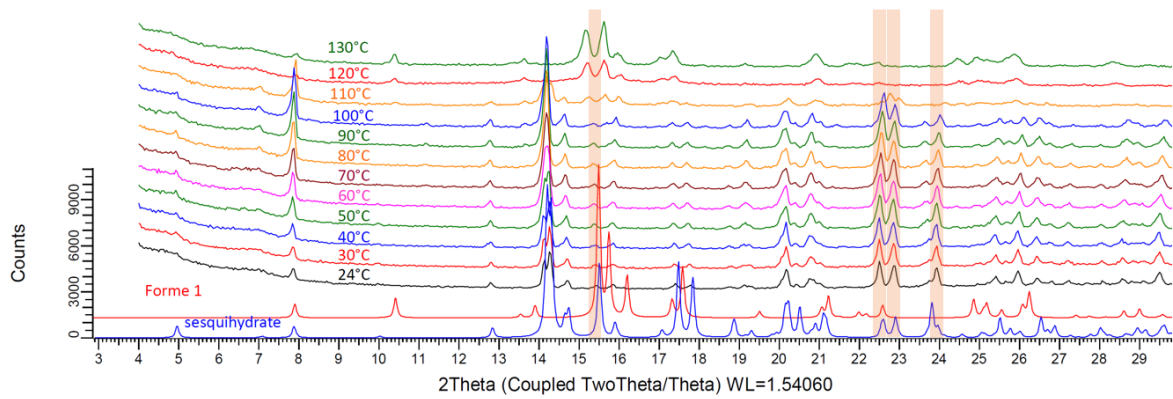


Figure 2-10: Temperature Resolved-XRPD patterns from 20 °C to 130 °C starting from prednisolone sesquihydrate

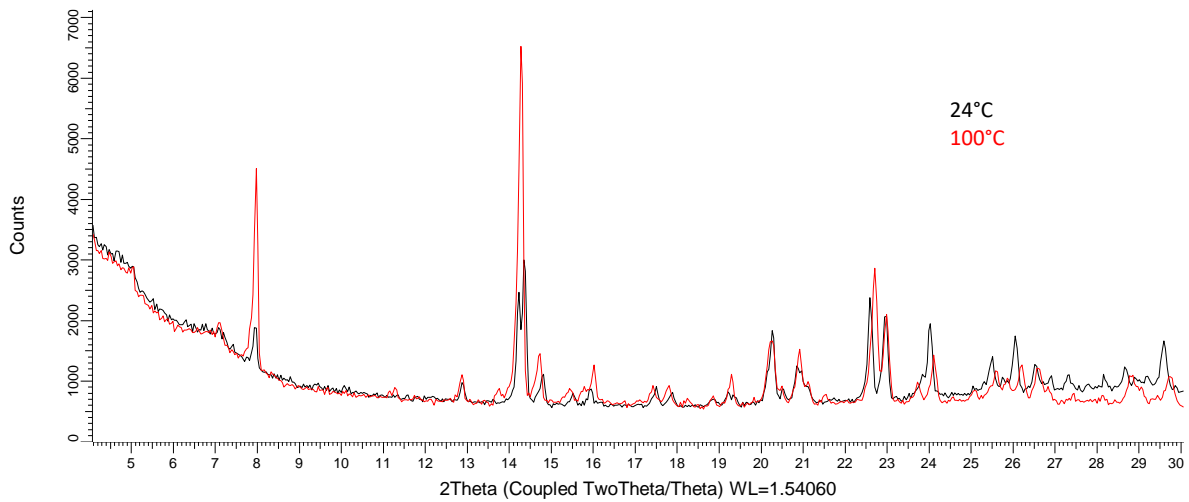
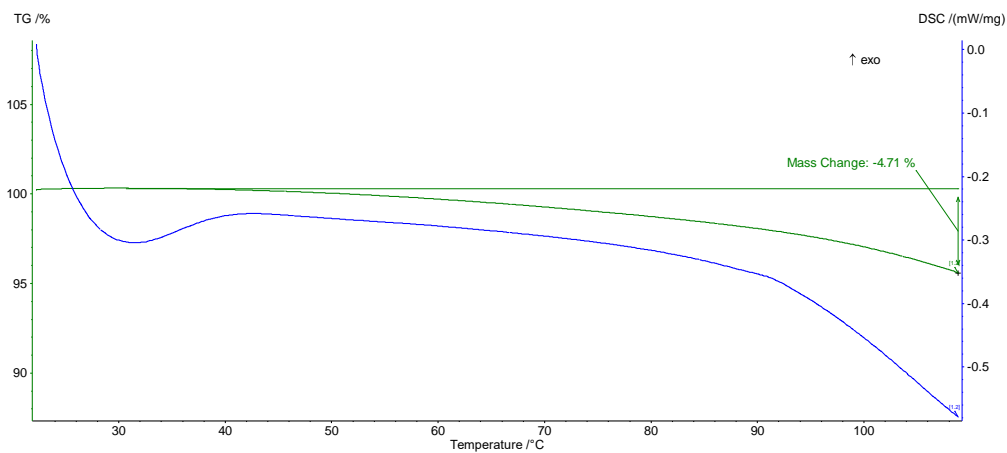


Figure 2-11: Overlay between XRPD patterns of the solid at 24 °C (sesquihydrate) and the solid at 100 °C (Form III: isomorphous desolvate)

Moreover, its reversible rehydration was proven by successive TGA-DSC (first heating ramp up to 110 °C, storage of the dehydrated sample under air atmosphere and second heating ramp which confirmed the full rehydration upon storage under room conditions).



Hydration – Dehydration behavior of Prednisolone, a case study of an isomorphous desolvate

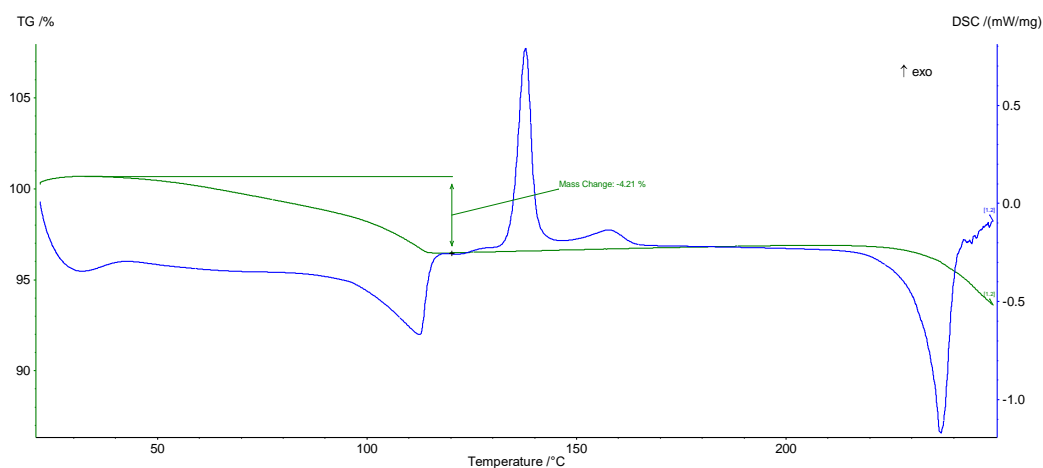


Figure 2-12: TGA-DSC of prednisolone sesquihydrate up to the dehydration (top). The resulting solid was left 48h under ambient conditions and reanalyzed in TGA-DSC (bottom) at 5 K/min

From Hot-stage microscopy figures, we can assign the small endotherm in DSC at circa 120 °C as the melting of the form III, *i.e.*, 100 °C below the two other anhydrous forms (Figure 2-8).

From the viscous melt obtained, recrystallization takes place (1st exothermic peak in DSC, at circa 130 °C, zone 3 on Figure 2-5). The obtained solid was analyzed with X-ray diffraction and consists in a mixture of defective Form I and II (Figure 2-13). The mixture of crystals then fully converts into Form I (second small exotherm in DSC at circa 150 °C, zone 4 on Figure 2-5), which will be the final solid phase of the sample (Figure 2-13).

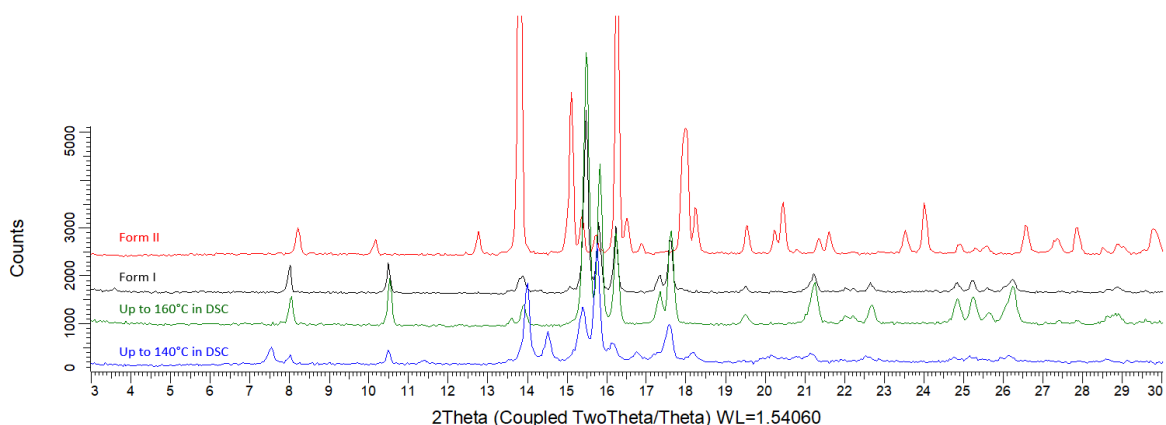


Figure 2-13: Comparison between XRPD patterns of the solid isolated after the first exothermic peak in DSC (in blue), the solid isolated after the second exothermic peak (in green), Form I and Form II of Prednisolone

Such a behavior, with the existence of an isomorphous hydrate displaying a melting point far below (*ca.* 120 °C) the “usual” anhydrous forms, was already reported for different compounds by Stephenson⁸⁷ and presents great similarities with that of Rimonabant, which crystallizes (among several solvates) as a monohydrate whose “smooth” dehydration under dry atmosphere led to isolate an isomorphous hydrate which melts more than 70 °C below the two anhydrous forms.⁸⁸

2.2.2 Hydration/dehydration behavior versus RH of prednisolone

All prednisolone solid phases were submitted to RH variations using DVS analyses at two fixed temperatures 24.9 and 48.7 °C.

DVS isotherms of form I and II (Figure 2-14) were obtained at 24.9 °C, following a cycle range type: 0 - 90 - 0 (in RH%).

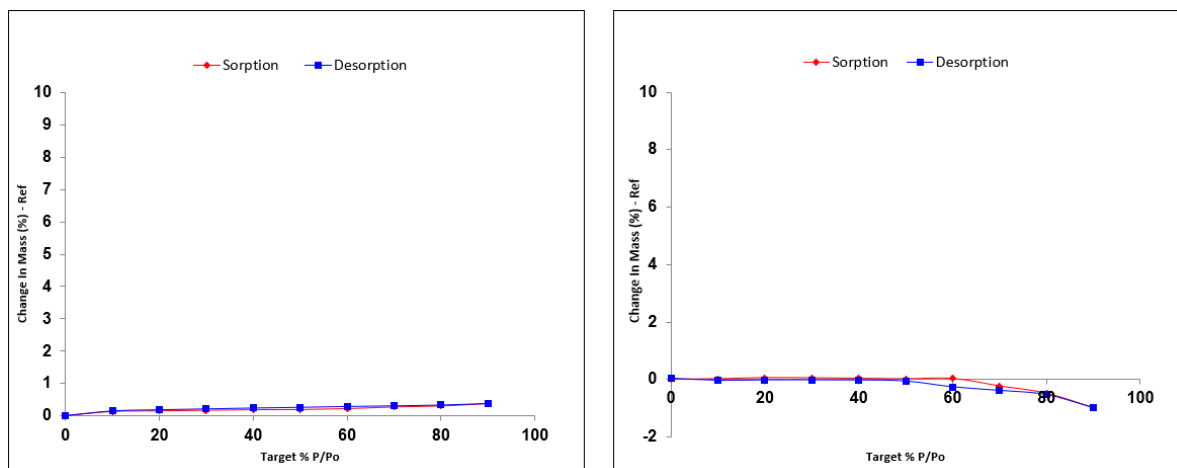


Figure 2-14: sorption/desorption isotherms of prednisolone at 24.9 °C of Form I.(left) and Form II (right).

It appears from these experiments that both Form I and Form II of prednisolone are non-sensitive to humidity at room temperature and do not tend to uptake water during long exposure to high RH.

The sesquihydrate was also submitted to RH variations cycles (between 0% and 90% RH) at 24.9 °C and 48.7 °C (Figure 2-15).

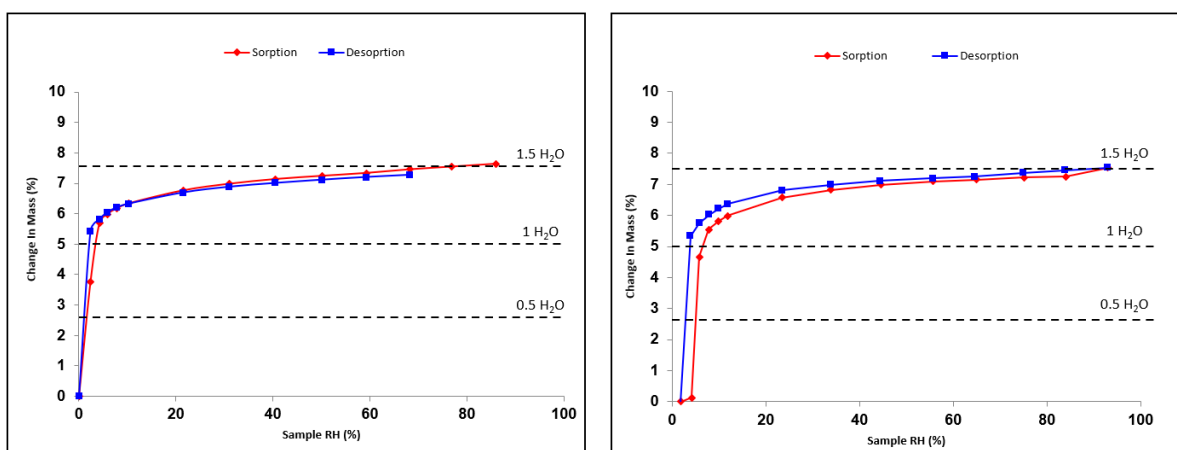


Figure 2-15: sorption/desorption isotherms of prednisolone sesquihydrate at 24.9 °C (left) and 48.7 °C (right).

First, we can conclude that the hydration-dehydration mechanism is perfectly reversible, in the 0-2 %RH domain) at 24.9 °C. This revealed the great stability of the sesquihydrate versus relative

humidity, the latter being able to fully dehydrate only in extremely dry atmospheres. Moreover, the resulting anhydrous form isolated at 0 %RH is highly sensitive to humidity as it fully rehydrates as soon as the RH increases. The anhydrous form obtained by soft dehydration at 24.9 °C is very likely to be different from Form I or Form II of prednisolone where no hydration was observed whatever the RH and behaves mostly as an isomorphous dehydrate or channel hydrate,^{87,89} which could be considered as a new anhydrous polymorphic form. Even with the increase of the temperature to 48.7 °C, the isomorphous dehydrate rehydrates between 2 and 4 %RH.

One can note that the stoichiometry of the hydrate is varying between 1 and 1.5 equivalent of water molecules, depending on the RH value. This indicates that a continuum in water molecules content exists between 1 and 1.5 H₂O depending on the RH surrounding the solid (between 4 and 95 %RH). In dry conditions (0-2 %RH), the equivalent of one water molecule is “extracted” from the structure without destroying the global organization of the Periodic Bond Chain to get access to Form III. All these experimental facts seem to indicate that the water molecules inside the structure do not play the same role for the global maintaining of the packing. Nevertheless, molecular modeling failed to differentiate the binding energy of the three water molecules.

Figure 2-16 shows the crystal packing of prednisolone sesquihydrate.

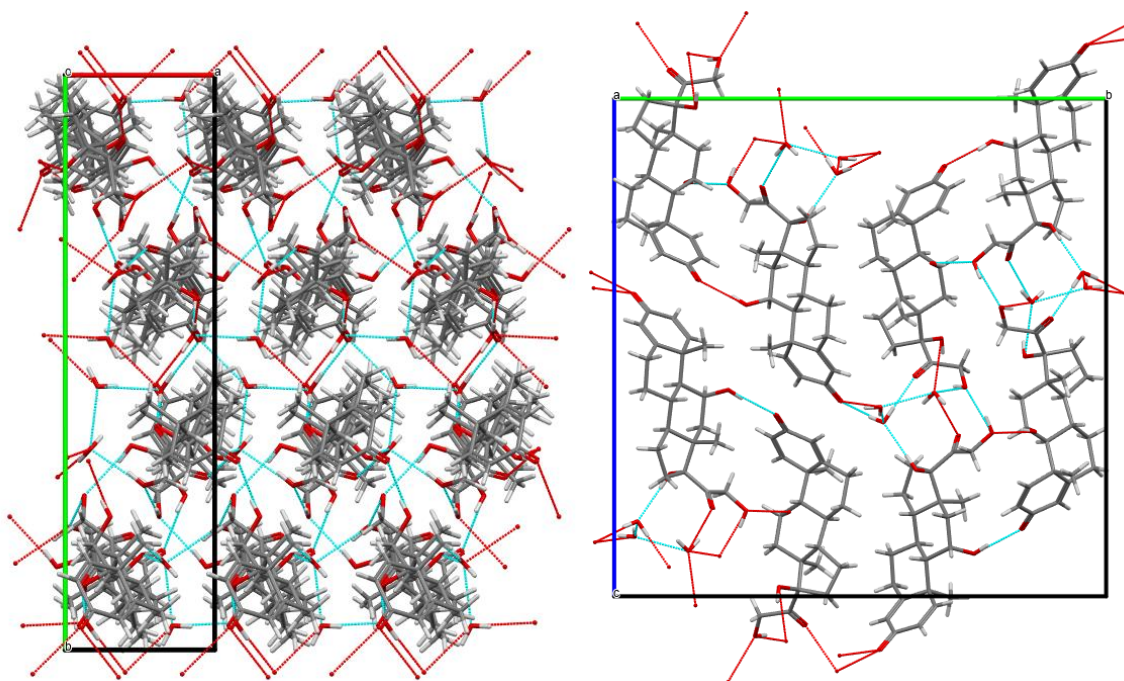


Figure 2-16: Crystal packing of prednisolone sesquihydrate along c axis (left) and a axis (right)

Cohesion of the crystal packing is ensured by both intermolecular H-bonds between prednisolone molecules and H-bonds between water and prednisolone molecules giving rise to a 3-dimensional PBC network. Even if crystal structure of form III was not resolved, the crystal packing

of prednisolone sesquihydrate has been considered without the water molecules (deleted from the crystallographic data of prednisolone sesquihydrate) and presented in Figure 2-17.

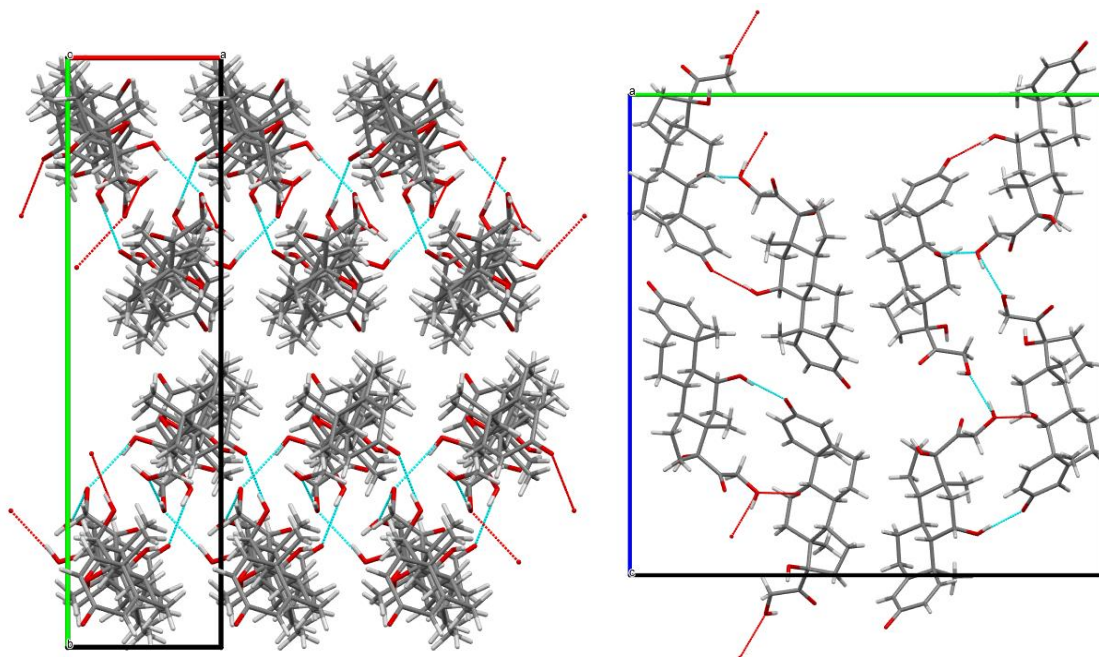


Figure 2-17: Crystal packing of prednisolone sesquihydrate (water molecules not shown) along c axis (left) and a axis (right)

If water molecules are artificially removed from the crystal structure, the cohesion of the structure can be still ensured by the intermolecular interactions (H-bonds and Van der Waals interactions) between prednisolone molecules which is in accordance with the existence of an isomorphous desolvate and a topotactic dehydration.

By comparing the crystallographic structures of each solid forms, and in consistency with experimental data, it is possible to conclude that there is a destructive/reconstructive process between the sesquihydrate and Form I (or between sesquihydrate and Form II). Switchmejian⁸¹ has shown that even if the conformation of prednisolone remains the same in each solid forms, there is no filiation between the three packing (sesquihydrate and forms I & II) which is in accordance with the observed behaviors.

2.3 CLASSIFICATION OF THE SESQUIHYDRATE

Several authors have proposed to classify the different hydrates as a function of different properties such as activation energy of dehydration or mechanistic classification (i.e. related to the nature of the product obtained after dehydration).⁸⁹⁻⁹³

2.3.1 Energetically based classification

Prednisolone sesquihydrate was classified according to the Dehydration-Rehydration Classification System (DRS) proposed by Takahashi and Uekusa.⁹³ The authors proposed to classify the hydrates into 3 classes according to their hydration and dehydration activation energies.

- Class 1: readily rehydrate to their hydrate forms when RH increases
- Class 2: crystal structure destroyed in the dehydration process, resulting in an amorphous phase which does not revert to the hydrate form when RH increases
- Class 3: crystal structure destroyed in the dehydration process, resulting in an amorphous phase which recrystallizes to an anhydrous form when RH increases

With an activation energy of circa 68 kJ/mol and a fully reversible hydration-rehydration mechanism, prednisolone perfectly fits the average value for dehydration of class 1 hydrates (hydrates displaying full dehydration-rehydration cycles) as ranked by Takahashi and Uekusa (Figure 2-18).⁹³ Due to the complexity of measuring rehydration energy no data are provided for the rehydration activation energy.

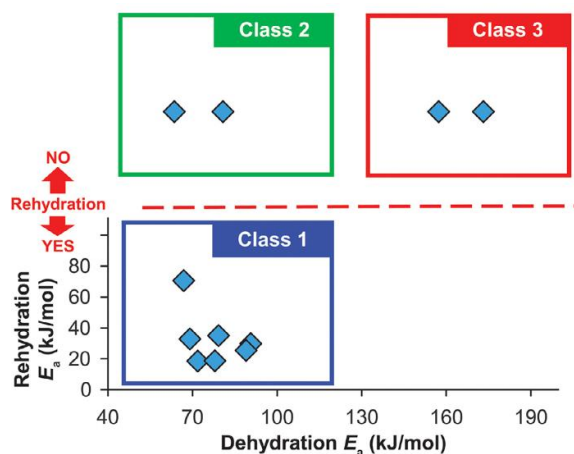


Figure 2-18: Dehydration-Rehydration Classification System (DRS) for the classification of pharmaceutical hydrates. Diamonds indicate the relation between dehydration E_a , rehydration E_a , and rehydration propensity for each hydrate. Rehydration "YES" and "NO" indicate the presence or absence of rehydration, respectively. Squares indicate the energetic areas of Class 1 (blue), Class 2 (green), and Class 3 (red). Extracted from Takahashi et al.⁹³

2.3.2 Dehydration mechanistic based classification

Rouen-96 is a classification of hydrates based on the dehydration mechanism of molecular crystals (Figure 2-19).⁸⁹

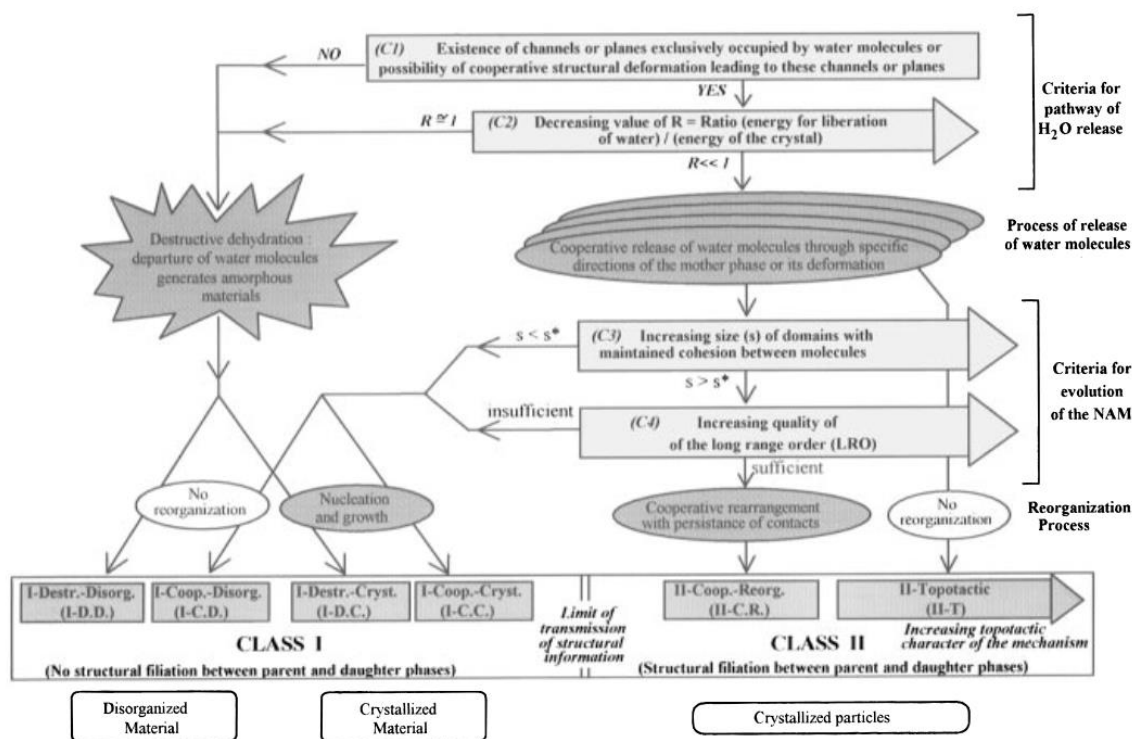


Figure 2-19: Organization chart for dehydration mechanism of molecular crystals proposed by Petit et al.⁸⁹

In the case of prednisolone sesquihydrate, the dehydration being non-destructive the criterion C1 is fulfilled. C2 depicts the energetic difference between the hydrated and related anhydrous phase. It was shown for the sesquihydrate that intermolecular interactions between prednisolone molecules could exist, even after the release of water which is in accordance with a cooperative release of water molecules. C3 criterion refers to the conservation (or not) of the crystal structure after the release of water. The healing of dehydrated crystals of prednisolone was observed (Figure 2-9), meaning that the crystal structure of the mother phase was preserved and corresponds to the case $s > s^*$. The long-range order seems sufficient to ensure the stability of the anhydrous dehydrate phase until its melting. Thus, the sesquihydrate falls in the Class II where a structural filiation between the mother and daughter phase is observed. However, access to the crystalline structure of Form III is required to choose between Class II-C.R. or II-T hydrate, depending on the possible relaxation of prednisolone molecules after the release of water. The healing of the crystals and the slight XRPD differences between sesquihydrate and Form III could indicate a relaxation in the crystal structure and a hydrate of Class II-C.R. according to the Rouen-96 model.

2.4 CONCLUSIONS ON THE PREDNISOLONE ANHYDROUS DESOLVATE

This study proposes a more complete version of the polymorphic landscape of prednisolone. Indeed, the behavior of the sesquihydrate upon dehydration was elucidated. A new solid form of prednisolone was isolated (*i.e.*, Form III) and characterized as a quasi-isomorphous desolvate of the sesquihydrate. This daughter phase shows a reversible dehydration – rehydration and extensive structure similarities with the corresponding mother phase due to topotactic desolvation and resolution mechanisms.

This study is a new case depicting the possibility to obtain isomorphous desolvates through a smooth dehydration. It demonstrates also that the exploration of a unary phase diagram can necessitate excursions in binary systems with solvents in order to discover new polymorphic form thanks to the management of soft desolvations.

Chapter III

Characterization of Safinamide Mesylate Solid-State Landscape

3 CHARACTERIZATION OF SAFINAMIDE MESYLATE SOLID-STATE LANDSCAPE

3.1 SAFINAMIDE MESYLATE

Safinamide mesylate, hereafter referred as SAFIM, IUPAC name: (S)-2-((4-((3-fluorobenzyl)oxy)benzyl) amino)propenamide methanesulfonate ($C_{18}H_{23}FN_2O_5S$) (Figure 3-1), is a chiral commercial drug (brand name Xadago) used as add-on treatment for Parkinson's disease. SAFIM, is crystallized from an acetone/water mixture during the industrial manufacturing process, and it exhibits needle like crystal shape inducing poor flowability properties.

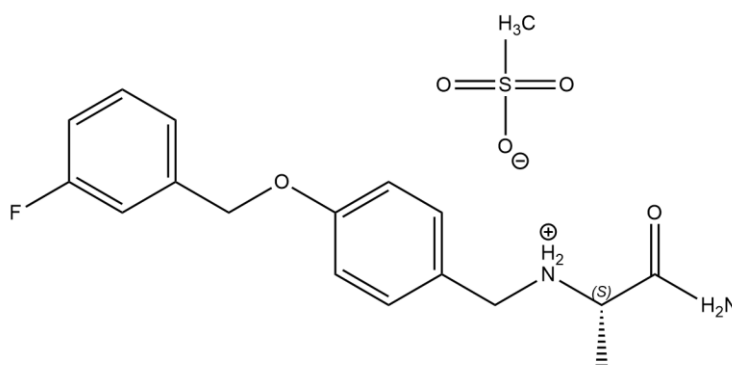


Figure 3-1. molecular structure of Safinamide mesylate ($M_w = 398.5$ g/mol)

To date, three crystalline phases of SAFIM have been reported: two enantiotropically related polymorphs with a solid-solid transition temperature of 2 °C (**A1** and **A2** for high and low temperature forms, respectively) and a hemi-hydrate (**H1**).^{94,95} As the structural purity is of key importance for pharmaceutical industry,⁹⁶ this chapter is dedicated to the study of the different SAFIM crystalline phases and more thoroughly on their relative stabilities.

3.2 SAFINAMIDE MESYLATE POLYMORPHISM

The different crystalline forms of anhydrous SAFIM were first reported in a patent application published in 2011 by Schlueter (WO 2011/047767A1).⁹⁴

Even if Schlueter proposes a single crystal resolution of the anhydrous forms, no single crystal of sufficient size and quality could be obtained during this study despite the numerous attempts (different crystallization conditions were tested as cooling crystallization and/or evaporation crystallization, in different solvents and solvent ratio). However, More recently, Pawlak et al.⁹⁵

proposed the crystalline structures resolved from powder x-ray diffraction of **A1** and **A2**. These later were used as reference phases in this study.

3.2.1 Characterization of the Safinamide mesylate high temperature form (A1)

Crystalline structure of SAFIM high temperature (**A1**) was also resolved by Pawlak⁹⁵ and Schlueter⁹⁴ from powder and single crystal X-ray diffraction. Crystallographic parameters are provided in Table 3-1.

Table 3-1: crystallographic parameters of SAFIM A1 according to Pawlak and Schlueter

	Pawlak ⁹⁵	Schlueter ⁹⁴
Resolution mode	Powder	Single crystal
Resolution temperature (°C)	25 °C	29 °C
Crystal system	Orthorhombic	Orthorhombic
Space group	$P2_12_12_1$	$P2_12_12_1$
<i>a</i> (Å)	5.5551(3)	5.5618(7)
<i>b</i> (Å)	15.5428(10)	15.568(2)
<i>c</i> (Å)	22.7568(3)	22.819(3)
α (°)	90	90
β (°)	90	90
γ (°)	90	90
Volume (Å³)	1964.86(5)	1975.8(4)
Calculated density	1.2686	1.339
Z	4	4
Z'	1	1
R1 (%)	6.992	6.83

SAFIM **A1** crystallizes in the $P2_12_12_1$ chiral space group, in an orthorhombic system. The asymmetric unit (represented in Figure 3-2) is composed of 1 molecule of SAFI and 1 molecule of mesylate ($Z'=1$), which is consistent with the stoichiometry 1:1 of the safinamide mesylate salt.

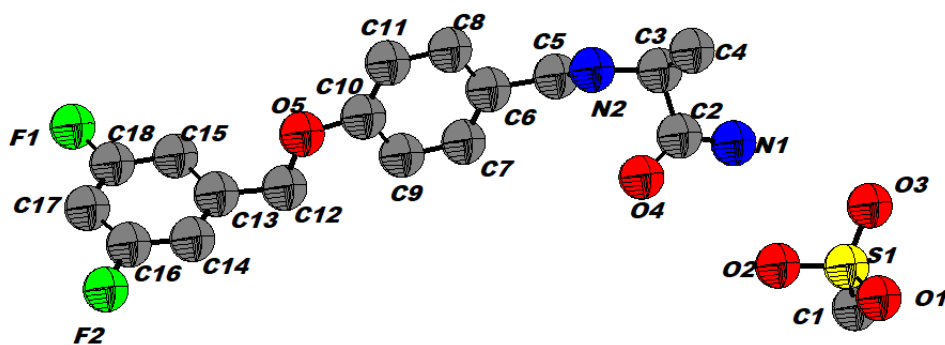


Figure 3-2: Asymmetric unit of SAFIM A1. The thermal displacement is isotropic as the data used are from the X-ray powder resolution

The fluorine atoms is a disordered atom with a statistical occupancy factor (SOF) of approximately 2/3 in position F1 and 1/3 in position F2. Therefore, the molecule exhibits two possible conformations, depending on the fluorinated-phenyl orientation. This feature will be discussed in part 2.3.

Molecules of mesylate and safinamide are connected through strong ionic-hydrogen bonds (Figure 3-3), where every mesylate anion is related to 4 different safinamide molecules along *b* and *a* directions. These interactions generate molecular layers in *ab* plane.

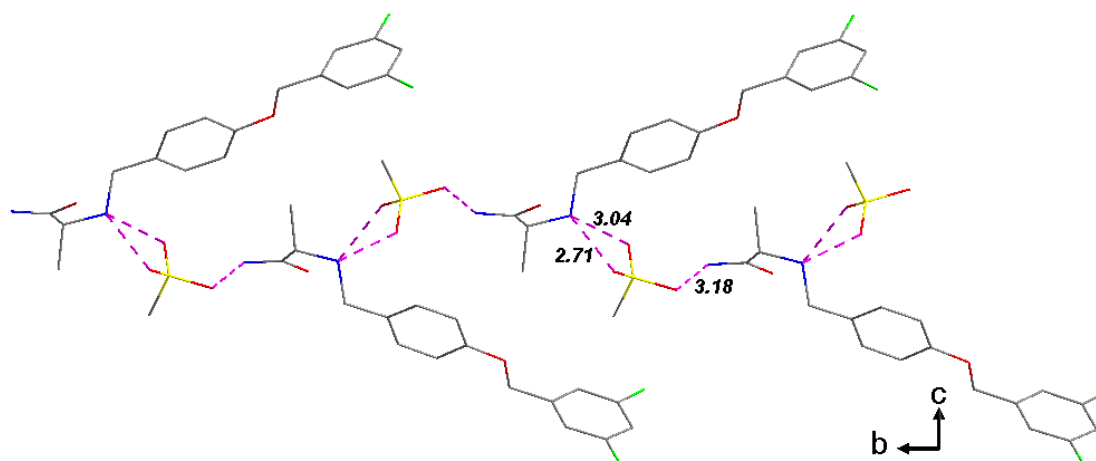


Figure 3-3: One molecular layer built from the ionic-hydrogen interactions between mesylate and safinamide molecules. These interactions are displayed in dashed purple line; the distances are given in angstrom. As hydrogen atoms are not calculated from XRPD resolution, the distances are measured from acceptor and donor of H-bonds.

The layers are stacked along *c* direction and the cohesion is ensured by van der Waals interactions (Figure 3-4). The location of the fluorine atom (either on F1 or F2 location) does not affect the packing as the main interactions are due to ionic-hydrogen bonds.

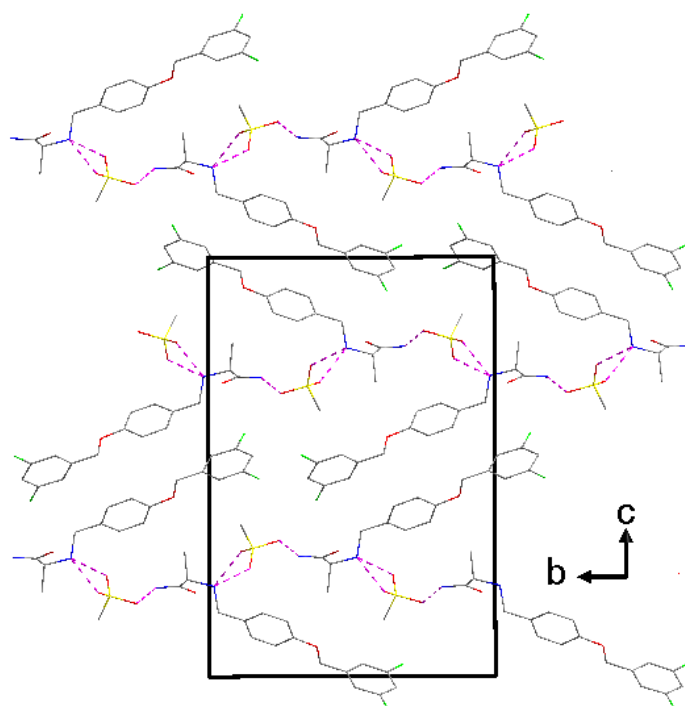


Figure 3-4: Crystal packing of SAFIM **A1**. The dashed lines represent the distance between H-bond donors and acceptors.
Top view: projection along *a* (layers are formed along *b* axis). Bottom view: stacking of the layers along *c* axis

Calculated powder x-ray diffraction pattern of SAFIM **A1** is given in Figure 3-5 and compared to SAFIM obtained industrially. The two powder X-ray diffraction patterns are similar indicating a good structural purity of our product.

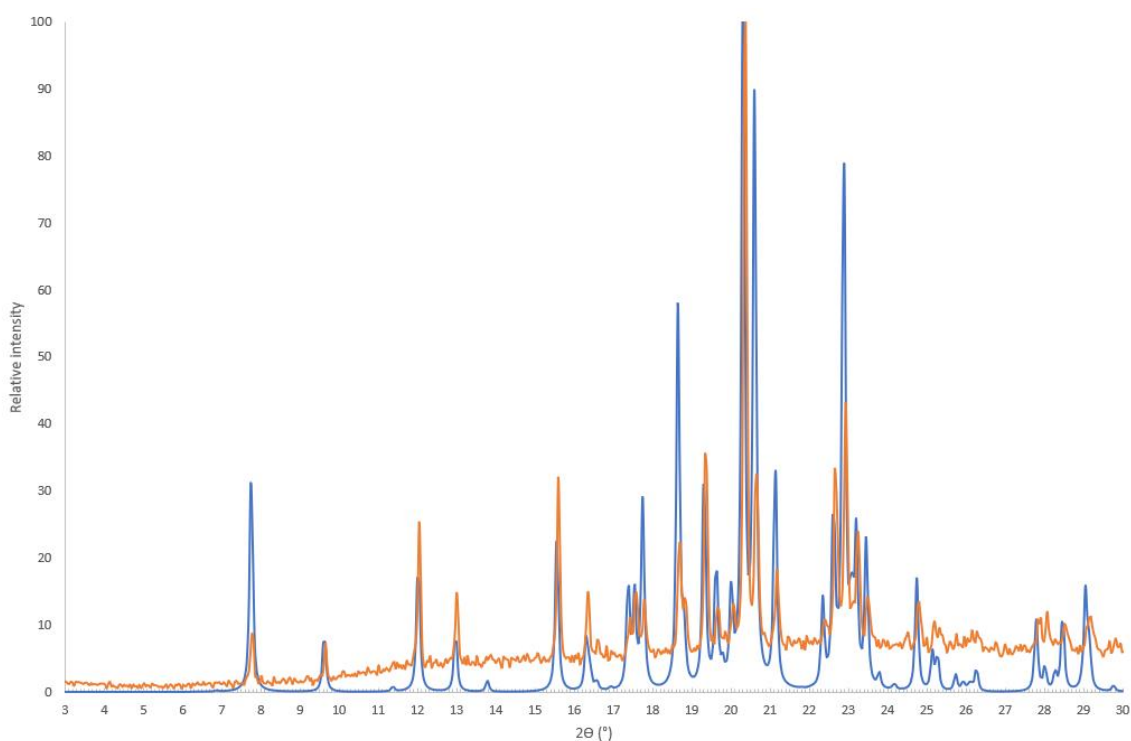


Figure 3-5: Comparison between calculated (blue) and experimental (orange) XRPD pattern of **A1**

3.2.2 Characterization of Safinamide mesylate low temperature form (**A2**)

Crystalline structure of SAFIM low temperature (**A2**) was also resolved by Pawlak⁹⁵ and Schlueter⁹⁴ from powder and single crystal X-ray diffraction. Crystallographic parameters are provided in Table 3-2.

Table 3-2: crystallographic parameters of SAFIM A2 according to Pawlak and Schlueter

	Pawlak ⁹⁵	Schlueter ⁹⁴
Resolution mode	Powder	Single crystal
Resolution temperature (°C)	-5	5
Crystal system	Orthorhombic	Orthorhombic
Space group	$P2_12_12_1$	$P2_12_12_1$
a (Å)	5.5227(3)	5.5427(6)
b (Å)	46.569(3)	46.639(8)
c (Å)	22.316(2)	22.324(3)
α (°)	90	90
β (°)	90	90
γ (°)	90	90
Volume (Å³)	5739.46(7)	5771(1)
Calculated density	1.3029	1.376
Z	12	12
Z'	3	3
R1 (%)	9.886	8.54

SAFIM **A2** crystallizes in the $P2_12_12_1$ the same chiral space group as **A1**. The asymmetric unit (represented in Figure 3-6) is composed of 3 molecules of SAFI and 3 molecules of mesylate ($Z'=3$), which is consistent with the stoichiometry 1:1 of the safinamide mesylate salt.

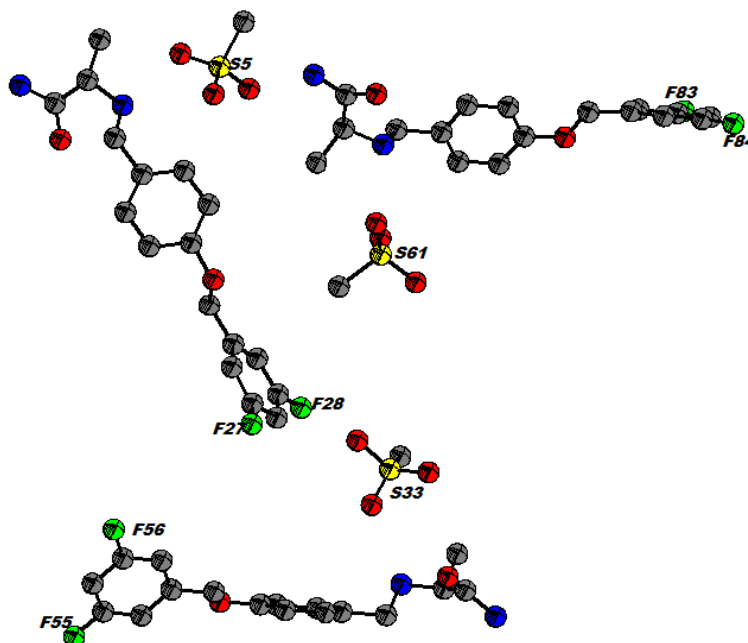


Figure 3-6: Asymmetric unit of SAFIM **A2**. The thermal displacement is isotropic as the data used are from the X-ray powder resolution

As encountered in **A1** structure, **A2** safinamide molecules exhibit a disorder on the fluorine atom position. Therefore, there is two possible safinamide conformations for each safinamide molecule (up to 6 conformations for this structure). However, the repartition of the SOF is different. For two of the safinamide molecules, the SOF is about 50% (for fluorine atom positions F55, F56, F83 and F84) whereas for the third safinamide molecule the SOF is at circa 93% for the F28, and 7% for the F27.

Molecules of mesylate and safinamide are connected through strong ionic-hydrogen bonds (Figure 3-7), where each mesylate is related to 4 different safinamide molecules along b and a directions. These interactions generate molecular layers in ab plane. The distances between acceptor and donor of ionic-hydrogen bonds are ranging from 2.2 to 3.2 Å.

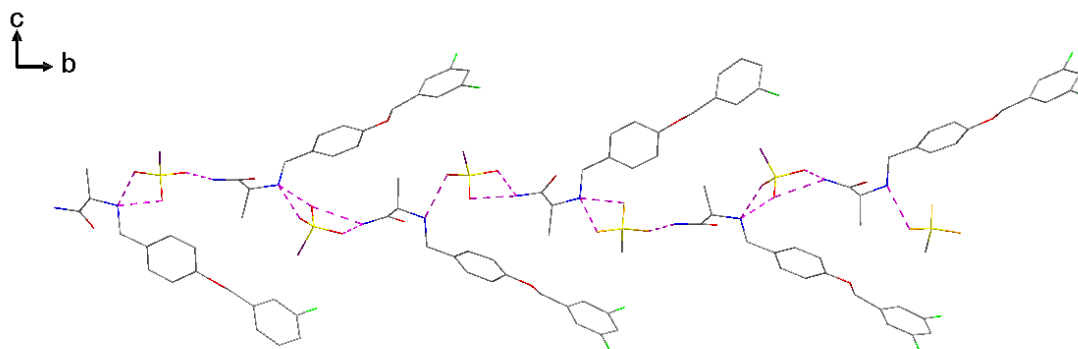


Figure 3-7: one molecular layer built from the ionic-hydrogen interactions between mesylate and safinamide molecules. These interactions are displayed in dashed purple lines. The layers are built in *ab* plane

The crystal packing of SAFIM **A2** is represented in Figure 3-8.

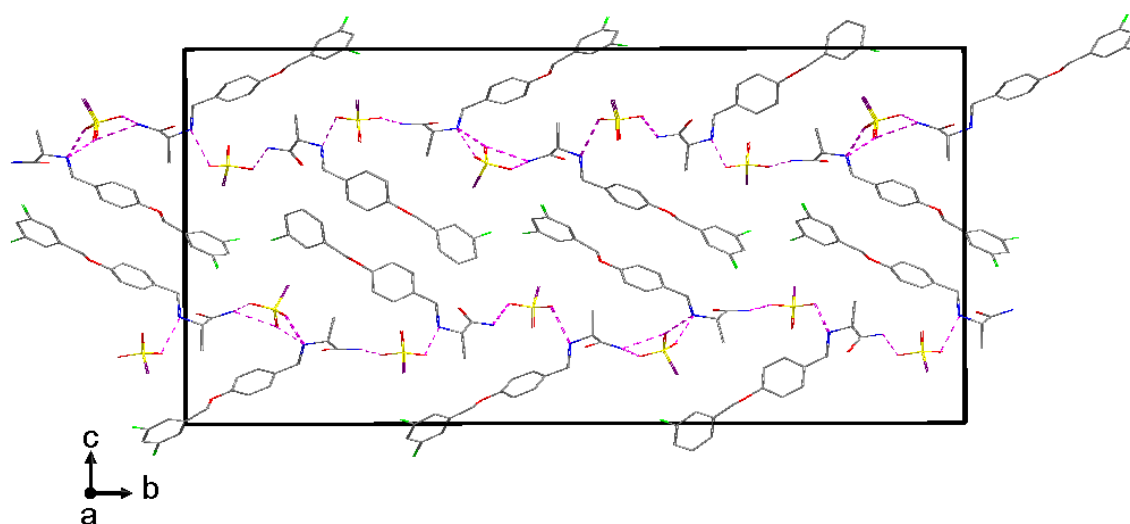


Figure 3-8: Crystal packing of **A2**. The dashed lines represent the distances between acceptor and donor of ionic-hydrogen bonds. The molecular layers are stacked along *c* direction

Layers are stacked along *c* axis through Van der Waals interactions (Figure 3-8). A distance of 2.2 Å for a donor to acceptor bond is too short, showing that the proposed structure presents some issues concerning the interatomic distances in the crystal packing and can explain the relative high value of *R*₁ (9.886%, Table 3-2).

Calculated powder X-ray diffraction pattern of SAFIM **A2** is given in Figure 3-9 and compared to experimental XRPD pattern obtained from a suspension of SAFIM in acetone at -20 °C. Even if the experimental XRPD exhibits a low resolution due to experimental conditions, the two XRPD patterns exhibit similar reflections.

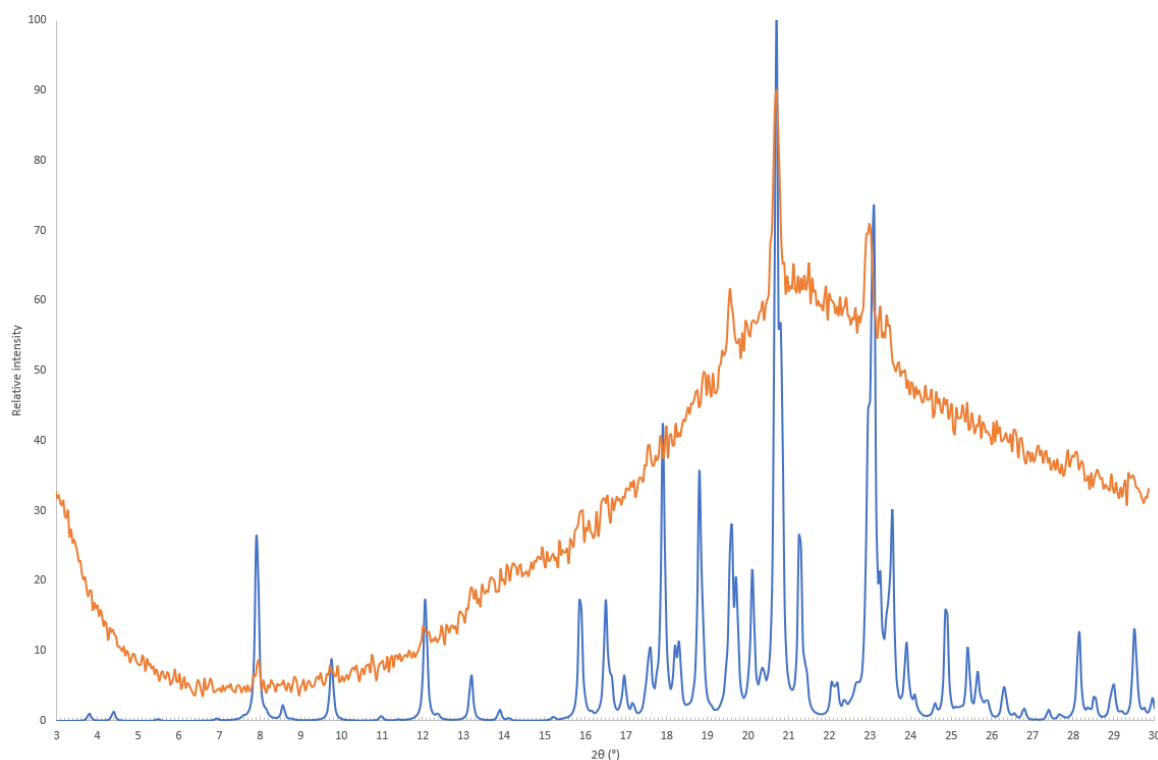


Figure 3-9: Comparison between calculated (blue) and experimental (orange) XRPD pattern of **A2**

Polymorphs having different physicochemical properties (e.g., solubility, melting point, density...) they exhibit different pharmaco-properties (e.g., dissolution rate, bioavailability, ...).⁹⁷⁻¹⁰⁰ Then, the polymorphic transition of safinamide mesylate was thoroughly studied in the following part.

3.2.3 Structure filiation between **A1** and **A2**

Both polymorphs exhibit molecular layers that are built upon the same scheme. The only crystallographic difference between **A1** and **A2** relies in the b parameter: $b(\mathbf{A2}) = 3 b(\mathbf{A1})$, and therefore, the volume is also tripled. Consistently, the number of independent molecules in the asymmetric units change from $Z' = 1$ for **A1** to $Z' = 3$ for **A2**.

If the two crystal packing of **A1** and **A2** are superimposed, it can be noticed that the molecular arrangements are identical. (Figure 3-10, bottom view). Moreover, one can note that 3 lattices of **A1** can fit in 1 lattice of **A2** (Figure 3-10, top view), accordingly to the structure parameters.

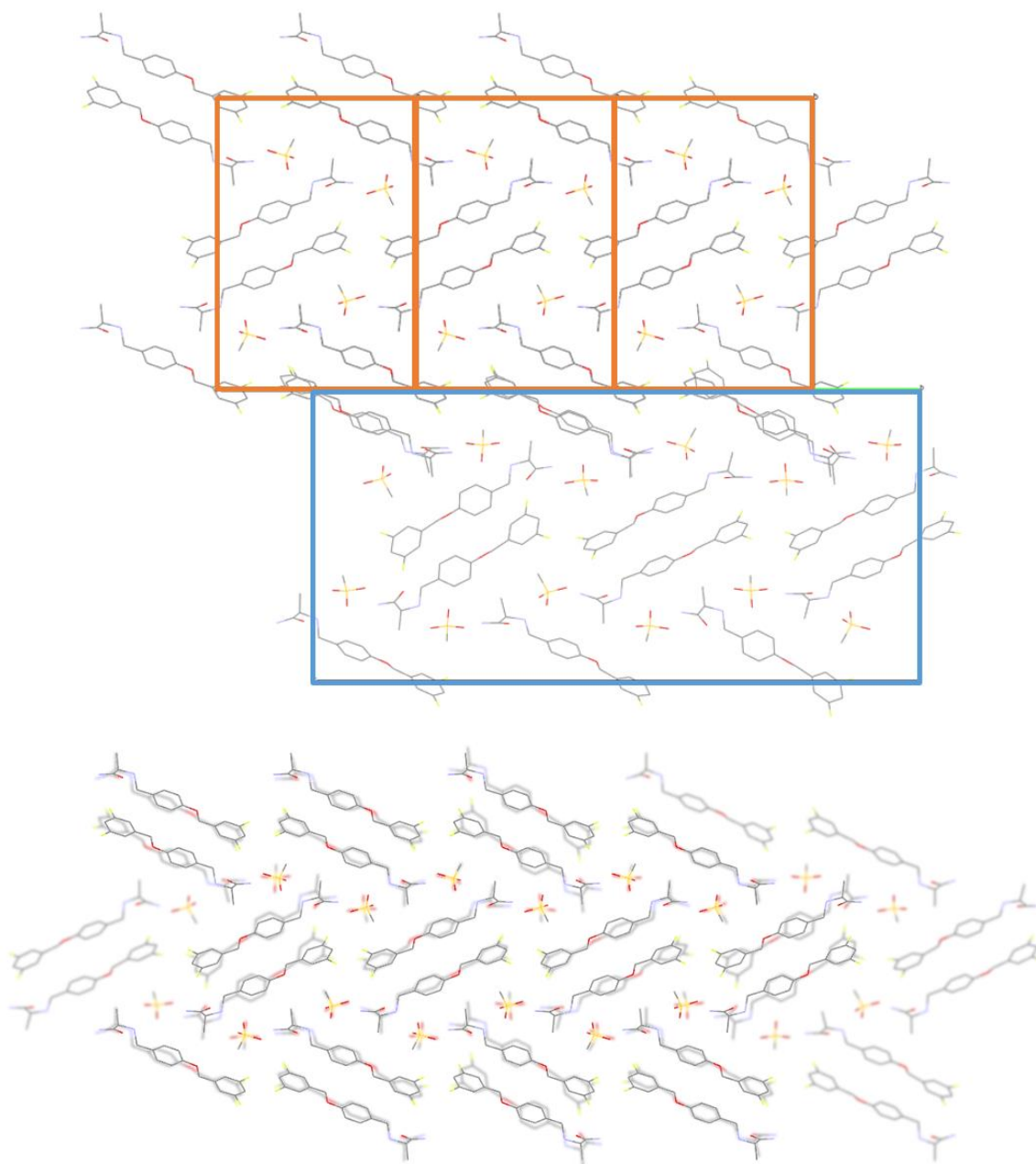


Figure 3-10: top view: comparison between three lattices of **A1** (orange rectangles) and one lattice of **A2** (blue rectangle) along a axis. Bottom view: Superimposition of **A1** crystal packing over **A2** crystal packing (displayed slightly blurred to distinguish the two packing)

Sefinamide molecules can adopt two conformations depending on the rotation of the fluorinated phenyl moiety along C12-C13 bond (Figure 3-2). According to Schlueter et al.⁹⁴ patent, the SOF of the fluorine atom is attributed to static disorder. During the growth period of the crystallization, sefinamide molecules can dock to the surface of the crystal either in the conformation *a* or in conformation *b* (Figure 3-11). Then, due to steric hindrance, the rotation along C12-C13 is blocked as well as the conformation of sefinamide.

In **A1** structure ($Z'=1$), the SOF of the fluor is about $2/3 : 1/3$, *i.e.*, in the crystal structure of SAFIM **A1**, $2/3$ of safinamide molecules are in conformation a. (Figure 3-11), and $1/3$ of safinamide molecules are in conformation b. (Figure 3-11).

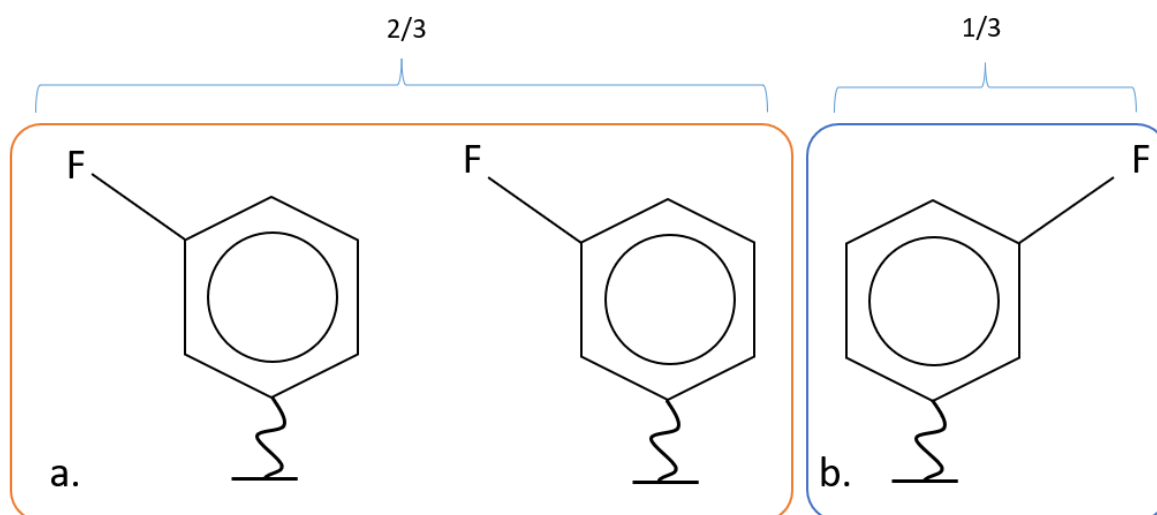


Figure 3-11: Possible configurations of safinamide fluorinated phenyl moiety according to SOF in **A1** structure

In the crystal structure of SAFIM **A2**, one molecule of safinamide exhibits a SOF around 93%, and around 50% for the two others, *i.e.*, one safinamide molecule is mostly blocked in one conformation, and the two others adopt equivalently one or other conformation (Figure 3-12). Nevertheless, the overall SOF of the fluorine atoms in **A2** remains equal to the **A1** fluorine SOF: $1/3$ and $2/3$.

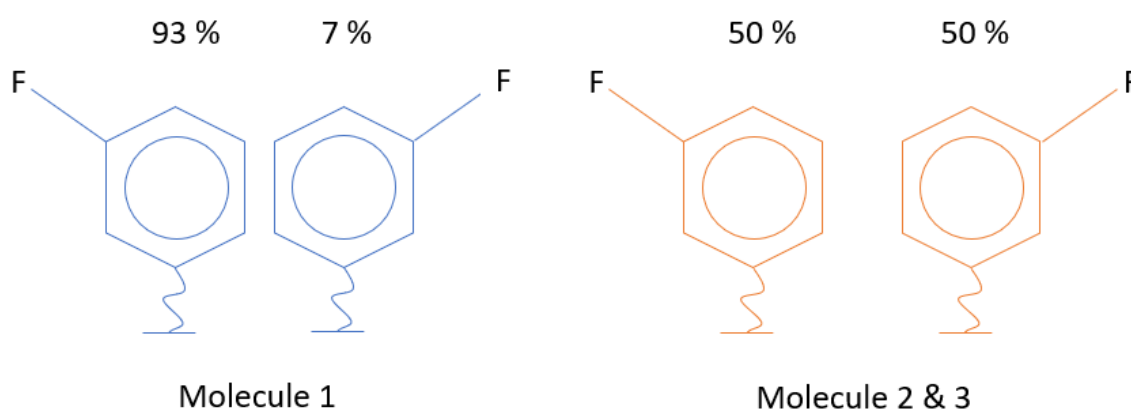


Figure 3-12: Possible configurations of the 3 safinamide fluorinated phenyl moieties according to SOF in **A2** structure. Molecule 1 might correspond to conformation a on Figure 3-11, and the molecules 2 and 3 to one conformation a and one conformation b.

These differences between **A1** and **A2** were attributed to the formation of a slightly different conformer of SAFIM due to the slowing down of molecular dynamics (*i.e.*, vibrational movement) on cooling. In **A2** structure, one molecule of SAFIM is “frozen” in a defined conformation on cooling (represented in green in Figure 3-13).

Moreover, from **A1** crystal lattice to **A2** crystal lattice, safinamide molecules keep the same orientation and the conformation is only modified through the vibration of the fluorinated phenyl moiety (Figure 3-13).

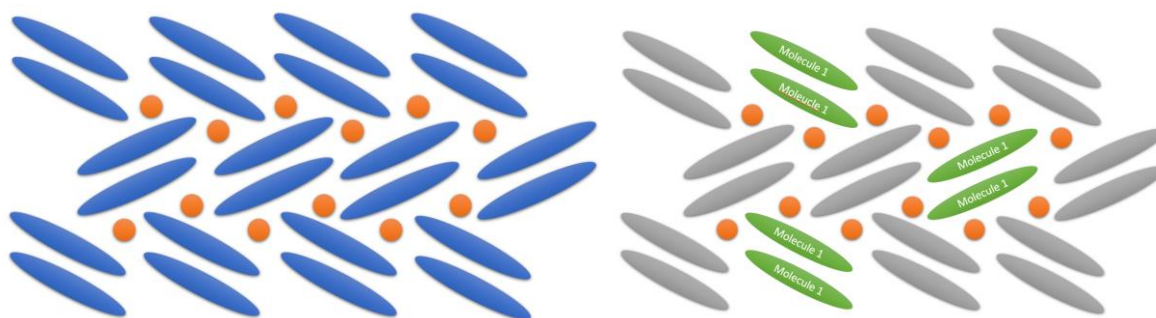


Figure 3-13: Schematic representation of the crystal packing of **A1** (left) and **A2** (right): safinamide molecules are displayed in oval and mesylate molecules in orange circles

This kind of transition refers to order/disorder transition through conformational polymorphism.¹⁰¹ Buerger¹⁰² defined such a transition as the ability of “molecules that statistically take several orientations to become ordered in one orientation”.

3.3 STUDY OF THE POLYMORPHIC TRANSITION **A1** \leftrightarrow **A2**

3.3.1 Thermal behavior of anhydrous safinamide mesylate

When heating a sample of industrial SAFIM at 2 K/min from room temperature up to 230 °C, the DSC curve (Figure 3-14) exhibits only a single sharp endothermic event at 217.8 °C (onset), corresponding to the melting of the form **A1** of SAFIM.

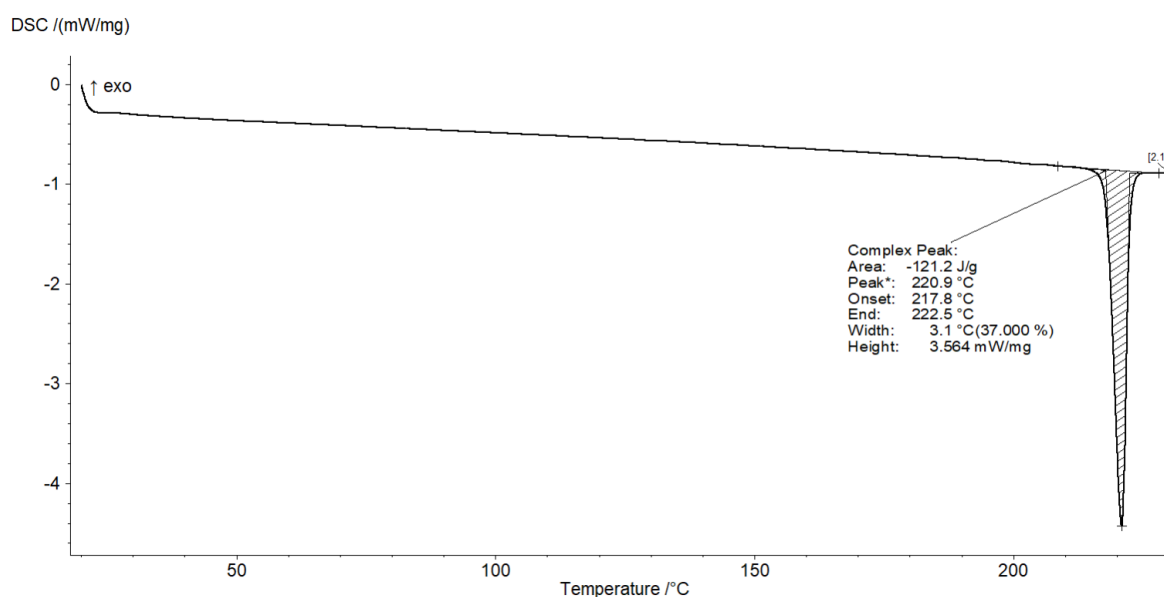


Figure 3-14: DSC analysis of SAFIM at 2 K/min

When the following temperature program is applied to a raw sample of SAFIM:

- (i) Cooling from 40 °C to -15 °C at 2 K/min
- (ii) Heating from -15 °C to 40 °C at 2 K/min

During cooling, the DSC curve exhibits an exothermic event at 5.0 °C (onset temperature; green curve, Figure 3-15), corresponding to the transition from the SAFIM high temperature form (**A1**) to the low temperature form (**A2**). During heating from -15 °C, an endothermic event is observed at 19.7 °C (onset temperature; blue curve on Figure 3-15). This event corresponds to the polymorphic transition **A2** → **A1** associated with an enthalpy of transition of -2.95 kJ/mol. The transition **A1** ↔ **A2** is fully reversible and repeatable which can be attributed to an enantiotropic behavior.

The polymorphic transition is accompanied with a large hysteresis (about 15 °C) typical of first order transition according to Ehrenfest classification.¹⁰³ This large hysteresis explains why SAFIM is always characterized in **A1** even at room temperature: on cooling, the polymorphic transition **A1** → **A2** occurs below the room temperature.

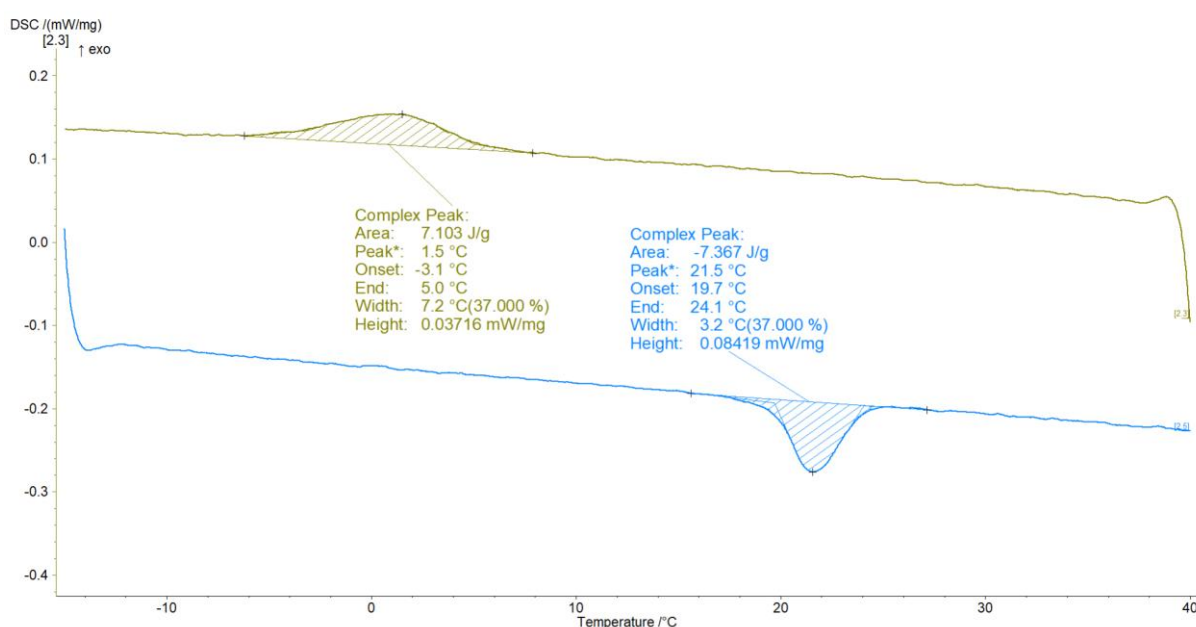


Figure 3-15: DSC analysis of SAFIM. Green curve: step (i); blue curve: step (ii).

3.3.1.1 Monitoring of the polymorphic transition with temperature-controlled x-ray diffraction by using In-situX[®] measurement

The polymorphic transition of SAFIM was monitored by using temperature-resolved powder X-ray diffraction. Figure 3-16 shows X-ray diffraction patterns of anhydrous SAFIM **A1**, starting from room temperature (ca. 20 °C) down to -50 °C at 0.1 K/min followed by an isotherm at -50 °C during 120 min (acquisition parameters: 1 sec of acquisition per step of 0.04 ° from 3° to 30°; 13 min between each pattern).

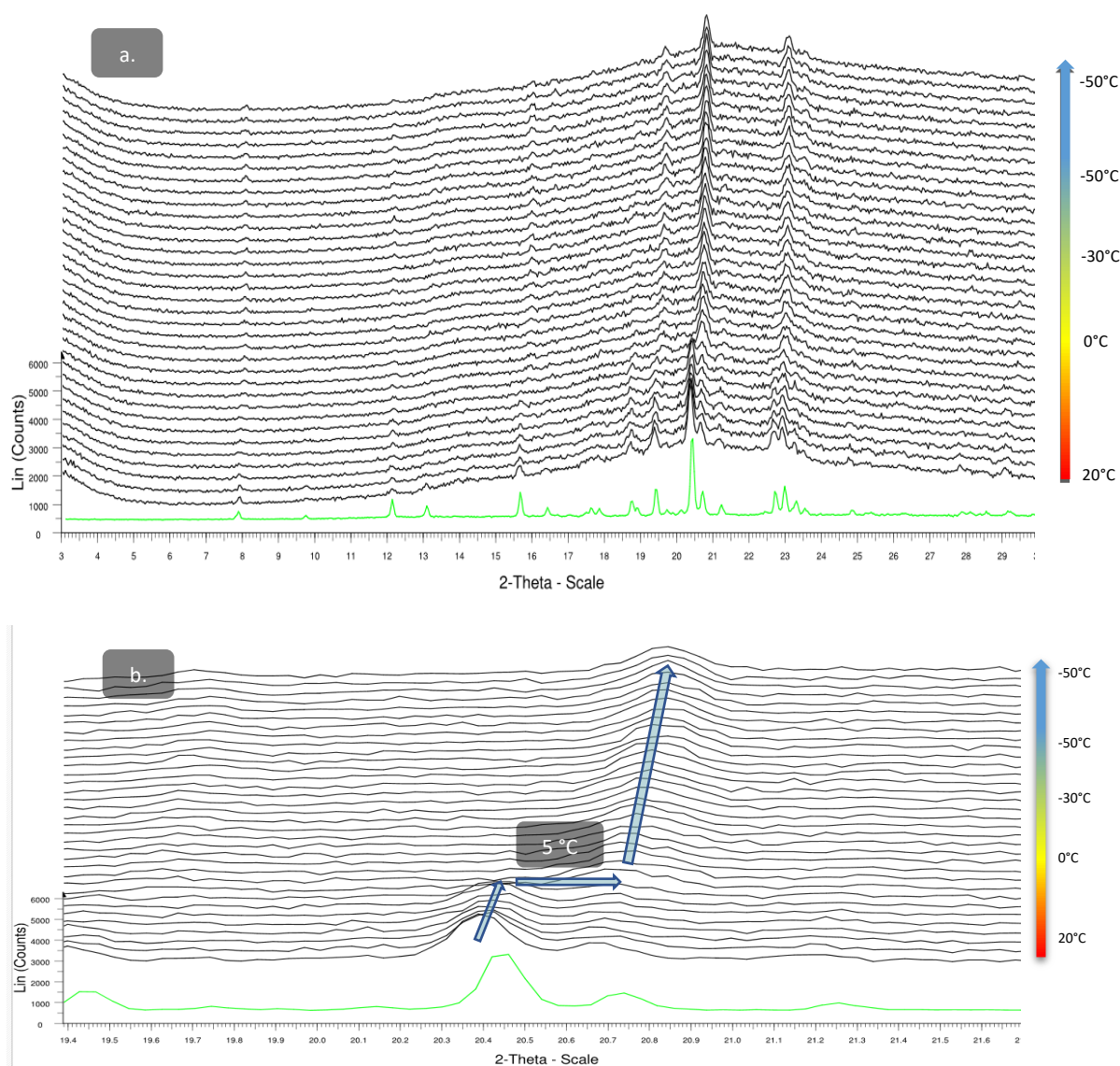


Figure 3-16: (a) In-situX Diffractograms of SAFIM by using In-situX diffractometer during the cooling of A1 (A1 reference in green) and (b) is an enlargement between 19° and 21° (2θ) showing the shift of diffraction peak corresponding to the transition of A1 to A2

Regarding the X-ray monitoring of the transition (Figure 3-16, a.) there is no major modification except the small peak displacements from 20.4° to 20.8° at 5 °C (Figure 3-16, b.) at 15.7° and 19.5°. Moreover, the merge of several peaks at 20.5° and 22.8° is also observed. These subtle variations recorded on diffraction peaks are consistent with a rearrangement of the crystal lattice related to an order/disorder transition.

3.3.2 Calculation of the A1 ⇌ A2 activation energy of the polymorphic transition

In this study, the transition was studied in non-isothermal conditions by means of calorimetric measurements, first with the Kissinger⁸⁵ approach, and then with the Ozawa-Flynn-Wall⁸⁴ approach (Table 3-3).

Table 3-3: Different methods used for determination of the activation energy in non-isothermal conditions

Method	Approach
Kissinger	$\ln\left(\frac{\varphi}{T_p^2}\right) = -\frac{E_a}{RT_p} + \ln\left[\frac{AR}{E_a}\right]$
Ozawa-Flynn-Wall	$\ln(\varphi) = -1.052 \frac{E_a}{RT_p} + cst$

With φ the heating rate, T_p the peak temperature, R the molar gas constant, and A a constant.

These two methods rely on the use of different heating rates (φ), and the associated temperature of transition **A2** → **A1** (T_p) to determine the activation energy of the transition E_a .

SAFIM was submitted to different heating rates (φ) in DSC: 1 K/min, 2 K/min, 4 K/min, 8 K/min, 16 K/min, and 32 K/min in the -30 °C to 60 °C range. Thermograms are presented in Figure 3-17 and the corresponding thermal data are listed in Table 3-4. All thermograms exhibit an endothermic event which corresponds to the polymorphic transition of **A2** into **A1**.

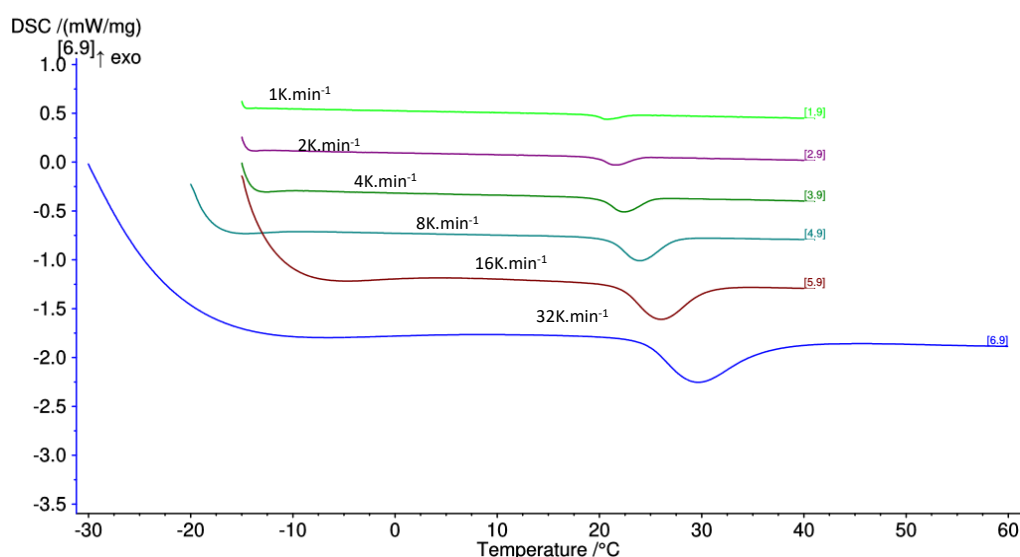


Figure 3-17: Thermograms of safinamide mesylate at different heating rates. All endothermic events are attributed to order-disorder polymorphic transition.

Table 3-4: Thermal data for SAFIM at six different heating rates (average of two set of measurements)

Heating rate φ (K/min)	T_{onset} (°C)	T_{peak} (°C)	Enthalpy of transformation (kJ/mol)
1	19.45	20.8	-2.95
2	19.75	21.6	-2.95
4	20.20	22.4	-2.95
8	21.10	24	-3.07
16	23.00	27.1	-2.43
32	24.40	29.3	-2.79

The average enthalpy of transformation **A2** → **A1** is 2.86 kJ/mol.

With the Kissinger based method, The plot of $\ln\left(\frac{\varphi}{T_p^2}\right)$ versus $\frac{1000}{T_p}$ at 4, 8, 16 and 32 K/min (1 and 2 K/min are not taken into account because of the non-linearity at low heating rates, Figure 3-18) gives an activation energy about 203 kJ/mol with a regression coefficient of 0.9847. The activation energy was also calculated with the Ozawa-Flynn-Wall method (Figure 3-18). The calculated activation energy with this method is 198 kJ/mol, in agreement with the 203 kJ/mol found with Kissinger's method and with a similar regression coefficient (0.9854).

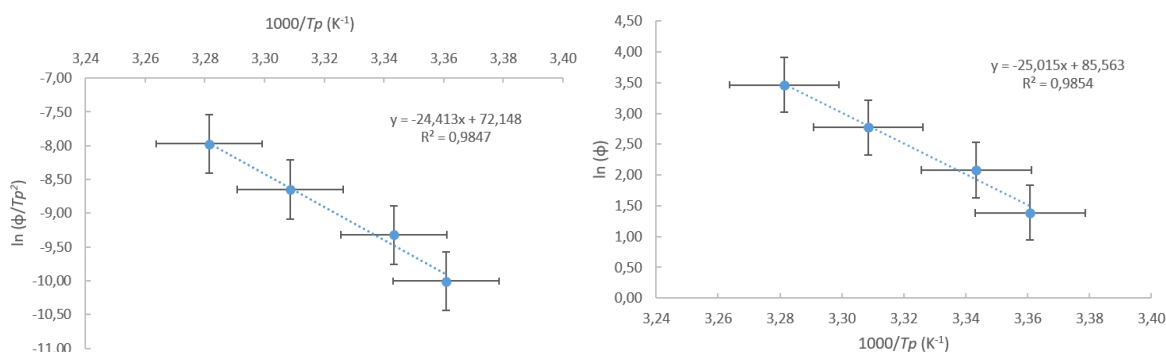


Figure 3-18: Left: Kissinger plot of $\ln\left(\frac{\varphi}{T_p^2}\right)$ versus $\frac{1000}{T_p}$; Right: Ozawa-Flynn-Wall plot of $\ln(\varphi)$ versus $\frac{1000}{T_p}$

The activation energy is surprisingly high for an order-disorder supposed mechanism, such values are usually observed for transitions exhibiting a destruction-reconstruction mechanism, which require more energy for the new phase to nucleate and grow, as in the case of Phenobarbital: Form A → Form B, 257 kJ/mol,¹⁰⁴ Furosemide: Form III → form IV, 246 kJ/mol⁹⁹ and 3-hydroxybenzoic acid: monotropic transition, 139 kJ/mol.¹⁰⁵ Up to date, no explanation was found for the particular behavior of our system.

Even if the calculated value of activation energies maybe not in accordance with a non-destructive process, several parameters are in accordance with the presence of an order/disorder transition between **A1** and **A2** form:

- (i) Regarding the crystal structure of **A1** and **A2**, there is a clear structural filiation between the two solids.
- (ii) The same single crystal was used to resolve the structure of both polymorphic forms, this is a case of a Single Crystal to single Crystal polymorphic transition. Indeed, in the case of a destructive/reconstructive transition, crystals must be altered by the transition due to the nucleation and growth mechanisms. This was confirmed by performing cold-stage microscopy on crystals of SAFIM where no surface or alteration were observed during heating or cooling (data not shown).

3.4 SAFINAMIDE MESYLATE HEMI-HYDRATE

In addition to the two polymorphic forms, safinamide mesylate also exhibits a hydrate which refers to **H1** hereafter. The structure and stability of this one are discussed in the following part.

3.4.1 Characterization of Safinamide mesylate H1

Crystalline structure of SAFIM hydrate (**H1**) was resolved from single crystal diffraction by Pawlak et al.⁹⁵ and from x-ray powder diffraction for Schlueter.⁹⁴ Crystallographic parameters are provided in Table 3-5.

Table 3-5: Structure parameters of SAFIM H1 according to Pawlak and Schlueter

	Pawlak ⁹⁵	Schlueter ⁹⁴
Crystal system	Monoclinic	Monoclinic
Resolution mode	Single crystal	Powder
Temperature of resolution	-173 °C	NC
Space group	$P2_1$	$P2_1$
a (Å)	5.6001(3)	5.7
b (Å)	20.4399(9)	20.9
c (Å)	16.7486(9)	17.2
α (°)	90	90
β (°)	95.839(4)	76.9
γ (°)	90	90
Volume (Å³)	1907.19(17)	1985
Calculated density	1.419	NC
Z	2	4
Z'	1	1
R1 (%)	7.67	N/C

SAFIM **H1** crystallizes in the $P2_1$ non-centrosymmetric space group, in a monoclinic system. The asymmetric unit (represented in Figure 3-19) is composed of 2 molecules of SAFI and 2 molecules of mesylate ($Z'=1$), which is consistent with the stoichiometry 1:1 of the safinamide mesylate salt. Moreover, the asymmetric unit also contains 1 molecule of water, meaning that the stoichiometry of the hydrated form is 2:1 (2 molecules of SAFIM for 1 molecule of water). The hydrate is then a hemi-hydrate.

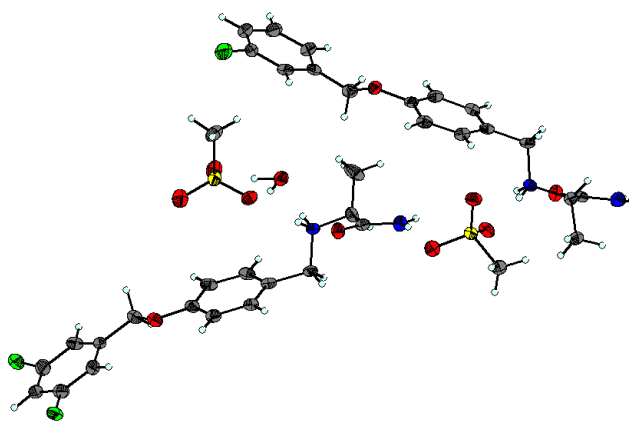


Figure 3-19: Asymmetric unit of SAFIM H1

The crystal packing of SAFIM H1 is represented in Figure 3-20.

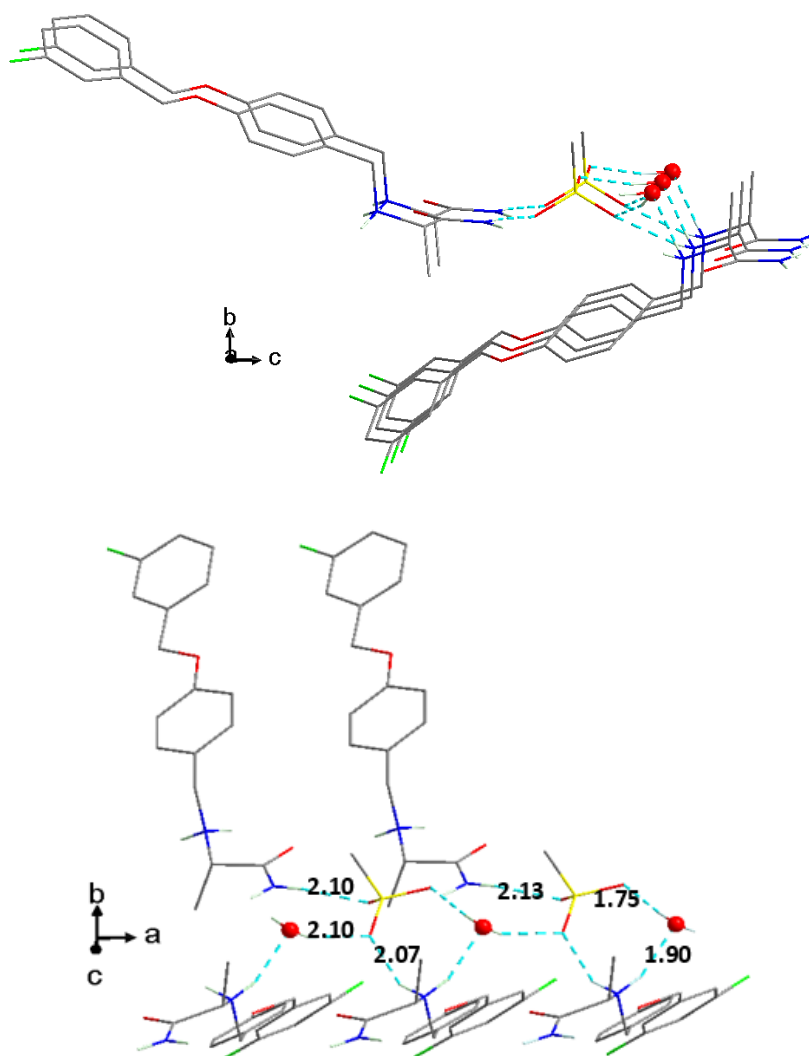


Figure 3-20: Crystal packing of SAFIM H1. Top view: representation along *a* axis. Bottom view: representation along *c* axis. H-bonds are displayed in blue dashed lines.

The Periodic Bond Chain (PBC) is constructed along *a* axis due to both ionic and hydrogen bonds (distances in the range of 1.9 to 2.1 Å, Figure 3-20). Water molecules ensure the formation of

the PBC along a direction (Figure 3-20, displayed in ball and stick representation) with only one mesylate.

The second mesylate connects the PBC together and leads to the formation of plan in the ac direction (Figure 3-21)

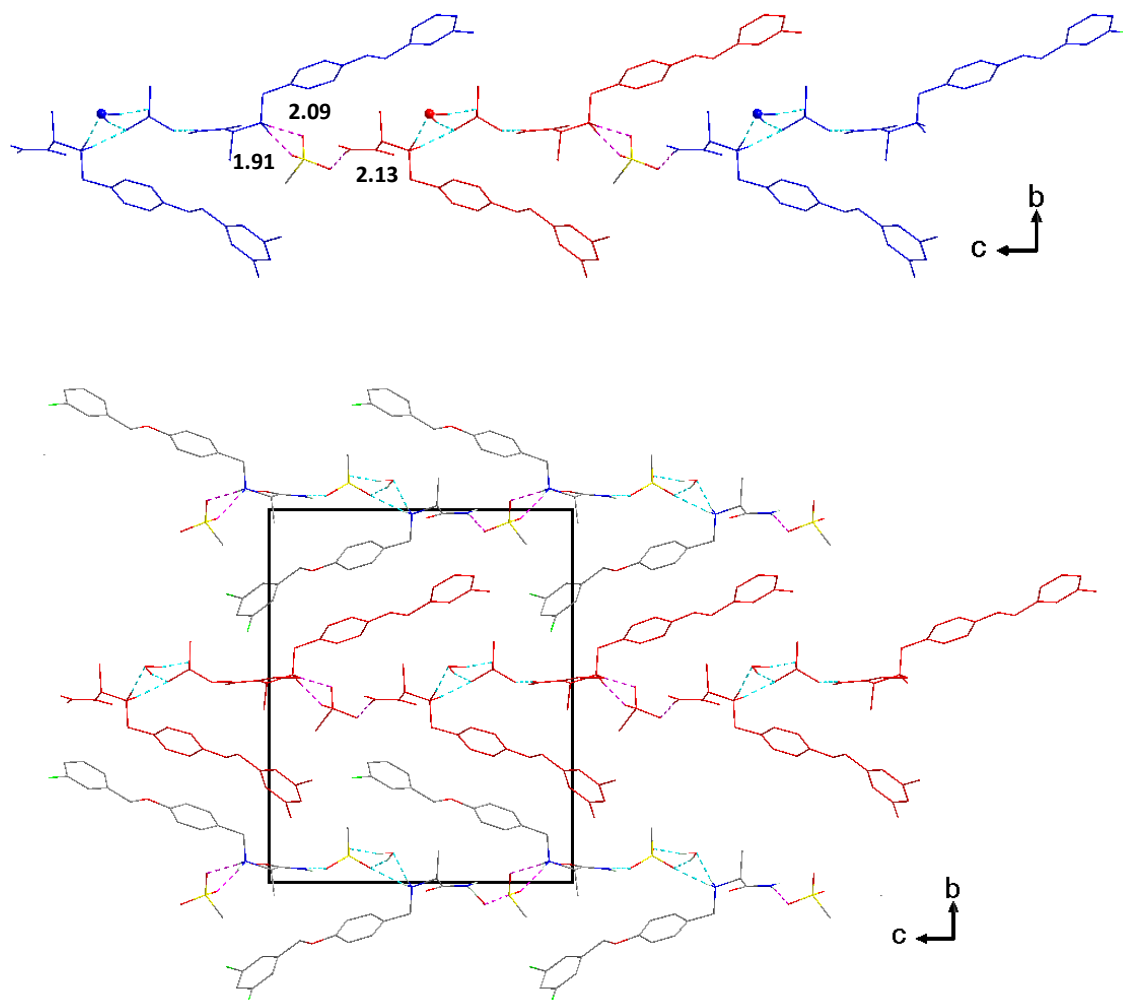


Figure 3-21: Top view: stacking of three PBC along c , ensured by second mesylate molecule (PBC are alternatively represented in blue and red). The H-bonds are displayed in dashed purple line). Bottom view: projection of the crystal packing along a (a PBC is represented in red)

One can note that one of the two molecules of safinamide displays two possible conformations for the fluorinated phenyl moiety (molecule 2, Figure 3-22).

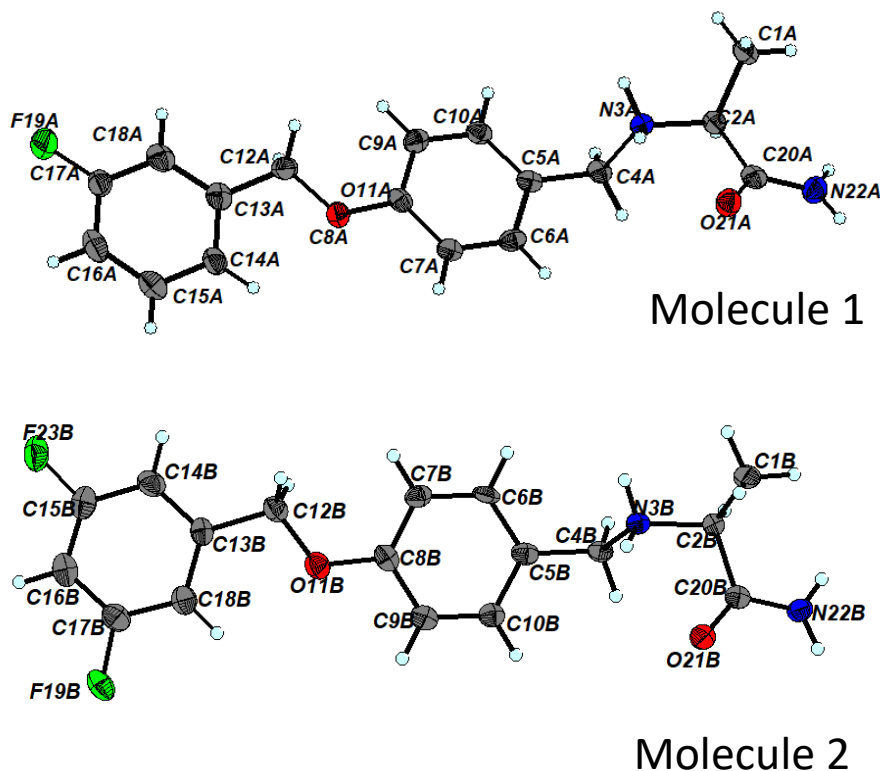


Figure 3-22: Safinamide molecules in **H1** form. Molecule 2 displays two possible positions for the fluorine atom (F23B or F19B)

Pawlak *et al.*⁹⁵ have calculated a SOF of 50% for position F19B and F23B. During crystallization, molecule 2 can dock to the surface of the crystal either in a conformation or in the other with a limited impact on the total energy of the crystal lattice: the conversion of a crystal of **H1** where the fluorine atoms are in position F23B to a crystal where the fluorine atoms are in position F19B leads to an increase of 1.12 kJ of the total crystal lattice energy (DFT calculations).⁹⁵

Moreover, due to steric hindrance, the conformation adopted by molecule 2 during the crystallization is blocked at the solid state leading to static disorder. They also shown that fluorinated phenyl moiety of molecule 1 being involved in the PBC construction, only one conformation can be adopted (molecule 1, Figure 3-22)

3.4.2 Study of the binary system Safinamide mesylate/water

3.4.2.1 Thermodynamic behavior of binary system Safinamide mesylate/water

In order to obtain pure SAFIM **H1**, SAFIM was recrystallized in a water/acetone mixture (10/90; vol./vol.) by cooling crystallization (from 60 °C to 20 °C). The obtained suspension was characterized by mean of powder x-ray diffraction (Figure 3-23) and TGA-DSC (Figure 3-24).

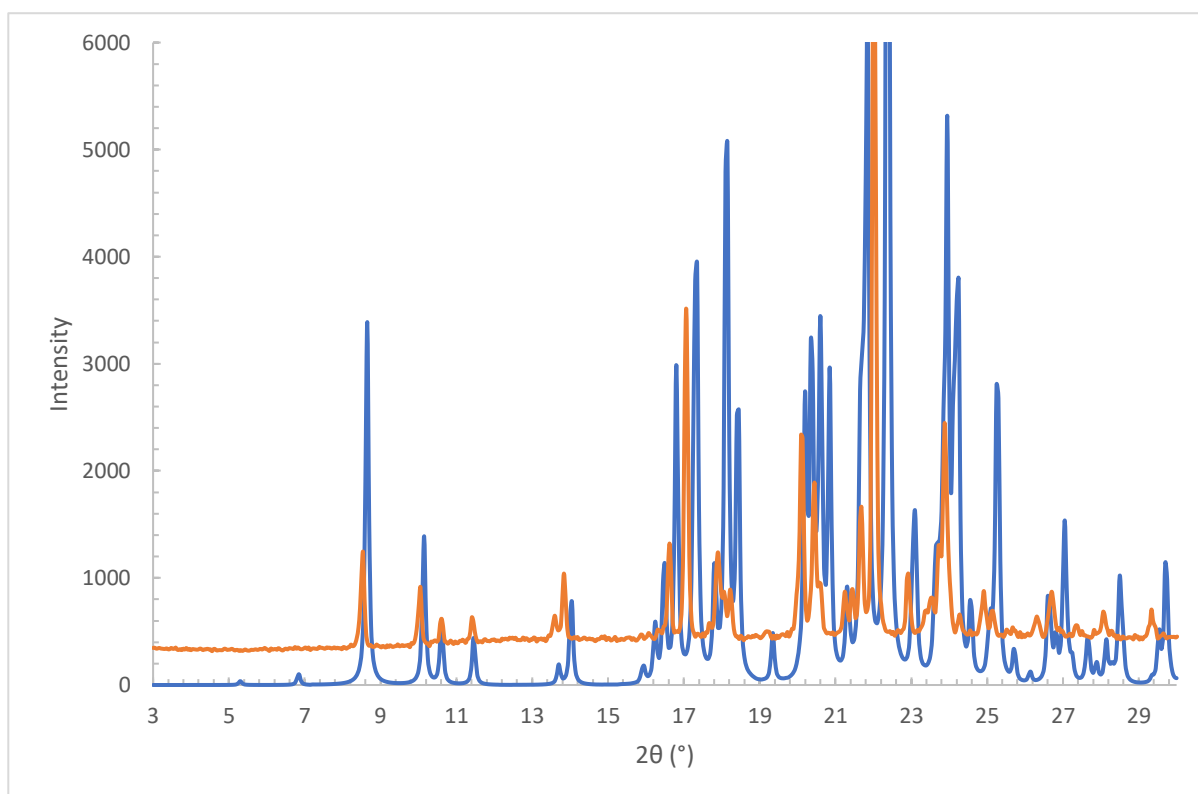


Figure 3-23: Compared XRPD patterns: SAFIM H1 calculated (blue), SAFIM obtained from slurry in water/acetone mixture at 25 °C

Comparison between calculated and experimental XRPD patterns of SAFIM **H1** exhibits some differences:

- (i) Additional reflections of low intensity can be observed at 5.3° and 6.8° on the calculated pattern (preferred orientation effect)
- (ii) The peaks of the calculated pattern are shifted to higher angles of diffraction

The shift of the peaks can be explained by the resolution of the structure that was conducted at 100 K while the experimental XRPD was carried out at room temperature (about 25 °C). Such a difference in temperature leads to modification of lattice parameters due to contraction/expansion of the crystal lattice, leading to slight modification of the diffraction angles.

Moreover, despite the peak shifts, the calculated and experimental XRPD patterns exhibit the same reflections.

According to XRPD, the solid obtained from slurry in acetone/water mixture corresponds to the hemi-hydrate **H1** (this experimental XRPD pattern will be used as reference for the next comparisons).

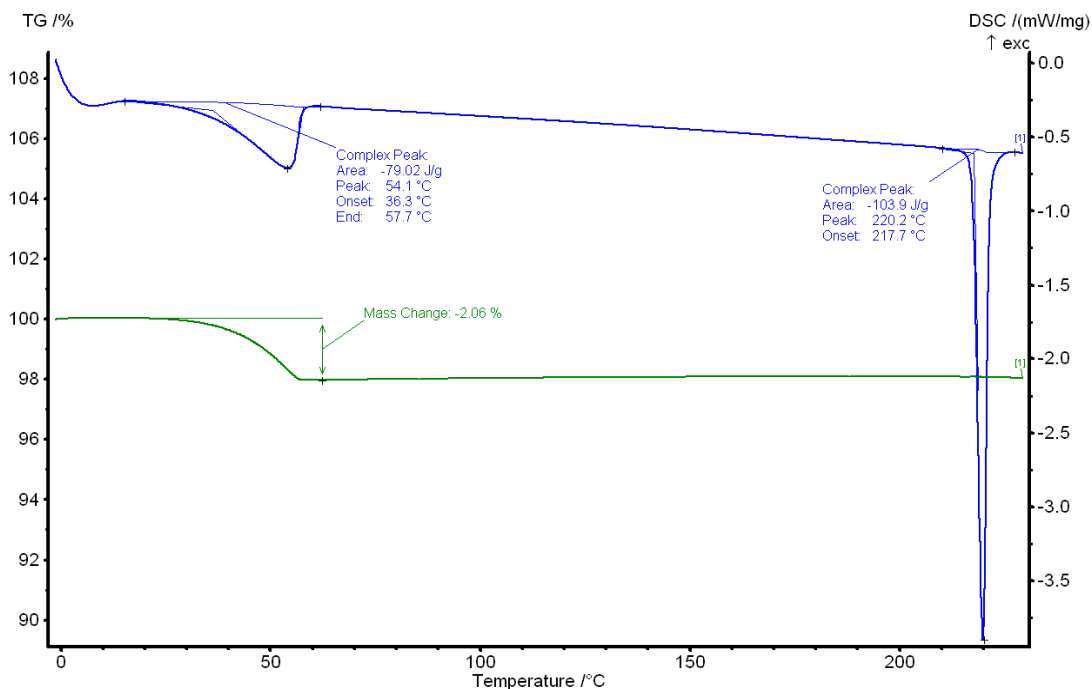


Figure 3-24: TGA-DSC of SAFIM obtained from slurry in a water/acetone mixture. Starting point at 0 °C with a heating rate of 5K/min (The theoretical mass loss is 2.2 %wt)

On the TGA-DSC curve, the first endothermic event has an onset temperature of 36.3 °C and an end set of 57.7 °C (blue curve, Figure 3-24), corresponding to the dehydration of the initial solid. It is associated to a mass loss of 2.06 %_{wt} which is consistent with the stoichiometry of a hemi-hydrate (theoretical value: 2.2 %_{wt}). No thermal events were observed until the melting of SAFIM form **A1** at 217.7 °C. One can note that no degradation occurs until the maximum analysis temperature (230 °C).

3.4.2.2 Saffinamide mesylate behavior vs relative humidity

Anhydrous SAFIM (**A1**) was submitted to DVS analyses at 25.7 °C and 38.5 °C, following a sorption-desorption cycle: 0-90-0-90-0 (in RH%). Figure 3-25 displays the sorption-desorption isotherms.

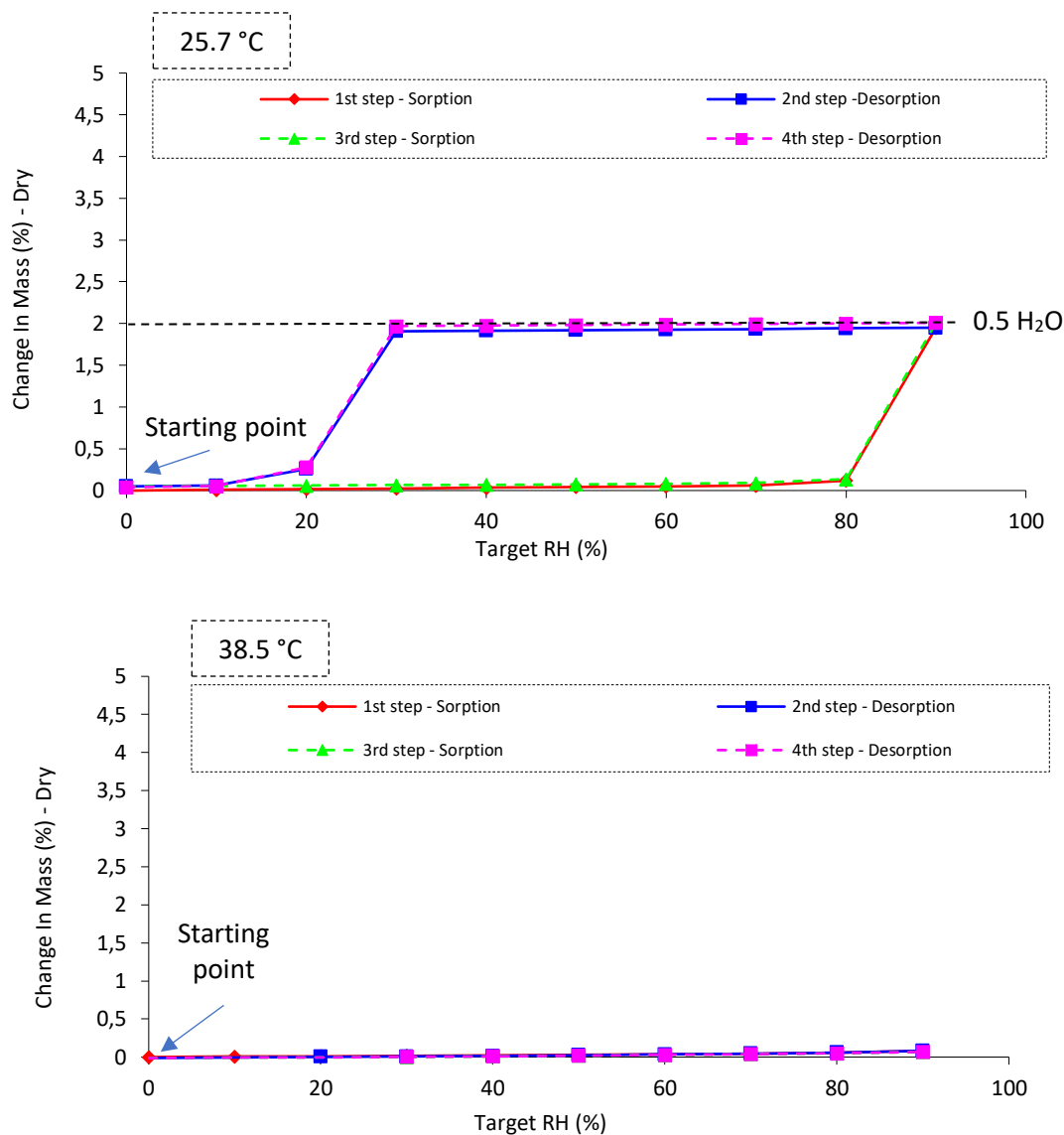


Figure 3-25: Sorption/desorption isotherms of SAFIM at: 25.7 °C (top), 38.5 °C (bottom). The horizontal dashed line corresponds to the maximum mass uptake

At 25 °C, the hydration of **A1** occurred between 80 %RH and 90 %RH with a maximum mass uptake of 2.2% as expected for a hemihydrate stoichiometry. At 38.5 °C, no hydrate was observed from 0 %RH to 90 %RH, which means that above this temperature the formation of the hydrated form via solid-vapor equilibria is inhibited.

A comparable behavior was obtained when starting the DVS analyses from the hemi-hydrate (Figure 3-26).

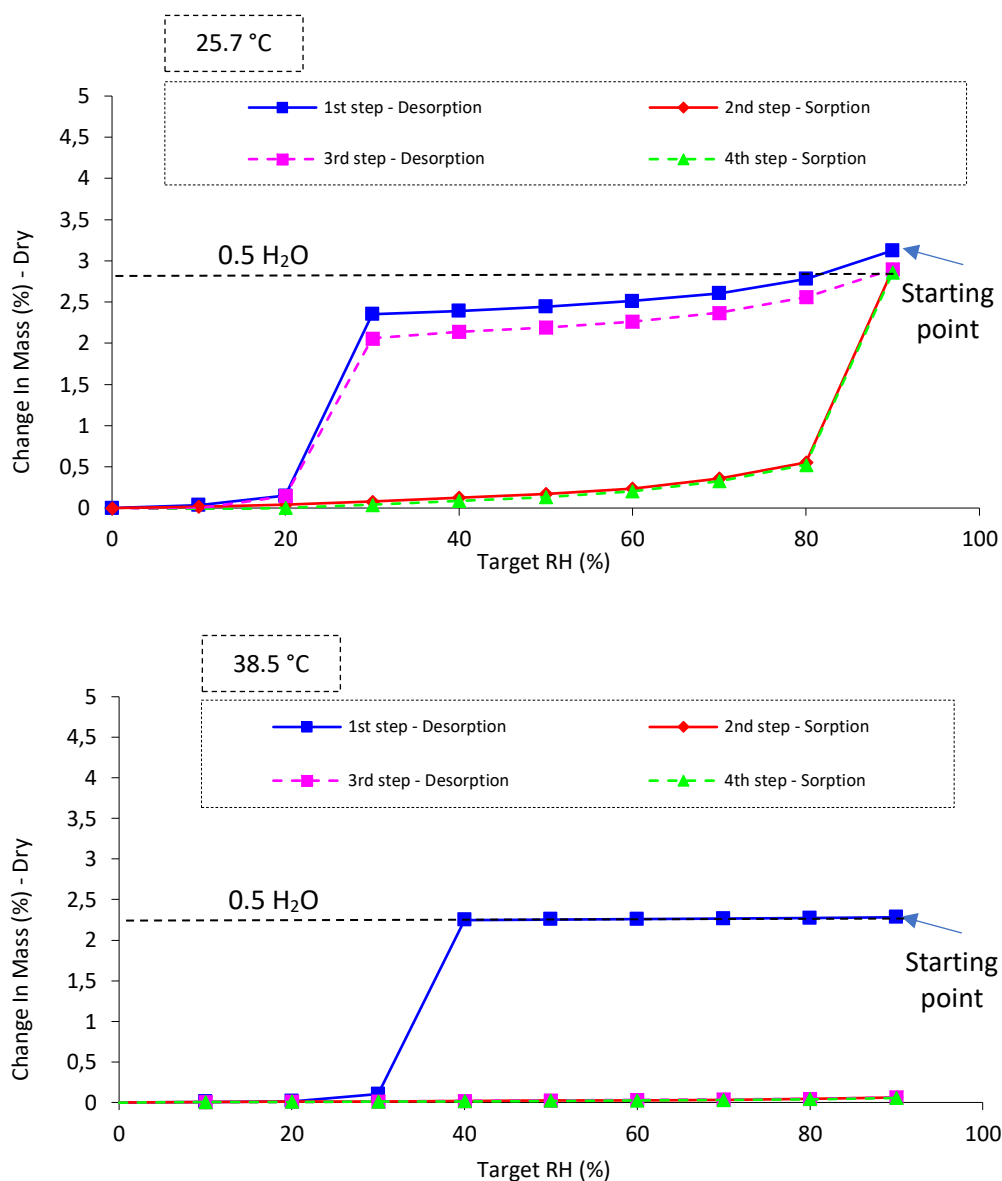


Figure 3-26: Sorption/desorption isotherms of SAFIM at: 25.7 °C (top), 38.5 °C (bottom). The horizontal dashed line corresponds to the maximum mass uptake

The dehydration studies (starting from **H1**) showed that at 25.5 °C, dehydration occurred between 30 %RH and 20 %RH, while at 38.5 °C, it occurred between 40 %RH and 30 %RH. Both desorption curves exhibit a mass loss of 2.2 %_{wt}, consistently with a hemihydrate stoichiometry. At 38.7 °C, the dehydration of **H1** under dry atmosphere is irreversible. The large hysteresis between adsorption and desorption recorded at 25.5 °C is consistent with reversible destructive-reconstructive (de)hydration mechanisms:⁸⁹ $\mathbf{H1} \leftrightarrow \mathbf{A1} + (\mathbf{H_2O})_v$.

The $\mathbf{A2} + (\mathbf{H_2O})_v \leftrightarrow \mathbf{H1}$ transition was investigated with an In-situX monitoring at different temperature and relative humidity, XRPD patterns are presented in Figure 3-27.

Starting from pure **A1** (Figure 3-27, grey XRPD pattern), **A2** is obtained by cooling down the powder from 25 °C to -5 °C at 0 %RH (Figure 3-27, yellow XRPD pattern). Then, the powder is heated

up to 5 °C for a better control of relative humidity (no transition from **A2** to **A1** observed) and the RH set at 90 %RH. A rapid transition is observed from **A2** to **H1**, until complete hydration of the anhydrous phase (Figure 3-27, light blue XRPD pattern). After the hydration, the powder is heated to 10 °C and RH set at 5 %RH, after the equilibration of RH in the crystallizer, the dehydration of **H1** to **A2** is observed (Figure 3-27, green XRPD pattern). Last, the powder is heated up to 25 °C at 2 %RH, **A2** converts to **A1** (Figure 3-27, indigo XRPD pattern).

At low temperature the hydration/dehydration from **A2** to **H1** is possible by varying RH. This information is consistent with a destructive/reconstructive mechanism of (de)hydration: at low temperature, once the hydrated structure is destroyed, the nucleation and growth of the most stable anhydrous form could appear.

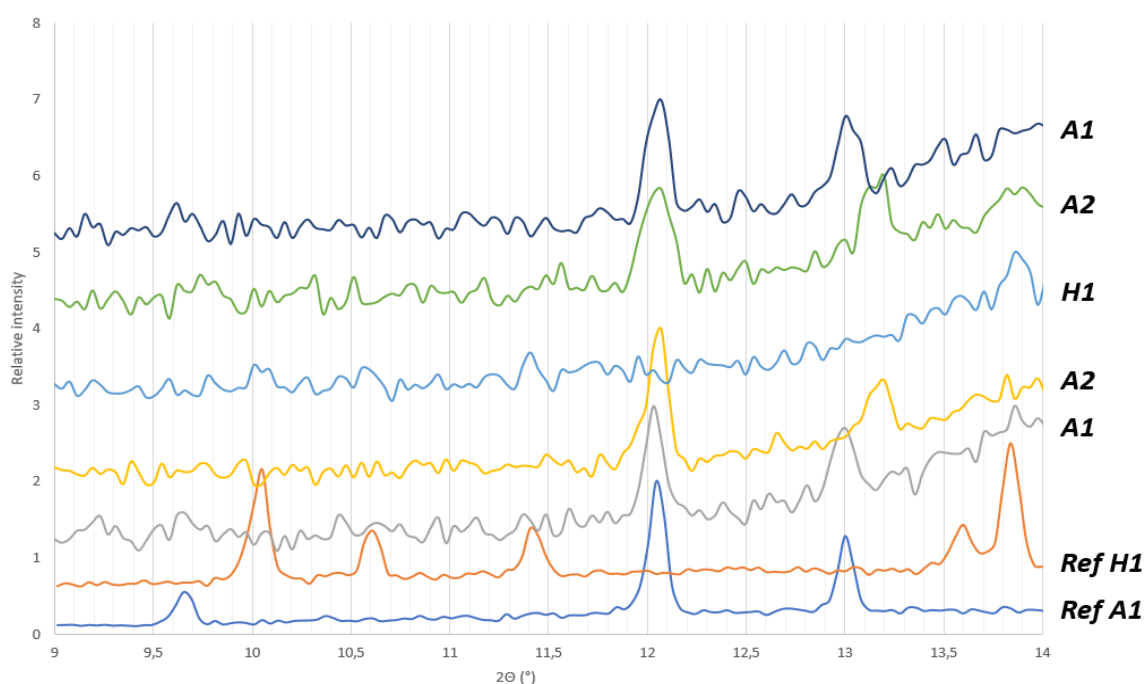


Figure 3-27: Monitoring of SAFIM crystalline form for different temperature and relative humidity by using In-situX diffractometer. From bottom to top Reference **A1** (dark blue); reference **H1**(orange); At 25 °C and 5 %RH (grey), At -5 °C and 5 %RH (yellow); At 5 °C and 25 %RH (light blue); At 5 °C and 5 %RH (green); and at 25 °C and 5 %RH (indigo)

3.4.2.3 Effect of storage conditions

The effect of the storage conditions was studied with an industrial batch of SAFIM **A1** at 21 °C and under different RH (regulated by solid P₂O₅ (for 0 %RH) or by saturated salt solutions, 11.3 %RH (LiCl), 32.8 %RH (MgCl₂), 43.2 %RH (K₂CO₃), 75.3 %RH (NaCl), 84.2 %RH (KCl), and 97.3 %RH (K₂SO₄)) during few weeks. The hydration behavior of the batch is monitored by gravimetric measurements (Figure 3-28).

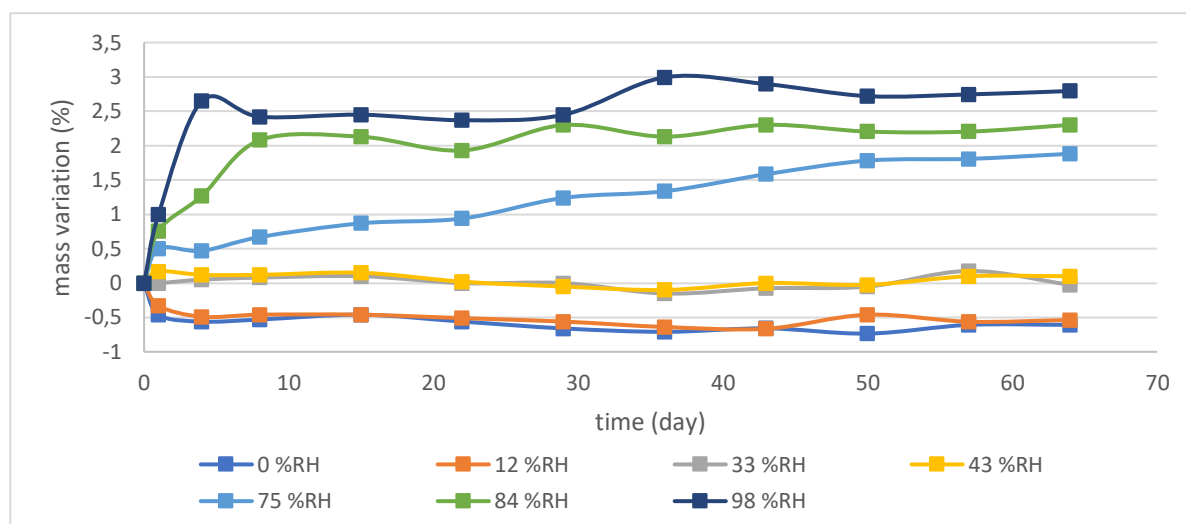


Figure 3-28: variation of the **A1** mass vs time for different RH AT 21 °C

For all batches, when RH > 75%, the solid transforms into **H1** form. One can see that with at 98 %RH, the mass variation exceeds the theoretical value of 2.2 %_{wt}, up to 3 %_{wt}. This excessive mass uptake (above hemihydrate stoichiometry) can be attributed to surface adsorption of water on the crystal surface or on the vessel.

The crystalline phase was analyzed with XRPD after 64 days. Sample over 98 and 84 %RH are pure **H1**. Sample at 75 %RH exhibits a mix of two crystalline phase **A1** and **H1**. Below 75 %RH, all the samples remain in **A1** phase. These results obtained in static conditions are in accordance with dynamic measurements (DVS) and show that without control of the atmosphere conditions, conversion from **A1** into **H1** can occur upon storage.

In order to estimate an autocatalytic process of hydration governed by the presence of **H1** in **A1** batches, several batches of SAFIM **A1**, with a varying percentage of **H1** (0.5%, 1%, 2%, 5%, and 10%), were prepared and stored at different RH in between 20 %RH and 70 %RH (32.8 %RH, 43.2 %RH, and 57.6 %RH, Appendix II). No significant evolution of the masses was observed indicating that seeding with **H1** has no impact on the hydration of **A1**.

3.5 CONCLUSIONS ON THE SAFINAMIDE CRYSTALLINE LANDSCAPE

The different crystalline phases and their stability domains (vs Temperature or RH variations) of SAFIM were described in this chapter by using a combination of XRPD, DVS, TGA-DSC, and microscopy:

- The enantiotropic transition **A1** ↔ **A2** is a first order transition according to Ehrenfest's classification¹⁰³. The disorder/order transition might involve the blockage of a safinamide conformation with an activation energy that is calculated around 203 kJ/mol.

- Concerning the hemi-hydrate, the studies conducted on its stability upon different RH conditions and temperature, have highlighted the importance of controlling the storage parameters. The anhydrous phase converts into the hemi-hydrate if RH is superior to 80 %RH at 25 °C. Once it is formed the hemi-hydrate exhibits a high stability (dehydration if RH < 20%). The hemihydrate does not form at 38 °C and above.

Figure 3-29 gathered the information obtained in this chapter into a stability chart.

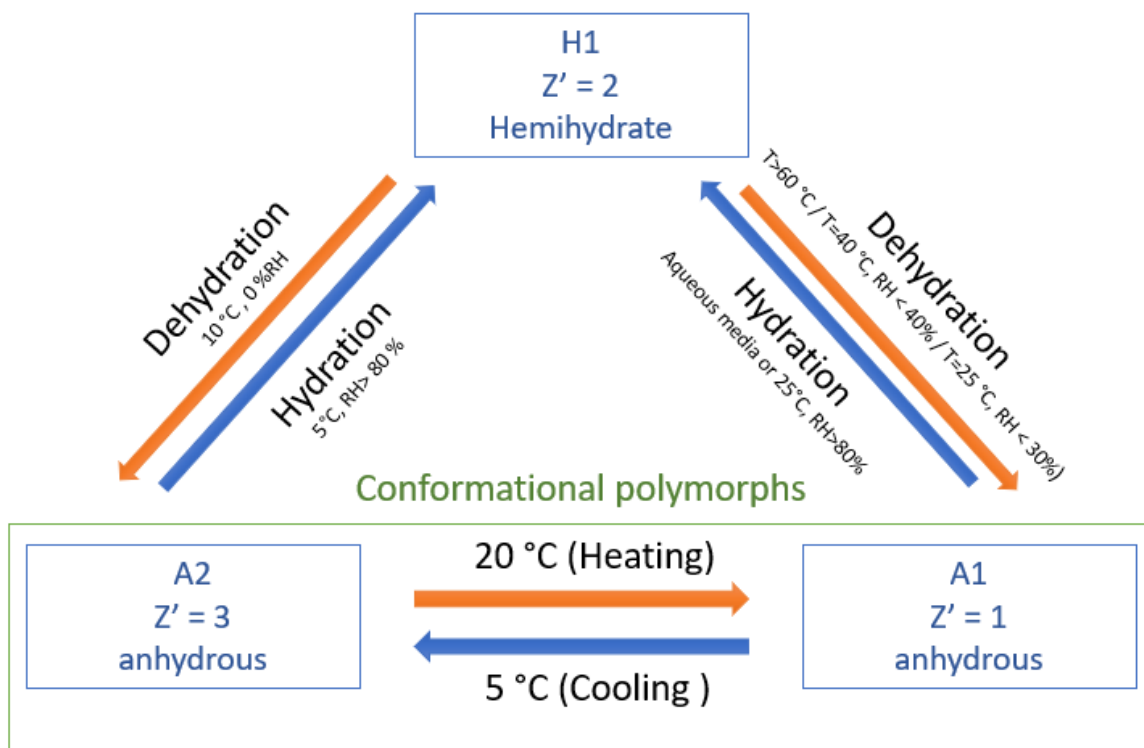


Figure 3-29. Stability diagram of SAFIM crystalline phases

Chapter IV

Development of the Spherical Agglomeration Process of Safinamide Mesylate

4 DEVELOPMENT OF THE SPHERICAL AGGLOMERATION PROCESS OF SAFINAMIDE MESYLATE

In the previous chapter, the different crystalline forms of SAFIM were identified and their stability discussed. This chapter is focused on the development of the spherical agglomeration process of SAFIM.

4.1 CRYSTALLIZATION OF SAFINAMIDE MESYLATE

4.1.1 Industrial crystallization procedure

Safinamide mesylate (SAFIM) is an API produced industrially. Its crystallization process, already used by the manufacturer, is detailed hereafter and summarized in Figure 4-1.

A solution of 1.00 kg of Safinamide in 8.2 L of acetone and 0.6 L of demineralised water is heated to 45 °C. The solution is clarified and rinsed with 0.4 L of acetone. The solution is heated to reflux for 30 minutes, then 0.32 kg of methane sulfonic acid (0.99 equiv.) is added over 20 minutes. The temperature is maintained at 50 °C. 0.12 L of demineralised water is added. The temperature is adjusted to 20 °C and maintained for 45 minutes or until the fluidization of the suspension. The suspension is cooled to -7 °C and maintained for 2 hours under stirring filtered and washed with 2.0 L of acetone at 5 °C. The resulting solid is dried under reduced pressure at 40 °C.

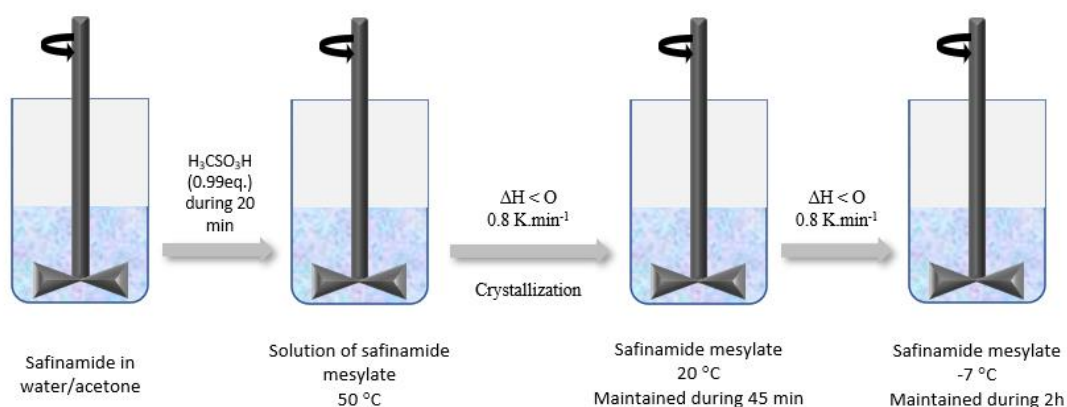


Figure 4-1: Schematic representation of safinamide mesylate crystallization process

As mentioned in the previous chapter, safinamide mesylate exhibits different crystalline form as a function of the temperature and of the presence of water. The evolution of safinamide mesylate during the crystallization process was monitored thanks to In-situX® measurements.

4.1.2 Monitoring of the crystalline phase during crystallization

The crystallization process was monitored with In-situX® starting from 45 °C (starting point of the crystallization) until the filtration of the obtained powder. Results are presented in Figure 4-2.

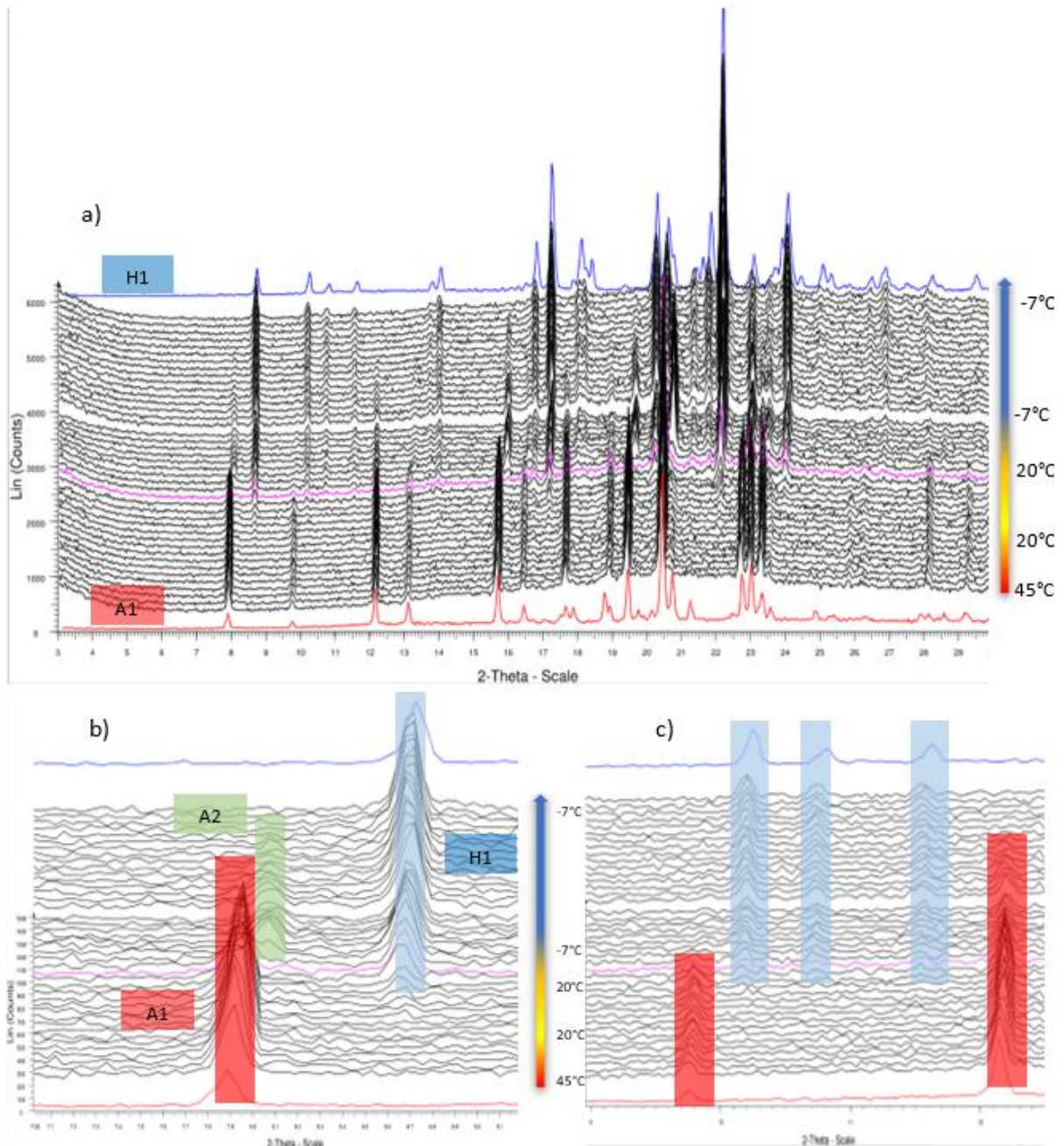


Figure 4-2. (a) X-ray diffraction patterns of SAFIM during the monitoring of the crystallization process (b) zoom between 7° and 9° (2θ), (c) zoom between 9° and 12.5° (2θ) (in blue, H1 reference and in red, A1 form)

The crystallization of SAFIM starts at 45 °C with the crystallization of **A1** (characteristic peaks at 7.9°, 9.8° and 12.2° (red frames, Figure 4-2)). Then, the suspension is cooled from 45 °C to 20 °C with a cooling rate of 1 K/min. During the isotherm at 20 °C, the partial transition from **A1** into **H1** begins (appearance of peaks at 8.7°, 10.3° and 10.7°, blue frames). At circa 5 °C, the remaining **A1** converts into **A2** (shift of the peak at 7.9° to 8.1°, green frames, characteristics of the polymorphic transition).

During the isotherm at $-7\text{ }^{\circ}\text{C}$, SAFIM fully converts into **H1** and remains the stable form until the end of the process.

Regarding the X-ray monitoring, only **H1** can be obtained at the end of the crystallization process in this solvent system (acetone/water). Thus, the industrial drying conditions of SAFIM lead to the conversion of **H1** into **A1**.

In order to understand the crystallization pathway of SAFIM, two isothermal sections of the ternary system SAFIM/water/acetone were studied at $20\text{ }^{\circ}\text{C}$ and $40\text{ }^{\circ}\text{C}$.

For these temperatures, several mixtures of **A1** with acetone (80/20 acetone_(wt)/SAFIM_(wt), 50/50 SAFIM_(wt)/acetone_(wt), 90/10 SAFIM_(wt)/acetone_(wt)) were prepared and water was added in order to describe the isoplethal section represented in Figure 4-3. Each composition was repeated three times for reproducibility.

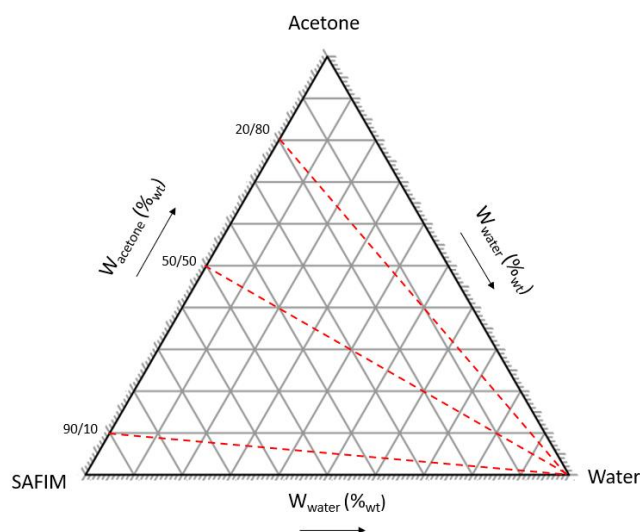


Figure 4-3: Isothermal section of the ternary phase diagram SAFIM/water/acetone where isoplethal sections used are depicted with dashed red lines

The temperature of the mixtures was adjusted to $20\text{ }^{\circ}\text{C}$ or $40\text{ }^{\circ}\text{C}$ and stirred for 24 hours. Phase equilibria domains could be proposed thanks to direct visual observations in case of total solubilization or by checking the solid phase in the suspension by XRPD. Two isothermal sections at $40\text{ }^{\circ}\text{C}$ and $20\text{ }^{\circ}\text{C}$ could be proposed (Figure 4-4).

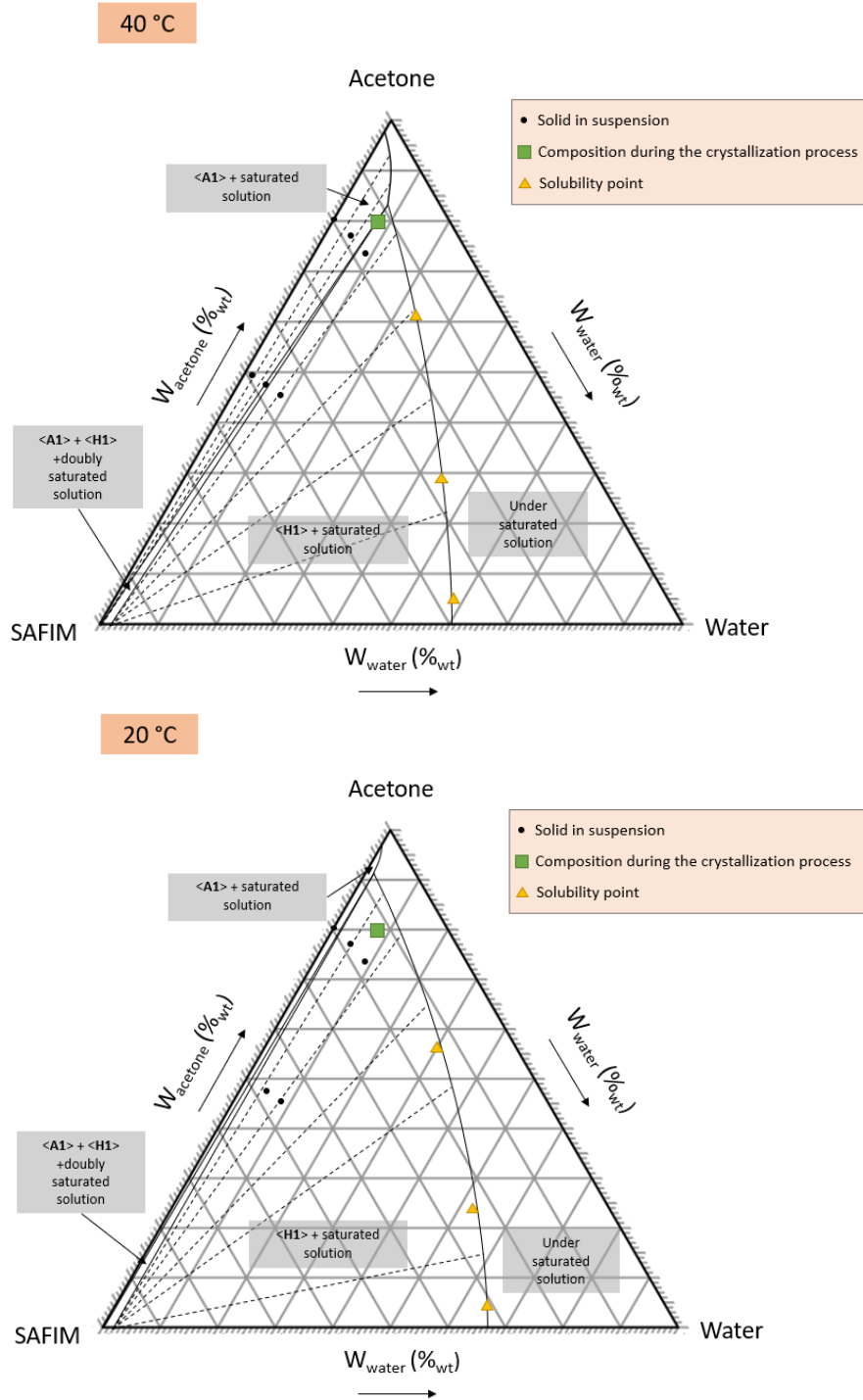


Figure 4-4: Isothermal sections at 40 °C (top) and 20 °C (bottom) of the ternary phase diagram SAFIM/acetone/water. Green dot depicts the composition of the system during the industrial crystallization process. Solubility curves and boundaries are drawn to be consistent with experimental observation

The isothermal section at 20 °C depicts the high stability of the hemi-hydrate form H1. Indeed, the crystallization zone of **A1** (biphasic domain $\langle \mathbf{A1} \rangle + liq$) is close to the SAFIM/acetone side of the ternary phase diagram. The isothermal section at 40 °C shows that the crystallization domain of **A1** is enlarged compared to that at 20 °C. It is extended up to an acetone/water ratio close to 90/10 vol/vol.

These two isothermal sections are in accordance with the crystallization behavior observed during In-situX experiments. At 40 °C and at the industrial composition, the system crystallizes in the triphasic domain: **A1** and **H1** should crystallize at the same time. However, the crystallization of **A1** seems kinetically favored and occurs first. When the reaction medium is cooled down, **H1** become the stable form and **A1** converts progressively into **H1**. One can note that due to the slow kinetic of transition **A1** → **H1** during cooling, the remaining **A1** could transform into **A2** before its irreversible transformation towards **H1**. Regarding thermodynamic data and monitoring of the crystalline phase during crystallization process, it clearly appears that **H1** is the most stable phase in presence of water in the system and the drying step seems to be solely responsible for the dehydration of **H1** into **A1** at the end of the process.

Under the conditions of the crystallization process SAFIM is isolated as needle-like shape crystals (average length of 200 µm and fragments of needles) and exhibits poor flowability properties. Therefore, an agglomeration process was developed in order to have access to powder material exhibiting enhanced flowing behavior.

Conventionally, the spherical agglomeration process involves two steps: crystallization and agglomeration. These two steps can occur simultaneously by adding the Bridging Liquid (BL) to the solution prior to the crystallization, or deferred by first crystallizing the material and subsequently agglomerating upon addition of the bridging liquid to the suspension. In the case of SAFIM there are two major issues to apply the conventional method:

- (i) The actual crystallization system of SAFIM consists of acetone and water. To perform the spherical agglomeration, the BL must exhibit an oiling out with the crystallization solvents. However, almost all solvents are miscible with acetone.¹⁰⁶ Even with 20% of water, only few solvents are able to form an oiling out with this mixture of solvents. Therefore, a special study must be carried out aimed to find out a suitable solvent system.
- (ii) A recent study has shown that the dehydration of agglomerated crystals leads to the modification of the agglomerate physical properties (e.g., compressive strength, plasticity).¹⁰⁷ As previously discussed, SAFIM is isolated as **H1** under the conditions of the current crystallization process. Therefore, if the agglomeration is performed under the same conditions, agglomerates of **H1** will be obtained. SAFIM being commercialized as **A1**, dehydration of **H1** to **A1** will be achieved upon drying, which will likely induce the modification of the agglomerate physical properties.

Thus, it has been decided to focus the study only on the agglomeration step of SAFIM using the commercial material (*i.e.*, **A1** crystalline form), agglomeration hence being an additional process step to be carried out on the crystallized material. The next part of the chapter is then dedicated to the development of an agglomeration process with the following objectives:

- (i) Find a suitable solvent system to induce spherical agglomeration
- (ii) Obtain agglomerates with an acceptable average diameter (close to 500 μm) and with a good flowability of the final powder
- (iii) Obtain agglomerates directly under the **A1** form (commercialized solid form)

4.2 SPHERICAL AGGLOMERATION OF SAFINAMIDE MESYLATE

4.2.1 Selection of the agglomeration solvents

4.2.1.1 Determination of the solvent system from the literature

The very first step in the development of a spherical agglomeration process is the selection of the agglomeration solvents. Two conditions are commonly mentioned in the literature:

- (i) The dispersion solvent and the bridging liquid must exhibit an oiling out.
- (ii) The solid must have a better affinity with the BL than with the dispersion solvent.

In the case of SAFIM, one condition can be added: the solvents must not change the crystalline form of SAFIM during the agglomeration process, meaning that water cannot be used as a solvent for the agglomeration of SAFIM and the presence of residual water in solvents will be discussed latter.

There are numerous examples of solvent systems fulfilling these two first conditions. Hereafter is a non-exhaustive list of such systems with the material involved on the agglomeration process (Table 4-1).

Table 4-1: non-exhaustive list of agglomerated material with spherical crystallization processes and their associated solvent system.

Solid	Solvent	anti-solvent	bridging liquid	Reference
Acebutolol hydrochloride	water	-	isopropyl acetate	108
Aceclofenac	acetone	water	dichloromethane	109
Acetylsalicylic acid	ethanol	carbon tetrachloride/water	(QESD method)	44
Ascorbic acid	water	-	ethyl acetate	56
Atorvastatin calcium	ethanol	water	dichloromethane	77
Barium sulphate	benzene	-	water	38

Development of the Spherical Agglomeration Process of Safinamide Mesylate

Benzoic acid	ethanol	water	chloroform	76
Benzoic acid	ethanol	water	n-heptane	71
Benzoic acid	ethanol	water	toluene	110
Bucillamine	ethanol/dichloromethane	-	water	69
Calcium carbonate	carbon tetrachloride	-	aqueous calcium chloride	37
Cefatoxime sodium	2-propanol/water	-	chloroform	111
Cefatoxime sodium	methanol-water	-	ethyl acetate	72
Celecoxib	Acetone	Water	dichloromethane	112
Coal	water	-	oil	39
Di-methyl-quinacridone	sulphuric acid	water	di-N-butylamine	65
Etodolac	acetone	aqueous solution of polymer	dichloromethane	113
Fenbufen	THF	water	isopropyl acetate	114
Glass	carbon tetrachloride	-	aqueous calcium chloride	37
Graphite	water	-	kerosene/lubricating oil	40
Griseofulvib	DMF	water	dichloromethane	107
Ibuprofen	aqueous sodium hydroxide	aqueous chlorohydric acid	isopropyl acetate	115
Lactose	chloroform	-	saturated aqueous lactose solution	46
Limestone	water	-	kerosene/lubricating oil	43
Lobenzarit disodium	water	-	n-hexane	63
Norflaxacin	acetone/dichloromethane	-	ammonia-water	52
Salbutamol sulfate	water	ethyl acetate	(QESD method)	57
Salicylic acid	ethanol	water	chloroform	42
Salicylic acid	water	sulfuric acid	chloroform	70
Silica sand	carbon tetrachloride	-	aqueous calcium chloride	37
Steroid KSR-592	acetone	water	ethyl acetate	116
Theophylline	Ethylene diamine	aqueous sodium chloride	water	60
Tranilast	ethanol/ acetone	water	chloroform	41

Among these different systems, 100% of the agglomeration processes involve the use of water either as solvent or anti-solvent or as bridging liquid, none of these systems can be used to perform the spherical agglomeration of SAFIM.

Moreover, if we look at the guidelines on the selection of the agglomeration solvents proposed by Chow et al.⁶¹ (Table 4-2), an aqueous solvent is involved for each of the four groups.

Table 4-2: Chow's classification for the choice of the bridging liquid.

	Solubilization solvent of the compound	Anti-solvent	Bridging liquid
Group 1	Water soluble	Water-miscible organic solvent	Salt solution of high concentration
Group 2	Organic solvent	water	Organic solvent
Group 3	Water-miscible organic solvent	Saturated aqueous solution	Organic solvent mixture
Group 4	Insoluble in water and organic solvent	Water-immiscible organic solvent	Salt solution of high concentration + binding agent

After an intensive review of the literature on spherical agglomeration, no suitable solvent systems where an aqueous solution is not involved were identified. Therefore, another approach was used to find an agglomeration system.

4.2.1.2 Determination of the solvent system based on phase equilibria and European pharmacopoeia

The approach used to determine the agglomeration solvent system of SAFIM is based on the polarity of the mesylate salt. Such salts exhibit high solubility in water due to the hydrophilic interactions.^{117,118} Therefore, an aprotic polar solvent will be used as BL and a non-polar solvent as the dispersion phase. Moreover, these solvents must fulfill the previously mentioned conditions. According to the miscibility database,¹⁰⁶ different solvents can be suitable for the agglomeration (Table 4-3):

Table 4-3: Various polar and non-polar solvent exhibiting an oiling out for the spherical agglomeration of SAFIM.

Polar solvent	Non-polar solvent
Acetonitrile	n-Hexane
Propionitrile	Cyclohexane
	n-Heptane
	Heptane mix isomers

SAFIM, like all APIs, due to the toxicity of organic solvents, is subjected to strict regulatory constraints of residual solvent content in the material entering the final drug intended to be taken by

patients. The European Medicines Agency ICH Q3C guidelines deal with solvents classification and their recommended maximum residual content in pharmaceutical ingredients and drugs. Solvents are classified into 3 classes: solvents to be avoided (class 1), solvents to be limited (class 2) and solvents with low toxic potential (class 3).

According to this classification n-hexane and cyclo-hexane fall in class 2, whereas n-heptane is a class 3 solvent. Acetonitrile is a class 2 solvent, while propionitrile does not appear in the ICH classification, though having a lower median lethal dose than acetonitrile (39 mg/kg vs 500 mg/kg orally tested on mice). Bearing in mind these regulatory aspects, it has been decided to use n-heptane as the dispersion solvent and acetonitrile as bridging liquid for the development of the spherical agglomeration process of SAFIM.

The solubility of SAFIM in both solvents was measured at 10 °C, 20 °C, and 30 °C thanks to the dry residue method. Table 4-4 shows the evolution of the solubility in acetonitrile and n-heptane as a function of the temperature.

Table 4-4: solubilities of SAFIM A1 in acetonitrile and n-heptane at different temperatures

Temperature (°C)	Solubility (%wt) / standard deviation	
	Acetonitrile	n-Heptane
10	0.04 / 0.01	0.01 / 0.01
20	0.07 / 0.01	0.03 / 0.01
30	0.10 / 0.01	0.05 / 0.01

SAFIM A1 exhibits a very low solubility in both acetonitrile and n-heptane (< 0.1%_{wt}) which limits the solubilization of SAFIM during the agglomeration process and thus, enhances the agglomeration yield.

A preliminary agglomeration test was performed in a beaker without any control of the different agglomeration parameters (e.g., temperature, stirring rate, amount of BL, suspension concentration). A stirred suspension of SAFIM in n-heptane was prepared and acetonitrile subsequently added to the suspension. Due to preferential interactions between SAFIM and acetonitrile, SAFIM particles were only observed in acetonitrile after few seconds of stirring (Figure 4-5).



Figure 4-5: Suspension of SAFIM in n-heptane (left) and suspension of SAFIM in n-heptane after the addition of acetonitrile (BL) (right)

The solvent system being identified for the spherical agglomeration of SAFIM, the next step was the determination of the agglomeration setup (*i.e.*, the geometry of the reactor and of the stirrer).

4.2.2 Presentation of the agglomeration setup

4.2.2.1 Geometry of the crystallizer

When developing a new crystallization or agglomeration process, the geometry of the reactor is an important parameter. The hydrodynamics of the fluid phase in a vessel depend on the geometry of the vessel itself (e.g., cylindrical, conical, flat bottom or rounded bottom).

In the case of SAFIM, the choice of the reactor geometry was made in the perspective of scaling up the process at industrial scale. Indeed, at the lab scale, the geometry can be easily modified by changing the vessel or the stirring elements (shaft, blades, baffles), whereas it is much more complicated to change the geometry of industrial vessels. Therefore, for the experimental activity it has been chosen to use a laboratory glass vessel which is a scale down replication of an industrial crystallizer available in Zach System facilities.

The agglomeration process of SAFIM was then developed in a flat bottom HWS 0.5 L crystallizer (Figure 4-6) equipped with mechanical stirrer and temperature regulation (Lauda ECO RE 415 S).



Figure 4-6: Picture of the HWS flat flange crystallizer use to perform spherical agglomeration of SAFIM

Another critical aspect of hydrodynamics is the stirring geometry, including stirrer shape and size, as well as baffles.

4.2.2.2 Determination of the stirring setup

There is a wide panel of stirrer available for different applications (e.g., dispersion of a gas in a liquid, stirring of suspension, mixing of two liquid)¹¹⁹. To perform a spherical agglomeration, the stirrer must ensure the dispersion of two immiscible solvents (the dispersion solvent and the BL) and the suspension of SAFIM in these two solvents. Moreover, the flow in the crystallizer is impacted by the presence of baffles¹²⁰.

In order to choose the most suitable stirring setup, a reaction medium which consists of 300 mL of n-heptane and 20 mL of acetonitrile colored with phenolphthalein was stirred in the HWS crystallizer with different stirring setup (Figure 4-7):

- 3 blades TTP propeller (based on a design from Mixel™ and 3D printed, diameter = 6 cm) + disk turbine with vertical 4 blades (Rushton turbine, diameter = 4 cm).
- 3 blades glass propeller (diameter = 6 cm)
- Dispersion turbine (diameter = 5 cm)
- 3 blades TTP propeller (based on a design from Mixel™ and 3D printed, diameter = 6 cm) + dispersion turbine (diameter = 5 cm) (not shown in Fig. 4-7)

Moreover, experiments were carried out with and without a 3D-printed 3 blades baffle (blades width = 1 cm) at different stirring rates. The stirrers were placed at 2 cm of the reactor bottom.

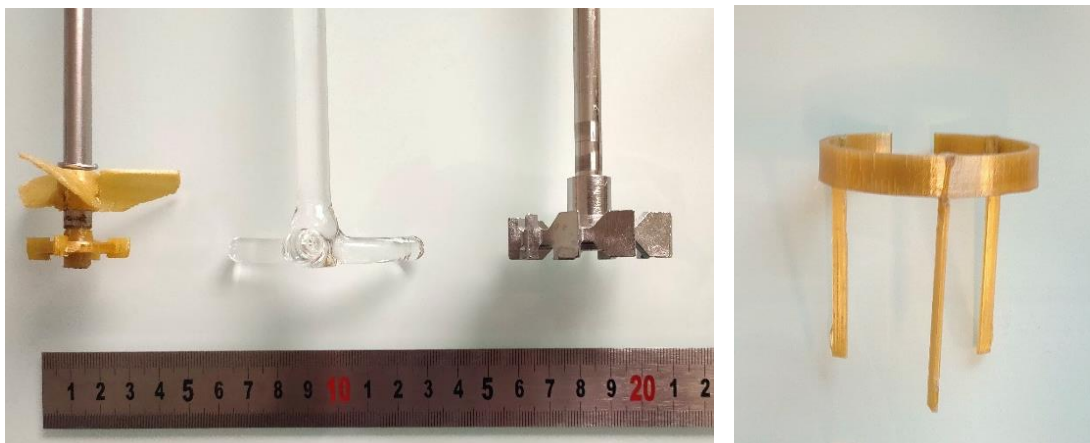


Figure 4-7: Pictures of the different stirrers (from left to right: 3 blades TTP propeller+ Rushton turbine; glass propeller, dispersion turbine) and the three blades baffle

The quality of the emulsions was visually assessed, and videos are available by scanning the following QR-code:



Figure 4-8: QR-code to flash to visualize the comparison between the different stirrers

According to Roustan,¹¹⁹ the two propellers exhibit an axial flow whereas the two turbines exhibit a radial flow (Figure 4-9).

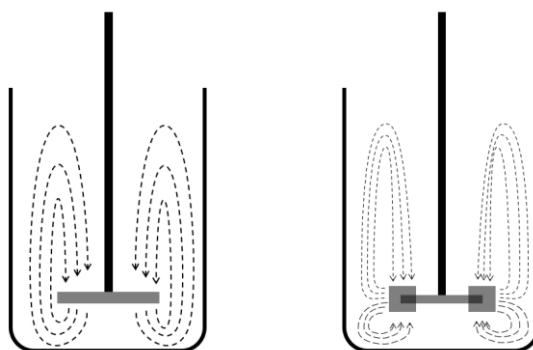


Figure 4-9: Schematic representation of an axial flow (left) and a radial flow (right)

Regarding the different experiments, the use of baffles is required to ensure the formation of the emulsion between the two solvents. Moreover, the baffles prevent the formation of vortices at high stirring rates (Figure 4-10) which limit the dispersion of the biphasic liquid.

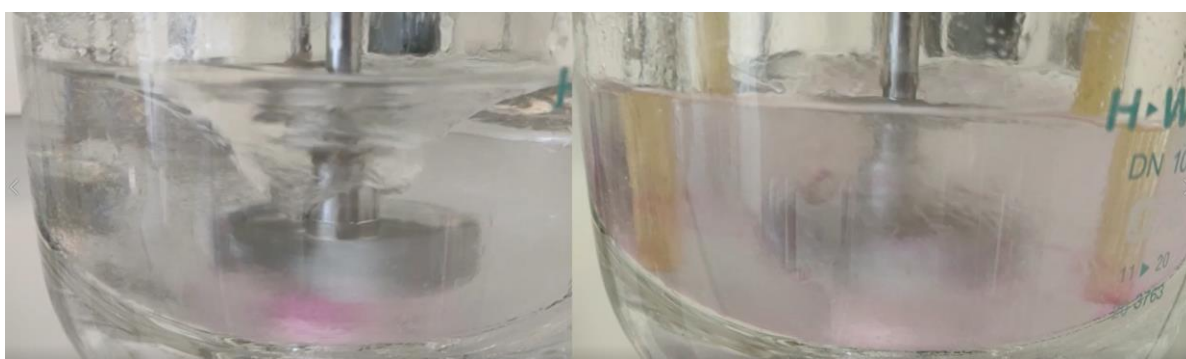


Figure 4-10: Formation of a vortex at 300 rpm with the dispersion turbine (left) and the same reaction medium at 300 rpm with baffle (right) where the vortex is not formed

As shown on Figure 4-11, even in the presence of baffles, the flow generated by the glass propeller with an axial flow was not sufficient to disperse the two immiscible liquids and generate the emulsion. Without the baffles acetonitrile remains at the bottom of the crystallizer, creating a high concentration zone. In this zone the ratio *dispersion solvent/BL* will cause the formation of a pasty zone during agglomeration. The presence of baffles helps generating the emulsion. However, one can note the presence of non-agitated acetonitrile at the bottom of the crystallizer.



Figure 4-11: snapshots of the two immiscible solvents being stirred at 400 rpm with a glass propeller without baffles (left) and with baffles (right)

Then, the attention was focused on the stirrers exhibiting a radial flow and with baffles. Usually, stirrers with a radial flow generate a more turbulent flow than axial flow stirrers and favor the dispersion of the two immiscible liquids.¹²⁰ Table 4-5 compares the three stirrers with a radial flow as a function of the stirring rate.

Table 4-5: Comparison of the dispersion states for different stirrers as a function of the stirring rate.

RPM	TTP propeller + Rushton turbine	Dispersion turbine	Dispersion turbine + TTP propeller
200			
300			
400			
500			

In all cases, a suitable emulsion was obtained at high stirring rates (500 rpm), there was no colored acetonitrile which remained at the bottom of the reactor. When looking at lower stirring rates, the quality of the emulsion rapidly decreased for the TTP propeller equipped with the Rushton turbine. The latter was not retained to develop the agglomeration process.

There were no significant differences between the dispersion turbine alone and the dispersion turbine topped with the TTP propeller, also because the TTP propeller was only partially immersed in the reaction medium, due to the vessel filling level: the two solvents were homogeneously dispersed even at 300 rpm. Therefore, in order to simplify the crystallizer setup, the dispersion turbine will be used alone.

Table 4-6 shows the quality of the emulsion as a function of the stirrer geometry, stirring rate and the presence of baffles.

Table 4-6: Evolution of the emulsion of acetonitrile in n-heptane as a function of the stirring setup and stirring rate.

rpm	No baffles				baffles			
	Glass propeller	TTP propeller + Rushton turbine	Dispersion turbine	TTP propeller + Dispersion turbine	Glass propeller	TTP propeller + Rushton turbine	Dispersion turbine	TTP propeller + Dispersion turbine
0	No emulsion	No emulsion	No emulsion	No emulsion	No emulsion	No emulsion	No emulsion	No emulsion
100	No emulsion	No emulsion	No emulsion	No emulsion	No emulsion	No emulsion	No emulsion	No emulsion
200	No emulsion	No emulsion	No emulsion	No emulsion	poor emulsion	poor emulsion	poor emulsion	poor emulsion
300	No emulsion	No emulsion	Poor emulsion	Poor emulsion	poor emulsion	poor emulsion	Good emulsion	Good emulsion
400	No emulsion	No emulsion	Poor emulsion	Poor emulsion	poor emulsion	poor emulsion	Good emulsion	Good emulsion
500	No emulsion	No emulsion	Poor emulsion	Poor emulsion	poor emulsion	Poor emulsion	Good emulsion	Good emulsion

The final spherical agglomeration setup consists of a jacketed HWS flat bottom crystallizer equipped with a dispersion turbine and 3 baffles. The BL will be added dropwise thanks to a syringe pump (Figure 4-12). This setup will be used during the whole development of the agglomeration process.

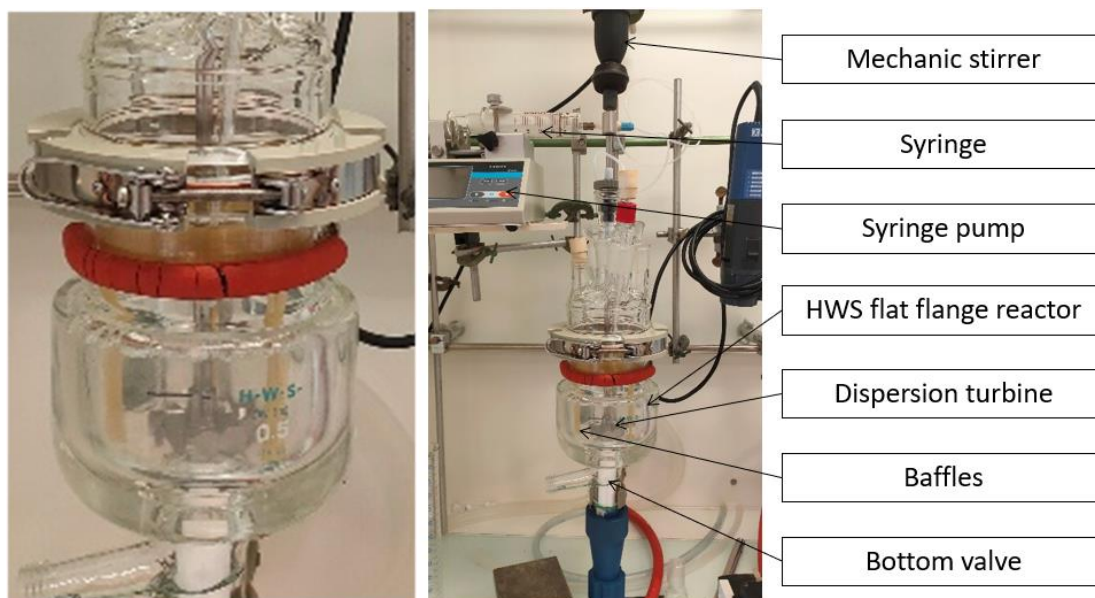


Figure 4-12: Pictures of the crystallizer setup used to perform the spherical agglomeration of SAFIM

4.2.3 Development of the spherical agglomeration process

4.2.3.1 Evaluation of the most influencing parameters

A spherical agglomeration process is impacted by several factors (e.g., crystallizer geometry, stirring rate, temperature, nature of the solvents, amount of BL, addition mode of the BL, ...): given that the crystallizer set up and the solvent system have been defined, the process has been optimized by investigating the remaining parameters to obtain spherical agglomerates with the desired micromeritic properties.

4.2.3.1.1 Effect of the amount of bridging liquid on the agglomeration of SAFIM

First, the concentration of the suspension as well as the amount of bridging liquid need to be determined. Based on a previously developed agglomeration process by Zach System on a different molecule, the following conditions were used as a first approach to perform the spherical agglomeration of SAFIM:

- In the HWS 500 mL crystallizer, 30.30 g of SAFIM were added in 300 mL of *n*-heptane at 3 °C and stirred at 425 rpm with a dispersion turbine.

- After 1 hour of equilibration, 25 mL of acetonitrile were added dropwise for 1 hour (feeding rate = 25 mL/h) through a PTFE tube of 2 mm inner diameter right above the reaction medium.

- The reaction medium was left under stirring for 6 hours after the beginning of the addition of acetonitrile.

The evolution of the system during the 6 hours of stirring is presented in Figure 4-13 (one can note that no baffles were used for this experiment).

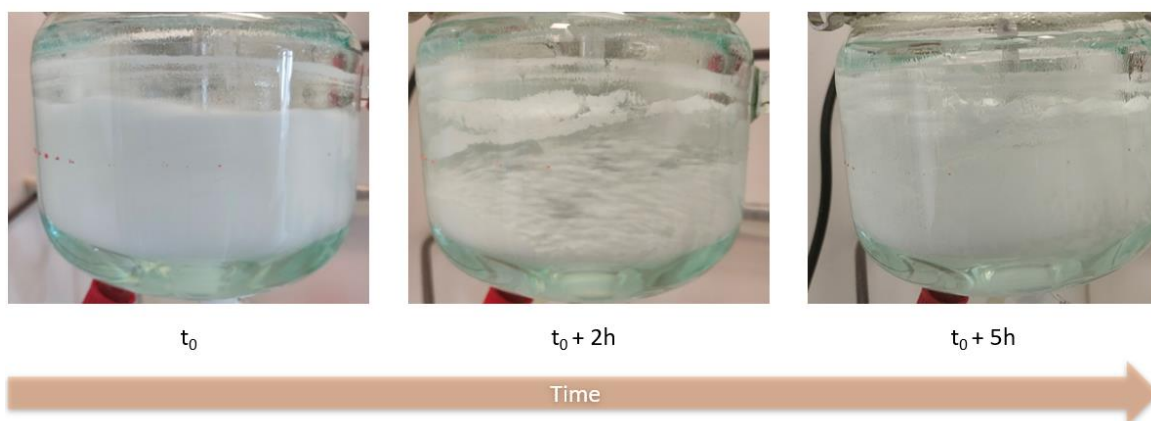


Figure 4-13: Evolution of the reaction medium of SAFIM as a function of time under stirring

Under these conditions, agglomeration of the reaction medium occurred stirring over 2 h. Then, after 5 h, the reaction medium was partially de-agglomerated and the solid adhered to the vessel's wall. At the end of the process, the reaction medium was filtered and the solid (agglomerated and non-agglomerated SAFIM, Figure 4-14) was dried under reduced pressure at 30 °C. After 24 h of drying, the solid was analyzed thanks to XRPD measurement (Figure 4-15) and characterized as **A1** with traces of **H1**.



Figure 4-14: picture of SAFIM after the agglomeration process with the conditions of a previous agglomeration process developed by Zach System for another molecule

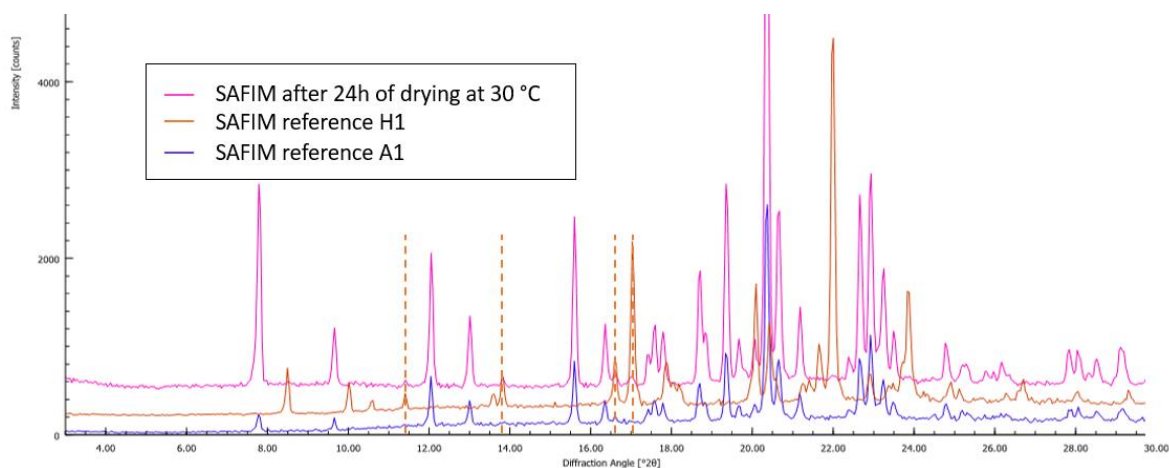


Figure 4-15: XRPD patterns of SAFIM A1 (blue) and H1 (orange) references and SAFIM after the agglomeration process with the conditions of a previous agglomeration process developed by Zach System for another molecule (traces of H1 are spotted with vertical orange dashed lines)

The partial agglomeration of the reaction medium as well as the adhesion of particles on the crystallizer wall can be explained by a too large amount of BL due to the formation of the pasty medium when the ratio $\frac{BL}{solid}$ is too important. Therefore, the amount of bridging liquid was reduced to 20 mL with a feeding rate of 20 mL/min.

By decreasing the amount of BL to 20 mL, smaller agglomerates (average diameter about 2 mm) were obtained after 6 h of stirring, without observing any de-agglomeration (Figure 4-16: dried agglomerates). This observation is in accordance with the literature where it is mentioned that decreasing the bridging liquid amount decreases the probability of cohesion of between particles and therefore reduces the agglomerate size.⁶⁸

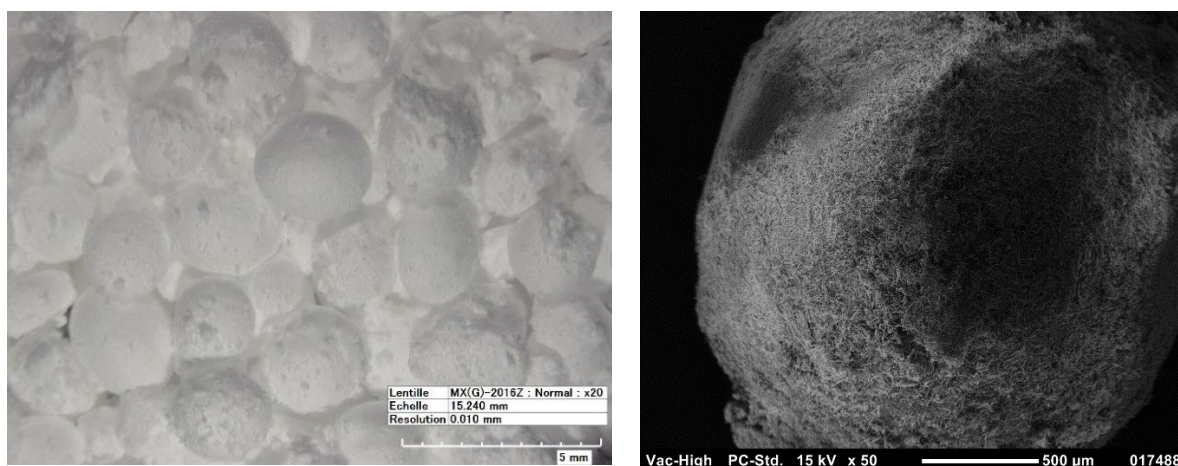


Figure 4-16: Optical microscopy picture (left) and SEM picture (right) of spherical agglomerates of SAFIM obtained after the agglomeration process with 20 mL of BL

This study aimed to produce agglomerates of SAFIM with an average size about 500 μm . In order to further reduce the size of the agglomerate, the BL amount was reduced to 15 mL with the

previous conditions (feeding rate = 15 mL/h). Under these conditions no agglomerates were obtained at the end of the process. The range of BL amount for the agglomeration to occur is located between 15 mL and 25 mL of BL (Figure 4-17).

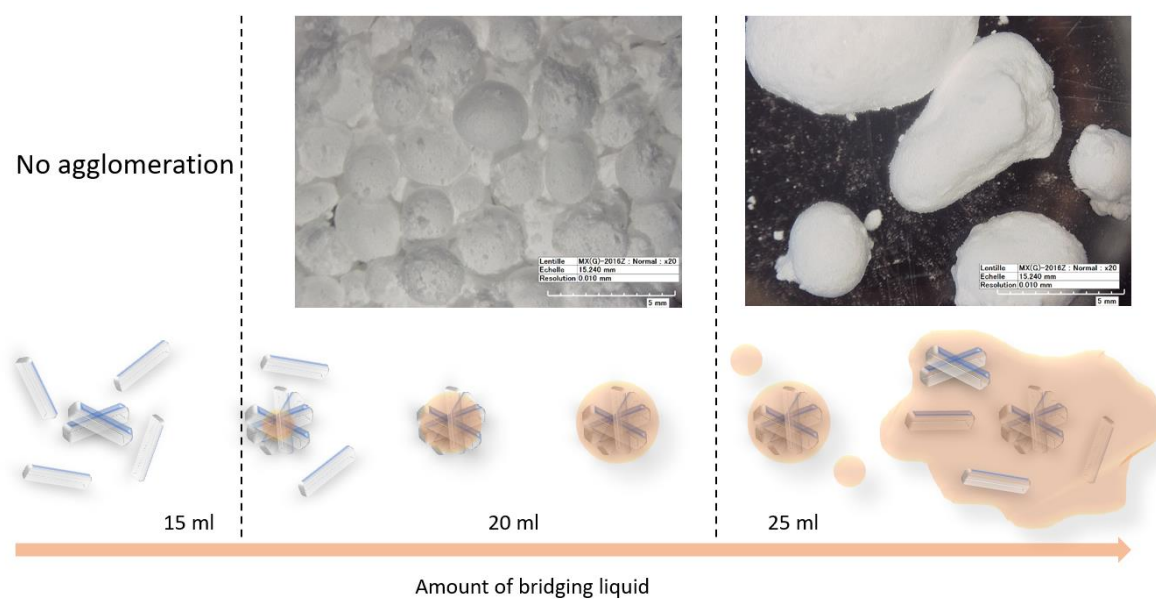


Figure 4-17: Evolution of the agglomeration process of SAFIM as a function of the BL amount

4.2.3.1.2 Effect of the temperature on the agglomeration of SAFIM

Even if the amount of BL is often mentioned as the most influencing parameter of the spherical agglomeration, the temperature can impact not only the process by modifying the solubility of the API both in dispersion solvent and BL but also the miscibility of the BL in the dispersion solvent and thus, reducing the amount of available BL to agglomerate the API.

For SAFIM, it has been shown that reducing the temperature of the crystallization will increase the stability of the hemi-hydrate (classical crystallization way, see section 1.1). Therefore, an agglomeration of SAFIM was performed at higher temperature (*i.e.*, 40 °C) with the previous conditions and 20 mL of bridging liquid. In this case, only partial agglomeration of the reaction medium was observed and that can be attributed to the increasing solubility of acetonitrile in n-heptane.

4.2.3.1.3 Influence of the initial particle size distribution on the agglomeration of SAFIM

Another parameter which could impact the agglomerate size distribution is the initial particle size distribution, *i.e.*, the size of the non-agglomerated particles. This parameter is usually controlled during the crystallization step of the process by modifying, for instance, the supersaturation. However, in the case of SAFIM, the particles are already crystallized before the agglomeration process. A possible way to overcome this issue is to implement a homogenization step of the crystal size. An Ultra Turrax

equipped with a mixing head of 18 mm was used to perform this step. The operation was implemented after the preparation of the suspension of SAFIM in n-heptane.

The experimental process was as follow:

- Suspension of SAFIM in n-heptane (30 g in 300 mL) prepared in a temperature-controlled crystallizer at 30 °C

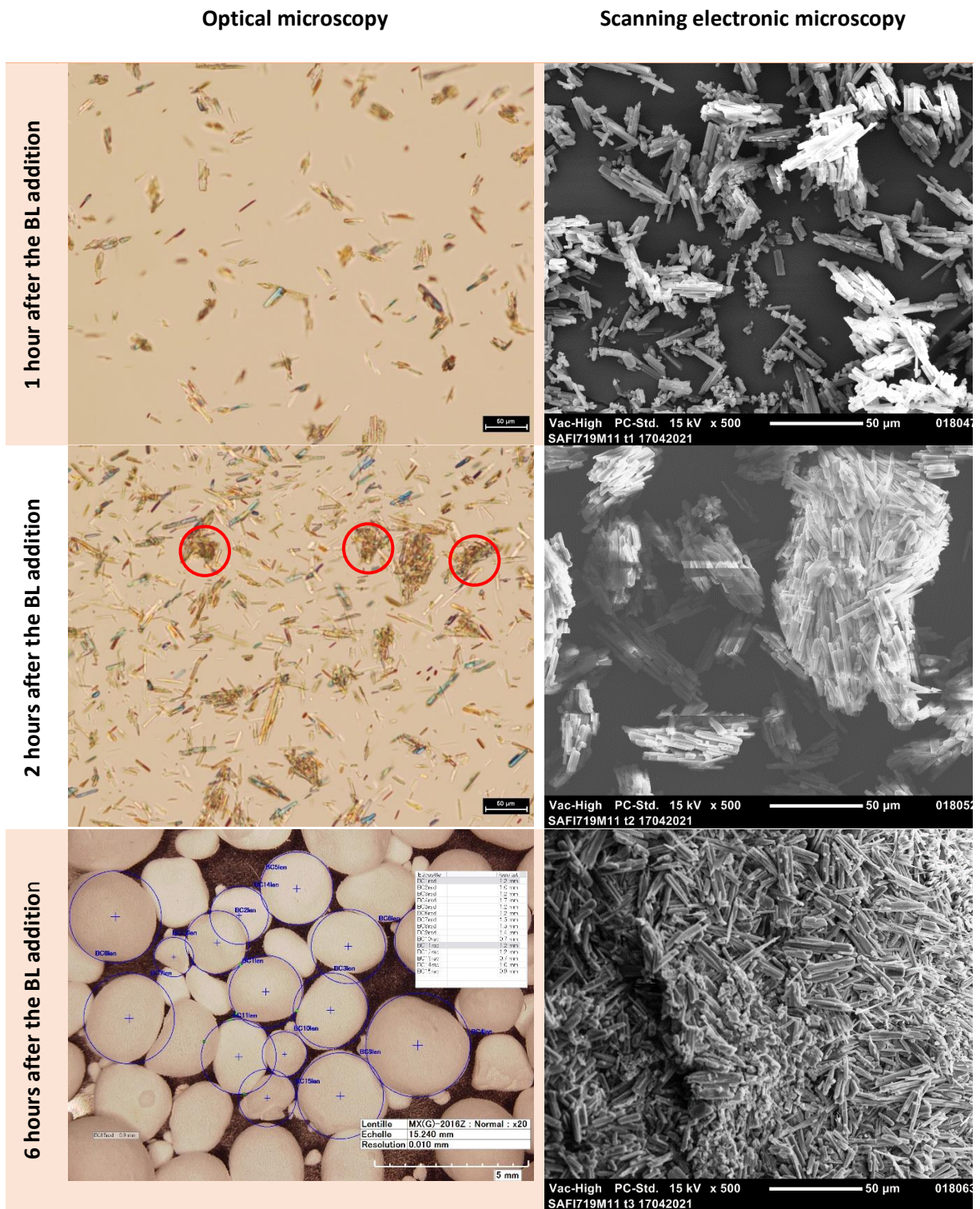
- Suspension homogenized for 5 min at the lower power of the Ultra Turrax

- After 1 hour of stirring at 400 rpm with a dispersion turbine, 25 mL of acetonitrile were added dropwise for 1 hour

- Reaction medium left under stirring for 12 hours

Table 4-7 exhibits the monitoring of the agglomeration process with optical and scanning electronic microscopy. After 2 hours of stirring the reaction media was partially agglomerated. To reduce the agglomerate size, the batch was left under stirring for 12 hours and then filtered and dried under reduce pressure at 40 °C for 24 hours.

Table 4-7: Monitoring of the agglomeration with a homogenization step performed with Ultra Turrax.



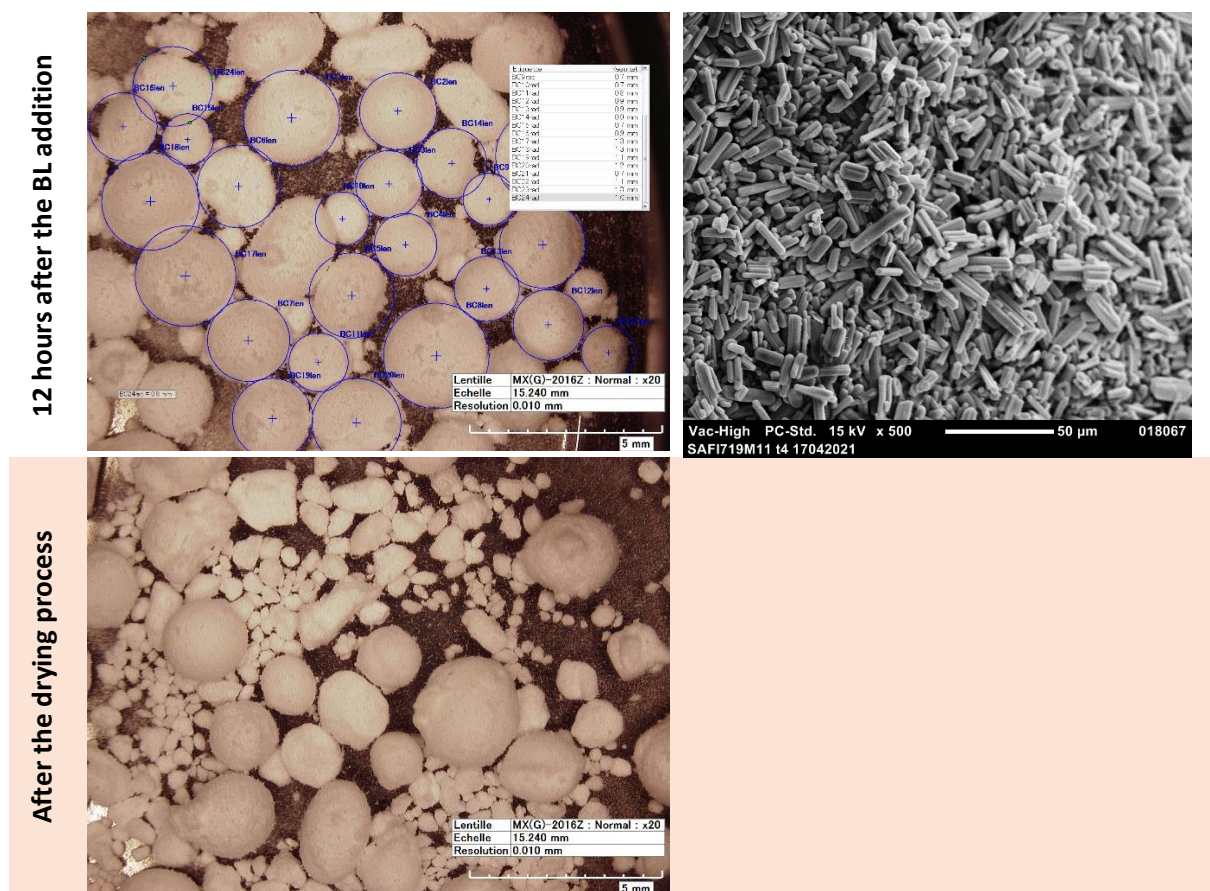


Table 4-8 summarizes the evolution of both initial particles and agglomerates when either the Ultra Turrax is used or not.

Table 4-8: Size of the initial particles and agglomerates before and after agglomeration process when using Ultra Turrax.

	Size without Ultra Turrax	Size with Ultra Turrax
Initial particle (before agglomeration)	Needle shape with an average length of 200 µm	Fragment of needles with an average length of 50 µm
Agglomerates (before drying)	Average diameter above 1 mm	Average diameter below 1 mm

Homogenization with Ultra Turrax leads to the decrease of the initial crystal size with an average length lower than 50 µm and consequently to the decrease of the final agglomerate size, even if agglomerates still exhibit an average particle size close to the millimeter. Upon crystal size homogenization (with the Ultra Turrax device) coupled with enhanced shearing forces during stirring, a target size around 500 µm looks achievable.

4.2.3.2 Effect of water amount in bridging liquid on the crystalline phase of SAFIM

The final goal of this study is to produce spherical agglomerates of SAFIM isolated in the anhydrous form **A1**. During the monitoring of the crystalline phase of the first agglomeration experiment, traces of **H1** (the hemi-hydrate) were observed even after the drying process at 30 °C. The

first hypothesis for this partial hydration is the presence of residual water in acetonitrile. Therefore, the evolution of SAFIM crystalline structure during the agglomeration as a function of the amount of water in acetonitrile was monitored thanks to XRPD.

The agglomeration was performed with the following parameters in a 500 mL temperature-controlled crystallizer at 30 °C and 425 rpm (dispersion turbine for stirring with baffles):

- Addition of 30 g of SAFIM (raw industrial batch) and 300 mL of n-heptane HPLC grade
- Stirring at 425 rpm for about 1 hour
- Addition of 20 mL of dried acetonitrile +x%_{wt} of water over 1 hour with a syringe pump (x being the amount of added water = 0; 1; 2; 3; 4 and 10 %_{wt})
- 6 hours after the end of BL addition the reaction medium was filtered and dried either under reduce pressure at 30 °C.

A regular sampling of the reaction medium was performed during the whole process. The amount of water in the dried acetonitrile was estimated to 40 ppm according to coulometric Karl-Fischer measurements.

Figure 4-18 shows the evolution of the XRPD patterns along the agglomeration process.

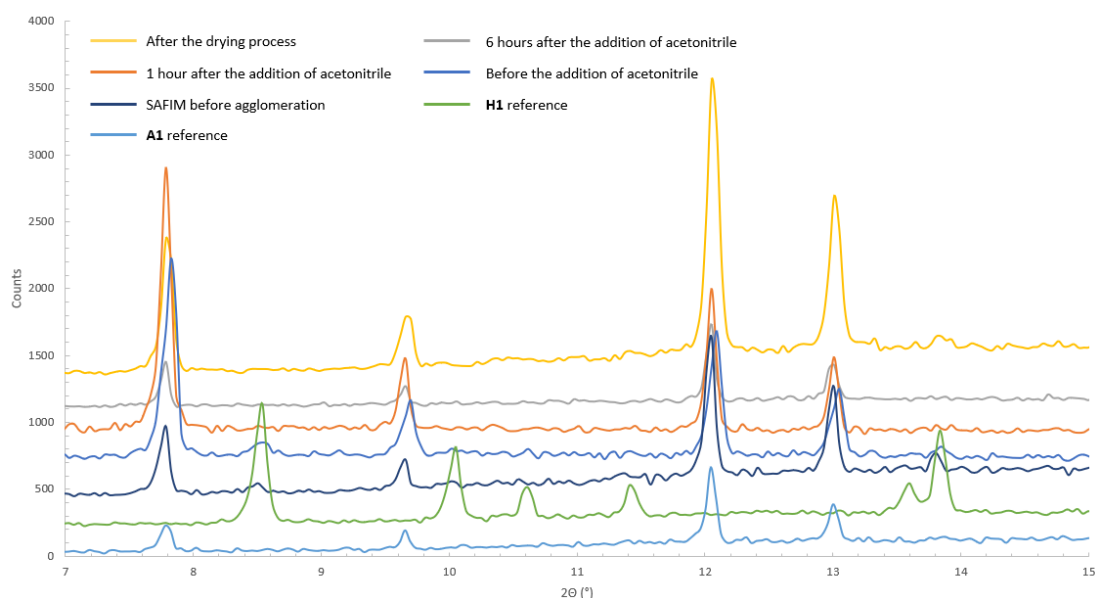


Figure 4-18: XRPD patterns of the evolution of the crystalline form of SAFIM during the agglomeration process with dried acetonitrile

The monitoring of the experiment shows that initial SAFIM product exhibits trace of **H1**. After 1 hour of stirring in n-heptane no evolution of the crystalline form was noted. Then, after the addition of dry acetonitrile, SAFIM was completely converted into **A1**. This form remains the stable one even after the drying step. The use of dried acetonitrile as BL leads to the conversion of partially hydrated SAFIM into the anhydrous form **A1**.

Figure 4-19 shows the XRPD patterns of the different agglomeration batches for different amount of water in the BL after the drying process and Table 4-9 resumes the form obtained after the drying process (all the XRPD patterns performed until the addition of 10 %_{wt} of water in the BL. are available in appendix III)

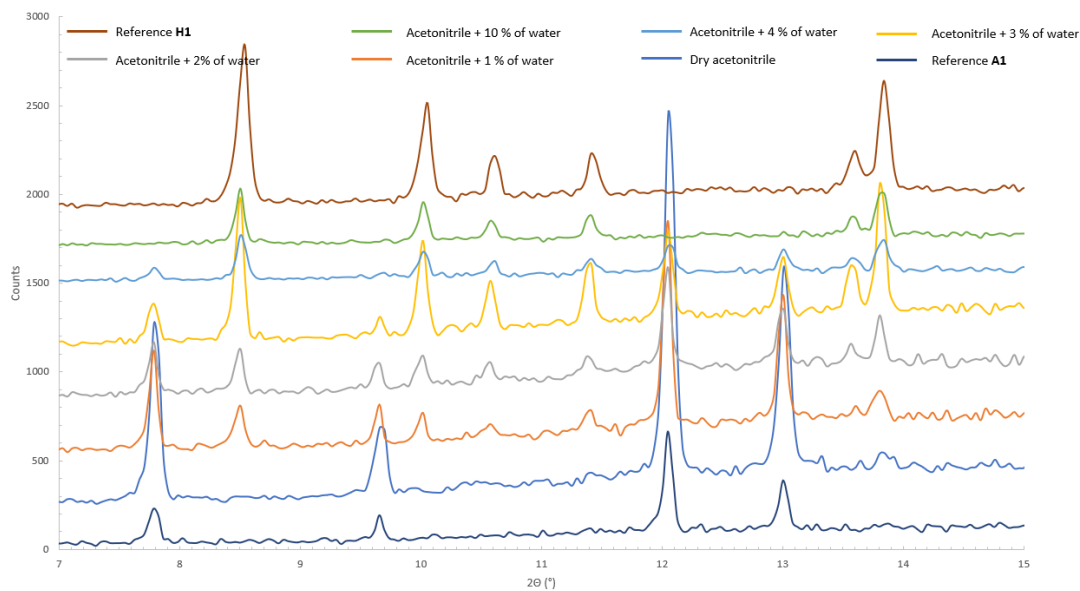


Figure 4-19: Evolution of the crystalline form of SAFIM after the drying process for different amount of water added in acetonitrile

Table 4-9: Evolution of the crystalline form during the agglomeration process of SAFIM for different amount of water in acetonitrile.

<i>x</i> % _{wt} water in acetonitrile	Initial crystalline form	1 hour after the addition of acetonitrile + <i>x</i> % _{wt} of water	After filtration	After drying
< 40 ppm	A1 (+ trace of H1)	A1	A1	A1
1%	A1 (+ trace of H1)	A1/H1	A1/H1	A1/H1
2%	A1 (+ trace of H1)	A1/H1	A1/H1	A1/H1
3%	A1 (+ trace of H1)	A1/H1	A1/H1	A1/H1
4%	A1 (+ trace of H1)	A1/H1	N/A	A1/H1
10%	A1 (+ trace of H1)	A1/H1	N/A	H1

By increasing the amount of water in the bridging liquid, the progressive hydration of SAFIM was observed, up to a complete hydration of the batch with 10 % of water in the bridging liquid.

Moreover, no dehydration occurs during the drying process, the hemi-hydrate remains stable under the tested conditions (*i.e.*, 24 hours at 30 °C under reduced pressure). One can envisage to convert the hydrated solids into anhydrous by an adapted drying step by tuning parameters (time, temperature, use of dry gas), but the dehydration implies a significant change in term of particles morphologies leading to embrittlement of the agglomerates. That is why dried acetonitrile will be preferentially used to perform the spherical agglomeration process of SAFIM in order to obtain pure **A1** at the end of the process. Moreover, to avoid the presence of traces of **H1** phase in the final agglomerates, the drying temperature under reduce pressure will be increased to 50 °C.

4.2.3.3 Optimization of SAFIM spherical agglomeration process

Preliminary parameters were found to perform a spherical agglomeration of SAFIM. Even if spherical agglomerates were produced, different parameters need to be optimized to obtain the desired micromeritic properties (average agglomerate size of 500 µm diameter with a good flowability). There are two common approaches to optimize a process: the One Factor At a Time (OFAT) or the Design of Experiment (DoE).

Recently, the pharmaceutical industry has moved toward the implementation of the Quality by Design (QbD) approach to the validation of manufacturing process to replace the Quality by Test. This new approach is based on a thorough knowledge of the manufacturing process and the impact of the process parameters on the quality of the final product (“knowledge management”). The DoE is one of the tools used within this approach, which will be applied to the development of the spherical agglomeration process of SAFIM.

The first step of a QbD approach is the identification of the target quality profile of the product, which is defined by a set of critical quality attributes (CQA), as well as the critical process parameters (CPP) affecting the CQAs. The spherical agglomeration aimed at producing spherical agglomerates with a desired particle size distribution and enhanced flowability properties starting from a material exhibiting poor flowability properties. Four CPPs (called factors of the DoE) were identified for the agglomeration of SAFIM:

- (i) The agglomeration temperature (X1)
- (ii) The stirring speed (X2)
- (iii) The bridging liquid amount (X3)
- (iv) The suspension concentration (X4)

The influence of these factors will be measured on four responses:

- (i) The average diameter of the agglomerates

- (ii) The span of particle size distribution
- (iii) The angle of repose (see Appendix I)
- (iv) The compressive strength of an agglomerate when submitted to a normal stress¹²¹

Preliminary remarks:

- No conditions being found to perform laser PSD measurement without altering the agglomerates, the average diameter and the span of the PSD were measured by using image analysis.
- The angle of repose was measured thanks to a fixed funnel apparatus (flodex™, see Appendix I).

The compressive strength of the agglomerates was estimated thanks to the failure point. The agglomerates were submitted to a normal stress applied with the powder rheometer FT4 from Freeman technology. The failure point is given by the following relation. Five agglomerates were tested for each experiment:

$$\frac{\text{normal stress applied to break an agglomerate}}{\text{surface of the projected area of the agglomerate}}$$

4.2.3.3.1 Design of experiment initial matrix

The factors and responses being identified, the next step of the DoE is the determination of the matrix of experiments, *i.e.*, the selection of the different level of factors and the number of experiments. For a full characterization of the system a full factorial plan with two levels was established, utilizing the JMP® software.

Choice of the factor levels:

From previous experiments, it has been shown that the higher the temperature the higher the risk of hydration of SAFIM. However, above 40 °C, the agglomeration only partially occurs. Therefore, the temperature for the DoE was set between 25 °C (-1 level) and 35 °C (1 level).

For the stirring speed, the emulsion between the dispersion solvent and the BL was obtained between 300 and 500 rpm with the dispersion turbine. This parameter was set at 350 rpm (-1 level) and 450 rpm (1 level) for the DoE.

The amount of BL for the agglomeration to occur was estimated around 20 mL. However, the addition of the homogenization step with the Ultra Turrax has increased the surface area of the solid. Thus, more BL was needed to wet all the particles. The BL amount was studied with 20 mL (-1 level) and 24 mL (1 level) by using a constant feeding rate of 20 mL/h.

Lastly, the slurry concentration was studied at 60 g/L (-1 level) and 80 g/L (1 level).

The spherical agglomeration process was performed as follow:

- (i) SAFIM was poured in the HWS crystallizer with temperature set at the agglomeration temperature
- (ii) 30 mL of n-heptane were added and the stirring set at the desired rate
- (iii) After 15 minutes, the reaction medium was homogenized with the Ultra Turrax at the lower power level for 5 minutes
- (iv) The reaction medium was left under stirring for 15 minutes
- (v) The addition of the BL is started with a feeding rate of 20 mL/h
- (vi) The reaction medium is left under stirring until the complete agglomeration
- (vii) The reaction medium was filtered and agglomerates dried at 50 °C under reduced pressure for 24 hours

The DoE consists of 16 experiments and a center point (experiment 17). The matrix of experiment is presented hereafter (Table 4-10).

Table 4-10: first matrix of experiments for the DoE of SAFIM agglomeration process.

Experiment	Agglomeration temperature (°C)	Stirring rate (rpm)	BL amount	Suspension concentration
1	25	350	20	60
2	35	350	20	60
3	25	450	20	60
4	35	450	20	60
5	25	350	24	60
6	35	350	24	60
7	25	450	24	60
8	35	450	24	60
9	25	350	20	80
10	35	350	20	80
11	25	450	20	80
12	35	450	20	80
13	25	350	24	80
14	35	350	24	80
15	25	450	24	80
16	35	450	24	80
17	30	400	22	70

Development of the Spherical Agglomeration Process of Safinamide Mesylate

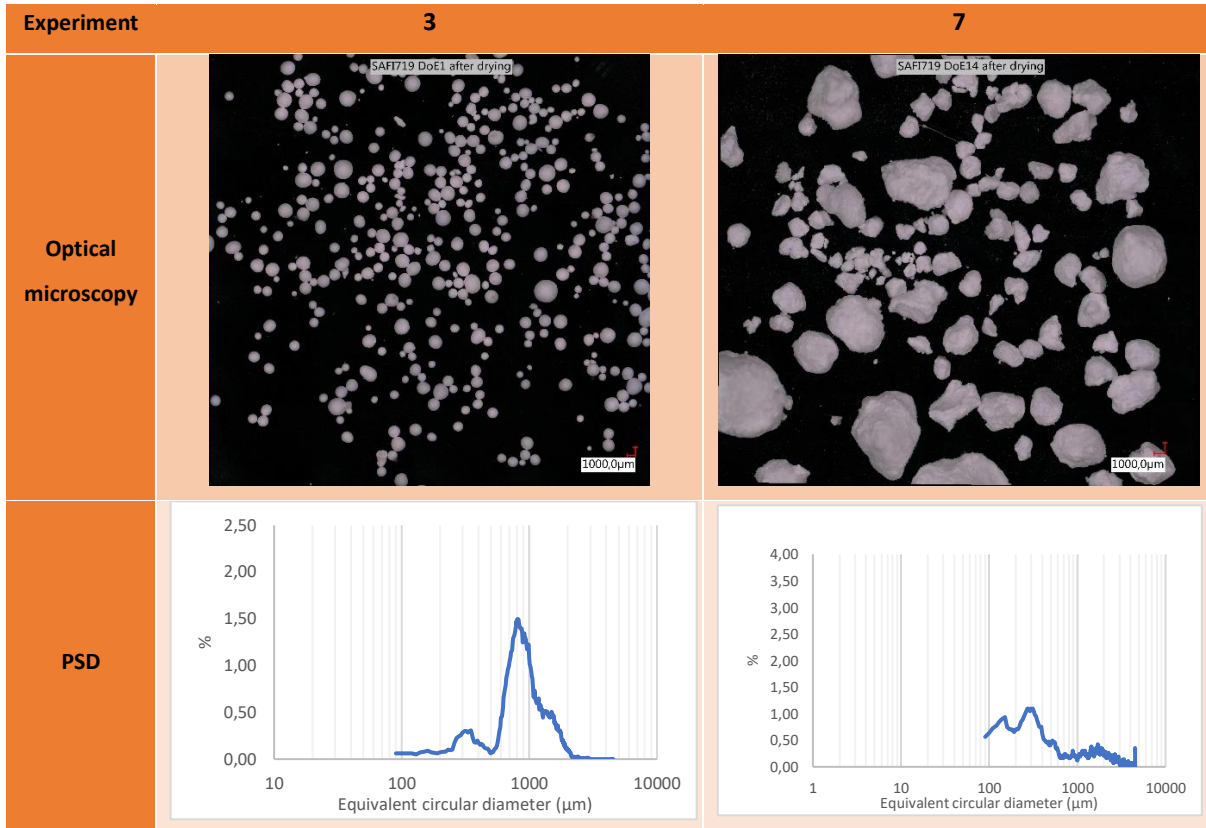
Table 4-11 displayed the results obtained for the first matrix of experiments.

Table 4-11: Responses for every experiment of the first matrix of experiment

<i>Experiment</i>	<i>Temperature</i>	<i>Stirring rate</i>	<i>BL amount</i>	<i>Slurry concentration</i>	<i>PSD (D50) (μm)</i>	<i>PSD (span)</i>	<i>Angle of repose ($^{\circ}$)</i>	<i>Failure point</i>
1	25	350	20	60	1278.7	646.6	39.54	0.22
2	35	350	20	60	1053.3	641.3	40.3	0.19
3	25	450	20	60	1101.5	408.4	34.41	0.14
4	35	450	20	60	990	528.5	36.91	0.11
5	25	350	24	60	831.4	887.1	N/A	0.11
6	35	350	24	60	1441.5	602.8	38.25	0.21
7	25	450	24	60	1504.4	1293.2	60	0.15
8	35	450	24	60	1617.2	666.4	38.86	0.1
9	25	350	20	80	968.9	674.6	41.32	0.13
10	35	350	20	80	905.3	845.7	44.64	0.12
11	25	450	20	80	1489.6	445.7	34.93	0.49
12	35	450	20	80	852.4	672.2	N/A	0.13
13	25	350	24	80	704.8	636.1	42.92	0.16
14	35	350	24	80	1087.9	694.4	38.85	0.16
15	25	450	24	80	815.6	571	40.14	0.22
16	35	450	24	80	1368.5	421	36.95	0.18
17	30	400	22	70	1159.4	442.2	34.12	0.20

Surprisingly, the model cannot find any principal effects of the factors in the tested conditions (*i.e.*, individually, the factors have no effect on the responses) even if there are visual differences between the experiments. For example, Table 4-12 shows the differences between two experiments of the DoE.

Table 4-12: Comparison of the agglomerate shape and particle size distribution between two experiments of the first design of experiment.



There is a significant difference between these two experiments in terms of morphology and particle size: experiment 3 exhibits spherical agglomerates with a bimodal distribution of the PSD where experiment 7 exhibits rough agglomerates with a large span of the PSD. However, the model of the DoE was not able to explain these differences.

This difficulty to model can be explained by a too restraint design space. For example, the variation of the average agglomerate diameter is not significant enough between 350 and 450 rpm. Therefore, the design space was extended.

4.2.3.3.2 Design of experiment extended matrix

To extend the design space, additional experiments were added as well as repetition at the center point. Figure 4-20 gives a schematic representation of the design space extension.

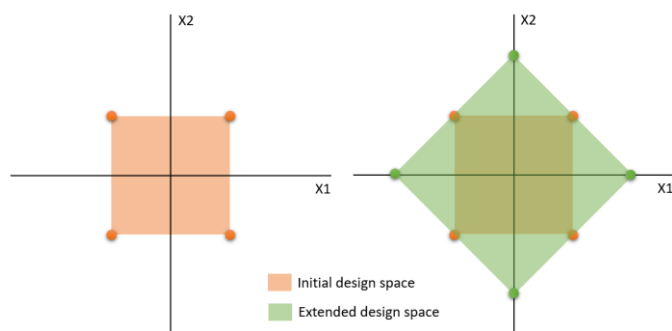


Figure 4-20: Schematic representation of a design space extension

Table 4-13 displayed the matrix with the additional experiments to perform.

Table 4-13: Extended matrix of experiments for the DoE of SAFIM spherical agglomeration.

Experiment	Temperature (°C)		Stirring rate (rpm)		BL amount (mL)		Slurry concentration (g/L)	
	Code	Value	Code	Value	Code	Value	Code	Value
18	0	30	0	400	0	22	0	70
19	1.5	35	0	400	0	22	0	70
20	0	30	0	400	0	22	1.5	85
21	0	30	-1.5	325	0	22	0	70
22	0	30	0	400	0	22	0	70
23	0	30	1.5	475	0	22	0	70
24	0	30	0	400	0	22	-1.5	55
25	0	30	0	400	1.5	25	0	70
26	-1.5	22.5	0	400	0	22	0	70
27	0	30	0	400	0	22	0	70
28	0	30	0	400	-1.5	19	0	70

The experiments were carried out in the same conditions as before and results are presented in Table 4-14.

Table 4-14: Responses for every experiment of the extended matrix of experiment.

Experiment	Temperature	Stirring rate	BL amount	Slurry concentration	PSD (D50)	PSD (spawn)	Angle of repose	Failure point
18	30	400	22	70	1182.3	320.5	38.24	0,24
19	35	400	22	70	1052.9	504.1	37.58	0,16
20	30	400	22	85	1333.9	373.0	34.34	0,13
21	30	325	22	70	1290.9	774.6	38.74	0,15
22	30	400	22	70	1269.9	443.5	34.30	0,18
23	30	475	22	70	710.5	232.0	34.54	N/A
24	30	400	22	55	1430.4	985.5	41.46	0,14
25	30	400	25	70	1412.9	1089.0	39.43	0,18
26	22.5	400	22	70	1010.2	966.0	-	0,19
27	30	400	22	70	1206.4	455.4	36.53	0,13
28	30	400	19	70	1149.8	506.8	38.13	0,15

Even with the extended matrix no significant effects of the factor were identified by the DoE. This simple approach seems inappropriate when dealing with agglomeration processes probably because of cross interferences between parameters.

However, thanks to the DoE, experimental conditions were found with experiment 23 to produce agglomerates with an average agglomerate diameter around 500 μm (710.5 μm) and exhibiting an angle of repose which corresponds to a “good flow”. The enhanced shearing forces due to the increase of the stirring rate leads to the decreasing of the agglomerate size distribution. Figure 4-21 shows a microscopy picture and the PSD of the experiment.

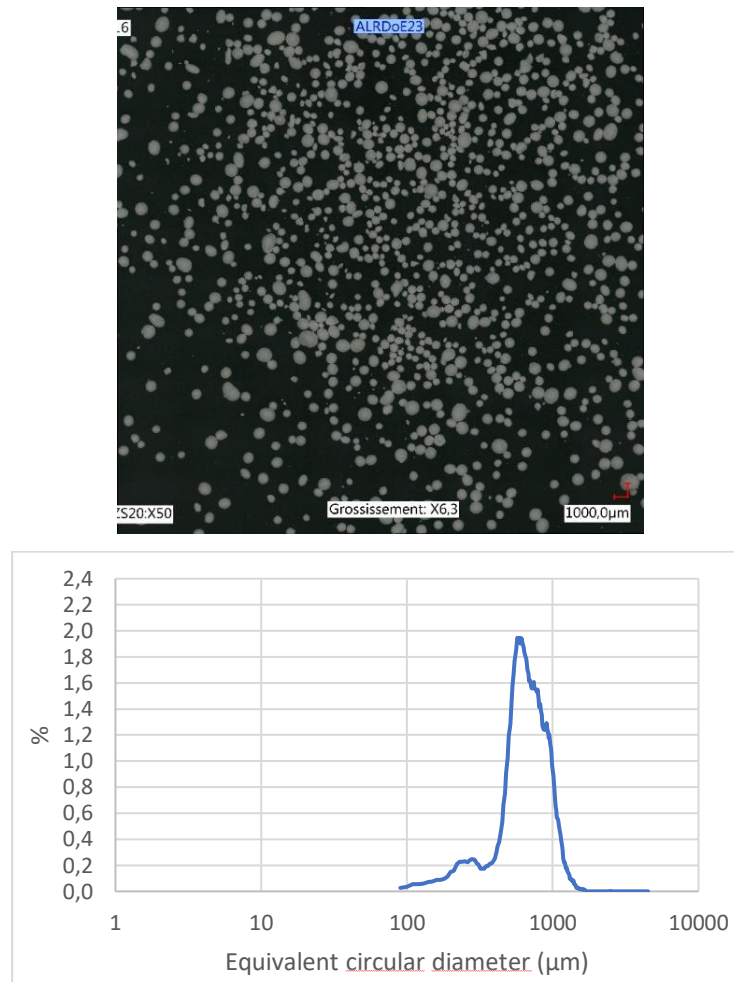


Figure 4-21: (Top) microscopy pictures of the experiment 23 of the DoE of SAFIM spherical agglomeration and (bottom) PSD of experiment 23

This experiment almost fulfills the PSD target of an average diameter of 500 µm. Moreover, Carr's index and Hausner's ratio for this experiment were measured (see Appendix I).

The Hausner's ratio and Carr's index were measured at 1.08 and 7% respectively, which corresponds to a free-flowing powder. The initial SAFIM (*i.e.*, before the agglomeration) exhibits a Hausner's ratio and a Carr's index of 1.70 and 41% respectively, which corresponds to a very cohesive powder. Therefore, the flowability properties of SAFIM were significantly enhanced by the agglomeration process.

Table 4-15 compares the initial SAFIM properties with SAFIM agglomerated in the optimized conditions.

Table 4-15: Comparison between SAFIM properties before and after spherical agglomeration with the set of optimized conditions.

Initial SAFIM			Agglomerated SAFIM			
Shape	needles		Spherical agglomerates			
PSD	200 μm (average length)		710.5 μm (D50)			
Flowability	HR	CI (%)	Angle of repose ($^{\circ}$)	HR	CI (%)	Angle of repose ($^{\circ}$)
	1.70	41	60.8	1.08	7	34.5

4.2.4 Study on the amount of residual solvent after agglomeration procedure

In order to perform the spherical agglomeration of SAFIM two solvents were used: n-heptane and acetonitrile. According to ICH Q3C (R8),¹²² n-heptane is considered as a solvent with a low toxic potential (class 3) and acetonitrile is a solvent to be limited (class 2). Therefore, their recommended limits are respectively 5000 ppm and 410 ppm. Residual solvents trapped in agglomerated particles were measured by means of Head Space Gas Chromatography (HS-GC). A description of the used method and the sample preparation is provided in Appendix I.

A spherical agglomeration of SAFIM following the optimized conditions was performed. The isolated agglomerates were dried at 50 $^{\circ}\text{C}$ under reduced pressure (350 mBar) for 1 week and a regular sampling was performed during this week. Figure shows the drying curve of n-heptane and acetonitrile.

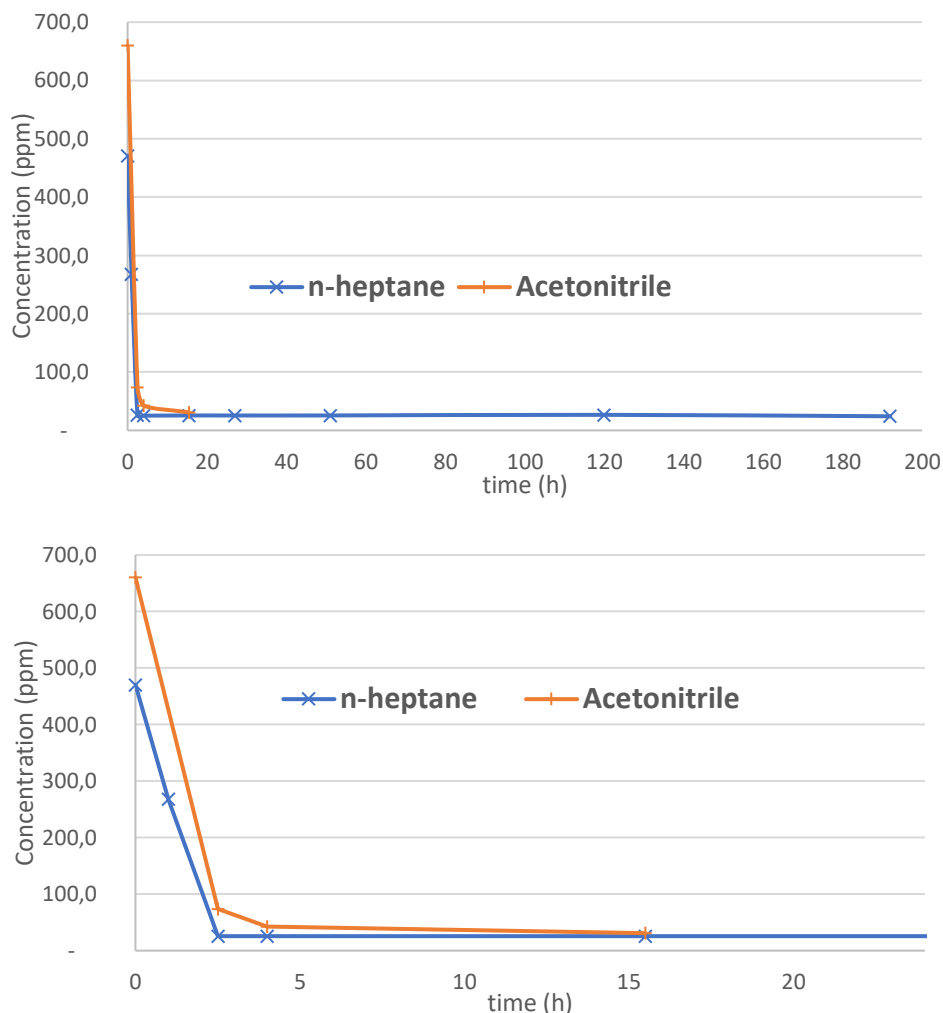


Figure 4-22: Drying curve obtained from GC-MS of acetonitrile and n-heptane in agglomerated SAFIM and magnification between 0 h and 24 h

A rapid decrease of the concentration of both n-heptane and acetonitrile was observed. After 2.5 hours of drying, the concentrations fell below the recommended limit concentrations. Moreover, after 20 hours of drying acetonitrile was under the limit of detection of the apparatus, the concentration of n-heptane remained stable even after 1 week of drying.

The applied drying process on spherical agglomerates is then in accordance with the ICH Q3C standards of the European pharmacopeia.

4.3 CONCLUSIONS AND PERSPECTIVES ON THE SPHERICAL AGGLOMERATION OF SAFIM

The aim of this study was to develop the spherical agglomeration process of an industrially product API: safinamide mesylate together with the control of the crystalline form of the product. Figure 4-23 sums up the different steps of the spherical agglomeration process development of safinamide mesylate.

Development of the Spherical Agglomeration Process of Safinamide Mesylate

Initial conditions	<p><u>Crystalline form:</u> A1 + traces of H1</p>	<p><u>Particle size et shape:</u> Needles of 200 µm length</p>	<p><u>Flowability:</u> Very cohesive</p>			
Preliminary results	<p><u>Determination of solvents:</u> <i>Phase diagram and European Pharmacopeia approach</i></p> <p>Dispersion solvent → n-heptane Bridging liquid → acetonitrile</p> <hr/> <p><u>BL amount:</u> Minimum amount of BL = 15 mL Maximum amount of BL = 25 mL</p>	<p><u>Geometry of the reactor and stirring geometry:</u> <i>Guided by industrial scale up and evaluation of the non-miscible solvent dispersion</i></p> <p>Performed in a HWS flat bottom reactor Use of a dispersion turbine with baffles</p>	<p><u>Temperature</u> <i>Low temperature → stabilization of H1</i> <i>High temperature → modification of the solubilities</i></p> <p>Minimum temperature = 30 °C Maximum temperature = 40 °C</p>	<p><u>Initial particle size</u> <i>Modification of the initial particle size with an Ultra Turrax device</i></p> <p>5 mins of Ultra Turrax before agglomeration → reduction of the final agglomerate size</p>		
Optimization of spherical agglomeration	<p style="text-align: center;"><u>Criteria to fulfill</u></p> <ul style="list-style-type: none"> • Final crystalline form: A1 • Agglomerate size: circa 500 µm diameter • Flowability: Angle of repose < 35° Hausner ratio > 1.18 Carr's index > 15% • Residual solvent: Lower to the European Pharmacopeia criteria (n-heptane = 5000 ppm and acetonitrile = 410 ppm) 	<p style="text-align: center;"><u>Experimental parameters</u></p> <table border="1" style="width: 100%; border-collapse: collapse;"> <tr> <td style="width: 50%; text-align: center; vertical-align: top;"> <p><u>Set parameters</u></p> <ul style="list-style-type: none"> • Initial particle size : pretreatment by Ultra-Turrax • Amount of water in solvent → dry solvents • Crystallizer (HWS) and stirring geometry : dispersion turbine + baffles • Bridging liquid introduction time : introduction over 1 hour </td> <td style="width: 50%; text-align: center; vertical-align: top;"> <p><u>To optimize</u></p> <ul style="list-style-type: none"> • Stirring rate (from 325 to 475 rpm) • Agglomeration temperature (from 25 to 35 °C) • Concentration of SAFIM in n-heptane (from 55 to 85 g/L) • Amount of bridging liquid (from 19 to 25 ml) </td> </tr> </table>			<p><u>Set parameters</u></p> <ul style="list-style-type: none"> • Initial particle size : pretreatment by Ultra-Turrax • Amount of water in solvent → dry solvents • Crystallizer (HWS) and stirring geometry : dispersion turbine + baffles • Bridging liquid introduction time : introduction over 1 hour 	<p><u>To optimize</u></p> <ul style="list-style-type: none"> • Stirring rate (from 325 to 475 rpm) • Agglomeration temperature (from 25 to 35 °C) • Concentration of SAFIM in n-heptane (from 55 to 85 g/L) • Amount of bridging liquid (from 19 to 25 ml)
<p><u>Set parameters</u></p> <ul style="list-style-type: none"> • Initial particle size : pretreatment by Ultra-Turrax • Amount of water in solvent → dry solvents • Crystallizer (HWS) and stirring geometry : dispersion turbine + baffles • Bridging liquid introduction time : introduction over 1 hour 	<p><u>To optimize</u></p> <ul style="list-style-type: none"> • Stirring rate (from 325 to 475 rpm) • Agglomeration temperature (from 25 to 35 °C) • Concentration of SAFIM in n-heptane (from 55 to 85 g/L) • Amount of bridging liquid (from 19 to 25 ml) 					
Final process	<p style="text-align: center;"><u>Process parameters</u></p> <ul style="list-style-type: none"> • Crystallizer: <i>HWS flat bottom</i> • Stirring geometry and rate: <i>dispersion turbine + baffles, 475 rpm</i> • Pre-treatment of the initial powder : Reduction of the initial particle size with 5 min of Ultra Turrax • Agglomeration temperature: 30 °C • Concentration of the suspension: 70 g/L • Ratio bridging liquid/dispersion solvent: 0.07 		<p style="text-align: center;"><u>Agglomerate characteristics</u></p> <ul style="list-style-type: none"> ✓ Crystalline phase: A1 ✓ Agglomerate average diameter: around 700 µm ✓ Flowability: free flowing ✓ Residual solvent: below the concentration limit of European Pharmacopeia 			

Figure 4-23: Conclusion chart of SAFIM agglomeration process

First, the solvents to perform the spherical agglomeration were identified. Even if no system was extrapolated from the review of the agglomeration literature because of the presence of water in every system, the pharmacopeia standards and the study of phase equilibria led to identify **n-heptane** as the dispersion medium and **acetonitrile** as the bridging liquid. Nevertheless, other methods could be used to determine a best solvent system such as those based on the wettability of SAFIM with different solvents. During this study, wettability measurements with the Washburn capillary rise method were performed on SAFIM with n-heptane and acetonitrile. However, inconclusive results were obtained with this method. One perspective for this point is to measure the wettability angle thanks to a goniometer. This method gives a direct access to the angle of wettability and can be easily developed with a suitable equipment. Other parameters were also preliminary studied (*i.e.*, temperature, BL amount, stirring geometry, and initial particle size (see Figure 4-23)).

In order to reduce the number of parameters during the development of the agglomeration process, some of them were set at the beginning of the study (e.g., the geometry of the reactor). One of these parameters is the addition mode of the bridging liquid. The BL was added dropwise through a capillary of 2 mm inner diameter which generates large droplet of BL. The generated droplets having an average diameter larger than the initial particle size of SAFIM, an “immersion mechanism” to produce agglomerates can be envisaged. A study of Orlewski et al.¹¹⁰ has shown that the higher the inner diameter of the tube, the higher the PSD of the agglomerates attributed to the formation of smaller droplets. For a further reduction of agglomerate size, a thinner capillary could be used to perform the spherical agglomeration of SAFIM and change to a distribution mechanism. Moreover, the BL was added few centimeters above the reaction medium. Orlewski also shown that by adding the BL directly and horizontally into the crystal suspension produces smaller agglomerates.

In order to develop an optimized agglomeration process within the quality by design approach, a DoE was performed. However, it seems that there are too many variations or interference between the parameters in the responses to obtain acceptable results on the influence of the chosen factors, even with the extension of the design space.

Even if the simple DoE used could not explain the variations in the agglomeration process, spherical agglomerates of SAFIM with an average diameter close to the targeted value (500 μm) were obtained with the conditions of experiment 23. These agglomerates exhibit enhanced flowability properties compared to raw SAFIM with an acceptable amount of residual solvent according to the ICH Q3C.

Thus, the targeted solid form **A1** was obtained in the final agglomerates by adopting a phase diagram approach: (i) by increasing the temperature of the medium in order to decrease the stability domain of the hydrate and (ii) by limiting the amount of residual water in the solvent system to stay in the crystallization domain of **A1**.

Chapter V

Feasibility of the Spherical Agglomeration in a Couette Taylor Reactor

5 FEASIBILITY OF THE SPHERICAL AGGLOMERATION IN A COUETTE TAYLOR REACTOR

This chapter provides preliminary experiments on the possibility to perform spherical agglomeration process in a continuous mode by using a Couette-Taylor Reactor.

5.1 INTRODUCTION TO THE COUETTE TAYLOR TECHNOLOGY

5.1.1 Historical of Couette-Taylor technology

The Couette-Taylor reactor (CTR) is a reactor used to perform different processes such as chemical reactions, polymer synthesis, crystallization, or aggregation-flocculation. Due to the possibility of a continuous feed into the reactor, the technology presents a particular interest for continuous processing.

Mallock¹²³ has reported the flow behavior occurring between two rotating cylinders in 1888. In 1890, Maurice Couette has thoroughly described this particular fluid flow between two concentric cylinders at low level of turbulence (i.e., at low rotating speed).^{124,125} It has been shown through different studies that different flow regimes can occur in the CTR as a function of the rotation rate of the cylinders (see appendix IV). Taylor, in 1923, has investigated the formation of counter-rotating toroidal vortices generated in the interstitial space between the cylinders at higher turbulence levels. He described “square” vortices with a size equal to the distance between the two cylinders as shown in Figure 5-1.¹²⁶

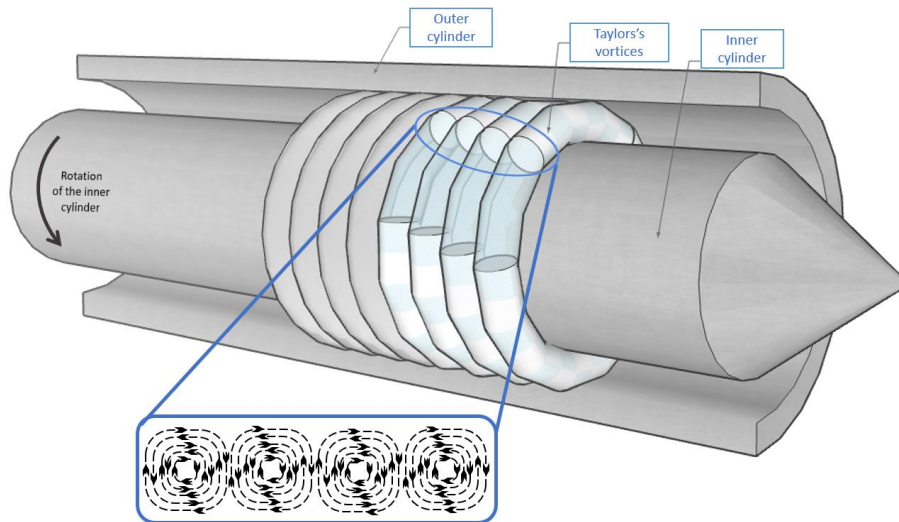


Figure 5-1: Schematic representation of Taylor's vortices occurring between two concentric cylinders (rotation of the inner cylinder)

Gu *et al.*¹²⁶ and Moore *et al.*¹²⁷ have focused their studies on the design of the first CTR based on numerical simulation and observation of the vortex formation and axial dispersion. It has been shown that such reactors exhibit enhanced heat and mass transfers and can be very efficient tools for crystallization processes.¹²⁹

5.1.2 Presentation of the Couette Taylor crystallizer

Recently, the original Couette-Taylor design has been modified to implement crystallization procedure, agglomeration, or symmetry breaking methods in the group of Professor Kim (University of Kyung Hee, South Korea). The modified CTR exhibits temperature-controlled cylinders inlets and outlets to plug different feeding solutions, PAT (Process Analytical Technologies), etc. It has been shown that CTR impacts the particle size distribution as well as the crystal morphology and the polymorphism.¹³⁰⁻¹³²

The Taylor Couette reactor used in this study consists in two coaxial cylinders with independent temperature regulation: the inner cylinder rotates while the outer cylinder remains static. It was manufactured specifically for the SMS lab by Laminar Co., Ltd (Figure 5-2).

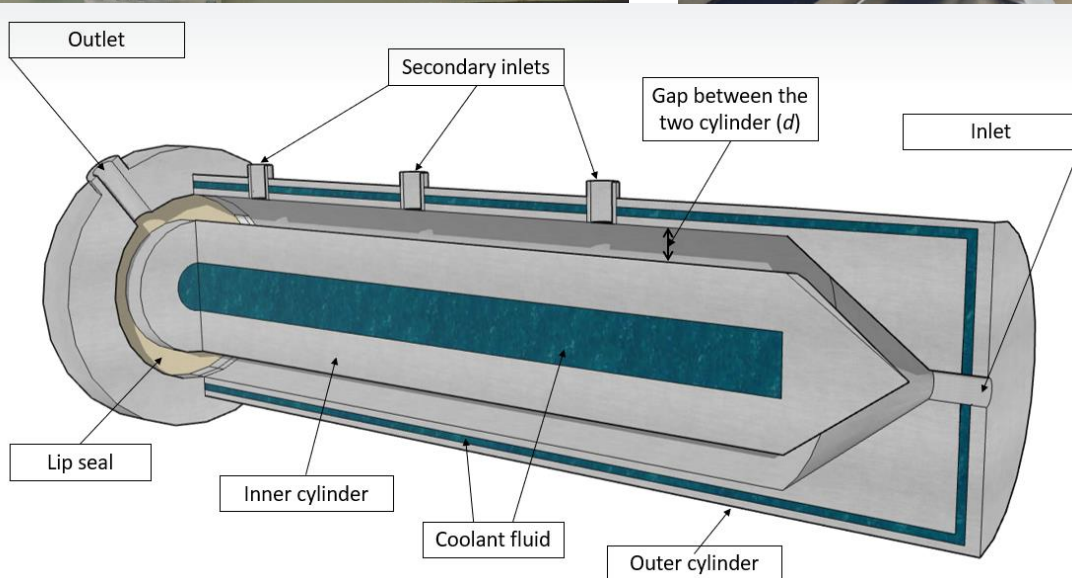
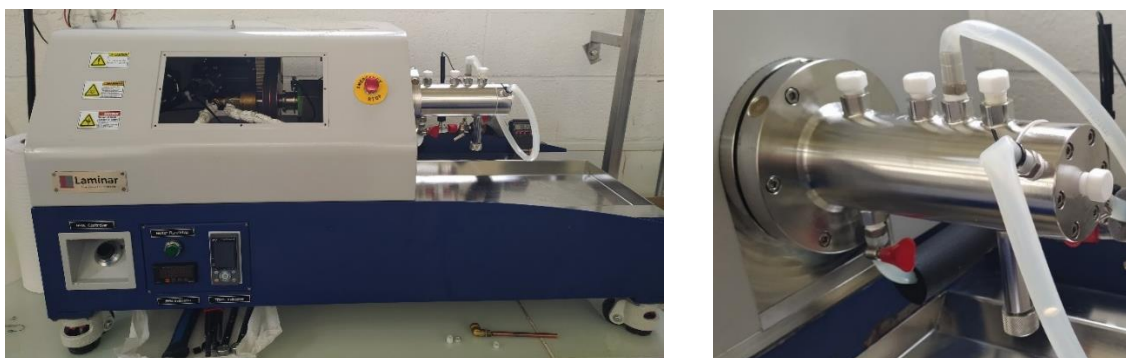


Figure 5-2: Photos of the Couette Taylor reactor (top) and its 3D representation (bottom)

Inner and outer cylinder radii are 19.5 and 23.4 mm, respectively. The distance d between the two cylinders is 3.9 mm, the total capacity of the reactor is 93 mL. In addition to the inlet and outlet, 3 secondary inlets are available to inject reactant, for sampling or accommodating probes (temperature, pH) and PAT (e.g., IR, Raman, granulometry, ...).

5.2 APPLICATION OF SPHERICAL AGGLOMERATION IN COUETTE TAYLOR CRYSTALLIZER

5.2.1 State of the art

Several authors have reported the agglomeration of inorganic entities in a Couette Taylor reactor such as calcium carbonate or metal hydroxides.^{130–135} The reported agglomeration mechanisms for these compounds relies on the Van der Waals attractive interactions between nanoparticles. Due to the shearing forces and enhanced mass transfer in CTR, micrometric agglomerates can be obtained during crystallization procedure in CTR.

To the best of our knowledge, there is no mention in the literature of a spherical agglomeration process conducted with a Couette Taylor reactor.

To validate the use of our specific reactor for spherical agglomeration purposes, the process was first applied to Timapiprant (Figure 5-3), an antagonist to the prostaglandin D2 receptor.¹³⁶

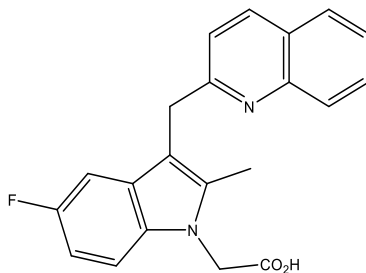


Figure 5-3: molecular structure of Timapiprant (Mw = 348.37 g/mol)

For this compound, Zach System has developed a “classical” spherical agglomeration procedure in solution:

- i) *Timapiprant is added to a solution of potassium hydroxide, purified water, and ethanol to fully dissolved the solid.*
- ii) *After one hour and the complete dissolution of the reaction medium (RM), it was clarified with purified water at 60 °C.*
- iii) *Formic acid was added with a controlled flow rate with a syringe pump in order to precipitate the API.*
- iv) *After 1 hour of stirring, the RM was cooled to 40°C and the bridging liquid (toluene) added.*
- v) *The reaction medium was left under stirring during at 40 °C until complete agglomeration. The RM was then filtrated and dried 24 hours under reduced pressure at 50 °C.*

This spherical agglomeration procedure can lead to highly spherical agglomerates (Figure 5-4). However, several days of stirring are required to obtain such sphericities and agglomerate size distribution.

Due to the enhanced shear forces and mass transfer in a CTR, a reduction of the agglomeration time and a higher productivity could be expected. The spherical agglomeration process was then adapted to the CTR in order to obtain agglomerates in a batch mode.

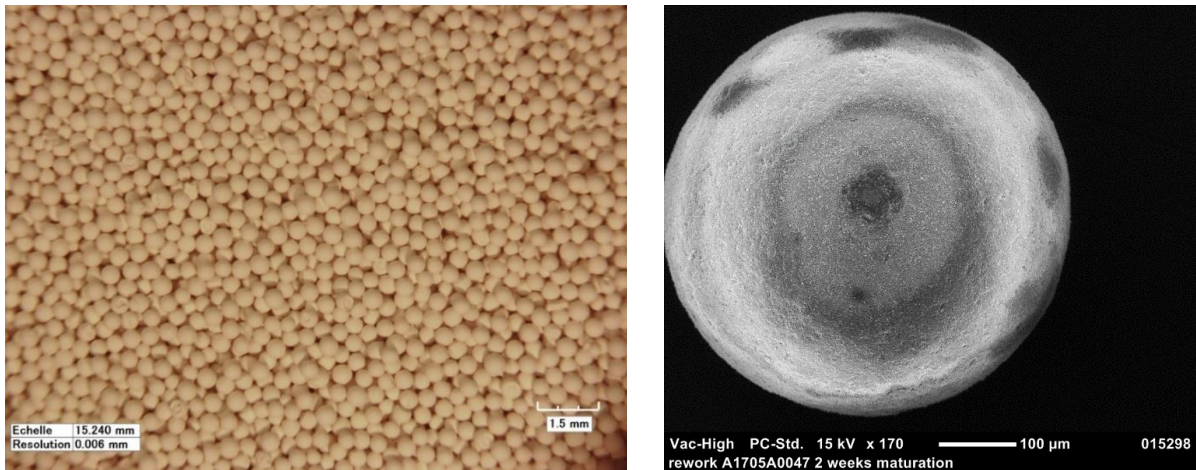


Figure 5-4: Spherical agglomerates pictures of Timapiprant obtained in conventional agitated crystallizer. Left: optical microscopy picture and right: SEM picture

5.2.2 Spherical Agglomeration of Timapiprant with Couette Taylor Reactor

5.2.2.1 Experimental conditions

Different agglomeration parameters were tested with the CTR:

- Rotation rate (Ω) of the inner cylinder
- Precipitation of Timapiprant in or out of the CTR
- Addition of the toluene (Bridging Liquid) before or after the precipitation of Timapiprant

Experiments were performed in isothermal mode, *i.e.*, the inner and outer cylinders were set at the same temperature (30 °C).

Table 5-1 summarizes the different experimental parameters tested in CTR.

Table 5-1: Different experimental conditions used to perform spherical agglomeration of Timapiprant in CTR.

Exp.	Ω (rpm)	Agglomeration temperature (°C)	Concentration of Timapiprant in water (g/L)	Precipitation of the API	Addition of the BL	Amount of BL (ml/ml of suspension)
1	500	30	90	External crystallizer	Addition of the BL in the CTR	0.06
2	1000	30	90			0.06
3	500	30	90	In the CTR	Addition of the BL before the CTR (in the solution of dissolved API)	0.06
4	250	30	90			0.06

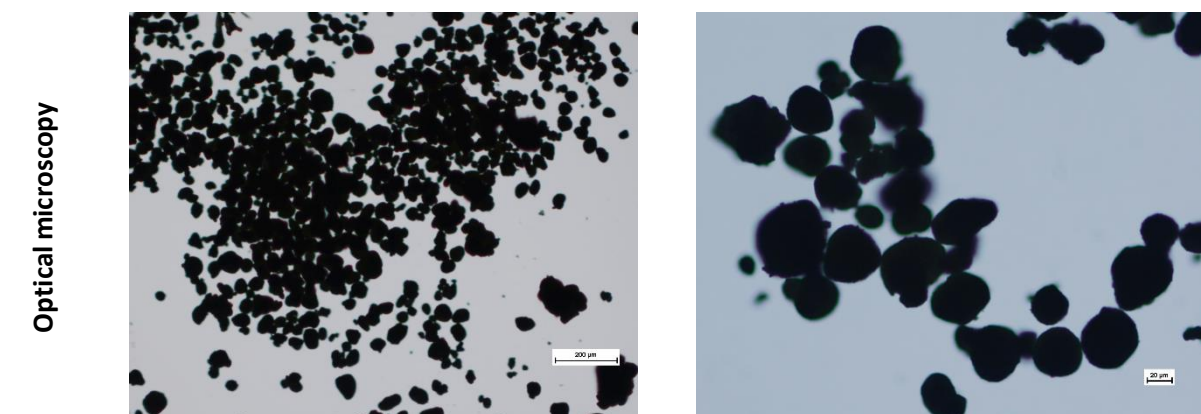
For experiments 1 et 2, Timapiprant was precipitated in an external stirred crystallizer. After the precipitation, the suspension was added in the CTR, and the BL added dropwise.

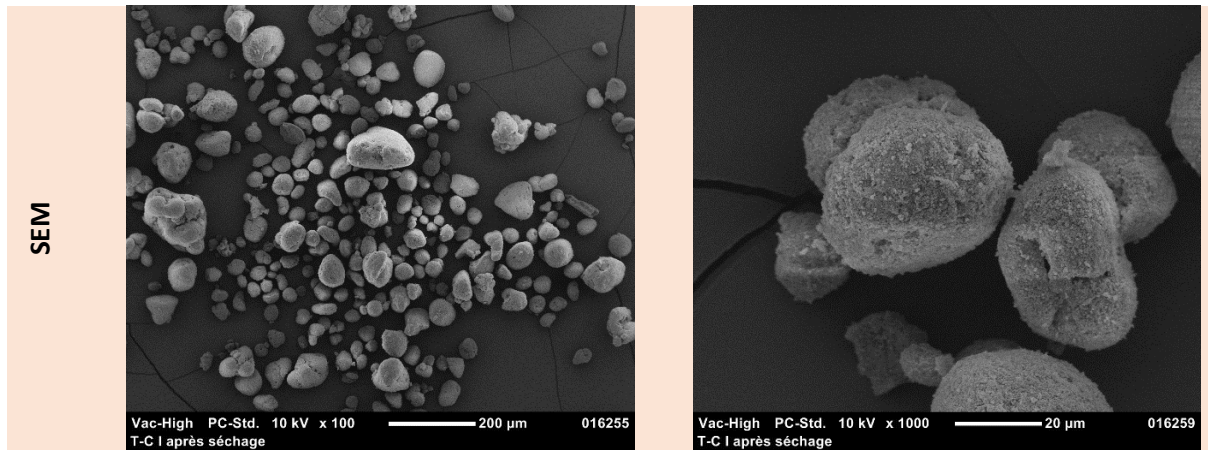
For experiments 3 and 4, a solution of Timapiprant was prepared in an external crystallizer and mixed with the BL. Then, the CTR was filled with the biphasic liquid solution and formic acid added dropwise to precipitate Timapiprant.

5.2.2.2 Results

For the experiment 1 at 500 rpm, agglomerates were observed after 8 hours of rotation. Table 5-3 exhibits optical and electronic microscopy pictures for this experiment.

Table 5-2: Microscopy pictures of agglomerates after 8 hours of stirring from experiment 1 in CTR; agglomeration at 500 rpm with addition of toluene in the CTR.





The batch exhibits irregular shaped agglomerates with different population size. Granulometric measurements were performed with a Mastersizer 2000 from Malvern.

Granulometric measurements exhibits a bimodal particle size distribution, the first is centered at *circa* 80 µm and the second one at 1 mm (Figure 5-5 and Table 5-3).

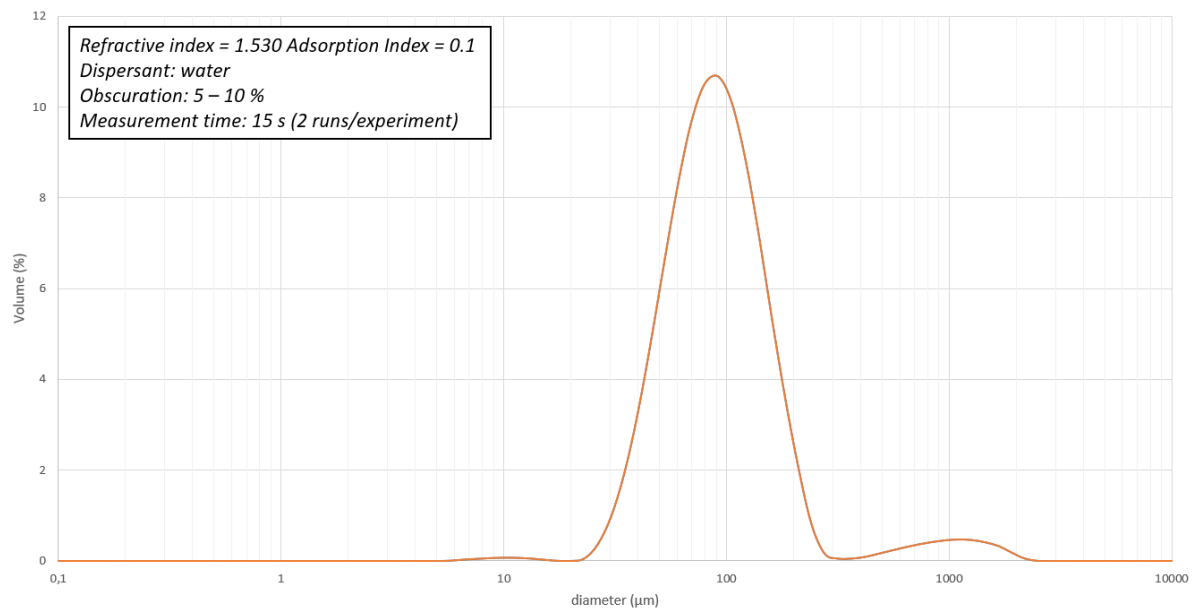


Figure 5-5: Figure 6: Particle size distribution of agglomerates from experiment 1 (addition of toluene in CTR) at 500 rpm

Table 5-3: Experimental data from granulometric measurement; agglomeration in CTR (addition of toluene in CTR) at 500 rpm.

Parameter	Result	
	Run 1	Run 2
$D[5,0]$ (μm)	82,97	84,19
$D[3,2]$ (μm)	73,2	76,1
Span	1,432	1,171
Residual (%)	0,454	0,466

Then, by increasing the rotation rate to 1000 rpm (experiment 2), Spherical agglomerates were observed in the CTR after 6 hours of stirring (Figure 5-6). However, after 8 hours of stirring, a partial leak of the reaction medium was observed through the lip seal. The reaction medium was then filtered and dried.

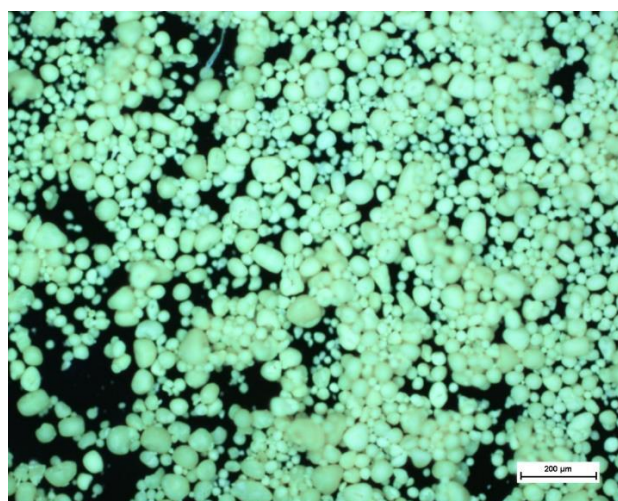
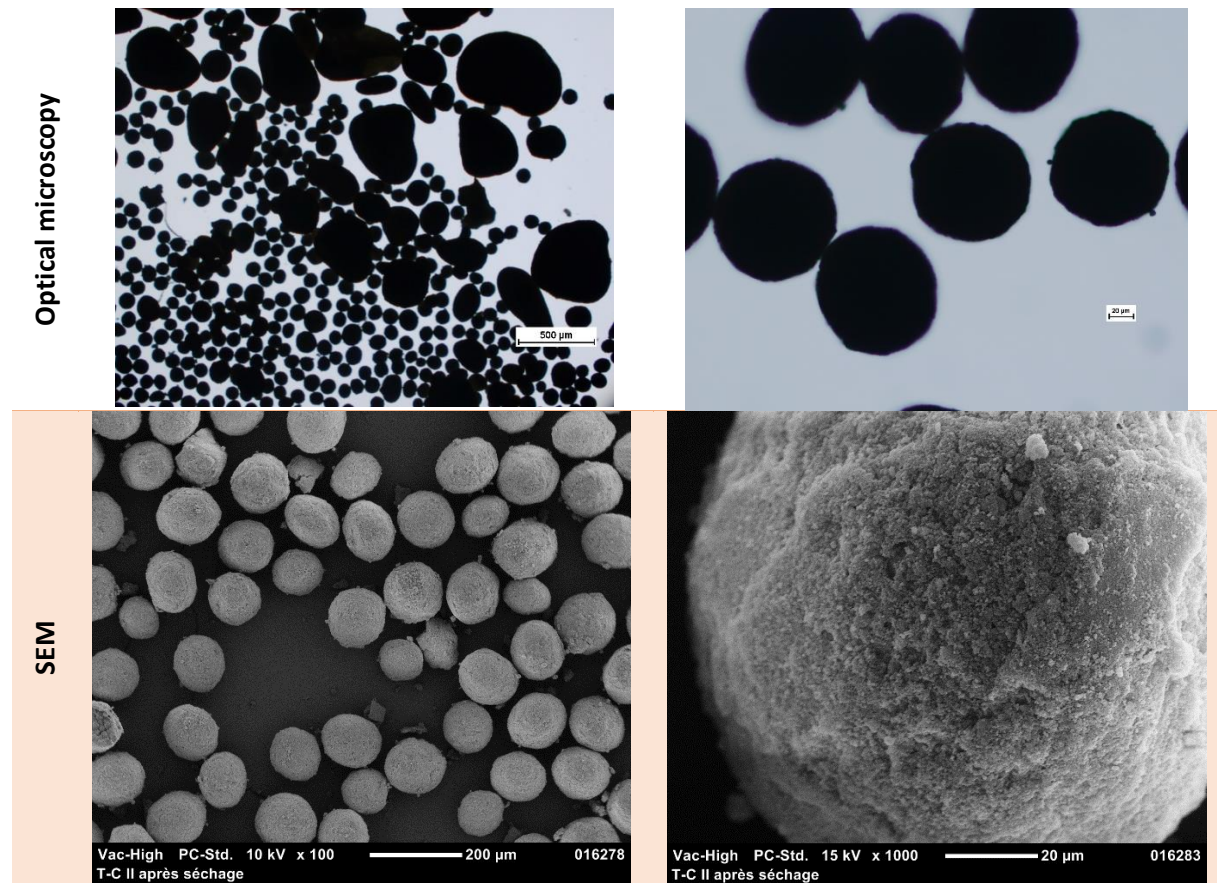


Figure 5-6: Optical microscopy picture of reaction medium sampling after 6 hours of stirring at 1000 rpm (addition of toluene in CTR)

Increasing the rotation rate of the inner cylinder seems to lead to a decrease of the agglomeration time due to the enhanced shearing forces in the CTR and more spherical agglomerates.

For experiment 3 (*i.e.*, precipitation of Timapiprant in the CTR), 8 hours after the addition of the formic acid, spherical agglomerates were observed in the reaction medium. Microscopy pictures are presented in Table 5-4.

Table 5-4: Microscopy pictures of agglomerates from agglomeration in CTR; agglomeration at 500 rpm with precipitation of RM in CTR.



By precipitating Timapiprant in the CTR, the agglomerates seem more spherical for an equal residence time in the reactor. Granulometric measurement of the batch is presented in Figure 5-7 and Table 5-5.

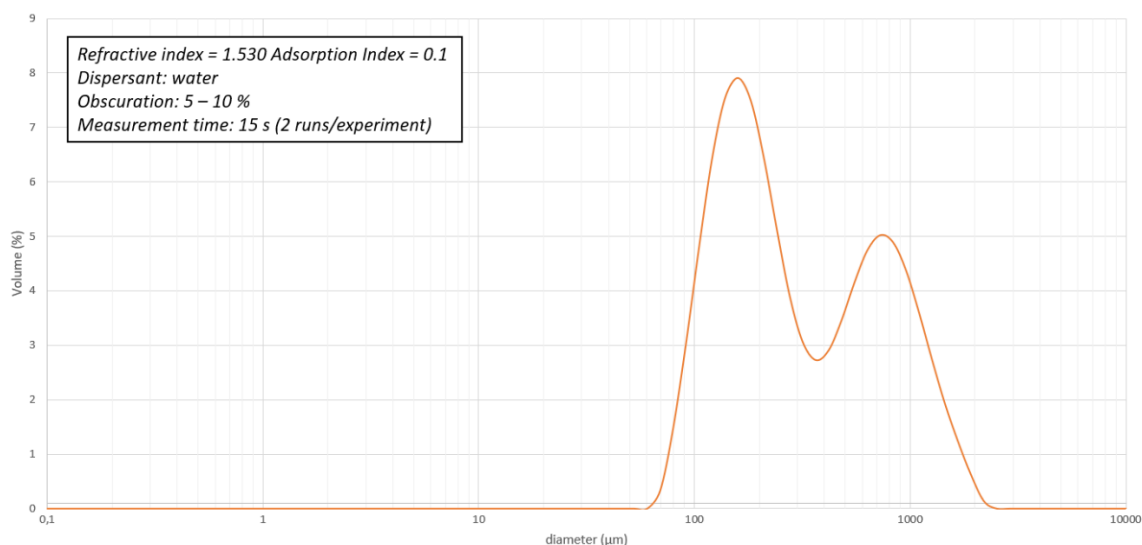


Figure 5-7: Particle size distribution of agglomerates from agglomeration in CTR (precipitation in CTR) at 500 rpm

Table 5-5: Experimental data from granulometric measurement; agglomeration in CTR (precipitation in CTR) at 500 rpm.

Parameter	Result	
	Run 1	Run 2
$D[5,0]$ (μm)	217,1	235,9
$D[3,2]$ (μm)	175,3	212,3
Span	4,176	3,634
Residual (%)	1,099	1,290

Granulometric measurement shows that the agglomerates also exhibit a bimodal particle size distribution. For the smallest PSD, the agglomerates are bigger than for the first experiment (average size of 105 μm) and the second particle size distribution exhibits smaller agglomerates (average size of 750 μm). One can note the presence of small particles for both experiments with an average diameter of 20 μm . and correspond to the population of fine particles (*i.e.*, non-agglomerated particles).

For the last experiment (experiment 4) with the precipitation of Timapiprant in the CTR the rotation rate of the inner cylinder was decreased down to 250 rpm. The reaction medium was left under stirring during several hours and no agglomeration occurs. After 7 hours of stirring, the experiment was aborted due to a leak of the reaction medium out of the CTR. Non-agglomeration can be attributed to the low rotation rate which was not high enough to ensure sufficient shearing forces to agglomerate the fine particles.

From these preliminary results, it has been shown that spherical agglomeration can be performed in a CTR. Even if the process parameters were not optimized, the precipitation of

Timapiprant directly in the CTR leads to spherical agglomerates at moderate rotation rates (around 500 rpm).

Secondly, the agglomeration process of safinamide developed in the previous chapter was applied with the CTR. Different conditions were tested to produce spherical agglomerates in a continuous mode.

5.2.3 Spherical agglomeration of SAFIM

5.2.3.1 Experimental conditions

Regarding the encouraging results obtained for the spherical agglomeration of Timapiprant, the process was applied to SAFIM. It was first applied as a “batch mode” in CTR and then with a continuous feeding of a SAFIM suspension in n-heptane and BL (acetonitrile), based on the conditions found in the previous chapter during the development of the classical spherical agglomeration of SAFIM.

Table 5-6 sums up the different experimental parameters investigated during this study:

Table 5-6: Different experimental conditions used to perform SAFIM spherical agglomeration in CTR.

Exp	Ω (rpm)	Suspension concentration (g/L)	Suspension flow rate (ml/min)	BL amount (ml)	BL feeding rate (ml/min)	Stirring time (h)	Ultra Turrax on the suspension (pre-treatment)	
Batch mode								
1	550	100	-	5	5	1	No	-
2	950	100	-	6	12	1	Yes (5 min lowest power)	-
Continuous mode								
3	1000	100	30	-	2	-	Yes	CTR initially filled with n-heptane
4	1000	100	30	-	4	-		
5	1000	100	30	-	4	-		
6	1000	65	30	-	4	-		
7	1000	100	30	-	4	-		

8	1000	100	20	-	4	-	CTR initially filled with SAFIM suspension
9	1000	100	20	-	4	-	
10	500	100	30	-	2	-	

To perform spherical agglomeration in batch mode, the following spherical agglomeration process was used:

- i) Suspension of SAFIM in 300 mL of n-heptane HPLC grade prepared in an external temperature-controlled crystallizer at 30 °C stirred at 200 rpm with a 3 blades stirrer with a homogenization step with an Ultra Turrax for 5 min at the lowest power if required.*
- ii) The CTR (temperature set at 30 °C; $\Delta T=0^{\circ}\text{C}$) was filled with the required amount of the prepared suspension.*
- iii) After 30 min of stirring, acetonitrile HPLC grade (BL) was added with a syringe pump in the CTR with different feeding rate.*
- iv) After a defined agglomeration time, the CTR was emptied, and the reaction medium filtered.*

The only differences between batch and continuous flow mode are: (i) the addition of the SAFIM suspension with a peristaltic pump through the main inlet of the CTR and (ii) the BL addition through the first secondary inlet with different feeding rate.

5.2.3.2 Results

5.2.3.2.1 Agglomeration in batch mode

Figure 5-8 exhibits optical microscopic pictures of SAFIM before the agglomeration process in CTR. The powder exhibits needle shape particles with a length around 100 μm and needle fragments observed due to the brittleness of the needles.

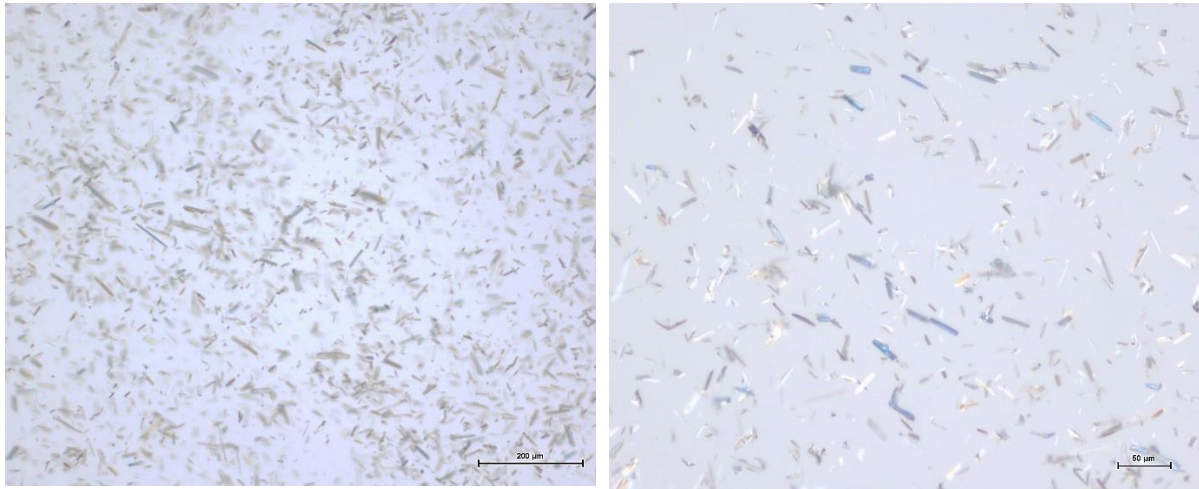
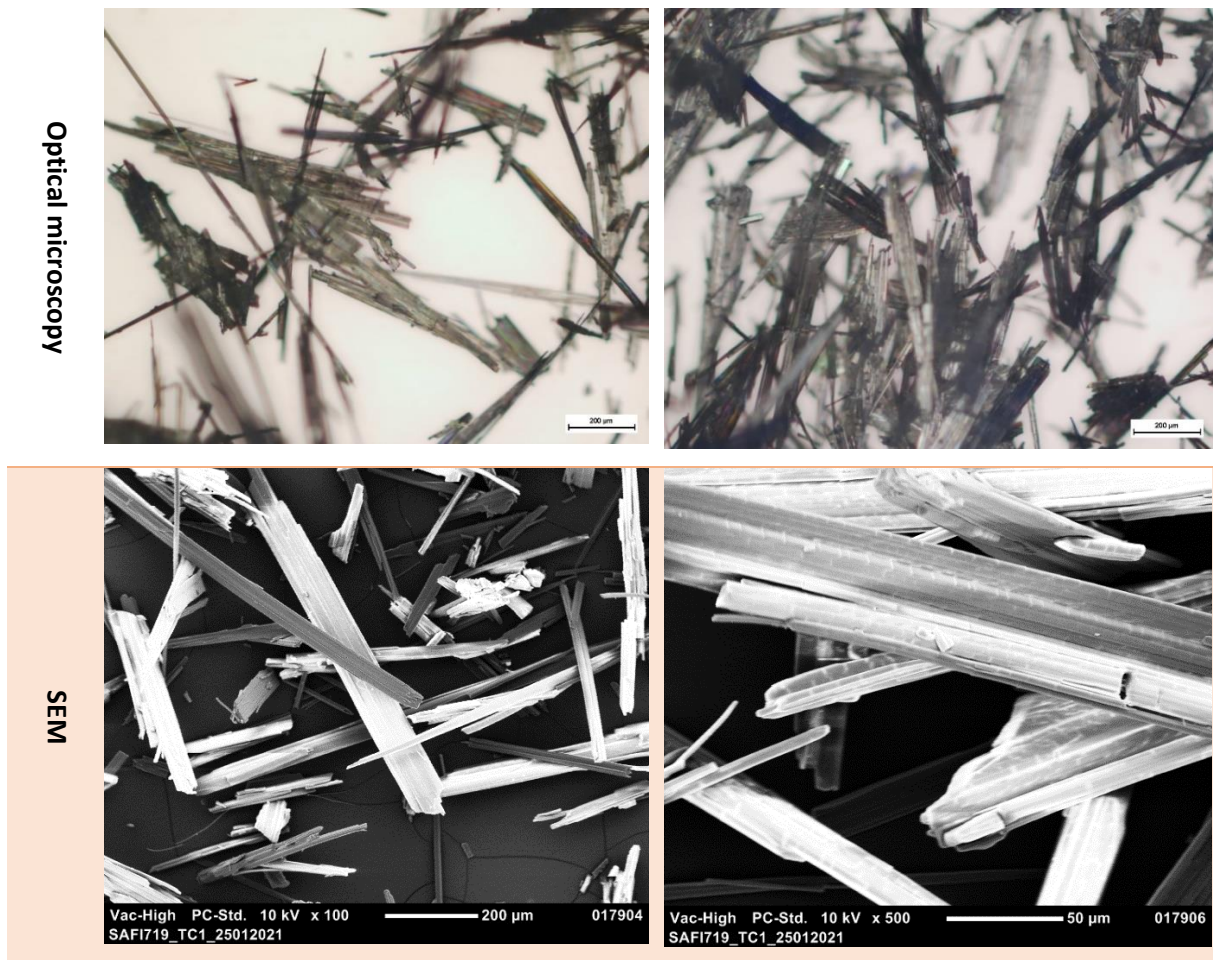


Figure 5-8: Optical Microscopy of SAFIM before agglomeration

In the conditions of experiment 1, no agglomerates were obtained as shown by microscopy of the final solids in Table 5-7.

Table 5-7: Optical microscopy and scanning electron microscopy pictures of SAFIM after agglomeration in CTR for experiment 1.



As mentioned in the previous chapter the size of the initial particle (*i.e.*, before the agglomeration) can impact the process. Then, the homogenization step with the Ultra Turrax was used

to reduce the size of the initial suspended particles. The amount of BL was also increased to 6 ml and added twice as fast, at a rate of 12 ml/h. Last, the rotation rate was set at 950 rpm.

For experiment 2, the agglomeration process was stopped 1 hour after the end of the BL addition, and the reaction medium filtered. Observations during the agglomeration process show that agglomeration seems to occur. Figure 5-9 shows respectively the optical microscopy and the scanning electronic microscopy pictures of a sample 30 min after the end of the BL addition which exhibits agglomerated particles.

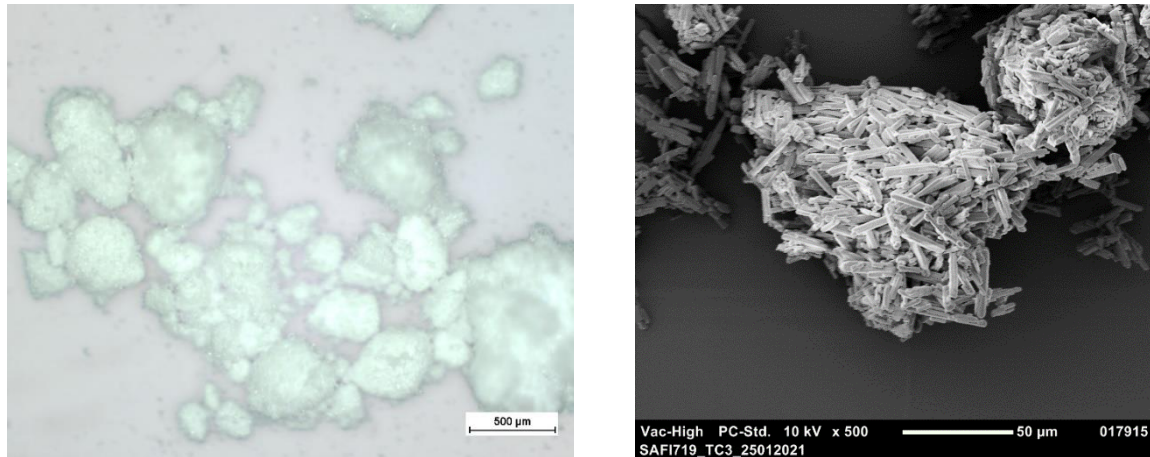


Figure 5-9: Optical microscopy (left) and scanning electronic microscopy (right) pictures of SAFIM 30 min after the end of BL addition for experiment 2 in CTR

However, after 1 hour of stirring, the reaction medium seems to be partially de-agglomerated and only few agglomerates were still observable after the filtration.

Shearing forces are sufficient to initiate the agglomeration of SAFIM. However, after 1 hour of stirring, these shearing forces seem to be responsible of the de-agglomeration. Figure 5-10 shows optical and scanning electronic pictures of the experiment 2 after the filtration process.

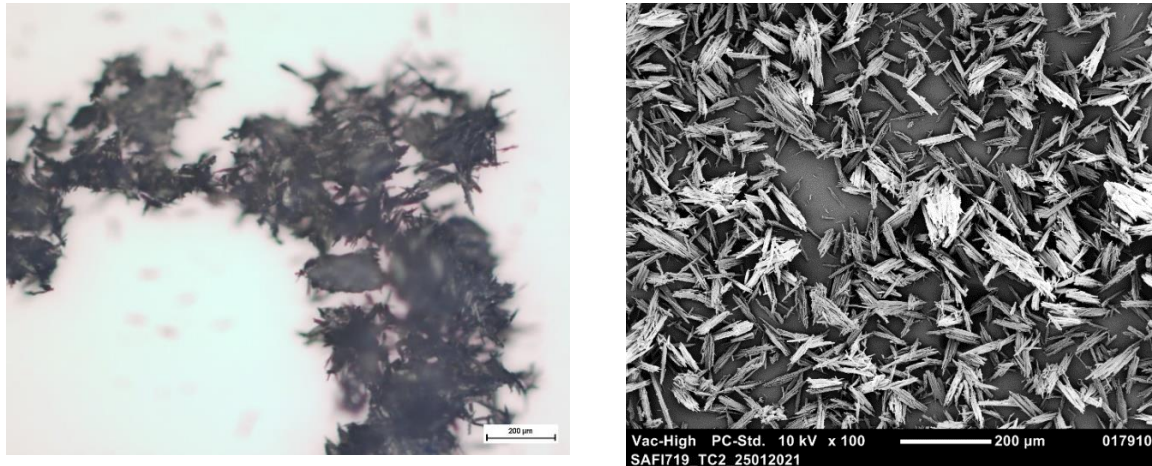


Figure 5-10: Optical microscopy (left) and scanning electronic microscopy (right) pictures of SAFIM 1 hour after the end of BL addition for experiment 2 in CTR

Conditions of the experiment 2 shows that the agglomeration of SAFIM can be performed in a CTR. Nevertheless, parameters such as rotation rate or BL feeding rate need to be optimized.

One can note that the mechanism of formation of the agglomerates for this experiment could be attributed either to spherical agglomeration or classical agglomeration of fine particles due to attractive forces (*i.e.*, Van der Waals interactions).

5.2.3.2.2 Continuous agglomeration

The most interesting feature of a CTR is the possibility to implement continuous processes through the continuous flow of a reaction medium. From experiment 3 to 10 (Table 5-6), different parameters were tested to perform the continuous spherical agglomeration of SAFIM.

To perform experiment 3 of continuous agglomeration in CTR, parameters from experiment 1 were used. Figure 5-11 shows optical microscopy pictures of the batch after 10 minutes of flow.

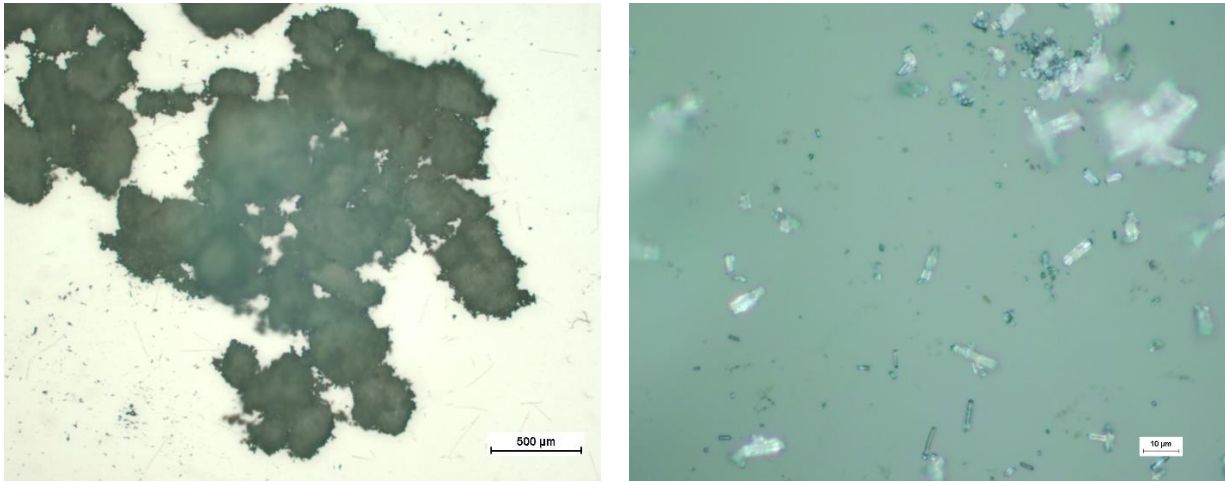


Figure 5-11: Optical microscopy pictures of SAFIM after agglomeration in CTR for experiment 3.

Only few agglomerates with poor mechanical properties (agglomerates broke when handled) and non-agglomerated particles were observed after the drying of the batch.

Different parameters were then modified to obtain spherical agglomerates (e.g., BL flow rate, suspension concentration, and suspension flow rate). However, from the experiment 4 to 8 only clogging of the reactor was observed and no solid was obtained at the reactor outlet.

As mentioned in Table 5-6, from the experiment 3 to 8 the CTR was initially filled only with n-heptane prior to initializing the suspension and BL flow rates. When looking at the clogging spot in the CTR, the accumulation of BL seems responsible of the clogging: the reaction medium exhibits a pasty behavior obtained when the amount of BL is higher than the critical amount to perform the spherical agglomeration. Then, for the experiments 9 and 10, the suspension flow rate was initiated before starting the addition of BL.

During experience 9, even if the reactor was clogged after few minutes of experiment, agglomerates were observed during sampling of the reaction medium. Figure 5-12 exhibits microscopic pictures of the observed agglomerates.

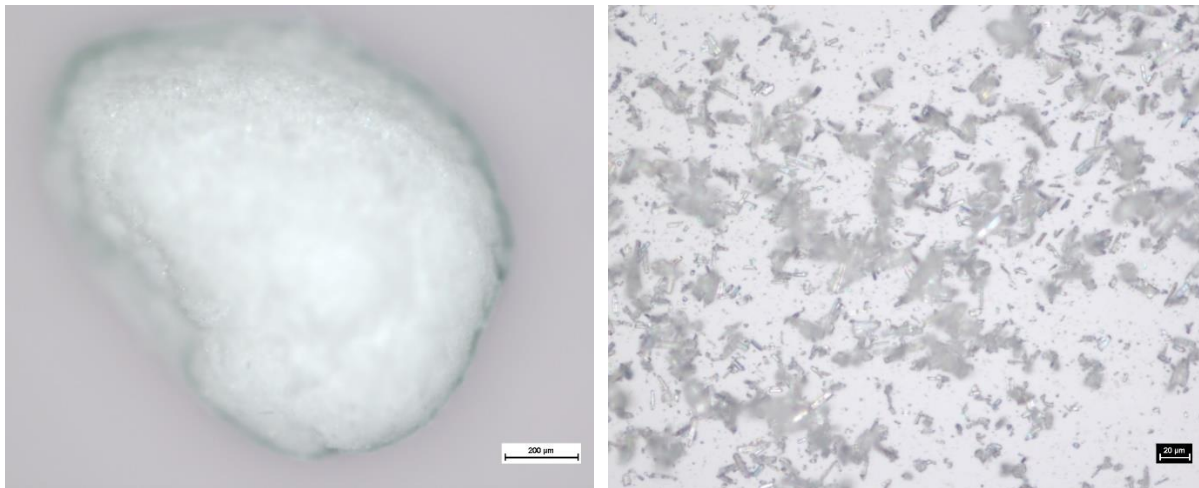


Figure 5-12: Optical microscopy pictures of experiment 9 after spherical agglomeration in CTR.

The sample was mostly composed of non-agglomerated particles. However, some agglomerates were observed in the reaction medium. These conditions seem more suitable to perform continuous spherical agglomeration in CTR if the clogging of CTR is prevented.

The clogging of CTR occurs near to the BL inlet, resulting in an accumulation of BL. Consequently, for the last experiment, in order to limit the accumulation, the BL flow rate was reduced as well as the stirring rate (experience 10).

As shown on Figure 5-13, the batch exhibits agglomerated and non-agglomerated particles during 5 minutes of stirring. Agglomerates exhibit a polydisperse PSD up to 500 µm. Then, the CTR was clogged.

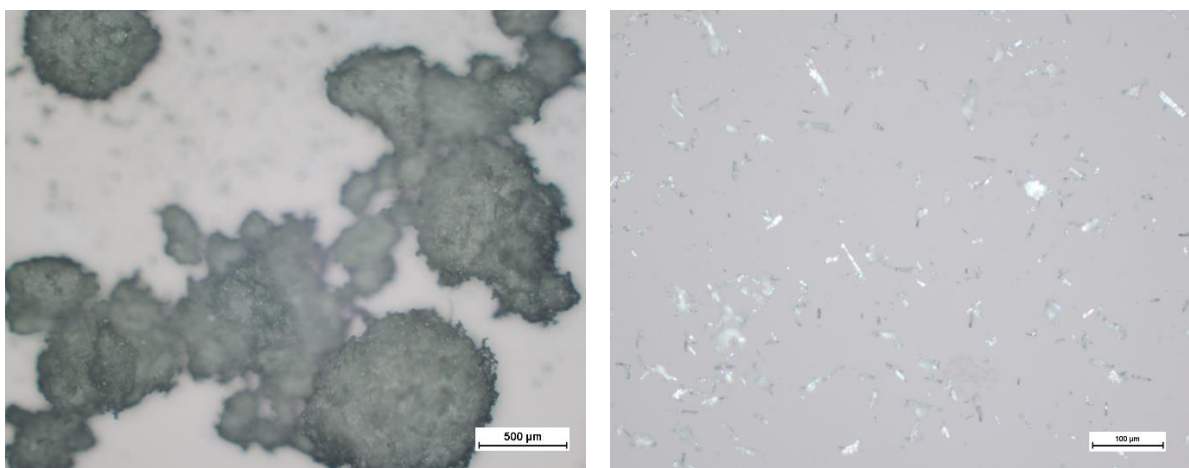


Figure 5-13: Optical microscopy pictures of experiment 10 after spherical agglomeration in CTR.

The tested conditions seem closed to the one to obtain spherical agglomerates of SAFIM. Indeed, spherical agglomerates were obtained during few minutes with an acceptable agglomerate size. However, in the continuous mode, the clogging of the CTR is the main difficulty encountered during these first attempts (even if it was delayed for the two last experiments). This behavior is not

suitable for a continuous process, and a thorough optimization must be conducted in order to obtain a spherical agglomeration thanks to the CTR process.

5.3 DISCUSSIONS AND PERSPECTIVES

This study aimed to prove the feasibility of the spherical agglomeration with the help of CTR, for a continuous process.

After these first attempts, one can say that the efficiency of this reactor for spherical agglomeration depends on the systems itself (API, solvent/Bridging Liquid). Indeed, in the case of Timapiprant the direct transposition of “classical” spherical agglomeration parameter led to the success of the use of CTR by adjusting process parameters (e.g., rotation rate of the inner, cylinder, influence of the introduction mode in the CTR). This opened the way to envisage a spherical agglomeration process with CTR on SAFIM.

Unfortunately, in SAFIM case, clogging of the device was often observed. For continuous experiments, this clogging occurred right after the introduction of the BL, whatever the BL feeding rate or rotation rate of the cylinder explored. Different explanations can be proposed:

- (i) The stagnation of the BL at the introduction inlet: due to the oiling out between n-heptane and acetonitrile, the fluid flow occurring in CTR is not able to produce a stable emulsion necessary to produce a spherical agglomeration. Acetonitrile being denser than n-heptane, it will remain at the bottom of the CTR and start to form a clog which avoid the agglomeration.
- (ii) The concentration of the feeding suspension: if the suspension concentration is too high, the shearing forces will not be sufficient to ensure the stability of the suspension. Then, the solid will settle in the reactor and provoke the clogging. However, in the case of SAFIM, before the addition of the BL the suspension was obtained at the outlet of the CTR as long as the BL introduction does not start.

Moreover, the BL is added dropwise while the SAFIM suspension is continuously fed. It means that in the suspension, there is a modulation of the BL concentration in the suspension. Concentration of BL in the suspension having an important impact on the agglomeration, it can be an explanation of the difficulties encountered to perform the spherical agglomeration. In order to smooth this phenomenon without increasing the overall concentration of BL, the inner diameter of the BL tubing can be reduced to produce smaller droplets in larger quantities. The distance between the two cylinders could also be reduced to increase the shear forces.

Spherical agglomeration seems feasible in a Couette Taylor reactor if the BL is added in the API solution and the crystallization step perform in the CTR. With more investigation of the different parameters, it might be possible to implement continuous spherical agglomeration with higher productivity than in batch production.

General conclusion

This work was dedicated to two major issues of the pharmaceutical industry: The crystalline landscape of the APIs including the relative stabilities between the phases, and the flowability of powders.

First, the behavior of the API prednisolone sesquihydrate upon dehydration was elucidated. A new solid form of prednisolone was isolated (*i.e.*, Form III) and characterized as an isomorphous desolvate of the sesquihydrate. This daughter phase shows a reversible hydration – dehydration and extensive structure similarities with the corresponding mother phase due to quasi-topotactic desolvation and resolution mechanisms. These similarities were highlighted by the self-healing of the crystal after dehydration during an annealing above the dehydration temperature. A classification of the sesquihydrate was proposed according to two different classification models: it was identified as a class 1 hydrate according to the Dehydration-Rehydration Classification System⁹³ and of Class II-C.R. according to Rouen-96 model.⁸⁹ This study is a new case depicting the possibility to obtain isomorphous desolvates through a smooth dehydration. It demonstrates also that the exploration of a unary phase diagram (polymorphism) can necessitate excursions in binary systems with solvents in order to discover new polymorphic form thanks to the management of soft desolvations.

Then, the crystalline landscape of another API: safinamide mesylate, was studied. Three crystalline phases were confirmed: two polymorphs **A1** and **A2** and a hemi-hydrate **H1**. Their behaviors and relative stabilities have been discussed:

- The enantiotropic transition **A1** ↔ **A2** is a first order transition according to Ehrenfest's classification¹⁰³ and identified as a disorder/order transition. The conversion from **A1** to **A2** involve the blockage of a SAFIM conformation with an activation energy that is calculated around 203 kJ/mol. The two conformational polymorphs exhibit similar structure parameters which supports the disorder/order transition.
- The different conditions of formation of the hemi-hydrate have highlighted the importance of controlling both crystallization and downstream parameters (e.g., solvents, temperature, RH, ...). First, the hemi-hydrate exhibits a high domain of stability during the industrial crystallization process, the amount of water and final temperature of the crystallization process unequivocally led to the formation of the hemi-hydrate. Secondly, even if the drying process of SAFIM leads to the isolation of the commercial form **A1**, a special attention must be paid to the storage parameters. Stability experiments at different RH conditions and temperature, have shown that the anhydrous phase converts into the hemi-hydrate if RH is higher than 80 %RH at 25 °C. Once it is formed the hemihydrate exhibits a high stability

(dehydration if RH < 20%). Therefore, experimental conditions are proposed to isolate **A1** and to convert **A1** into **H1** if required.

After the characterization of the different crystalline phases, the last part of this study focuses on improving the flowability of SAFIM powder.

The industrially produced SAFIM powder crystallizes as needles and exhibits poor flowability properties. Therefore, a spherical agglomeration of SAFIM was developed with two main objectives: to increase the flowability of SAFIM and to produce agglomerates of the marketed anhydrous form **A1** (marketed form by Zambon).

A challenging part of this work is the determination of the solvent system of the spherical agglomeration. Indeed, in almost all spherical agglomeration cases, an aqueous phase is involved in the solvent system. However, in the case of SAFIM, the presence of water leads to the formation of the undesired **H1** form. n-Heptane and acetonitrile were identified as the two immiscible solvents (dispersion solvent and bridging liquid, respectively) able to conduct the spherical agglomeration of SAFIM. A set of experimental parameters were proposed to successfully implement the spherical agglomeration. Even if some of the experimental parameters were set at the beginning of the study (e.g., crystallizer geometry and stirring geometry, introduction setup of the BL), four of them were identified as key parameters and attempted to be optimized through a design of experiment (agglomeration temperature, stirring rate, amount of BL and slurry concentration). By this mean, the influence of every individual parameter was not conclusive, but a set of conditions was found to produce agglomerates of SAFIM with acceptable properties: an average agglomerate size around 750 μm , good flowability properties and the isolation of the targeted anhydrous form with an acceptable amount of residual solvents (acetonitrile and n-heptane) according to the European Pharmacopoeia standards.

Finally, the preliminary results of the spherical agglomeration conducted with a Couette Taylor reactor were presented. Agglomeration tests were carried out on two different API: Timapiprant and SAFIM. Significant results were obtained for the agglomeration of Timapiprant in batch mode (final agglomerates with an average diameter of 220 μm). However, the continuous spherical agglomeration of SAFIM in the CTR seems more challenging. Indeed, most of the experiments were aborted after few minutes due to the clogging of the reactor attributed to an accumulation of BL in the reactor. The process needs to be further studied in terms of process engineering to solve this problem.

The spherical agglomeration process is often described in the literature by the different experimental parameters to tune in order to obtain the targeted particle properties (e.g., particle size, flowability, shape, ...) and to elucidate the formation mechanisms of the agglomerates from the

process engineering point of view. Therefore, this work brings a new approach of the process thanks to the phase equilibria. With this approach, we proposed an agglomeration process to obtain the "classical" target properties (flowability properties in particular) but also to isolate the powder in the required crystalline form. From a pharmaceutical point of view, the implementation of this double objective (*i.e.*, mastering of flowability and crystalline phase properties) during a crystallization/granulation process could be implement to other potential systems. This original approach could be of importance considering the actual standards and the evolution of the manufacturing processes (*i.e.*, Quality by Design).

REFERENCES

- (1) Hancock, B. C.; Zografi, G. Characteristics and Significance of the Amorphous State in Pharmaceutical Systems. *J. Pharm. Sci.* **1997**, *86* (1), 1–12.
- (2) Ediger, M. D.; Angell, C. A.; Nagel, S. R. Supercooled Liquids and Glasses. 13.
- (3) Tschoegl, N. W. *Fundamentals of Equilibrium and Steady-State Thermodynamics*; Elsevier, 2000.
- (4) Porter, D. A.; Easterling, K. E.; Easterling, K. E. *Phase Transformations in Metals and Alloys (Revised Reprint)*, 3rd ed.; CRC Press: Boca Raton, 2009.
<https://doi.org/10.1201/9781439883570>.
- (5) Jacobs, M. H. G.; Oonk, H. A. J. *Equilibrium Between Phases of Matter*; Springer Netherlands: Dordrecht, 2012. <https://doi.org/10.1007/978-94-007-1948-4>.
- (6) Ostwald, W. Studien Über Die Bildung Und Umwandlung Fester Körper; 1897; Vol. 1, pp 289–330.
- (7) Nývlt, J. The Ostwald Rule of Stages. *Cryst. Res. Technol.* **1995**, *30* (4), 443–449.
- (8) Gibbs, J. W. *On the Equilibrium of Heterogeneous Substances*, Transactions of the Connecticut Academy of Arts and Sciences.; 1874; Vol. 3.
- (9) McCrone, W. C. Polymorphism. In *Physics and Chemistry of the Organic Solid State*; 1965; Vol. 2, pp 725–767.
- (10) Hilfiker, R.; von Rauner, M.; Blatter, F. Relevance of Solid-State Properties for Pharmaceutical Products. In *Polymorphism : in the Pharmaceutical Industry*; 206AD; pp 1–19.
- (11) Threlfall, T. L. Analysis of Organic Polymorphs. A Review. *The Analyst* **1995**, *120* (10), 2435.
<https://doi.org/10.1039/an9952002435>.
- (12) Lohani, S.; Grant, D. J. W. Thermodynamics of Polymorphs. In *Polymorphism*; Hilfiker, R., Ed.; Wiley-VCH Verlag GmbH & Co. KGaA: Weinheim, FRG, 2006; pp 21–42.
<https://doi.org/10.1002/3527607889.ch2>.
- (13) Burger, A.; Ramberger, R. On the Polymorphism of Pharmaceuticals and Other Molecular Crystals. I. *Mikrochim. Acta* **1979**, *72* (3–4), 259–271. <https://doi.org/10.1007/BF01197379>.
- (14) Ricci, J. E. *The Phase Rule and Heterogeneous Equilibrium*, Dover Publications, INC.; Dover Publications, INC.: New York, 1966.
- (15) Zhao, J.-C. *Methods for Phase Diagram Determination*; Elsevier, 2011.
- (16) Legendre, B.; Querniard, F. Glossary for Binary Phase Diagram Reactions. *J. Phase Equilibria Diffus.* **2014**, *35* (1), 11–14. <https://doi.org/10.1007/s11669-013-0266-6>.
- (17) Bennett, L. H.; Carter, G. C. Enhanced Lever Rule for High-Precision Phase Diagram Determination. *Metall. Trans.* **1971**, *2*, 3079–3081.
- (18) Hartshorn, R. M.; Hellwich, K.-H.; Yerin, A.; Damhus, T.; Hutton, A. T. Brief Guide to the Nomenclature of Inorganic Chemistry. *Pure Appl. Chem.* **2015**, *87* (9–10), 1039–1049.
<https://doi.org/10.1515/pac-2014-0718>.
- (19) Schultheiss, N.; Henck, J.-O. Role of Co-Crystals in the Pharmaceutical Development Continuum. In *Pharmaceutical Salts and Co-crystals*; Wouters, J., Quéré, L., Eds.; Royal Society of Chemistry: Cambridge, 2011; pp 110–127. <https://doi.org/10.1039/9781849733502-00110>.
- (20) Halebian, J. K. Characterization of Habits and Crystalline Modification of Solids and Their Pharmaceutical Applications. *J. Pharm. Sci.* **1975**, *64* (8), 1269–1288.
<https://doi.org/10.1002/jps.2600640805>.
- (21) Griesser, U. J. The Importance of Solvates. In *Polymorphism*; Hilfiker, R., Ed.; Wiley-VCH Verlag GmbH & Co. KGaA: Weinheim, FRG, 2006; pp 211–233.
<https://doi.org/10.1002/3527607889.ch8>.
- (22) Reutzel-Edens, S. M.; Newman, A. W. Physical Characterization of Hygroscopicity in Pharmaceutical Solids. In *Polymorphism*; Hilfiker, R., Ed.; Wiley-VCH Verlag GmbH & Co. KGaA: Weinheim, FRG, 2006; pp 235–258. <https://doi.org/10.1002/3527607889.ch9>.

-
- (23) Authelin, J.-R. Thermodynamics of Non-Stoichiometric Pharmaceutical Hydrates. *Int. J. Pharm.* **2005**, *303* (1–2), 37–53. <https://doi.org/10.1016/j.ijpharm.2005.07.007>.
- (24) de Romé de l'Isle, J.-B. L. *Cristallographie*, IMPRIMERIE DE MONSIEUR, Paris.; Paris, 1783.
- (25) Haüy, R.-J. *Traité de Cristallographie*, Bachelier et Huzard, Paris.; 1822; Vol. 1.
- (26) Miller, W. H. *A Treatise on Crystallography*; J. & J. J. Deighton Trinity Street; Cambridge, 1839.
- (27) Dunitz, J. D. *X-Ray Analysis and Structure of Organic Molecules*, Verlag Helvetica Chimica Acta.; Switzerland, 1995.
- (28) Bravais, A. *Etudes Cristallographiques*, Gauthier-Villars, Paris.; 1866.
- (29) *International Tables for Crystallography. A: Space-Group Symmetry*, Theo Hahn.; Springer: Dordrecht, 2005.
- (30) Coquerel, G. Crystallization of Molecular Systems from Solution: Phase Diagrams, Supersaturation and Other Basic Concepts. *Chem Soc Rev* **2014**, *43* (7), 2286–2300. <https://doi.org/10.1039/C3CS60359H>.
- (31) *Nucleation Theory and Applications*; Schmelzer, J. W. P., Schmelzer, J., Eds.; WILEY-VCH-Verl: Weinheim, 2005.
- (32) Kashchiev, D.; van Rosmalen, G. M. Review: Nucleation in Solutions Revisited. *Cryst. Res. Technol.* **2003**, *38* (78), 555–574. <https://doi.org/10.1002/crat.200310070>.
- (33) Mullin, J. W. *Crystallization*, Elsevier.; Oxford, 2001; Vol. 4th.
- (34) *Industrial Crystallization*; Mullin, J. W., Ed.; Springer US: Boston, MA, 1976. <https://doi.org/10.1007/978-1-4615-7258-9>.
- (35) Liu, X. Y.; Maiwa, K.; Tsukamoto, K. Heterogeneous Two-Dimensional Nucleation and Growth Kinetics. *J. Chem. Phys.* **1997**, *106* (5), 1870–1879. <https://doi.org/10.1063/1.473325>.
- (36) Voorhees, P. W. The Theory of Ostwald Ripening. *J. Stat. Phys.* **1985**, *38* (1–2), 231–252. <https://doi.org/10.1007/BF01017860>.
- (37) Kawashima, Y.; Capes, C. E. Further Studies of the Kinetics of Spherical Agglomeration in a Stirred Vessel. *Powder Technol.* **1976**, *13*, 279–288.
- (38) Smith, H. M.; Puddington, I. E. Spherical Agglomeration of Barium Sulfate. *Can. J. Chem.* **1960**, *38*, 1911–1916.
- (39) Sirianni, A. F.; Capes, C. E.; Puddington, J. E. Recent Experience with the Spherical Agglomeration Process. *Can. J. Chem. Eng.* **1969**, *47* (2), 166–170.
- (40) Sutherland, J. P. The Agglomeration of Aqueous Suspensions of Graphite. *Can. J. Chem. Eng.* **1962**, *40* (6), 268–272. <https://doi.org/10.1002/cjce.5450400609>.
- (41) Kawashima, Y.; Niwa, T.; Takeuchi, H.; Hino, T.; Itoh, Y. Characterization of Polymorphs of Tranilast Anhydrate and Tranilast Monohydrate When Crystallized by Two Solvent Change Spherical Crystallization Techniques. *J. Pharm. Sci.* **1991**, *80* (5), 472–478.
- (42) Kawashima, Y.; Okumura, M.; Takenaka, H. Spherical Crystallization: Spherical Agglomeration of Salicylic Acid Crystals During Crystallization. *Science* **1982**, *216*, 1127–1128.
- (43) Müller, M.; Löffler, F. Development of Agglomerates Size and Structure During Spherical Agglomeration in Suspension. *Part. Part. Syst. Charact.* **1996**, *13*, 322–326.
- (44) Szabó-Révész, P.; Hasznos-Nezdei, M.; Farkas, B.; Göczó, H.; Pintye-Hódi, K.; Erős, I. Crystal Growth of Drug Materials by Spherical Crystallization. *J. Cryst. Growth* **2002**, *237* (239), 2240–2245.
- (45) Stock, D. I. Micro-Spherical Aggregation of Barium Sulphate. *Nature* **1952**, *170* (4323), 423–423. <https://doi.org/10.1038/170423a0>.
- (46) Kawashima, Y.; Furukawa, K.; Takenaka, H. The Physicochemical Parameters Determining the Size of Agglomerate Prepared by the Wet Spherical Agglomeration Technique. *Powder Technol.* **1981**, *30*, 211–216.
- (47) Fincher, J. H. Particle Size of Drugs and Its Relationship to Absorption and Activity. *J. Pharm. Sci.* **1968**, *57* (11), 1825–1835. <https://doi.org/10.1002/jps.2600571102>.
- (48) Kovačič, B.; Vrečer, F.; Planinšek, O. Spherical Crystallization of Drugs. *Acta Pharm.* **2012**, *62* (1), 1–14. <https://doi.org/10.2478/v10007-012-0010-5>.
-

-
- (49) Yadav, A. V.; Bhagat, N.; Khutale, R. A. An Overview of Optimization of Spherical Crystallisation Process. *Int. J. Sci. Nanotechnol.* **2013**, *6* (4), 2203–2209.
- (50) Saini, S. Spherical Crystallization: An Overview. *Int. J. Drug Deliv. Technol.* **2017**, *4* (4). <https://doi.org/10.25258/ijddt.v4i4.8862>.
- (51) Ueda, M.; Nakamura, Y.; Makita, H.; Imasato, Y.; Kawashima, Y. Particle Design by Spherical Crystallization Techniques. I. Principle of Ammonia Diffusion. *Chem. Pharm. Bull. (Tokyo)* **1990**, *38* (9), 2537–2541.
- (52) Puechagut, H. G.; Bianchotti, J.; Chiale, C. A. Preparation of Norfloxacin Spherical Agglomerates Using the Ammonia Diffusion System. **1998**, *87* (4), 5.
- (53) Kawashima, Y.; Niwa, T.; Handa, T.; Takeuchi, H.; Iwamoto, T.; Itoh, K. Preparation of Controlled-Release Microspheres of Ibuprofen With Acrylic Polymers by a Novel Quasi-Emulsion Solvent Diffusion Method. *J. Pharm. Sci.* **1989**, *78* (1), 68–72. <https://doi.org/10.1002/jps.2600780118>.
- (54) Chadwick, K.; Davey, R. J.; Mughal, R.; Marziano, I. Crystallisation from Water-in-Oil Emulsions As a Route to Spherical Particulates: Glycine and the Hydrochloride Salts of Glutamic Acid and Ephedrine. *Org. Process Res. Dev.* **2009**, *13* (6), 1284–1290. <https://doi.org/10.1021/op900123n>.
- (55) Espitalier, F.; Biscans, B.; Laguérie, C. Particle Design Part A: Nucleation Kinetics of Ketoprofen. *Chem. Eng. J.* **1997**, *68* (2–3), 95–102. [https://doi.org/10.1016/S1385-8947\(97\)00089-2](https://doi.org/10.1016/S1385-8947(97)00089-2).
- (56) Kawashima, Y.; Imai, M.; Takeuchi, H.; Yamamoto, H.; Kamiya, K.; Hino, T. Improved Flowability and Compactibility of Spherically Agglomerated Crystals of Ascorbic Acid for Direct Tableting Designed by Spherical Crystallization Process. *Powder Technol.* **2003**, *130* (1–3), 283–289. [https://doi.org/10.1016/S0032-5910\(02\)00206-1](https://doi.org/10.1016/S0032-5910(02)00206-1).
- (57) Nocent, M.; Bertocchi, L.; Espitalier, F.; Baron, M.; Couarraze, G. Definition of a Solvent System for Spherical Crystallization of Salbutamol Sulfate by Quasi-Emulsion Solvent Diffusion (QESD) Method. *J. Pharm. Sci.* **2001**, *90* (10), 1620–1627. <https://doi.org/10.1002/jps.1112>.
- (58) Mahanty, S.; Sruti, J.; Niranjana Patra, Ch.; Bhanaji, R. Particle Design of Drugs by Spherical Crystallization Techniques. *International J. Pharmaceutical Sci. Nanotechnol.* **2010**, *3* (2), 912–918.
- (59) Huang, A. Y.; Berg, J. C. Gelation of Liquid Bridges in Spherical Agglomeration. *Colloids Surf. Physicochem. Eng. Asp.* **2003**, *215* (1–3), 241–252. [https://doi.org/10.1016/S0927-7757\(02\)00488-0](https://doi.org/10.1016/S0927-7757(02)00488-0).
- (60) Kawashima, Y.; Okumura, M.; Takenaka, H. The Effects of Temperature on the Spherical Crystallization of Salicylic Acid. *Powder Technol.* **1984**, *39*, 41–47.
- (61) Chow, A. H. L.; Leung, M. W. M. A Study of the Mechanisms of Wet Spherical Agglomeration of Pharmaceutical Powders. *Drug Dev. Ind. Pharm.* **1996**, *22* (4), 357–371.
- (62) Iveson, S. M.; Litster, J. D.; Hapgoog, K.; Ennis, B. J. Nucleation, Growth and Breakage Phenomena in Agitated Wet Granulation Processes: A Review. *Powder Technol.* **2001**, *117*, 3–39.
- (63) Amaro-González, D.; Biscans, B. Spherical Agglomeration during Crystallization of an Active Pharmaceutical Ingredient. *Powder Technol.* **2002**, *128*, 188–194.
- (64) Subero-Couroyer, C.; Mangin, D.; Rivoire, A.; Blandin, A. F.; Klein, J. P. Agglomeration in Suspension of Salicylic Acid Fine Particles: Analysis of the Wetting Period and Effect of the Binder Injection Mode on the Final Agglomerate Size. *Powder Technol.* **2006**, *161* (2), 98–109. <https://doi.org/10.1016/j.powtec.2005.08.014>.
- (65) Madec, L.; Muhr, H.; Plasari, E. Development of New Methods to Accelerate and Improve the Agglomeration of Submicron Particles by Binding Liquids. *Powder Technol.* **2002**, *128* (2–3), 236–241. [https://doi.org/10.1016/S0032-5910\(02\)00187-0](https://doi.org/10.1016/S0032-5910(02)00187-0).
- (66) Thati, J.; Rasmuson, Å. C. On the Mechanisms of Formation of Spherical Agglomerates. *Eur. J. Pharm. Sci.* **2011**, *42* (4), 365–379. <https://doi.org/10.1016/j.ejps.2011.01.001>.
-

- (67) Blandin, A. F.; Mangin, D.; Subero-Couroyer, C.; Rivoire, A.; Klein, J. P.; Bossoutrot, J. M. Modelling of Agglomeration in Suspension: Application to Salicylic Acid Microparticles. *Powder Technol.* **2005**, *156* (1), 19–33. <https://doi.org/10.1016/j.powtec.2005.05.049>.
- (68) Pitt, K.; Peña, R.; Tew, J. D.; Pal, K.; Smith, R.; Nagy, Z. K.; Litster, J. D. Particle Design via Spherical Agglomeration: A Critical Review of Controlling Parameters, Rate Processes and Modelling. *Powder Technol.* **2018**, *326*, 327–343. <https://doi.org/10.1016/j.powtec.2017.11.052>.
- (69) Morishima, K.; Kawashima, Y.; Takeuchi, H.; Niwa, T.; Hino, T.; Kawashima, Y. Tableting Properties of Bucillamine Agglomerates Prepared by the Spherical Crystallization Technique. *International J. Pharmaceutics* **1994**, *105*, 11–18.
- (70) Blandin, A. F.; Mangin, D.; Rivoire, A.; Klein, J. P.; Bossoutrot, J. M. Agglomeration in Suspension of Salicylic Acid Fine Particles: Influence of Some Process Parameters on Kinetics and Agglomerate Final Size. *Powder Technol.* **2003**, *130*, 316–323.
- (71) Thati, J.; Rasmuson, Å. C. Particle Engineering of Benzoic Acid by Spherical Agglomeration. *Eur. J. Pharm. Sci.* **2012**, *45* (5), 657–667. <https://doi.org/10.1016/j.ejps.2012.01.006>.
- (72) Cheng, X.; Li, F.; Luo, L.; Ding, Z.; Zeng, L.; Mao, Y.; Huang, X.; Hao, H. On the Selection of Wetting Liquid for Spherical Agglomeration of Cefotaxime Sodium. *Powder Technol.* **2020**, *363*, 593–601. <https://doi.org/10.1016/j.powtec.2019.12.002>.
- (73) Good, R. J.; van Oss, C. J. The Modern Theory of Contact Angles and the Hydrogen Bond Components of Surface Energies. In *Modern Approaches to Wettability Theory and Applications*; Springer Science: Boston, MA, 1992.
- (74) Washburn, E. W. The Dynamics of Capillary Flow. *Phys. Rev.* **1921**, *17* (3), 273–283. <https://doi.org/10.1103/PhysRev.17.273>.
- (75) Petela, R. Prediction of the Product Size in the Agglomeration of Coal Particles in a Water-Oil Emulsion. *Fuel* **1991**, *70* (4), 509–517. [https://doi.org/10.1016/0016-2361\(91\)90029-A](https://doi.org/10.1016/0016-2361(91)90029-A).
- (76) Katta, J.; Rasmuson, A. Spherical Crystallization of Benzoic Acid. *Int. J. Pharm.* **2008**, *348* (1–2), 61–69. <https://doi.org/10.1016/j.ijpharm.2007.07.006>.
- (77) Wu, S.; Li, K.; Zhang, T.; Gong, J. Size Control of Atorvastatin Calcium Particles Based on Spherical Agglomeration. *Chem. Eng. Technol.* **2015**, *38* (6), 1081–1087. <https://doi.org/10.1002/ceat.201400721>.
- (78) Maghsoodi, M. Effect of Process Variables on Physicomechanical Properties of the Agglomerates Obtained by Spherical Crystallization Technique. *Pharm. Dev. Technol.* **2011**, *16* (5), 474–482. <https://doi.org/10.3109/10837450.2010.492218>.
- (79) Madec, L.; Falk, L.; Plasari, E. Modelling of the Agglomeration in Suspension Process with Multidimensional Kernels. *Powder Technol.* **2003**, *130* (1–3), 147–153. [https://doi.org/10.1016/S0032-5910\(02\)00258-9](https://doi.org/10.1016/S0032-5910(02)00258-9).
- (80) Kuhnert-Brandstätter, M.; Gasser, P. Solvates and Polymorphic Modifications of Steroid Hormones. I. *Microchem. J.* **1971**, *16* (3), 419–428. [https://doi.org/10.1016/0026-265X\(71\)90024-5](https://doi.org/10.1016/0026-265X(71)90024-5).
- (81) Suitchmezian, V.; Jess, I.; Sehnert, J.; Seyfarth, L.; Senker, J.; Näther, C. Structural, Thermodynamic, and Kinetic Aspects of the Polymorphism and Pseudopolymorphism of Prednisolone (11,17 α ,21-Trihydroxy-1,4-Pregnadien-3,20-Dion). *Cryst. Growth Des.* **2008**, *8* (1), 98–107. <https://doi.org/10.1021/cg700866f>.
- (82) Corvis, Y.; Négrier, P.; Soulestin, J.; Espeau, P. New Melting Data of the Two Polymorphs of Prednisolone. *J. Phys. Chem. B* **2016**, *120* (41), 10839–10843. <https://doi.org/10.1021/acs.jpcc.6b07349>.
- (83) Bauer, M.; Lacoulonche, F.; Céolin, R.; Barrio, M.; Khichane, I.; Robert, B.; Tamarit, J.-L.; Rietveld, I. B. On the Dimorphism of Prednisolone: The Topological Pressure-Temperature Phase Diagram Involving Forms I and II. *Int. J. Pharm.* **2022**, *624*, 122047. <https://doi.org/10.1016/j.ijpharm.2022.122047>.
- (84) Flynn, J. H. The Isoconversional Method for Determination of Energy of Activation at Constant Heating Rates, Corrections for the Doyle Approximation. *J. Therm. Anal.* **1983**, *27*, 95–102.

-
- (85) Kissinger, H. E. Variation of Peak Temperature With Heating Rate in Differential Thermal Analysis. *J. Res. Natl. Bur. Stand.* **1956**, *57* (4), 227–221.
- (86) Vyazovkin, S. Kissinger Method in Kinetics of Materials: Things to Beware and Be Aware Of. *Molecules* **2020**, *25* (12), 2813. <https://doi.org/10.3390/molecules25122813>.
- (87) Stephenson, G. A.; Groleau, E. G.; Kleemann, R. L.; Xu, W.; Rigsbee, D. R. Formation of Isomorphic Desolvates: Creating a Molecular Vacuum. *J. Pharm. Sci.* **1998**, *87* (5), 536–542. <https://doi.org/10.1021/js970449z>.
- (88) Fours, B.; Cartigny, Y.; Petit, S.; Coquerel, G. Formation of New Polymorphs without Any Nucleation Step. Desolvation of the Rimonabant Monohydrate: Directional Crystallisation Concomitant to Smooth Dehydration. *Faraday Discuss.* **2015**, *179*, 475–488. <https://doi.org/10.1039/C4FD00222A>.
- (89) Petit, S.; Coquerel, G. Mechanism of Several Solid–Solid Transformations between Dihydrated and Anhydrous Copper(II) 8-Hydroxyquinolinates. Proposition for a Unified Model for the Dehydration of Molecular Crystals. *Chem. Mater.* **1996**, *8* (9), 2247–2258. <https://doi.org/10.1021/cm9600438>.
- (90) Brittain, H. G.; Morris, K. R.; Boerrigter, S. X. M. Structural Aspects of Solvatomorphic Systems. In *Polymorphism in Pharmaceutical Solids, Second Edition; Drugs and the Pharmaceutical Sciences*; 1999; Vol. 192, pp 233–281.
- (91) Mimura, H.; Kitamura, S.; Kitagawa, T.; Kohda, S. Characterization of the Non-Stoichiometric and Isomorphic Hydration and Solvation in FK041 Clathrate. *Colloids Surf. B Biointerfaces* **2002**, *26* (4), 397–406. [https://doi.org/10.1016/S0927-7765\(02\)00026-7](https://doi.org/10.1016/S0927-7765(02)00026-7).
- (92) Galwey, A. K. Structure and Order in Thermal Dehydrations of Crystalline Solids. *Thermochim. Acta* **2000**, *355* (1–2), 181–238. [https://doi.org/10.1016/S0040-6031\(00\)00448-2](https://doi.org/10.1016/S0040-6031(00)00448-2).
- (93) Takahashi, M.; Uekusa, H. Dehydration and Rehydration Mechanisms of Pharmaceutical Crystals: Classification Of Hydrates by Activation Energy. *J. Pharm. Sci.* **2022**, *111* (3), 618–627. <https://doi.org/10.1016/j.xphs.2021.10.033>.
- (94) Schlueter, D.; Saal, C.; Kuehn, C.; Schlueter, T. Novel Polymorphic Forms of (S)-2-[4-(3-Fluoro-Benzyloxy)-Benzylamino]-Propionamide Mesylate Salt and Processes of Manufacturing Thereof. patent WO 2011047767 A1, April 28, 2011.
- (95) Pawlak, T.; Oszejca, M.; Szczesio, M.; Potrzebowski, M. J. Solid-State Study of the Structure, Dynamics, and Thermal Processes of Safinamide Mesylate—A New Generation Drug for the Treatment of Neurodegenerative Diseases. *Mol. Pharm.* **2022**, *19* (1), 287–302. <https://doi.org/10.1021/acs.molpharmaceut.1c00779>.
- (96) Coquerel, G. The ‘Structural Purity’ of Molecular Solids—An Elusive Concept? *Chem. Eng. Process. Process Intensif.* **2006**, *45* (10), 857–862. <https://doi.org/10.1016/j.cep.2005.10.011>.
- (97) Aguiar, A. J.; Krc, J.; Kinkel, A. W.; Samyn, J. C. Effect of Polymorphism on the Absorption of Chloramphenicol from Chloramphenicol Palmitate. *J. Pharm. Sci.* **1967**, *56* (7), 847–853. <https://doi.org/10.1002/jps.2600560712>.
- (98) Pandit, J. K.; Gupta, S. K.; Gode, K. D.; Mishra, B. Effect of Crystal Form on the Oral Absorption of Phenylbutazone. *Int. J. Pharm.* **1984**, *21* (1), 129–132. [https://doi.org/10.1016/0378-5173\(84\)90210-2](https://doi.org/10.1016/0378-5173(84)90210-2).
- (99) Matsuda, Y.; Tatsumi, E. Physicochemical Characterization of Furosemide Modifications. *Int. J. Pharmaceutics* **1990**, *60*, 11–26.
- (100) Viscomi, G. C.; Campana, M.; Barbanti, M.; Grepioni, F.; Polito, M.; Confortini, D.; Rosini, G.; Righi, P.; Cannata, V.; Braga, D. Crystal Forms of Rifaximin and Their Effect on Pharmaceutical Properties. *CrystEngComm* **2008**, *10* (8), 1074. <https://doi.org/10.1039/b717887e>.
- (101) Cruz-Cabeza, A. J.; Bernstein, J. Conformational Polymorphism. *Chem. Rev.* **2014**, *114* (4), 2170–2191. <https://doi.org/10.1021/cr400249d>.
- (102) Buerger, M. J. *Phase Transformations in Solids*, Wiley.; New York, 1951.
- (103) Ehrenfest, P. Phasenumwandlungen Im Ueblichen Und Erweiterten Sinn, Classifiziert Nach Dem Entsprechenden Singularitaeten Des Thermodynamischen Potentials. *Verh. K. Akad. Van Wet. Amst.* **1933**, *75b* (36), 153–157.
-

-
- (104) Otsuka, M.; Onoe, M.; Matsuda, Y. Physicochemical Stability of Phenobarbital Polymorphs at Various Levels of Humidity and Temperature. *Pharm. Res.* **1993**, *10* (4), 577–582.
- (105) Clevers, S.; Simon, F.; Sanselme, M.; Dupray, V.; Coquerel, G. Monotropic Transition Mechanism of *m*-Hydroxybenzoic Acid Investigated by Temperature-Resolved Second Harmonic Generation. *Cryst. Growth Des.* **2013**, *13* (8), 3697–3704. <https://doi.org/10.1021/cg400712s>.
- (106) Jackson, W. M.; Drury, J. S. Miscibility of Organic Solvent Pairs. *Industrial Eng. Chem.* **1959**, *51* (12), 1491–1493.
- (107) Chen, H.; Wang, C.; Sun, C. C. Profoundly Improved Plasticity and Tableability of Griseofulvin by in Situ Solvation and Desolvation during Spherical Crystallization. *Cryst. Growth Des.* **2019**, *19* (4), 2350–2357. <https://doi.org/10.1021/acs.cgd.9b00053>.
- (108) Kawashima, Y.; Cui, F.; Takeuchi, H.; Niwa, T.; Hino, T.; Kiuchi, K. Improved Static Compression Behaviors and Tablettabilities of Spherically Agglomerated Crystals Produced by the Spherical Crystallization Technique with a Two-Solvent System. *Pharm. Res.* **1995**, *12* (7), 1040–1044.
- (109) Usha, A. N.; Mutalik, S.; Reddy, M. S.; Ranjith, A. K.; Kushtagi, P.; Udupa, N. Preparation and, in Vitro, Preclinical and Clinical Studies of Aceclofenac Spherical Agglomerates. *Eur. J. Pharm. Biopharm.* **2008**, *70* (2), 674–683. <https://doi.org/10.1016/j.ejpb.2008.06.010>.
- (110) Orlewski, P. M.; Ahn, B.; Mazzotti, M. Tuning the Particle Sizes in Spherical Agglomeration. *Cryst. Growth Des.* **2018**, *18* (10), 6257–6265. <https://doi.org/10.1021/acs.cgd.8b01134>.
- (111) Zhang, H.; Chen, Y.; Wang, J.; Gong, J. Investigation on the Spherical Crystallization Process of Cefotaxime Sodium. *Ind. Eng. Chem. Res.* **2010**, *49* (3), 1402–1411. <https://doi.org/10.1021/ie901001c>.
- (112) Gupta, V.; Mutalik, S.; Patel, M.; Jani, G. Spherical Crystals of Celecoxib to Improve Solubility, Dissolution Rate and Micromeritic Properties. *Acta Pharm.* **2007**, *57* (2), 173–184. <https://doi.org/10.2478/v10007-007-0014-8>.
- (113) Jitkar, S.; Thipparaboina, R.; Chavan, R. B.; Shastri, N. R. Spherical Agglomeration of Platy Crystals: Curious Case of Etodolac. *Cryst. Growth Des.* **2016**, *16* (7), 4034–4042. <https://doi.org/10.1021/acs.cgd.6b00563>.
- (114) Martino, P. D.; Barthélémy, C.; Piva, F.; Joiris, E.; Palmieri, G. F.; Martelli, S. Improved Dissolution Behavior of Fenbufen by Spherical Crystallization. *Drug Dev. Ind. Pharm.* **1999**, *25* (10), 1073–1081. <https://doi.org/10.1081/DDC-100102272>.
- (115) Parthasarathi, K. K.; Mudit, D. PREPARATION AND CHARACTERIZATION OF SPHERICAL AGGLOMERATES OF IBUPROFEN BY NEUTRALIZATION METHOD. **2010**, *10*.
- (116) Ikegami, K.; Kawashima, Y.; Takeuchi, H.; Yamamoto, H.; Isshiki, N.; Momose, D.; Ouchi, K. Simultaneous Particulate Design of Primary and Agglomerated Crystals of Steroid by Spherical Agglomeration in Liquid for Dry Powder Inhalation. *Powder Technol.* **2003**, *130*, 290–297.
- (117) Engel, G. L.; Farid, N. A.; Faul, M. M.; Richardson, L. A.; Winneroski, L. L. Salt Form Selection and Characterization of LY333531 Mesylate Monohydrate. *Int. J. Pharm.* **2000**, *198* (2), 239–247. [https://doi.org/10.1016/S0378-5173\(00\)00350-1](https://doi.org/10.1016/S0378-5173(00)00350-1).
- (118) Rajput, L. Stable Crystalline Salts of Haloperidol: A Highly Water-Soluble Mesylate Salt. *Cryst. Growth Des.* **2014**, *14* (10), 5196–5205. <https://doi.org/10.1021/cg500982u>.
- (119) Roustan, M. Agitation. Mélange - Caractéristiques des mobiles d'agitation. **2005**.
- (120) Roustan, M.; Pharamond, J.-C.; Line, A. Agitation. Mélange - Concepts théoriques de base. *Opérations Unit. Génie Réaction Chim.* **1999**. <https://doi.org/10.51257/a-v1-j3800>.
- (121) Saleh, K.; Guigon, P. Mise en œuvre des poudres - Granulation humide : bases et théorie. *Opérations Unit. Génie Réaction Chim.* **2009**. <https://doi.org/10.51257/a-v1-j2253>.
- (122) ICH Guideline Q3C (R8) on Impurities: Guideline for Residual Solvents, 2021.
- (123) Mallock, A. IV. Determination of the Viscosity of Water. *Proc R Soc Lond* **1889**, *45*, 126–132.
- (124) Couette, M. *Études sur le frottement des liquides, par M. Maurice Couette; Gauthier-Villars et fils, 1890.*
-

- (125) Couette, M. Distinction de deux régimes dans le mouvement des fluides. *J. Phys. Théorique Appliquée* **1890**, 9 (1), 414–424. <https://doi.org/10.1051/jphystap:018900090041401>.
- (126) Taylor, G. I. Stability of a Viscous Liquid Contained between Two Rotating Cylinders. *Proc. R. Soc. Lond. Ser. Contain. Pap. Math. Phys. Character* **1923**, 102 (718), 541–542. <https://doi.org/10.1098/rspa.1923.0013>.
- (127) Gu, Z. H.; Fahidy, T. Z. Characteristics of Taylor Vortex Structure in Combined Axial and Rotating Flow. *Can. J. Chem. Eng.* **1985**, 63 (5), 710–715. <https://doi.org/10.1002/cjce.5450630502>.
- (128) Moore, C. M. V.; Cooney, C. L. Axial Dispersion in Taylor-Couette Flow. *AIChE J.* **1995**, 41 (3), 723–727. <https://doi.org/10.1002/aic.690410329>.
- (129) Kataoka, K.; Doi, H.; Komai, T. Heat/Mass Transfer in Taylor Vortex Flow with Constant Axial Flow Rates. *Int. J. Heat Mass Transf.* **1977**, 20 (1), 57–63. [https://doi.org/10.1016/0017-9310\(77\)90084-9](https://doi.org/10.1016/0017-9310(77)90084-9).
- (130) Jung, T.; Kim, W.-S.; Choi, C. K. Effect of Monovalent Salts on Morphology of Calcium Carbonate Crystallized in Couette-Taylor Reactor. *Cryst. Res. Technol.* **2005**, 40 (6), 586–592. <https://doi.org/10.1002/crat.200410387>.
- (131) Kim, J.-M.; Chang, S.-M.; Chang, J. H.; Kim, W.-S. Agglomeration of Nickel/Cobalt/Manganese Hydroxide Crystals in Couette–Taylor Crystallizer. *Colloids Surf. Physicochem. Eng. Asp.* **2011**, 384 (1–3), 31–39. <https://doi.org/10.1016/j.colsurfa.2011.03.016>.
- (132) Jeon, D. H.; Song, J.-H.; Hong, J.-P.; Lee, S. H. Agglomeration of Li(NixMnyCoz)O2 Particles in Couette–Taylor Flow Reactor. *J. Ind. Eng. Chem.* **2019**, 76, 524–531. <https://doi.org/10.1016/j.jiec.2019.04.020>.
- (133) Thai, D. K.; Mayra, Q.-P.; Kim, W.-S. Agglomeration of Ni-Rich Hydroxide Crystals in Taylor Vortex Flow. *Powder Technol.* **2015**, 274, 5–13. <https://doi.org/10.1016/j.powtec.2015.01.008>.
- (134) Mayra, Q.-P.; Kim, W.-S. Agglomeration of Ni-Rich Hydroxide in Reaction Crystallization: Effect of Taylor Vortex Dimension and Intensity. *Cryst. Growth Des.* **2015**, 15 (4), 1726–1734. <https://doi.org/10.1021/cg501727v>.
- (135) Jung, T.; Kim, W.-S.; Choi, C. K. Effect of Nonstoichiometry on Reaction Crystallization of Calcium Carbonate in a Couette–Taylor Reactor. *Cryst. Growth Des.* **2004**, 4 (3), 491–495. <https://doi.org/10.1021/cg034240c>.
- (136) Wallace, C. H.; Oliveros, G.; Serrano, P. A.; Rockwell, P.; Xie, L.; Figueiredo-Pereira, M. Timapiprant, a Prostaglandin D2 Receptor Antagonist, Ameliorates Pathology in a Rat Alzheimer’s Model. *Life Sci. Alliance* **2022**, 5 (12), e202201555. <https://doi.org/10.26508/lsa.202201555>.
- (137) Coquerel, G.; Sanselme, M.; Lafontaine, A. Method of Measuring Scattering of X-Rays, Its Applications and Implementation Device. Patent WO2012136921, October 11, 2012.
- (138) Fardin, M. A.; Perge, C.; Taberlet, N. “The Hydrogen Atom of Fluid Dynamics” – Introduction to the Taylor–Couette Flow for Soft Matter Scientists. *Soft Matter* **2014**, 10 (20), 3523. <https://doi.org/10.1039/c3sm52828f>.
- (139) Esser, A.; Grossmann, S. Analytic Expression for Taylor–Couette Stability Boundary. *Phys. Fluids* **1996**, 8 (7), 1814–1819. <https://doi.org/10.1063/1.868963>.
- (140) Maron, D. M.; Cohen, S. Hydrodynamics and Heat/Mass Transfer near Rotating Surfaces. In *Advances in Heat Transfer*; Elsevier, 1991; Vol. 21, pp 141–183. [https://doi.org/10.1016/S0065-2717\(08\)70335-6](https://doi.org/10.1016/S0065-2717(08)70335-6).
- (141) Schrimpf, M.; Esteban, J.; Warmeling, H.; Färber, T.; Behr, A.; Vorholt, A. J. Taylor-Couette Reactor: Principles, Design, and Applications. *AIChE J.* **2021**, 67 (5), 1–24. <https://doi.org/10.1002/aic.17228>.

Appendices

Appendix I

Experimental part

Differential Scanning Calorimetry

DSC is a comparative method that serves to assess the thermal behavior of a sample with respect to a reference. DSC analyses were performed on a Netzsch Apparatus DSC 214 polyma with pierced aluminium pan. The used reference is an empty pierced aluminium pan.

Analyses were performed in a heat flux mode. HF-DSC consists in submitting two different systems, a reference and the sample to analyse, to a controlled temperature program. During the analysis, the temperature of the two pans is recorded, which serves to measure a difference of temperature (ΔT) between the sample and the reference. Then, the recorded signal is converted to specific heat flux absorbed by the sample using laws related to heat transfer. Deviations from baseline occur when the sample undergoes a thermal transformation (melting, glass transition, crystallization, etc).

By coupling the DSC thermic events with a thermogravimetric analysis (TGA-DSC), it is possible to assess the loss of mass during a thermic event related to desolvation or decomposition. TG-DSC-MS measurements were performed on Netzsch Simultaneous Thermal Analysis (STA) 449C under a helium gas flow in a pierced aluminium pan.

Powder X-ray diffraction

X-ray diffraction techniques are used to provide information about the crystal structure and to identify a crystalline(s) phase(s) of a material. The technic is based on the diffraction of an incident X-ray beam. The condition for diffraction is defined by Bragg's law:

$$n\lambda = 2d \sin \theta \quad \text{Equation I.1}$$

With n an integer, λ the characteristic wavelength of the X-ray hitting the sample, d the distance between reticular plans, and θ the angle of the X-ray beam

X-Ray diffraction patterns were measured with a D8-Discover diffractometer (Bruker, Germany) equipped with a θ/θ goniometer and operated at 40 kV. The incident X-ray beam wavelength is monochromatic (Cu K α radiation, $\lambda=1.5418 \text{ \AA}$) and samples scanned in the range of 3° to 30° (2θ) by steps of 0.04° (0.5 s per step) and 20 rpm of the sample holder at room temperature. Samples were prepared by gently crushing the agglomerates and spreading them on a glass plate. The Bruker software EVA was used for data treatment.

In-situX[®] is a diffraction technique designed to monitor crystallizations directly inside a reactor by means of XRPD with an inverted geometry ($-\theta / -\theta$). The sample is analyzed in-situ in suspension without any sampling¹³⁷. The sample to analyze (e.g., mixture of solid and liquid) is placed in a double-jacketed reactor. The temperature of the reactor can be accurately controlled in the $-80\text{ °C} / +70\text{ °C}$ temperature range. This set up could be adapted to analyze powder submitted to relative humidity (R.H.) variations. Inside a jacketed reactor few milligrams are stored, the R.H. can be controlled by using a humidity generator WETSYS (Setaram, France). In this configuration, the XRPD patterns of SAFIM powders were recorded in the range of 14 to 19° (2θ) by steps of 0.04° (0.5 s per step) for different RH and temperatures.

The presence of the different crystalline phases is given with respect to the limit of detection of the apparatus.

Optical and scanning electronic microscopy

Microscopic pictures were obtained thanks to different apparatus:

- Optical microscope NIKON Eclipse LV100 equipped with a CCD camera digital sight DS-RS1
- Numerical microscope KH-7700 from Hirox (Japan),
- Numerical microscope VHX-6000 from Keyence Corporation (Japan)

SEM was performed with a Jeol NeoScope JCM-5000. Prior to the analyses and in order to reduce the charges accumulations during observations, the particles were gold coated for 9 minutes with a NeoCoater MP-19020NCTR.

Dynamic Vapor Sorption (DVS)

Dynamic Vapor Sorption are used to characterize the interactions between solids and surrounding vapor under isothermal conditions. Water vapor sorption and desorption were carried out with a dynamic vapor sorption apparatus (DVS-one, Surface Measurement System, U.K.). Relative humidity (RH) was controlled through a continuous gas flow of pure nitrogen and a known amount of water vapor. Temperature and RH were measured with a precision of 0.1 °C and 0.5% , respectively. Mass variations were continuously recorded with a precision of $0.1\text{ }\mu\text{g}$.

Karl-Fischer titration

Determination of the water content was performed with both coulometric (899 Coulometer, Metrohm AG) and volumetric (795 KFT Titrino, Metrohm AG) Karl Fischer titrator equipped with an oven 860 KF Thermoprep (Metrohm AG). For coulometric measurement, solution was added directly in the Coulomat E reactant (HYDRANAL). For volumetric measurement, solutions were added directly in the reactant Composite 5 (HYDRANAL). Powders were heated to 200 °C during 300 s in a sealed vial

to be dehydrated. Gas water was trained through a 20 ml/min air flow into the reactant Composite 5 (HYDRANAL).

Flowability properties

Flowability was determined with Hausner's Ratio (HR; (Eq. I.II)), Carr's Index (CI; (Eq. I.III)), and the angle of repose.

$$HR = \frac{\text{tapped density}}{\text{bulk density}} \quad \text{Equation I.II}$$

$$CI (\%) = \frac{(\text{tapped density} - \text{bulk density})}{\text{tapped density}} \quad \text{Equation I.III}$$

Tapped density was obtained by adding a known volume of powder in a graduated cylinder (4 cm diameter). Then, after using a tapping device, the volume of the powder was measured after 200 taps.

The angle of repose (°) was measured by using a fixed funnel apparatus (Figure I-I) equipped with a digital gauge. The funnel was fixed at 15 cm from the base (7 cm diameter).

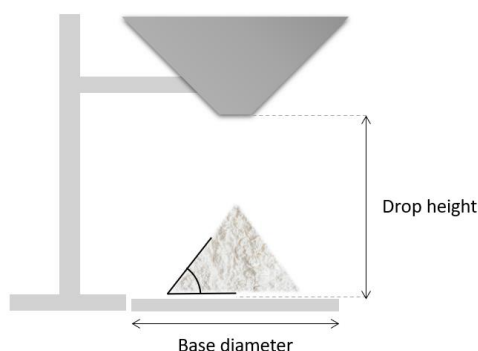


Figure I-I: Schematic representation of the fixed funnel apparatus (flowdex™)

Classification of powder flowability based on HR, CI and angle of repose is given in Table I-I.

Table I-I. Flowability classification according to Hausner ratio, Carr index and angle of repose

Description	HR	CI (%)	Repose angle (°)
Very free flowing	< 1.11	< 10	< 30
Free flowing	1.12 – 1.18	10 – 15	30 – 38
Fair to passable flow	1.19 – 1.25	16 – 20	38 – 45
Cohesive	1.26 – 1.34	21 – 25	45 – 55
Very Cohesive	1.35 – 1.45	> 26	> 55

Head Space Gas Chromatography

Analyses were performed using a Scion 436 GC system coupled to a quadrupole mass spectrometer and equipped with a Combipal headspace autosampler. Static headspace equilibrium was performed at 80 °C for 60 min, while shaking at 250 rpm was applied during sample heating 1000 µl of headspace gas were injected using a heated (90 °C) gastight syringe (2.5 mL) in split mode 1:20 (inlet temperature was 250 °C). Separation was performed on a column HP1 (30 m x 0.32 mm, 5.0 µm thickness). The carrier gas was He at a constant flow rate of 1.5 L/min. The column oven temperature was initially set at 30 °C for 20 min and then was increased to 250 °C at 10 °C/min and held for 10 min.

The quadrupole, source and transfer line were maintained at 250 °C. Electron ionization mass spectra in full scan (m/z 33 to 100 range) and SIM (acetonitrile: m/z 39 and 38 between 2.1±1 min; n-heptane: m/z 57 and 71 between 17.7±1 min) modes were recorded at 70 eV electron energy. 100, 200, 300, 400 and 1000 ppm acetonitrile and n-heptane external standards were used to determine the amount of residual solvent in the samples.

Calibration curve:

A calibration curve was made with the preparation of standard solution containing 100, 200, 300, 400, 500, 700, and 1000 ppm of acetonitrile and n-heptane with 1 mL of DMSO and 10 mL of deionized water in 20 mL headspace vials (figure I-II).

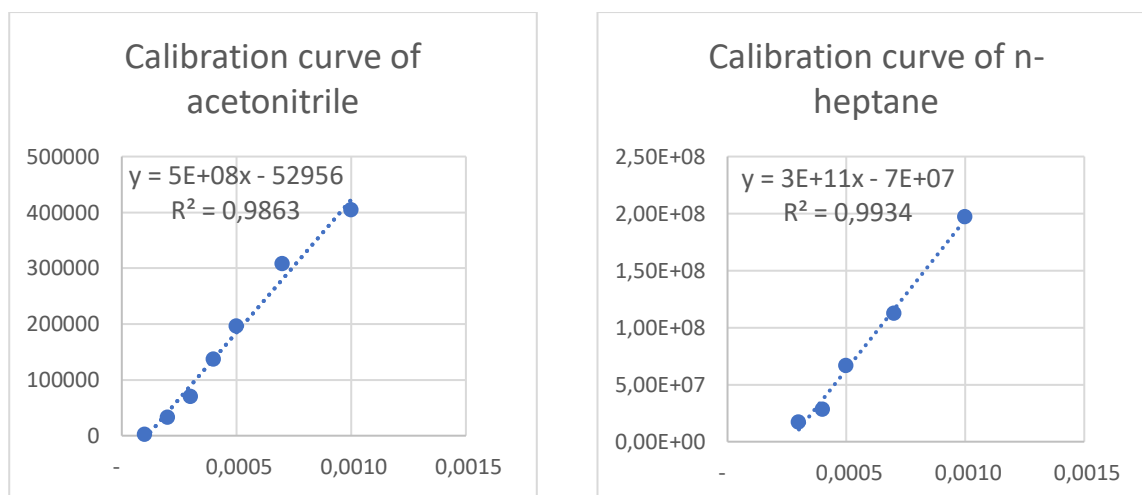


Figure I-II: GC-Head Space calibration curves of acetonitrile and n-heptane

HS-GC-MS Sample preparation:

Approximatively 100 mg of agglomerated SAFIM were placed in a 20 mL Headspace vials with 1 mL of DMSO and 10 mL of deionized water.

Solubility measurement (dry residue method)

Solubilities were determined according to the dry residue method.

Two suspensions of the solid were prepared in a jacketed vessel at a given temperature and stirred for 24 h. Then, the suspensions were filtered with a 0.45 μm PTFE filter and divided in 20 vials. After complete evaporation of the solvent, the solutes were weighted to determine the solubility of the solid.

Appendix II

Storage of **A1** with a varying amount of **H1** versus time for different relative humidities

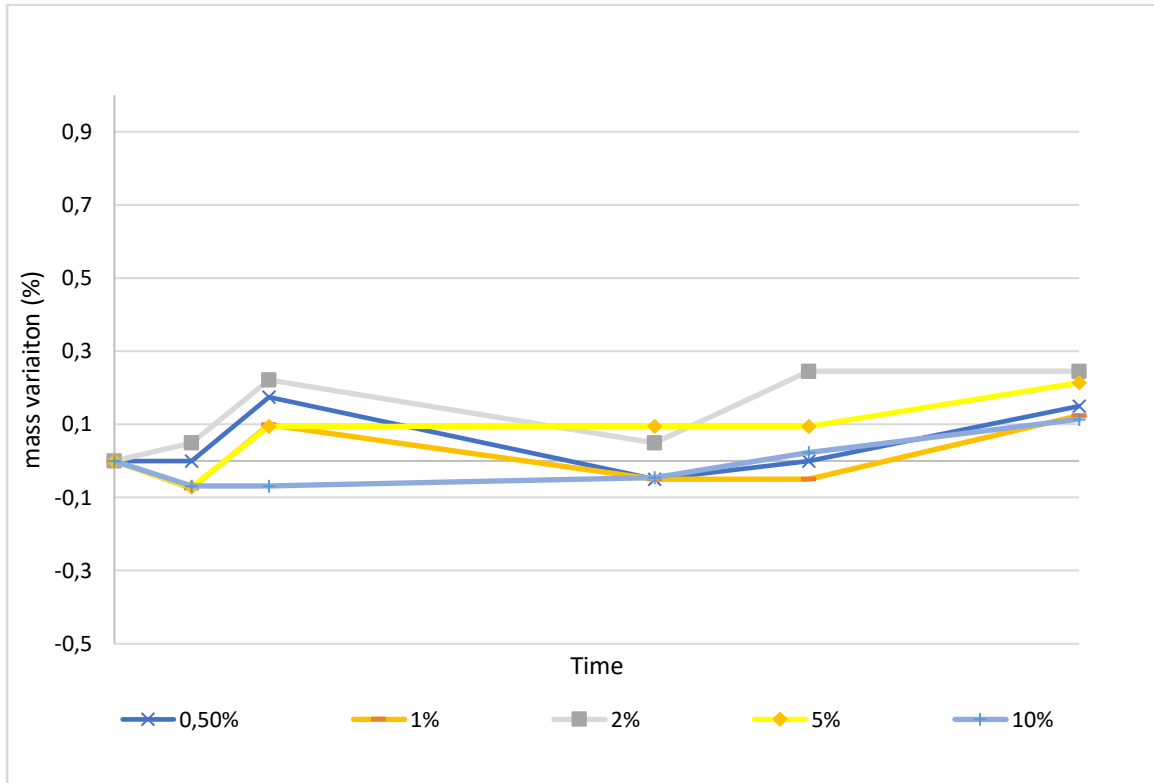


Figure II-I: variation of the mass vs time for different amount of H1 in A1 batch at 32.8 %RH

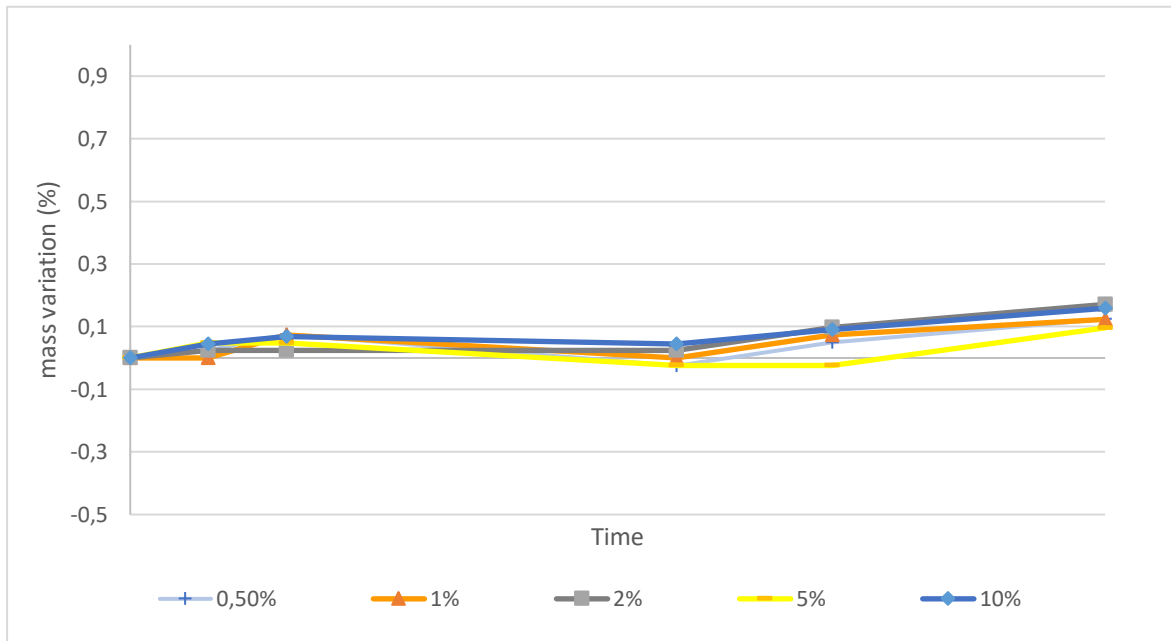


Figure II-II: variation of the mass vs time for different amount of H1 in A1 batch at 43%RH

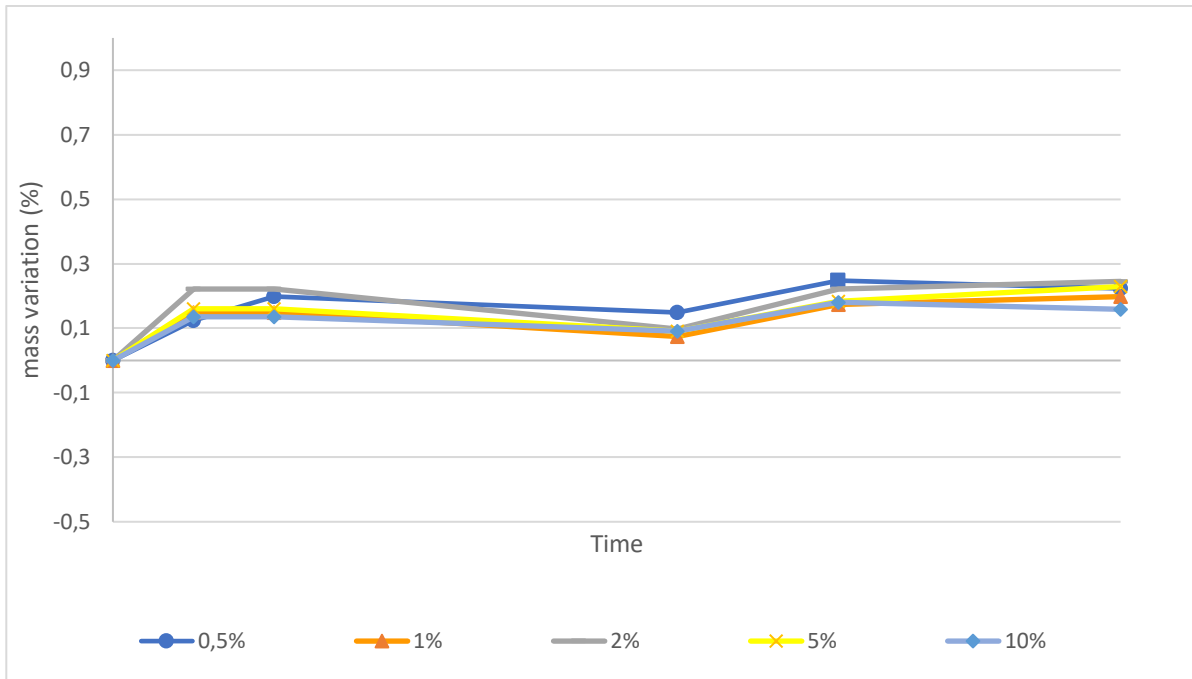


Figure II-III: variation of the mass vs time for different amount of H1 in A1 batch at 57,6%RH

Appendix III

Evolution of the crystalline phase for different amount of water in the BL

Addition of 1%_{wt} of water:

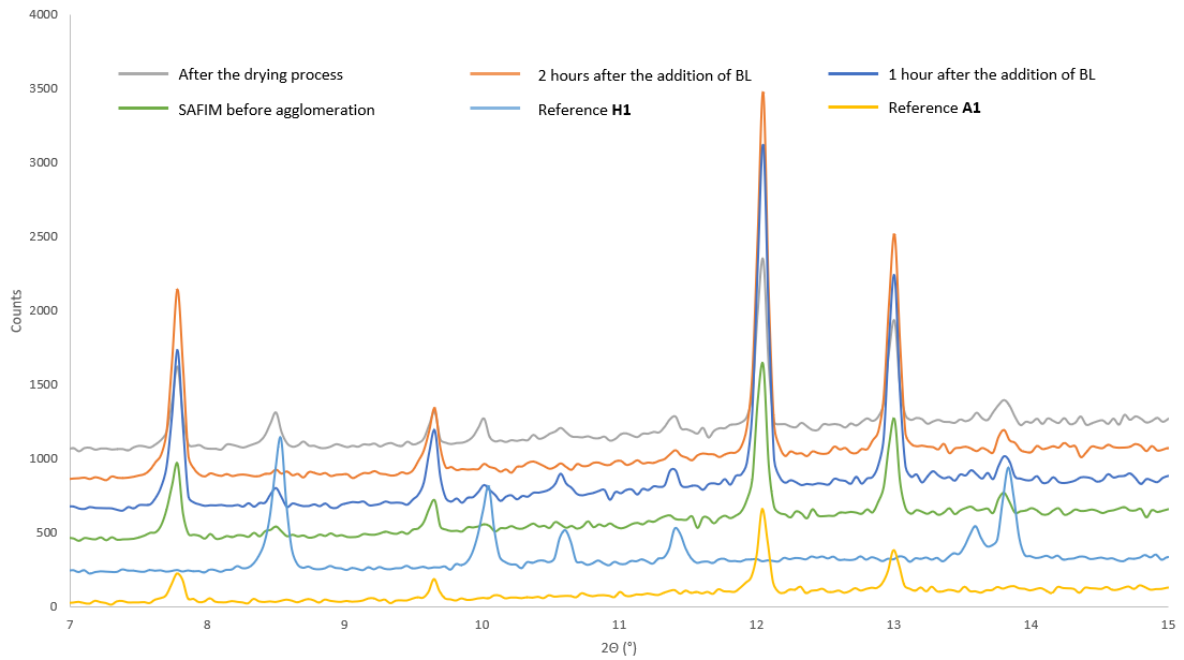


Figure III-I: XRPD patterns showing the evolution of the crystalline phase during SAFIM spherical agglomeration with the addition of 1%_{wt} of water in the BL

Addition of 2%_{wt} of water:

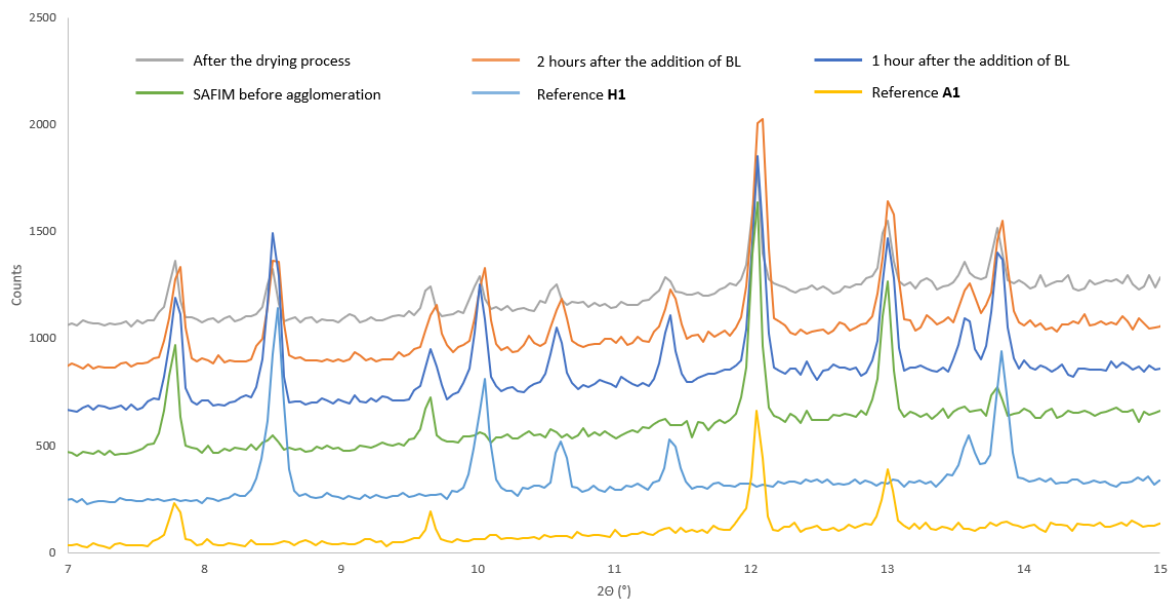


Figure III-II: XRPD patterns showing the evolution of the crystalline phase during SAFIM spherical agglomeration with the addition of 2%_{wt} of water in the BL

Addition of 3%_{wt} of water:

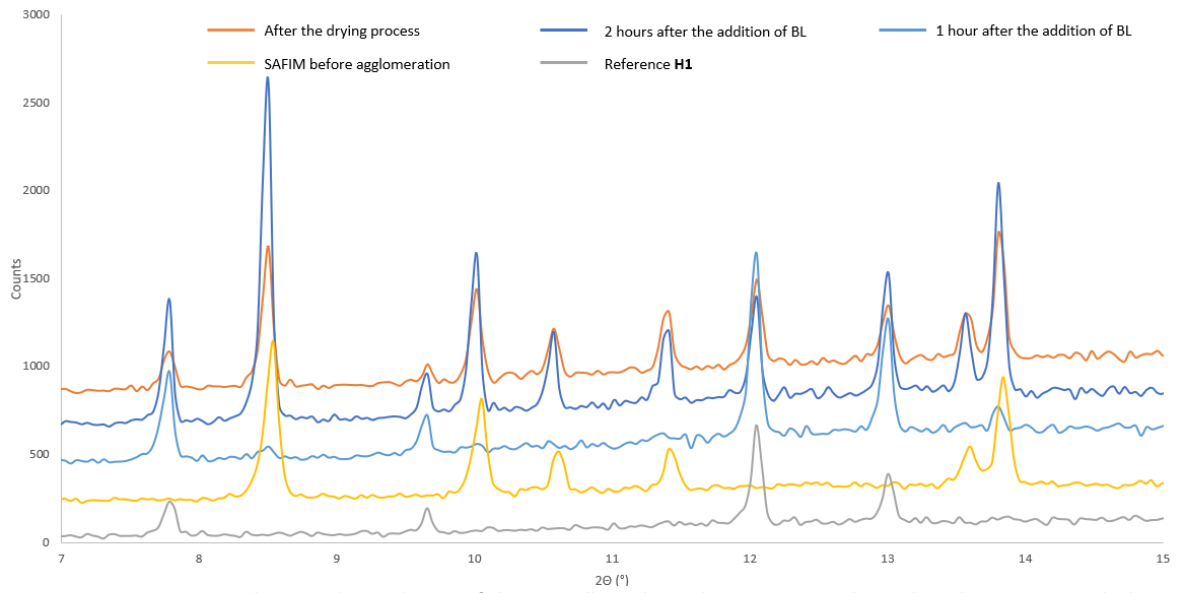


Figure III-III: patterns showing the evolution of the crystalline phase during SAFIM spherical agglomeration with the addition of 3%_{wt} of water in the BL

Addition of 4%_{wt} of water:

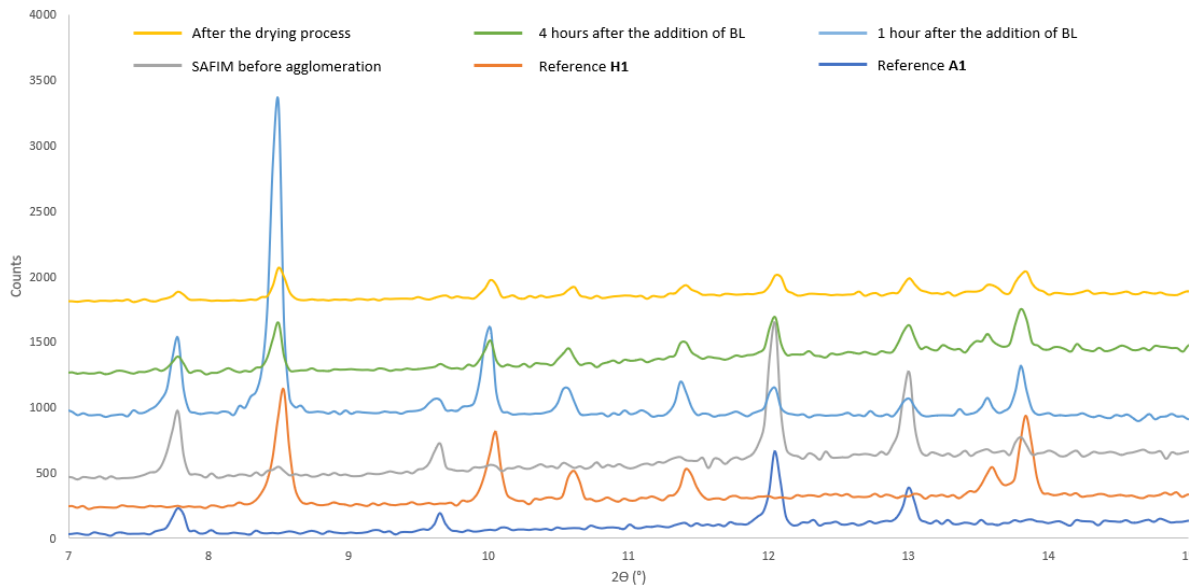


Figure III-IV: XRPD patterns showing the evolution of the crystalline phase during SAFIM spherical agglomeration with the addition of 4%_{wt} of water in the BL

Addition of 10%_{wt} of water:

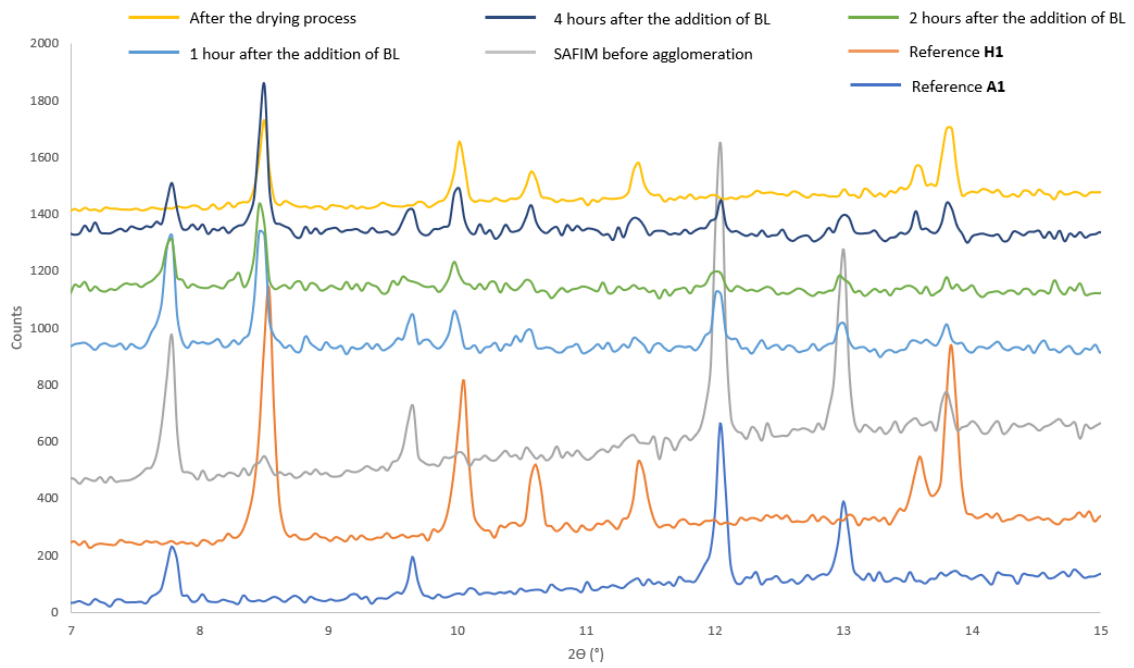


Figure III-V: XRPD patterns showing the evolution of the crystalline phase during SAFIM spherical agglomeration with the addition of 10%wt of water in the BL

Appendix IV

Flow regimes occurring in the Couette Taylor crystallizer

As previously mentioned, different flow regimes can occur between two rotating cylinders as a function of the rotation rate, ranging from laminar to turbulent flow regime. The Reynold's number (Re) is commonly used to characterize the flow regime in a cylinder:

$$Re = \frac{V D}{\nu}$$

With V the velocity of the fluid, D the inner diameter of the cylinder and ν the kinematic viscosity of the fluid.

Low value of Re leads to a laminar flow where higher value of Re leads to turbulent flow.

Based on the Reynold's number, Taylor has proposed the Taylor's number (Ta) to characterize the different flow regimes that occur in the CTR:

$$Ta = \frac{\Omega^2 r d^3}{\nu^2}$$

With Ω the rotation speed of the inner cylinder, r the inner cylinder radius, d the distance between the two concentric cylinders and ν the kinematic viscosity.

Taylor's vortices are obtained above a critical value of Ta called critical Taylor number (Ta_c). This mainly depends on the cylinder diameter ratio $\lambda = \frac{d_i}{d_o}$ and the rotation speed. Different equations for calculation of Ta_c have been proposed in the literature (Table IV-I).

Table IV-I: Equations to determine Taylor critical number

Equation	Reference
$Ta_c = 41.2 * \sqrt{\frac{\lambda}{1-\lambda}}$	138
$Ta_c = \frac{1}{0.1556^2} * \frac{(1+\lambda)^2}{\sqrt{(1-\lambda)(3+\lambda)}}$	139
$Ta_c = Ta_c(Re_z = 0) + 26.5 Re_z^2$	140

In the two first equations, there is no consideration about the presence of an axial flow in the CTR. Maron *et al.*¹⁴⁰ proposed a corrected critical Taylor number as a function of the axial flow (Re_z).

The different flow regimes can be characterized from the ratio $\frac{Ta}{Ta_c}$ and are given in Table and illustrated in Figure IV-1.

Table IV-II: The different flow regimes occurring in the CTR as a function of Ta/Ta_c ratio

Ta/Ta_c	Flow regime
$Ta/Ta_c < 1$	Laminar Couette flow
$1 < Ta/Ta_c < 9$	Laminar periodic Taylor vortex flow
$9 < Ta/Ta_c < 176.89$	Singly periodic wavy vortex flow
$176.89 < Ta/Ta_c < 324$	Doubly periodic wavy vortex flow
$324 < Ta/Ta_c < 1089$	Weakly turbulent wavy vortex flow
$1089 < Ta/Ta_c < 25600$	Turbulent vortex flow
$25600 < Ta/Ta_c$	Turbulent aperiodic flow

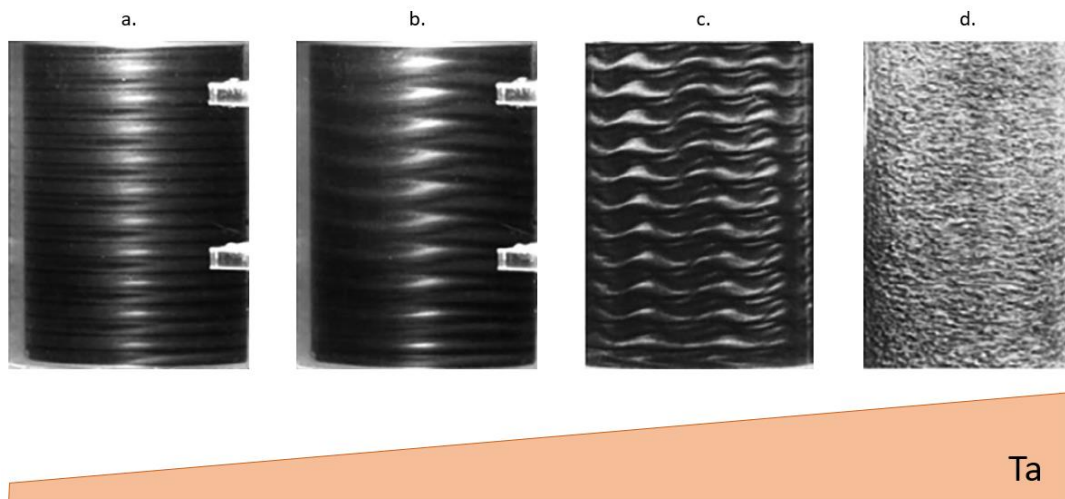


Figure IV-1: Transition of the major flow regimes in a CTR as a function of Ta : a. Taylor vortex flow, b. Wavy vortex flow, c. modulated wavy vortex flow, and d. turbulent flow from Schimpf et al.¹⁴¹

Control of Powder Flowability of Active Pharmaceutical Ingredients through Spherical Agglomeration: Case studies of crystal structure retention

Abstract

From an industrial pharmaceutical point of view, the control of crystalline landscape as well as flowability properties of powders are major issues. After the presentation of a new case of isomorphous desolvate of an API, this work describes the development of a method designed to control the crystalline phase and flowability properties of safinamide mesylate. First, with a complete study of the crystalline landscape, conditions were identified to obtain the targeted form (anhydrous **A1**). Then, the development and optimization of the spherical agglomeration are presented. The spherical agglomeration is a process to obtain spherical agglomerates from fine particles with poor flowability properties. The obtained agglomerates exhibit enhanced flowability properties. One of the benefits of this method is to combine both crystallization and granulation steps into a single one avoiding any industrial production extra cost. In the case of safinamide mesylate, spherical agglomerates with an average diameter of 750 μm were obtained in **A1** crystalline form. Finally, a last part is dedicated to the development of the continuous agglomeration process in a Couette-Taylor Crystallizer. Even if some agglomerates were obtained. The process needs further optimization to solve all the problems that occurred during the study.

Keywords: polymorphism, crystalline landscape, hydrate, solvate, spherical agglomeration, Couette-Taylor

Résumé

Parmi les enjeux majeurs de l'état solide dans l'industrie pharmaceutique, la forme cristalline ainsi que les propriétés d'écoulement des poudres font partis des plus importants. Après la présentation d'un nouveau cas d'isomorphe desolvate d'un ingrédient pharmaceutique, ces travaux décrivent le développement d'une méthode permettant de contrôler simultanément la forme cristalline du sel de mesylate de la safinamide ainsi que ses propriétés d'écoulement. Tout d'abord, l'étude complète de son paysage cristallin a permis d'identifier les conditions permettant d'obtenir la forme anhydre désirée (**A1**). Puis le développement du procédé d'agglomération sphérique de cette molécule est présenté. L'agglomération sphérique est un procédé d'obtention d'agglomérats sphériques à partir de particules fines permettant un contrôle de la taille des agglomérats finaux et par conséquent des propriétés d'écoulement du solide ainsi obtenues. Cette méthode présente l'avantage de combiner les étapes de cristallisation et de granulation évitant ainsi des surcoûts de production. Après le développement et l'optimisation du procédé, des agglomérats sphériques d'un diamètre moyen de 750 μm ont pu être obtenus sous forme anhydre **A1**. Enfin, une dernière partie est consacrée à l'étude de faisabilité du procédé continu d'agglomération dans un réacteur de type Couette Taylor. Bien que des agglomérats aient pu être obtenus au cours du procédé, celui-ci nécessite encore d'être amélioré pour résoudre les différents problèmes rencontrés.

Mots clés : polymorphisme, paysage cristallin, hydrate, solvate, agglomération sphérique, Couette-Taylor